



**NASA/ OHIO SPACE GRANT
CONSORTIUM**

**2021-2022 ANNUAL
STUDENT RESEARCH SYMPOSIUM
PROCEEDINGS XXIX**



NASA Astronaut, Jessica Watkins, floats in the International Space Station's cupola; a direct nadir viewing window from which Earth and celestial objects are visible.

Photo Courtesy of NASA

**March 25, 2022
Virtual Symposium
Cleveland, Ohio**



Follow OSGC on:



*Just click on any name, and it will link you
to the page immediately!*

TABLE OF CONTENTS

Table of Contents	<u>Page(s)</u> 2-5
Foreword	6
Membership	7
Acknowledgments	8
Symposium Presentations	9

<u>Fellows</u>	<u>University</u>	<u>Page</u>
Behnke, Lily C.	University of Dayton.....	11
Bensignor, Isaac S.....	The Ohio State University.....	14
Bowser, Blake A.	The University of Akron	17
Brooks, Scott L.	Ohio University	19
Brum, Jared T.....	Miami University	22
Eby, Oliver G.....	The University of Toledo	25
Ferguson, Christopher A.....	The University of Akron.....	31
Klausing, Lanna N.....	University of Dayton.....	34
Leahy, Ryan P.....	The Ohio State University.....	41
Martin, Jacob M.	Cleveland State University	47
O'Donnell, Jacob C.....	The University of Toledo	49
Pickering, Lynn K.	University of Cincinnati	53
Rickman, William L.....	Miami University	55
Stanley, Joshua W.	The University of Toledo	59
Wnek, James G.	Wright State University.....	61

<u>Scholars</u>	<u>College/University</u>	<u>Page</u>
Barto, Madeline G.	Case Western Reserve University	64
Beckett, Joseph G.	University of Dayton.....	67
Bidart Ferrer, Isabella	The Ohio State University.....	70
Blackey, Tyler L.	Youngstown State University	74
Bollinger, Alec C.	Marietta College.....	76
Bothe, Anthony M.	Ohio Northern University	79
Brandt, Patrick J.	The Ohio State University.....	82

<u>Scholars</u>	<u>College/University</u>	<u>Page</u>
Bryson, Elizabeth M.	Baldwin Wallace University	84
Carner, Zachary J.	Wright State University.....	86
Cephas, Zackry D.	Wilberforce University	88
Colbrunn, Boyd W.	Miami University	90
Connolly, Jacob A.	The University of Toledo	93
D'Alesandro, Sabrina R.	Wright State University.....	96
Decato, Kevin H.	The University of Toledo	99
Devillier, Amanda M.	University of Cincinnati	102
Douglass, Natalie S.	University of Dayton.....	105
Du, Kevin	Case Western Reserve University	108
Dundore, Trevor A.	The Ohio State University.....	110
Eaton, Miranda L.	Miami University	114
Ellis, Rebecca L.	Cleveland State University	117
Etheridge, Emily N.	Marietta College	119
Fetter, Gregory	Miami University	121
Floring, Grace N.	Case Western Reserve University	124
Galigher, Olivia F.	Ohio Northern University	128
Glaubitz, Peter H.	University of Cincinnati	131
Grant, Devin R.	Central State University	133
Gravenstein, Amy R.	The University of Akron.....	138
Hagerman, Jude V.	Baldwin Wallace University	141
Heitmeyer, Daniel R.	University of Cincinnati	144
Herbruck, Sarah C.	Miami University	147
Hughes, Allayah C.	Wilberforce University	149
Katterle, Karli T.	Ohio Northern University	151
Kent, Conrad M.	University of Cincinnati	153
Klinger, Zion E. J.	Ohio University	156
Larson, Tanner L.	Cleveland State University	159
Lemieux, Sebastian J.	University of Cincinnati	162
Lipec, Daniel E.	Ohio University	166
Mangel, Alexandra P.	Ohio State University	167
Mansell, Jacob G.	Baldwin Wallace University	171

<u>Scholars</u>	<u>College/University</u>	<u>Page</u>
Marshall, David K.	The Ohio State University.....	174
McGee, Derek I.	Wilberforce University	178
McKibben, Austin L.	Ohio University	180
Messuri, Victoria N.	Youngstown State University	182
Meyer, Brooke N.	Ohio Northern University	186
Motzko, Tyler J.	Wright State University.....	188
Nowery, Stuart T.	Cedarville University	192
Richards, Natalie S.	The University of Akron.....	194
Romeo, Anthony J.	Youngstown State University	197
Sauder, Ryan R.	Ohio Northern University	201
Schauer, Abigail C.	Ohio Northern University	203
Speare, Lindsey A.	Kent State University	205
Strong, Aubrey C.	Cedarville University	208
Swift, Andrew T.	Cedarville University	210
Sychla, Jakub	The University of Akron.....	213
Terry, Marcus J.	Marietta College.....	215
Tomlin, Kevin J.	Wright State University.....	217
Wang, Naomi C.	Kent State University	219
Ward, Joshua T.	Wright State University.....	221
Willi, Kaitlin R.	Wright State University.....	223
Wittlinger, Marcus W.	Cleveland State University	229
Wood, Madison M.	Kent State University	231
Yoder, Samuel T.	The Ohio State University.....	233

<u>Community College Scholars</u>	<u>Community College</u>	<u>Page</u>
Harris, Mickela N.	Cincinnati State Technical and Community College	239
Kump, Michael A.	Lorain County Community College.....	242
Martin, Sara A.	Lorain County Community College.....	244
Palmer, Ryan M.	Lorain County Community College.....	247
Surgeon, Nathaniel A.	Columbus State Community College.....	249
Valescu, Nicholas W.	Lorain County Community College.....	251
Williams, Emily T.	Lorain County Community College.....	253

<u>Education Scholars</u>	<u>College/University</u>	<u>Page</u>
Ackley, Alayna P.	Baldwin Wallace University	256
Brown, Joelena F.	Ohio Northern University	258
Chappell, Makenna R.	Ohio Northern University	260
Harbaugh, Rachael D.	Ohio Northern University	262
Hippich, Emily M.	Kent State University	264
Marcus, McKenna J.	Baldwin Wallace University	267
Penton, Kayleigh E.	The University of Akron.....	269
Reinhard, Isaiah A.	Cedarville University	271
Schwartz, Erica D.	Baldwin Wallace University	274

FOREWORD

The Ohio Space Grant Consortium (OSGC), a member of the NASA National Space Grant College and Fellowship Program, awards graduate fellowships and undergraduate scholarships to students working toward degrees in Science, Technology, Engineering and Mathematics (STEM) disciplines at OSGC-member universities. The awards are made to United States citizens, and the students are competitively selected. Since the inception of the program in 1989, over 1,395 undergraduate scholarships and 274 graduate fellowships have been awarded.

Matching funds are provided by the 24 member universities/community colleges, the Ohio Aerospace Institute (OAI), and the Ohio Department of Higher Education (State of Ohio). Note that this year ~ \$500,000 will be directed to scholarships and fellowships representing contributions from NASA, the Ohio Aerospace Institute, State of Ohio, member universities, foundations, and industry.

By helping more students to graduate with STEM-related degrees, OSGC provides more qualified technical employees to industry. The research conducted for the Master's fellowship must be of interest to NASA. A prime aspect of the scholarship program is the undergraduate research project that the student performs under the mentorship of a faculty member. This research experience is effective in encouraging U. S. undergraduate students to attend graduate school in STEM. The Education scholarship recipients are required to attend a workshop conducted by NASA personnel where they are exposed to NASA educational materials and create a lesson plan for use in their future classrooms.

Due to COVID-19, the Annual Student Research Symposium scheduled for Friday, March 25, 2022, at the Ohio Aerospace Institute was made virtual through WebEx. A recording of the virtual Symposium is available on the OSGC website at: <http://osgc.org/event-material/>

Research reports of students from the following schools are contained in this publication:

Affiliate Members

- The University of Akron
- Baldwin Wallace University
- Case Western Reserve University
- Cedarville University
- Central State University
- Cleveland State University
- University of Dayton
- Kent State University
- Marietta College
- Miami University
- Ohio Northern University
- The Ohio State University
- Ohio University
- University of Cincinnati
- The University of Toledo
- Wilberforce University
- Wright State University
- Youngstown State University

Community Colleges

- Cincinnati State Technical and Community College
- Columbus State Community College
- Lakeland Community College
- Lorain County Community College
- Sinclair Community College

MEMBER INSTITUTIONS

Affiliate Members

- Baldwin Wallace University..... James W. McCargar, Ph.D.
- Case Western Reserve University..... Roger D. Quinn, Ph.D.
- Cedarville University Robert Chasnov, Ph.D., P.E.
- Central State University Augustus Morris, Jr., Ph.D., P.E.
- Cleveland State University Wei Zhang, Ph.D.
- Kent State University Joseph D. Ortiz, Ph.D.
- Marietta College Dr. Andrew Beck
- Miami University James Moller, Ph.D., P.E.
- Ohio Northern University..... Jed E. Marquart, Ph.D., P.E.
- The Ohio State University Dr. Mo Samimy
- Ohio University Dr. Roxanne Male'-Brune
- The University of Akron Dr. Julie Zhao
- University of Cincinnati Dr. Kelly Cohen
- University of Dayton Dr. Robert J. Wilkens
- The University of Toledo Dr. Lesley M. Berhan
- Wilberforce University Deok Hee Nam, Ph.D.
- Wright State University Mitch Wolff, Ph.D.
- Youngstown State University Byung-Wook Park, Ph.D.

Campus Representative

Community Colleges

- Cincinnati State Technical and Community College Professor Abigail Yee
- Columbus State Community College Professor Jeffery M. Woodson, M.S., I.E.
- Cuyahoga Community College Prof. Michelle S. Davis
- Lakeland Community College..... Professor Rick Bartlett
- Lorain County Community College Regan L. Silvestri, Ph.D.
- Sinclair Community College..... Eric C. Dunn

Campus Representative

NASA Glenn Research Center - Representatives

- Dr. M. David Kankam
- Ms. Susan M. Kohler



ACKNOWLEDGMENTS

Thank you to all who helped with the OSGC's landmark 30th Annual Research Symposium!

Keynote Speaker:

★ Dr. Julian Earls, former NASA Glenn Center Director, for his witty, insightful talk.

Campus Representatives – 4-Year Universities

- Dr. James W. McCargar, Baldwin Wallace University
- Dr. Roger Quinn, Case Western Reserve University
- Robert Chasnov, Ph.D., P.E., Cedarville University
- Augustus Morris, Jr., Ph.D., P.E., Central State University
- Wei Zhang, Ph.D., Cleveland State University
- Dr. Joseph D. Ortiz, Kent State University
- Dr. Andrew Beck, Marietta College
- James Moller, Ph.D., P.E., Miami University
- Jed E. Marquart, Ph.D., P.E., Ohio Northern University
- Dr. Mo Samimy, The Ohio State University
- Dr. Roxanne Male'-Brune, Ohio University
- Dr. Julie Zhao, The University of Akron
- Dr. Kelly Cohen, University of Cincinnati
- Dr. Robert J. Wilkens, University of Dayton
- Dr. Lesley M. Berhan, The University of Toledo
- Deok Hee Nam, Ph.D., Wilberforce University
- Mitch Wolff, Ph.D., Wright State University
- Dr. Byung-Wook Park, Youngstown State University

Campus Representatives - Community Colleges

- Professor Abigail Yee, Cincinnati State Technical and Community College
- Professor Jeffery M. Woodson, M.S., I.E., Columbus State Community College
- Professor Michelle S. Davis, Cuyahoga Community College
- Professor Rick Bartlett, Lakeland Community College
- Regan L. Silvestri, Ph.D., Lorain County Community College
- Eric C. Dunn, Sinclair Community College

Special thanks go out to the following:

- Dr. John Sankovic, President and CEO – OAI, for supporting the OSGC and hosting this event.
- Mark Cline, Senior Manager, Information Technology – OAI, whose expertise made the virtual forum not only possible, but a huge success!
- Robert Romero, Director – OSGC, for his enthusiasm and vigor in leading the Ohio Space Grant Consortium.



30th Annual OSGC Student Research Symposium – Virtual Event
Ohio Aerospace Institute (OAI)
Friday, March 25, 2022

- 9 – 9:15 a.m. Welcome and Introductions (15 minutes)
John M. Sankovic, Ph.D., P.E.
 President and CEO, Ohio Aerospace Institute
- 9:15 – 9:25 a.m. Program Background and Updates (10 minutes)
Robert Romero
 Director, Ohio Space Grant Consortium
- 9:25 – 10:25 a.m. Student Presentations – Block 1
Tim Hale – Session Chair
 Interim Program Manager, OSGC, OAI
- Scott L. Brooks* Master’s 1, Biomedical Engineering, Ohio University
Sarah C. Herbruck Senior, Mechanical Engineering, Miami University
Isaac S. Bensignor Master’s 2, Aerospace Engineering, The Ohio State University
Andrew T. Swift Junior, Geology, Cedarville University
- 10:25 – 10:30 a.m. Break (5 minutes)
- 10:30 - 11:30 a.m. Student Presentations – Block 2
Tim Hale – Session Chair
 Interim Program Manager, OSGC, OAI
- Joseph G. Beckett*Senior, Mechanical Engineering, University of Dayton
Mickela N. HarrisSophomore, Pre-Engineering, Cincinnati State Technical and
 Community College
Jakub Sychla..... Junior, Aerospace Systems Engineering, The University of Akron
Zion E.J. KlingerSenior, Computer Science, Ohio University
- 11:30 a.m. – 12:00 p.m. Keynote Speech
 Dr. Julian Earls, Director (Ret.), NASA Glenn Research Center
- 12:00 – 12:10 p.m. Closing Remarks
Robert Romero
 Director, OSGC
- Tim Hale*
 Program Manager, OSGC, OAI
 Symposium Adjourns

Fellows

Optimized Sustainable Aviation Fuels for Increased Energy Consumption of Jet Engines

Student Researcher: Lily C. Behnke

Advisor(s): Dr. Joshua S. Heyne, Dr. Randall C. Boehm

University of Dayton

Department of Mechanical and Aerospace Engineering

Abstract

As anthropometric emissions continue to rise globally, reducing emissions from combustion systems is critical to environmental preservation. It is understood that a method for decreasing emissions contributions from the aviation sector is sustainable aviation fuel (SAF). SAF adoption relies on the ability to maintain or surpass the current performance metrics of petroleum derived fuels while also complying with critical operability limitations. High thermal stability SAFs have the potential to provide value in terms of reducing maintenance costs associated with coking and the ability to drive more heat into the fuel therefore increasing energy delivered to the combustor. It was determined that SAFs composed of mostly cycloalkanes with some aromatics maximize the engine-level energy savings for a general flight mission. This result is likely tied to the effects of H/C ratio on turbine performance. It is anticipated that with increased computational time, greater convergence will be achieved for the overall pareto front of optimized SAF mixtures. This work provides preliminary results for the design of a high thermal stability SAF that will increase savings over the course of a mission requiring operation at both low and high power engine conditions respectively.

Introduction and Objectives

A recent solution for minimizing the anthropometric emissions contributions from combustion systems is sustainable aviation fuel (SAF) [1]. It is understood that SAFs have the potential to improve upon performance characteristics in comparison to conventional aviation fuels through both increased fuel thermal stability and total energy content. Increased thermal stability allows greater waste heat recovery from the fuel and, in turn, more energy delivered to the combustor while also decreasing the reliability of air as a coolant [2]. Furthermore, increased thermal stability can have added cost benefits by reducing aircraft maintenance costs associated with fuel degradation and coking at high temperatures. Previous work has aimed to validate methodologies to model the effects of varying SAF properties on engine-level energy savings [3]. The focus of this report is to identify optimized SAF species and mixtures that simultaneously maximize LHV and savings benefits comparable to conventional fuels.

Methodology

The general methodology for this analysis can be observed in Fig. 1. It details the optimization process using JudO (Jet Fuel Blend Optimizer) for SAF compositions. First, a random initial guess operation selected SAF mixture mole fractions from a database of 1,125 SAF species. Due to the number of species in the database, the maximum number of species for each mixture was constrained to 20 to avoid species being selected with nearly negligible concentrations. Then the generated SAF mixture fuel properties were calculated using blending rules established in the literature [4]. The fuel properties were evaluated with a filter to determine if the SAF properties met ASTM specifications. If so the SAF

was then passed through a novel fuel system thermal model (FSTM) and engine performance model (EPM). These models were used to quantify the thermal stability benefits of the SAFs by calculating the waste heat recovery, temperature rise, and final savings value for SAFs as a function of its unique fuel properties. The FSTM and EPM contain both high and low engine operating conditions to simulate the extreme fuel flow metrics over the course of a standard flight mission. These two operating conditions were combined into a summary savings metric for the scope of this work. Next, utilizing mixed ant colony optimization software (MIDACO) and pareto front analysis, optimized fuel mixtures maximizing lower heating value (LHV) and savings were identified. The final optimized pareto front contains SAF mixtures of maximized LHV and savings metrics with properties within the required ASTM specifications for the aviation fuel approval process.

Results and Discussion

While previous work focused on outlining the methodology for obtaining the savings value, these results investigate the SAF species and functional groups best suited for simultaneous savings and LHV benefits. The results of the optimization show the relationship between the combined mission savings metrics and corresponding SAF fuel compositions. Fig 2. shows the breakdown by functional group of the overall pareto front of optimized SAF compositions. The blue inner wedge represents the frequency of alkanes present in the overall pareto front while the red and green inner wedges represent cycloalkane and aromatic frequencies respectively. In this analysis cycloalkanes included monocycloalkanes, bicycloalkanes, and tricycloalkanes, and aromatics include aromatics, cycloaromatics, and naphthalenes. It can be observed in the inner circle of Fig. 2 that the majority of molecules present in the pareto front are alkanes (56.4%) and cycloalkanes (38.7 %) with some aromatic content (< 5%). The outer pie chart of Fig 2. specifies the three most selected molecules from each functional group detailed in the inner circle. These three molecules are denoted by the darker shaded wedges of each color scheme in the outer circle. The lightest wedge for each color on the outer circle represents all other molecules present in the pareto front belonging to that functional group. Identifying these highly selected molecules from the overall pareto front allows for the determining of SAF species that have the potential to yield savings and LHV benefits to collectively improve upon conventional jet fuel performance metrics as a sustainable alternative. Future continuation of this work includes increased computational time allotted for exploration of optimal mixtures. Furthermore, following the combined optimization, SAF identified optimal species will be experimentally tested for thermal oxidative stability metrics.

Figures

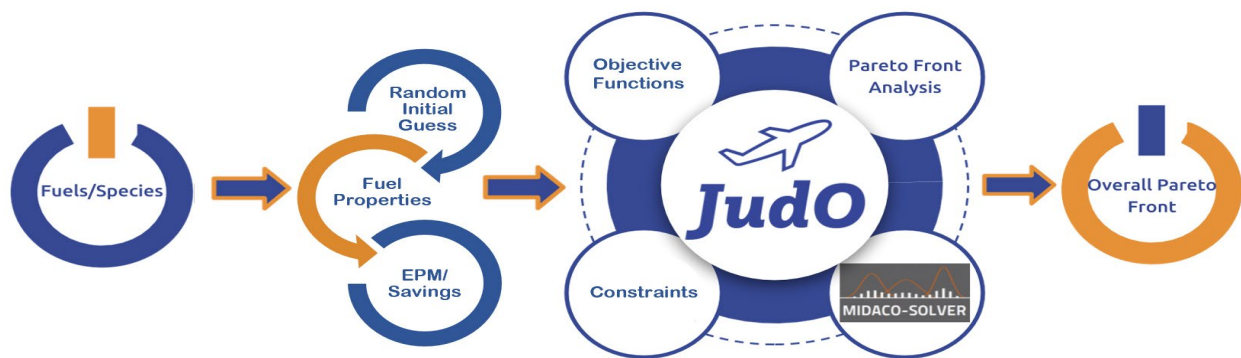


Fig 1. (above). Diagram of the optimization methodology used in this study.



Fig 2. (above). Pie chart showing the breakdown of the pareto front composition and the SAF species most prevalent in pareto front blends.

Acknowledgements

The authors would like to thank the Ohio Space Grant Consortium for their support, and the members of the Heyne Energy and Appropriate Technologies (HEAT) Lab for their guidance and encouragement.

References

- [1] Lee, D. S., Fahey, D. W., Skowron, A., Allen, M. R., Burkhardt, U., Chen, Q., Doherty, S. J., Freeman, S., Forster, P. M., Fuglestedt, J., Gettelman, A., De León, R. R., Lim, L. L., Lund, M. T., Millar, R. J., Owen, B., Penner, J. E., Pitari, G., Prather, M. J., Sausen, R., and Wilcox, L. J. "The Contribution of Global Aviation to Anthropogenic Climate Forcing for 2000 to 2018." *Atmospheric Environment*, Vol. 244, 2021, p. 117834. doi:10.1016/J.ATMOENV.2020.117834.
- [2] Bruening, G. B., and Chang, W. S. "Cooled Cooling Air Systems for Turbine Thermal Management." *Proceedings of the ASME Turbo Expo*, Vol. 3, 2014. doi:10.1115/99-GT-014.
- [3] Boehm, R. C., Scholla, L. C., and Heyne, J. S. "Sustainable Alternative Fuel Effects on Energy Consumption of Jet Engines." *Fuel*, Vol. 304, 2021, p. 121378. doi:10.1016/J.FUEL.2021.121378.
- [4] Kosir, S., Behnke, L., Heyne, J., Stachler, R., Flora, G., Zabarnick, S., George, A., Landera, A., Bambha, R., Denney, R., and Gupta, M. Improvement in Jet Aircraft Operation with the Use of High-Performance Drop-in Fuels. 2019.

“Rotor Propulsion Modeling for Low Reynolds Number Flow ($Re < 10^5$) for Martian Rotorcraft Flight”

Student Researcher: Isaac S. Bensignor

Advisors: Dr. Matthew McCrink and Dr. Dhuree Seth

The Ohio State University

Department of Mechanical and Aerospace Engineering

Abstract

An analysis of a novel rotor geometry optimized for low Reynolds number (Re) and high subsonic Mach number (Ma) flow was performed in support of NASA’s next aerial mission on Mars. The rotor geometry consists of a sharp leading-edge and angled plate sections that mainly promote natural laminar flow [1]. The results from a two-dimensional CFD investigation on a wide range of flow conditions at discrete airfoil sections along the rotor span are coupled with a Blade Element Momentum Theory (BEMT) analysis for discerning rotor performance. Current CFD results demonstrate an average percent error of less than 8% for the entire linear portion of the coefficient of lift vs. angle of attack curve with respect to a published literature condition for the same geometry and operating conditions. Additional CFD simulations are required for further substantiating the BEMT airfoil performance table, such as coefficients of lift and drag at specific Re and Ma conditions. Moreover, results obtained from the CFD analyses will be compared to the experimental results generated by an 85.3% scale rotor tested at low Re and high subsonic Ma conditions in a simulated Martian atmosphere. The conclusion sought by this research investigation is a correction to BEMT modeling for low Re flow that will be deduced from a comparison of the experimental and computational data collected.

Project Objectives

This research project is a combination of both computational and experimental efforts. Using ANSYS Fluent, Martian rotorcraft aerodynamics are being simulated for assessing the airfoils along the span of NASA’s Mars Science Helicopter (MSH) for their coefficients of lift (CL) and coefficients of drag (CD) for a range of angles of attack (AoA), Re , and Ma . Figure 1 demonstrates the unique airfoil and rotor geometries. The airfoil performance values (CL , CD) generated with Fluent are used in a BEMT model for computationally estimating the MSH’s thrust and torque for a given flight condition. Additionally, experiments will be performed on the MSH rotor blades to assess the thrust and torque in an analogous Mars environment created within a vacuum chamber. Generating a correction to BEMT for Martian flight based on a comparison of the computational and experimental data is the primary goal of this investigation.

Methodology

Due to the MSH’s airfoils having a sharp leading-edge, the separation point is fixed at this location and a laminar separation bubble forms due to flow reattachment on the top airfoil surface. This phenomenon – coupled with low Re and high subsonic Ma flow – causes the flow to transiently transition from laminar to turbulent flow. Therefore, a Spalart-Almaras flow model is employed in Fluent for capturing the steady state behavior occurring for the airfoil’s flow simulation. Simulations of such aerodynamic phenomena are computationally expensive, and thus the Ohio Supercomputing Center (OSC) is used for running expedited batch analyses for the cases of interest.

A BEMT analysis code was developed following the algorithm presented by Leishman [2] and validated by comparing performance results of a rotor disk to that of a reputable source using the same operating and geometric inputs [2, 3, 4]. Moreover, using the BEMT derivation and figures provided by Leishman [2], a graphical and statistical comparison of the primary BEMT parameters were performed.

Lastly, an experiment has been designed for assessing the performance of an 85.3% scale MSH rotor blades. The rotor span measures ~ 0.7 m [~ 28 in] in radius and has a maximum thickness of 6.3mm [0.24 in]. To manufacture a set of MSH rotors, a high precision CNC aluminum mold will be used to lay up uni-directional and bi-directional carbon fiber fabric weaves and fiber glass. Figure 2 shows the isolated rotor stand that will be used to measure the performance of the MSH rotors, and Figure 3 shows an example of an 85.3% scaled MSH rotor blade manufactured at OSU. The test stand is currently under validation processes to determine its operational range and measuring capabilities. After successfully completing the aforementioned step, the MSH rotor blades will be affixed, and the test stand will be mounted within a 4.4m diameter vacuum chamber for experimental testing.

Results Obtained and Discussion

Flow simulation results for the 75% span airfoil have been generated for a sweep of AoA for a select number of Re, Ma conditions. Ongoing simulation efforts are assessing the 7%, 25%, 50% and 100% span section's performance. Figure 4 shows the CL v. AoA relationship generated with Fluent for the 75% span airfoil at Re = 16,862, and Ma = 0.52. An average percent error of less than 8% is obtained for the values within the linear portion of the curve with respect to published literature for the same condition. Additionally, Figure 5 shows a velocity magnitude contour of the flow around the 75% rotor span airfoil at Re = 16,862 and Ma = 0.52. Notable flow characteristics include fixed leading-edge separation, and coherent bursting and downstream propagation of laminar separation bubbles. Moreover, since a steady state flow solver was implemented, time-averaged transient effects are shown.

Align 700 symmetric airfoil rotor blades are currently being used on the test stand for ensuring the automation scheme properly records data and delivers AoA and rotor speed commands successfully. Although the test stand depicted in Figure 2 is still being verified and validated, the system is operational and is capable of making thrust, torque, voltage, current, and RPM measurements.

Works in Progress

Further work on this research will continue in both the computational and experimental fronts. Batch analyses are being run on OSC for assessing the performance of the discrete airfoils for a sweep of AoA, Re, and Ma for further substantiating the BEMT look up table. The BEMT analysis on the MSH rotor will be performed after the data set is completely generated.

Upon delivery of the aluminum mold, the MSH rotor blades will be manufactured. Static stress and loading tests will be performed to ensure the rotor can withstand dynamic flight loading before spinning them up on the rotor stand. Thrust and torque measurements will be made with the MSH rotors inside of the large diameter vacuum chamber for a sweep of AoA and rotor speeds. After both the computational and experimental data sets are recorded, a correction to BEMT will be sought after in the post-processing analysis to be performed. The results of this research will be presented at AIAA's Aviation Forum in Chicago, Illinois in June 2022.

Acknowledgements and References

The author would like to acknowledge Dr. Matthew McCrink and Dr. Dhuree Seth for their help and guidance with this research effort. Moreover, a thank you to both Ross Heidersbach and Sage Herz for their assistance and support. Lastly, a thank you to the Ohio Space Grant Consortium for funding this research effort and to The Ohio State University for supporting the project.

[1] Johnson, Wayne, Shannah Withrow-Maser, Larry Young, Carlos Malpica, Witold J.F. Koning, Winnie Kuang, Mireille Fehler, Alyssa Tuano, Athena Chen, Anubhav Datta, et al., "Mars Science Helicopter Conceptual Design," NASA TM-2020-220485, March, 2020.

[2] Leishman, Gordon J., *Principles of Helicopter Aerodynamics*, Cambridge University Press, 2006,

Chaps. 1-4.

- [3] Knight, Montgomery, and Ralph A. Hefner, "Static Thrust Analysis of the Lifting Airscrew," NASA TN 626, December, 1937.
- [4] Harris, F.D., "Model Rotor Hover Performance at Low Reynolds Number," NASA CR-20205001147, May, 2020.
- [5] Koning, Witold J.F., Ethan A. Romander, and Wayne Johnson, "Performance Optimization of Plate Airfoils for Martian Rotor Applications Using a Genetic Algorithm," NASA ARC-E-DAA-TN71478, September, 2019.

Figures/Charts

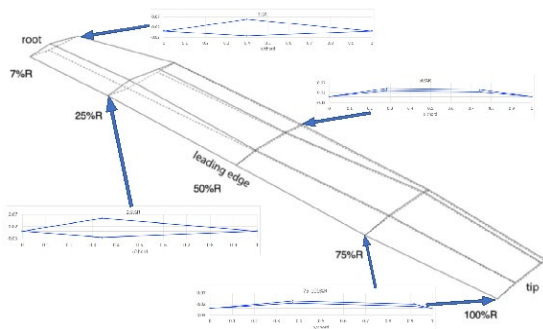


Figure 1. Isometric view of the MSH hexacopter rotor blade design with airfoil cutout representations [1]



Figure 2. Isolated rotor test stand with symmetric airfoil rotor blades



Figure 3. An example of a 85.3% scaled MSH rotor blade manufactured at OSU

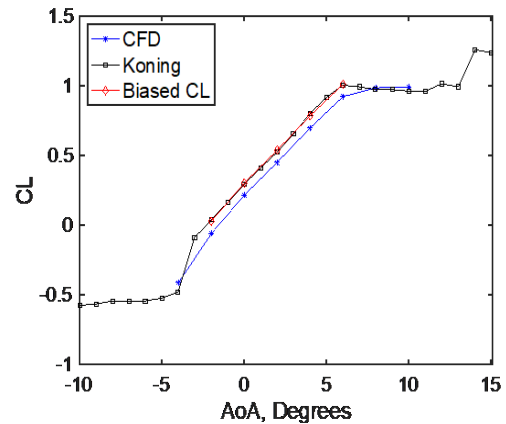


Figure 4. CL v AoA for $Re = 16,862$, $Ma = 0.52$ for the MSH 75% span airfoil by Koning [5] and data generated with Fluent

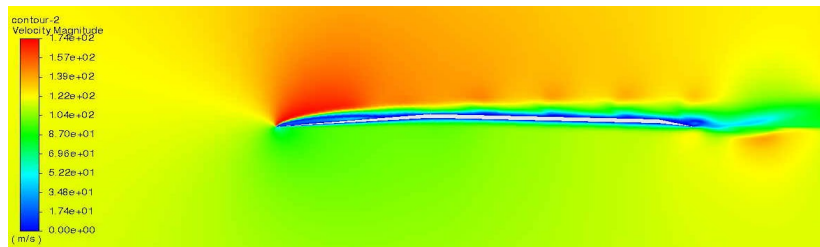


Figure 5. Steady state velocity magnitude contour, 75% span rotor airfoil, $\alpha=2^\circ$, $Re = 16,682$, $M = 0.52$

Characterization of a Nickel-based Additively Manufactured Alloy and Ultrasonic Nanocrystalline Surface Modification

Student Researcher: Blake A. Bowser

Advisor: Dr. Gregory N. Morscher

The University of Akron
Mechanical Engineering and Materials Science

Abstract

Jet propulsion and gas turbine engines are presently extraordinary systems that require materials that can withstand high load, high temperature, and highly corrosive environments. Considering this, components within these propulsive systems can be highly complex and made from advanced materials and alloys. When repairs are needed, it can cause significant downtime for a flight vehicle due to component lead times as well as a consistently high cost of replacement when using conventional manufacturing techniques for advanced materials. With the advent of additive manufacturing (AM), methodologies such as Directed Energy Deposition (DED) can be used to provide repairs on an existing wrought component, significantly reducing repair lead times, and considerably decreasing cost of service. Due to this, Nickel-based superalloys optimized for additive manufacturing processes are of high interest regarding this application. The Nickel-based superalloy (ABD-900AM) provided by the Air Force Research Lab (AFRL) will be analyzed using Non-Destructive Evaluation (NDE) techniques such as acoustic emission (AE), digital image correlation (DIC), and electrical resistance (ER) to characterize flaw propagation for the materials in various build orientations and manufacturing techniques under uniaxial tension and fatigue testing. The microstructural properties of the material will also be characterized via SEM, digital microscopy, and other analysis techniques. Amongst the characterization of this AM material, laser assisted ultrasonic nanocrystalline surface modification (LA-UNSM) will be used to modify surface structure via plastic deformation on conventional and AM Nickel-based alloys.

Project Objectives

The purpose will be to characterize the materials via mechanical testing with the associated NDE techniques and analyze the intrinsic differences in fatigue crack growth (FCG) testing similar to Shrestha [1], fracture toughness, and any other improvements provided by the new alloy composition over conventional alloys, typical AM Nickel alloys, as well as from the UNSM processing.

Methodology

Mechanical testing will be completed in FCG as well as fracture toughness testing for each material, including conventional Nickel-based samples, AM Nickel-based samples, and the ABD-900AM composition in AM and a conventional casting method. Once completed, test data will be compiled and fracture propagation data will be extracted from the NDE techniques presented and fracture propagation characteristics will be enumerated and cross-examined for each material type. Digital microscopy and SEM will also be completed to analyze the microstructure of each material type, as well as fractography to analyze fracture characteristics. LA-UNSM will also ideally be applied to each specimen and data will be acquired for treated and non-treated specimens alike.

Results

Due to project constraints regarding acquisition of the ABD-900AM materials, progress on mechanical testing of the materials will be made once materials are supplied to the University of Akron. Until then, progress has been made testing dog-bone specimens on conventional Inconel-718 (Specimen intra-test shown in *Figure 1*). AE, DIC, and ER were used to examine fracture occurrence for the specimens. This will serve as baseline data for when AM samples will be acquired and tested, along with the ABD-900AM composition when it arrives.

Figures



Figure 1 - Inconel 718 specimen under tensile loading with AE, DIC, and ER NDE techniques involved



Figure 2 - The University of Akron's LA-UNSM machine with accompanying CNC panel

References

[1] Shrestha, Sulochana, et al. "In-situ fatigue life analysis by modal acoustic emission, direct current potential drop and digital image correlation for steel." *International Journal of Fatigue* 142 (2021): 105924.

Stereochemistry and Stoichiometry in Aliphatic Polyester Photopolymers for 3D Printing Tailored Biomaterial Scaffolds

Student Researcher: Scott L. Brooks

Advisor: Dr. Andrew Weems

Ohio University
Mechanical Engineering

Abstract

Stereoselective aliphatic polyesters were synthesized through the ring opening copolymerization of cyclic anhydrides and epoxides using a tin catalyst to yield $M_n \sim 10\text{-}13$ kDa macromolecules ($\mathcal{D} < 1.6$). Isomerization of the *cis* poly(maleate-*co*-phenyl glycidol ether) (PMPGE) to the *trans* isomer poly(fumarate-*co*-phenyl glycidol ether) (PFPGE) may be used to tune physical properties such as viscosity, which displays an order of magnitude increase as PMPGE is isomerized to PFPGE. However, the formulated photopolymer resins consisting of a 4-arm thiol and the polyester photopolymer display Newtonian fluid behavior and viscosities of ~ 0.5 Pa \times s, ideal for digital light processing (DLP) 3D printing. Enhancement of the thermal, thermomechanical, mechanical, and gravimetric properties was achieved through off-stoichiometric imbalances in the photosets. For example, with a 20% excess of alkene both photopolymers display gelation times comparable with commercial resins (~ 5 s) and were 3D printed *via* DLP into complex porous tissue scaffolds. Finally, cytocompatibility with murine macrophages over 7 days demonstrated superior material surfaces compared to control tissue culture polystyrene, as determined by statistically increased aspect ratios (cell spreading) and proliferation, indicating the biomedical applications potential of these materials.

Project Objectives

The project's objectives were to synthesize stereoselective aliphatic polyesters through ring opening copolymerization of cyclic anhydrides and epoxides and investigate the impact the two stereoisomers, along with photoresin off-stoichiometry, had on resultant material properties. The *cis* and *trans* states, PMPGE and PFPGE, would be utilized in photopolymer resins for 3D printing *via* digital light processing (DLP). Regarding the thermoset analysis, the relationship between polyester stereochemistry along with photopolymer resin off-stoichiometry achieved *via* thiol-ene "click" reactions and the resultant thermoset thermal, mechanical, and gravimetric material properties were determined. Both materials showed cytocompatibility, satisfying the aim of potential biomaterial application. Lastly, showing that highly resolved porous tissue scaffolds could be printed in PMPGE and PFPGE formulations where only vat photopolymerization of the *trans* stereoisomer had been previously shown.

Methodology

The polyesters were synthesized through the ring opening copolymerization (ROCOP) of maleic anhydride and phenol glycidol ether in bulk, open air, using a tin catalyst. The PMPGE was subsequently isomerized in to the PFPGE. Confirmation of the polymerization and isomerization was done *via* ^1H NMR and the molecular weight and dispersity of the polyesters were verified through gel permeation chromatography.

The photoresins were prepared using the polyester's, the tetrathiol crosslinker pentaerythritol tetrakis(3-mercaptopropionate) (PETMP), the reactive diluent 1,3,5-triallyl-1,3,5-triazine-2,4,6(1H,3H,5H)-trione (trione), and the photoinitiator Irgacure 819. The off-stoichiometric ratios were created by using an excess of polyester alkene to the PETMP thiol going from a 30:1 ratio, to using stoichiometric amounts. The

photoresins were irradiated using 405 nm ultraviolet light to photocure and thermally cured for twenty-four hours at 120 °C.

The thermosets were characterized through thermal, mechanical, and gravimetric testing. These materials were seeded with murine macrophage cells measuring cell proliferation and aspect ratio over a seven-day span to analyze cytocompatibility. Finally, porous tissue scaffolds were 3D printed using digital light processing (DLP) methods.

Results [1]

Stereoselective aliphatic polyesters were synthesized through the ring opening copolymerization of cyclic anhydrides and epoxides using a tin catalyst to yield $M_n \sim 10\text{-}13$ kDa macromolecules ($\bar{D} < 1.6$) (figure 1). Both polyester photopolymer resins yielded Newtonian viscosities (~ 0.5 Pa \times s) indicating viable use for DLP type printing. Leveraging off-stoichiometric ratios, the gelation times of PMPGE and PFPGE resins were tuned to ~ 5 s, comparable to commercial resins. Through altering the stereochemistry, the PFPGE thermosetted materials showed significantly higher elastic modulus values than the PMPGE materials along with both polyesters showing full strain recovery over a span of a minute in 50 °C conditions proving these materials to have 4D behavior (figure 2). Utilizing thiol-ene “click” photochemistry, both PMPGE and PFPGE resins were 3D printed into highly resolved porous tissue scaffolds (figure 3). The PMPGE and PFPGE materials both showed controlled and tunable degradation profiles over the span of four months *via* off-stoichiometric ratios and cell proliferation over the span of seven days indicating cytocompatibility. These materials have highly tunable material properties and show promise as 4D plastics for biomaterial future applications.

Figures

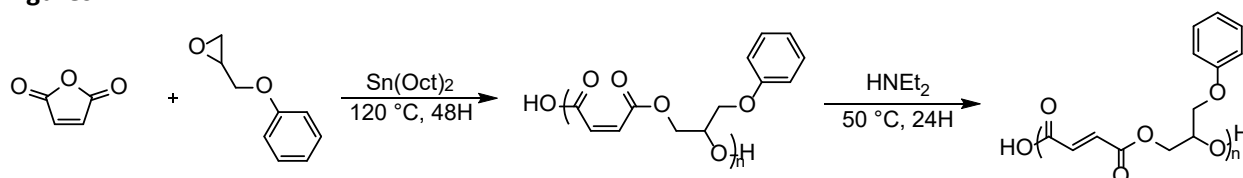


Figure 1: ROCOP synthesis and isomerization producing PMPGE and PFPGE polyesters

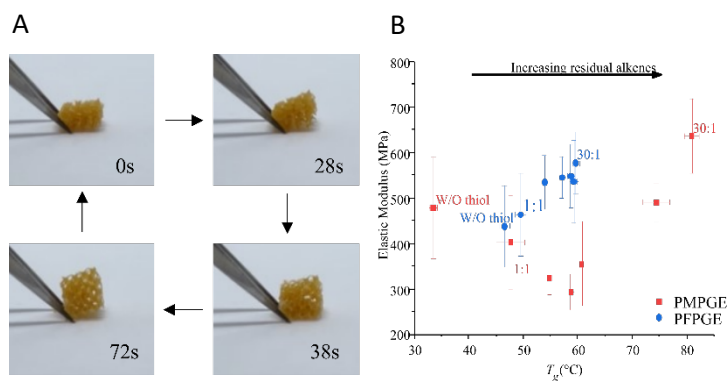


Figure 2: Shape memory of tissue scaffolds (A), and elastic modulus of PFPGE and PMPGE thermosets in comparison with their glass transition temperature (T_g) (B)

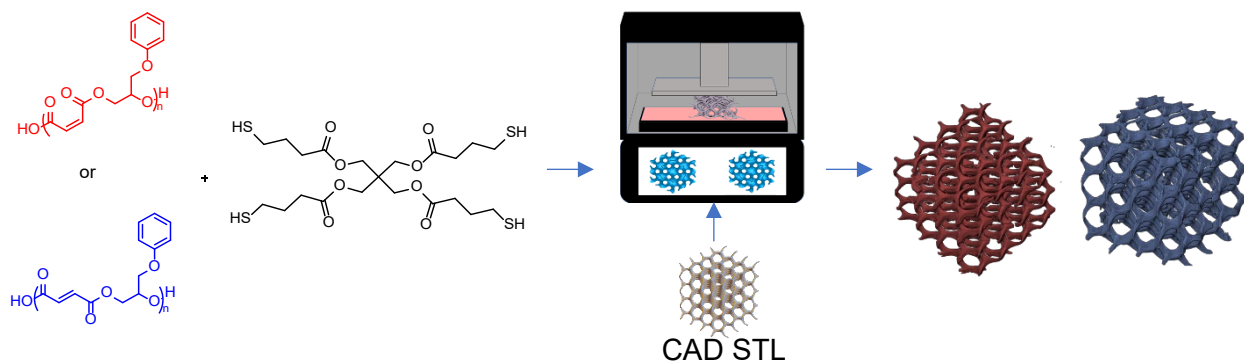


Figure 3: Thiol-ene “click” photoreaction and DLP printing of PMPGE and PFPGE photopolymer resins producing 3D tissue scaffolds

Acknowledgments and References

This work was supported by the Ohio Space Grant Consortium. A special thanks to Dr. Andrew Weems as the project advisor and additional funding from the mechanical engineering department of Ohio University.

1. Brooks, S.L., et al., *Stereochemistry and stoichiometry in aliphatic polyester photopolymers for 3D printing tailored biomaterial scaffolds*. *Polymer Chemistry*, 2022. **13**(14): p. 2048-2056.

NEW INSIGHTS INTO THE PETROGENESIS OF LUNAR METEORITE ALLAN HILLS 81005 (ALHA81005)

Student Researcher: Jared T. Brum

Advisor: Dr. Claire McLeod

Miami University

Department of Geology and Environmental Earth Science

Abstract

Observations of ALHA81005 via polarized light microscopy (PLM), scanning electron microscopy energy dispersive spectroscopy (SEM-EDS), and electron probe microanalysis (EPMA) are consistent with the classification of anorthositic regolith breccia. Clasts of anorthosite, basalt, granulite, and impact melt breccia are present. The breccia contains plagioclase, minor (clino)pyroxene, and rarer olivine in addition to trace oxides and sulfides. Phosphates, spinels, glass spherules, and crystalline spherules are rare and not ubiquitous. In section -92, a spinel-bearing dunite clast is present alongside several pink spinel-bearing troctolites. The composition of dunitic olivines is consistent with the lunar Mg-suite. Spinel in the dunite clast are also consistent with spinels in Mg-suite dunites while troctolitic pink spinels are consistent with Mg-suite spinel troctolites. Collectively, clasts and mineral assemblages support an origin of ALHA81005 from the lunar highlands. The observation of a lunar dunite contributes to our understanding of Mg-suite magmatism during lunar differentiation.

Objectives

While the returned Apollo samples are spatially constrained, they do represent a limited sampling of the lunar surface: approximately 5% (Eugster, 1989; Vaniman et al., 1991). The study of lunar meteorites therefore expands our understanding of the Moon's history as they represent a random sampling of the lunar surface (Korotev, 2005). Therefore, it is likely that lunar meteorites include different geological units from the lunar crust than are represented by samples collected by the spatially constrained crewed and robotic missions of the 1960s and 1970s. In this study we present a comprehensive petrographic, mineralogical, and geochemical study of a lunar anorthositic regolith breccia: ALHA81005. Three thin-sections of ALHA81005 were studied via light microscopy, scanning electron microscopy coupled with energy dispersive x-ray spectroscopy (SEM-EDS), and electron probe microanalysis (EPMA). Observations and results were used to evaluate the lithological diversity of lunar crustal materials, characterize the composition of major and minor phases, assess the petrogenesis of the meteorites' components, and place ALHA81005's origin in the current lunar framework.

Methodology

Images of each thin section were taken in plane-polarized light (PPL) and cross-polarized light (XPL) using a Leica DM2700P Petrographic Microscope attached to a MC190 HD Microscope Camera at Miami University. Images were automatically stitched together using Leica Application Suite X (LAS X) software. PPL and XPL observations aided in classification of mineral grains, clasts, and textures. These images helped guide the selection of clasts and grains for elemental mapping and *in-situ* chemical analysis. This approach ensured that the characteristics of each sample were comprehensively documented. Back-scatter electron (BSE) images were acquired on a Zeiss Supra 35 Variable Pressure Field Emission Gun-Scanning Electron Microscope (VP FEG-SEM) at Miami University's Center for Advanced Microscopy and Imaging (CAMI). Elemental data were collected on a Bruker Xflash 5010 Energy Dispersive X-ray Spectroscopy (EDS). EDS data was processed using Bruker eSpirit 2 imaging software. These analyses were complementary to PLM observations and aided in identification of clast types and mineral grains. After

initial imaging/mapping, representative selections of the samples' clasts, minerals, and textures were targeted for hyper-mapping over longer times. Final selection was determined by heterogeneity to ensure that diversity of meteoritic components was documented. Major and minor element analysis of select minerals in clasts and the matrix was conducted via Electron Probe Micro Analysis (EPMA) on a JEOL JXA-8230 Electron MicroProbe in the Chevron Geomaterials Characterization Lab, Department of Geology and Geophysics at Louisiana State University.

Results

All three thin-sections of ALHA81005 studied are characterized by a brecciated, glassy matrix with individual mineral fragments and subangular to subrounded polymineralic clasts. At times, flow structures are visible in the glass (quenched melt). The majority of mineral fragments within the brecciated matrix are plagioclase feldspar, with minor pyroxene, rarer olivines, trace oxides, sulfides, and metal. Phosphates, glass spherules, and crystalline spherules are extremely rare. Abundance of feldspathic components, the glassy matrix, and the identification of glass spherules are consistent with the classification of ALHA81005 as an anorthositic regolith breccia (e.g., Righter, 2010). Plagioclase feldspars in ALHA81005 are overwhelmingly anorthitic. Pyroxenes from section -23, compositions range from En_{21-78} , Fs_{07-54} , and Wo_{03-42} . In section -80, pyroxene compositions range from En_{32-85} , Fs_{11-56} , and Wo_{01-47} . For sections, -23, -80, and -92, Fo content ranged from: Fo_{91} to Fo_{72} , Fo_{88} to Fo_{51} , and Fo_{88} to Fo_{83} , respectively. The Mg# and Cr# of sampled spinels from sections -80 and -92 ranged from: Mg# 45.1 to 52.5, Cr# 72.5 to 75.7; Mg# 68.8 to 85.7, Cr# 1.7 to 8.3, respectively. Olivines within the dunite clast (section -92) are associated with Mg-suite dunites and exhibit similar compositions to Apollo sample 72417.

Significance: The dominance of feldspathic materials in ALHA81005, in combination with previous work, is consistent with an origin in the lunar feldspathic highlands. However, the petrogenesis of ALHA81005 must also have included delivery of mare basaltic material and Mg-suite material to the site of origin on the lunar surface, potentially on the lunar farside.

Images

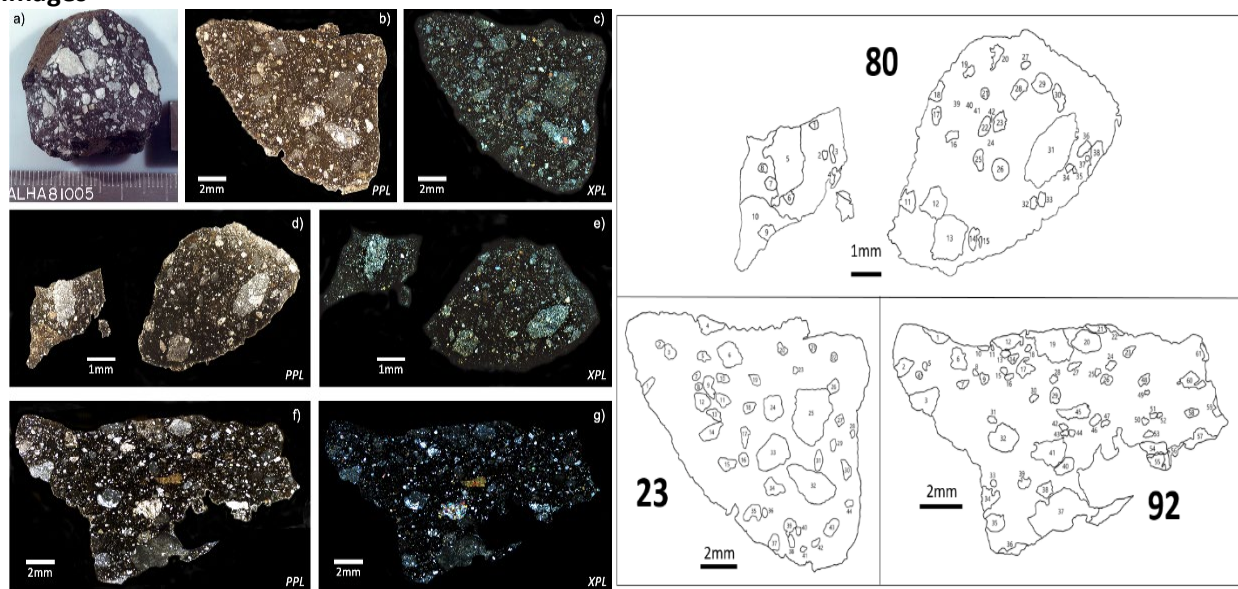


Figure 1 (left): a) ALHA81005, b), d), f) PPL image of thin-sections 23, 80, and 92, respectively; c), e) and g) XPL image of thin-section 23, 80, and 92, respectively. **Figure 2 (right):** Clast maps of thin-sections 23, 80, and 92.

Acknowledgements

US Antarctic meteorite samples are recovered by the Antarctic Search for Meteorites (ANSMET) program funded by NSF and NASA, and curated by the Department of Mineral Sciences of the Smithsonian Institution and Astromaterials Curation Office at NASA Johnson Space Center. Thanks to the Miami CAMI facility staff for continued support during acquisition of SEM-EDS data. Allocation of ALHA81005 sections -23, -80, and -92 were made possible through the Meteorite Working Group, request #3501. Thanks to the Miami University Graduate School Thesis fund, and the Naus Family Scholar Fund, for supporting data acquisition. Jared Brum was supported by a fellowship from the Ohio Space Grant Consortium (OSGC) for one year during this study. Preliminary dissemination of results was made possible by support from NSF GEOPATHS award #1801424. Personally, I would like to thank my committee members, Dr. McLeod, Dr. Krekeler, and Dr. Rakovan.

References

- Eugster, O., (1989). History of Meteorites from the Moon Collected in Antarctica. *Science*, v. 245; 1197-1202.
- Korotev, R. L. (2005). *Lunar geochemistry as told by lunar meteorites. Chemie Der Erde - Geochemistry*, 65(4), 297–346. doi: 10.1016/j.chemer.2005.07.00.
- Righter, K., (2010). Allan Hills A81005. Anorthositic regolith breccia. *Lunar Meteorite Compendium*.
- Heiken, G. H., Vaniman, D. T., and French, B. M., (1991). *Lunar Sourcebook: A User's Guide to the Moon*. Cambridge University Press; 792pp.

The Impact of a Co-Culturing Environment and IL-4 stimulation on the Immunomodulatory Capacity of an Injectable, 3D Musculoskeletal Tissue Analog

Student Researcher: Oliver G. Eby

Advisor: Eda Yildirim-Ayan

University of Toledo
Department of Bioengineering

Abstract

Musculoskeletal injuries are among the most common injuries across the US and globally. Novel therapies are always on the rise for these tissues but a better understanding of how the immune system responds to tissue damage is critical for expediting the healing process. Macrophages and fibroblasts are the primary cell types involved in the tissue rebuilding process but while they have often been studied for their specific roles, a deeper knowledge of how they interact in a 3D environment is needed in order to better study physiologically relevant cues and crosstalk. Therefore, in this study, we set out to understand and manipulate how macrophages respond to fibroblasts to promote healing in 3D tissue analogues by providing a sustained release of anti-inflammatory cytokine IL-4. Indirect cocultures of fibroblasts and macrophages were cultured with, or without, IL4 to observe the effect of co-culturing as well as the effect that IL4 has on tissue regeneration. The macrophages showed anti-inflammatory phenotypic expression and the scaffolds showed increased fiber diameter and decreased porosity following IL4 treatment.

Project Objectives

- 1: First to understand the instinctual phenotypic reactions of both fibroblasts and naïve macrophages when co-cultured together. The immune system is complex and so is the healing process. As cells come in contact with each other, they communicate and begin creating feedback loops that can differentiate or polarize each other into various phenotypes that express different proteins and create either an inflammatory or a regenerative environment.
- 2: The second objective was to utilize interleukin 4, an anti-inflammatory cytokine, to expedite the healing process by promoting the anti-inflammatory and regenerative phenotype in the macrophages. This would then encourage the fibroblasts to produce more extracellular matrix (ECM) proteins and so promote the final stages of the healing process.

Methodology

The fibroblast cells (HFF1) were purchased from ATCC and cultured in DMEM with 15% FBS, 1% Pen/Strep, and 1.5g/L sodium bicarbonate in T75 flasks until confluent. They were then detached using TripleE and encapsulated at 10^6 cells/mL within an injectable nanofibrous musculoskeletal tissue scaffold called PNCOL using our pre-established techniques^{1,2}. PNCOL scaffolds combine nanofibrous polycaprolactone (PCL) with neutralized type 1 collagen to provide more stability to the collagen gels as well as offer sustainable dosage release profiles of cytokines or other growth factors. The PNCOL was used in this study for the 3D matrix supporting the fibroblasts in co-culture as well as the vector for the IL-4 treatment in the experimental groups. IL4 conjugates with the PCL fibers which stabilizes the IL4 and prolongs its

bioactivity thereby allowing it to be released over an extended period of time¹. For the co-culture experiments, the scaffold size used was 250 μ L and 250K fibroblast cells were in each scaffold. U-937 monocytes are an immortalized cell line taken from pleural effusion of a histiocytic lymphoma. Despite being from a cancerous origin, they are common in research for *in vitro* studies³⁻⁶. The human-derived U-937 monocytes were cultured in RPMI media with 10% FBS and 1% pen/strep before being differentiated into naïve macrophages via incubation with 100ng/mL PMA. When ready for the co-culture, they were seeded at 10⁶ cells per well, such that the ratio of macrophages to fibroblasts was 4:1. Both cell lines were then co-cultured for 7 days with, or without IL4 treatment. See figures 1&2 for experimental process and group labeling methodology.

Results

Immunofluorescence (IF) staining revealed that the IL4-treated groups were successfully able to promote the M2, or anti-inflammatory phenotype in the macrophages(Fig3). Images taken via scanning electron microscopy (SEM), showed the IL4-treatment group had a decreased scaffold porosity when compared to the individually cultured fibroblasts(Fig4). There were no statistically significant differences between the co-cultured group without IL4 and the individual culture of fibroblasts scaffold. Finally, gene expression analysis, performed via RT-qPCR(reverse transcriptase-quantitative polymerase chain reaction) on fibroblasts and macrophages separately, showed that IL4-treated co-culture groups were able to decrease pro-inflammatory marker TNF- α and increase anti-inflammatory marker CD206(Fig 5) in the fibroblasts. However, degradation enzymes, such as matrix metalloproteinases were increased in the IL4 treatment group when compared to the controls. Similarly, aggrecan and collagen types 1&2 production, while being increased relative to the individual fibroblast culture, was downregulated when compared to the macrophage-fibroblast culture without IL4. Macrophage gene expression.....

Significance and Interpretation of Results

Initial hypotheses postulated that the IL4-treated co-culture group would increase the production of Collagen types 1&2 and other extracellular matrix proteins when compared to both the individual culture and the co-culture without IL4. While these genes were upregulated when compared to the individual cultures of each cell line, it was found that the fibroblast co-culture group without IL4 had much higher expression levels of these ECM proteins than the IL4-treated group. It must be noted that the IL4 treated co-culture group did increase the expression of those ECM genes when compared to the individual culture of just fibroblasts, which supports much of the literature claims that such ECM proteins are upregulated by fibroblasts in response to IL4⁷⁻¹¹. It was clear, however, that other factors needed to be taken into account. It must further be noted that an overexpression of ECM proteins is characteristic of fibrosis and chronic wound pathology¹². This typically occurs when fibroblasts in and around the wound area differentiate into myofibroblasts but fail to undergo apoptosis at the proper time and so continue to actively produce ECM proteins over extended periods of time. Since one of the main differentiating markers of myofibroblasts is alpha-smooth muscle actin (α -SMA), the fibroblast co-cultures were further studied for their expression of this protein (Fig5). This revealed that the IL4 group had significantly lower expressions of α -SMA suggesting that the IL4 treatment reduces the longevity of myofibroblasts and/or the differentiation of fibroblasts to myofibroblasts.

Macrophage characterization was more consistent with the literature as the IF staining showed significant polarization of macrophages into the M2, or anti-inflammatory, phenotype (Fig 3). Further

characterization via RT-qPCR showed that the IL4-treated group had increased expression of both IL-1 β and TNF- α as well as anti-inflammatory cytokines CD163 and CCL18. According to the literature, this is typical of M2b macrophages¹³, which are a subtype of the M2 polarization, where macrophages are still promoting the production of ECM proteins but still have remnants of the pro-inflammatory phenotype and still express elevated levels of both IL1- β and TNF- α specifically. Taking all the results together, the IL4 treated group increased scaffold fiber diameter and decreased porosity, while at the same time successfully polarizing the macrophages into the M2, anti-inflammatory/pro-regenerative phenotype. The increased expression of MMP genes could suggest that the IL4-treated group had progressed to the final stage of tissue healing, which is restructuring of the matrix¹⁴. This restructuring is characterized typically by increased levels of MMPs as well as decreases in the levels of ECM production¹⁵. These results therefore suggest, in conjunction with the literature, that our IL4-treated groups were able to successfully promote the pro-regenerative phenotype in macrophages and speed up the healing processes while preventing the overproduction of ECM proteins which commonly leads to fibrosis and chronic wound pathology.

Figures

Figure 1: Methodological process for creating the co-culture conditions.

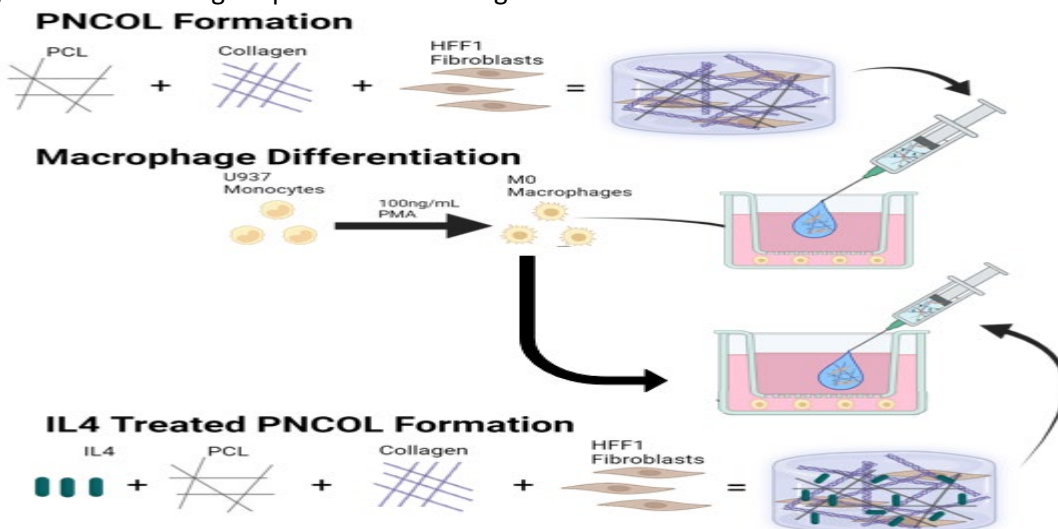


Figure 1: outlines the process for creating the co-culturing conditions. Macrophages were placed on the bottom of a 12-well plate in a 2D environment, while the fibroblasts were placed in a 3D collagen matrix. IL4 was added to some groups to observe the effect it had on changing cell phenotypes.

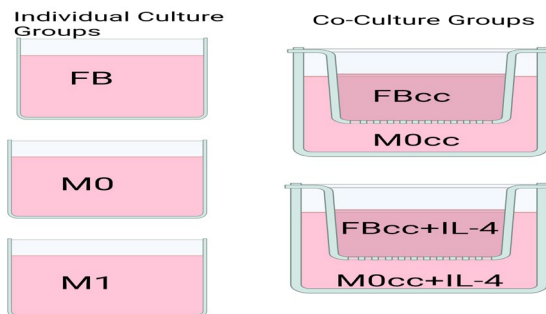


Figure 2: Labeling system for the various cell groups.

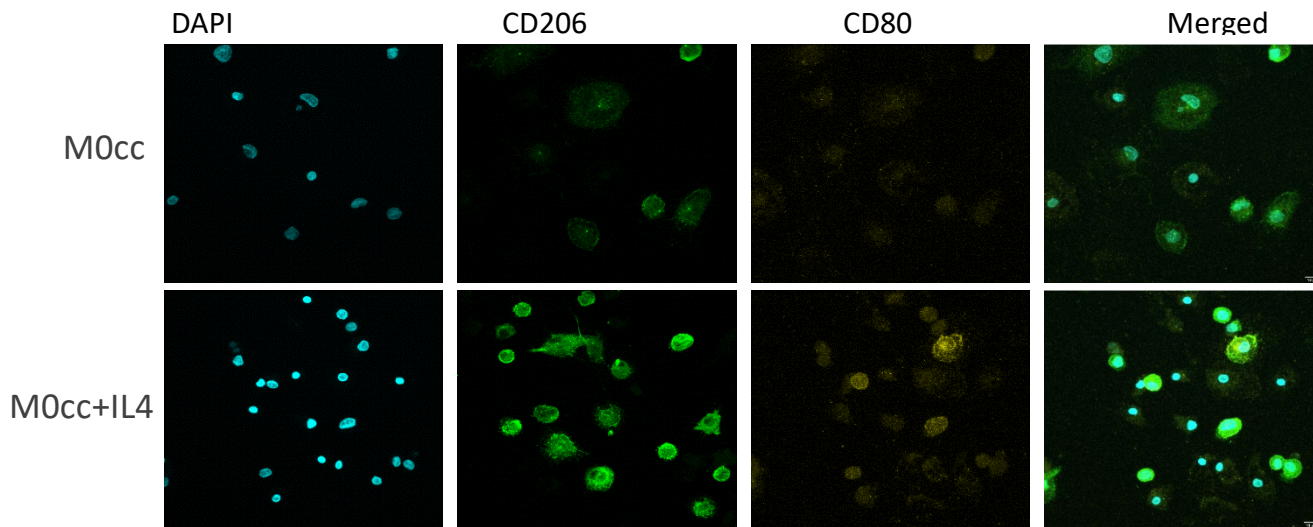


Figure 3: shows the immunofluorescence staining of the macrophages with DAPI, CD206 (anti-inflammatory), and CD80 (pro-inflammatory) antibodies.

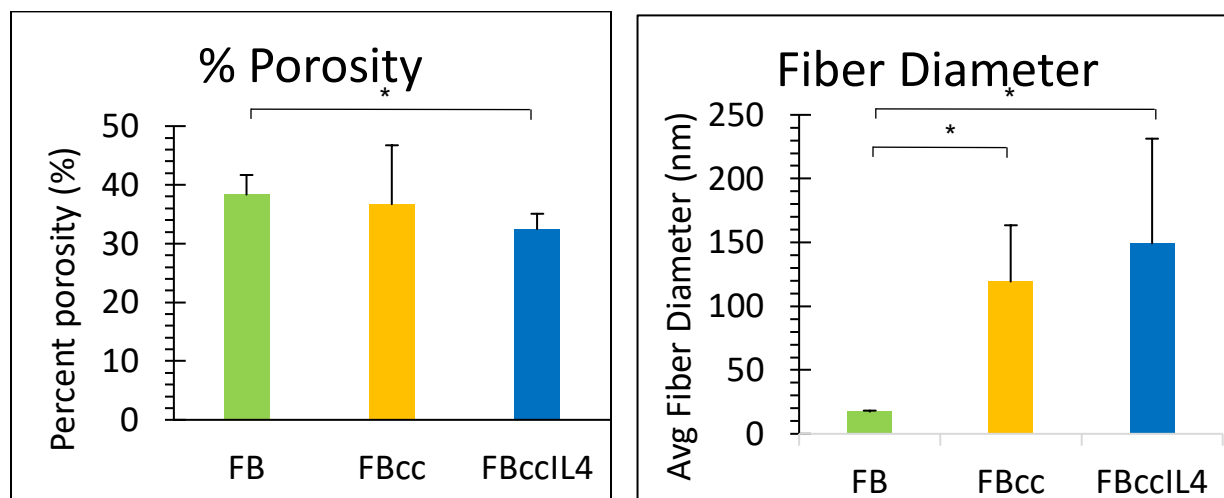
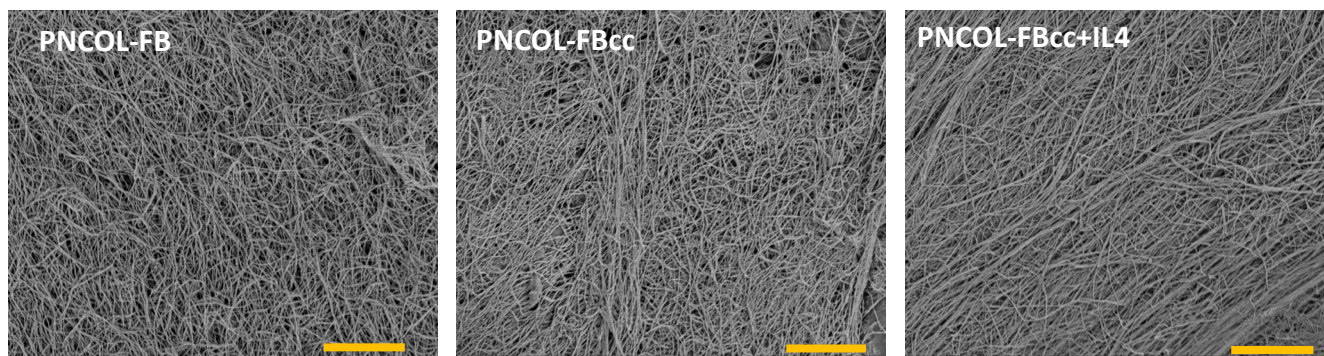


Figure 4: shows scanning electron microscope (SEM) images of the PNCOL scaffolds either from fibroblast mono-culture (PNCOL-FB), fibroblasts co-cultured with macrophages(PNCOL-FBcc), or fibroblasts co-cultured with macrophages and treated with IL4(PNCOL-FBcc+IL4). The scale bar in each is 10 μ m. The graphs represent the calculations (made using ImageJ) of the scaffold porosity as well as fiber diameter, both of which are a function of ECM production. The asterisk signifies statistical difference between 2 groups ($p < 0.05$).

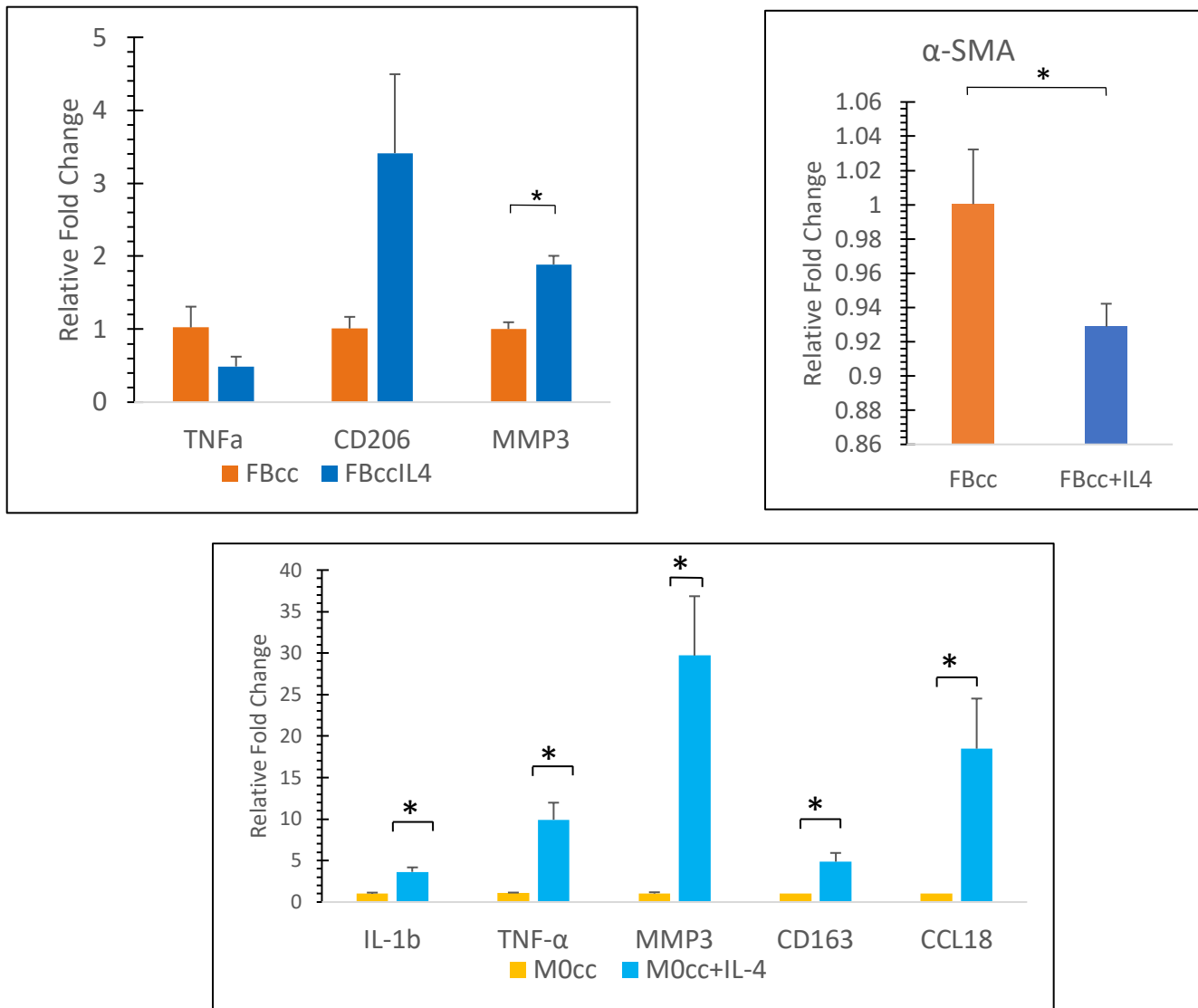


Figure 5: Shows the gene expression analysis of both fibroblasts and macrophages in co-culture with each other. The asterisk signifies statistical difference ($p < 0.05$) between groups.

References

1. Shortridge C, Akbari Fakhrabadi E, Wuescher LM, Worth RG, Liberatore MW, Yildirim-Ayan E. Impact of Digestive Inflammatory Environment and Genipin Crosslinking on Immunomodulatory Capacity of Injectable Musculoskeletal Tissue Scaffold. *Int J Mol Sci.* 2021;22(3).
2. Subramanian G, Bialorucki C, Yildirim-Ayan E. Nanofibrous yet injectable polycaprolactone-collagen bone tissue scaffold with osteoprogenitor cells and controlled release of bone morphogenetic protein-2. *Mater Sci Eng C Mater Biol Appl.* 2015;51:16-27.
3. Harris P, Ralph P. Human leukemic models of myelomonocytic development: a review of the HL-60 and U937 cell lines. *Journal of leukocyte biology.* 1985;37(4):407-422.
4. Kaba SI, Egorova EM. In vitro studies of the toxic effects of silver nanoparticles on HeLa and U937 cells. *Nanotechnology, science and applications.* 2015;8:19.
5. Dintakurti A, Dauletbaev N, Hamed R, Lands LC. The macrophage-like cell lines THP-1 and U937 are differentially inclined towards M1 and M2 phenotypes. In: *B36. MACROPHAGES: BASIC AND TRANSLATIONAL STUDIES.* American Thoracic Society; 2017:A3272-A3272.
6. Chanput W, Peters V, Wichers H. THP-1 and U937 Cells. *The impact of food bioactives on health.* 2015:147-159.

7. Chambers M, Kirkpatrick G, Evans M, Gorski G, Foster S, Borghaei RC. IL-4 inhibition of IL-1 induced Matrix metalloproteinase-3 (MMP-3) expression in human fibroblasts involves decreased AP-1 activation via negative crosstalk involving of Jun N-terminal kinase (JNK). *Exp Cell Res*. 2013;319(10):1398-1408.
8. Gillery P, Fertin C, Nicolas J, et al. Interleukin-4 stimulates collagen gene expression in human fibroblast monolayer cultures Potential role in fibrosis. *FEBS letters*. 1992;302(3):231-234.
9. Nguyen JK, Austin E, Huang A, Mamalis A, Jagdeo J. The IL-4/IL-13 axis in skin fibrosis and scarring: mechanistic concepts and therapeutic targets. *Archives of dermatological research*. 2020;312(2):81-92.
10. Postlethwaite AE, Holness MA, Katai H, Raghov R. Human fibroblasts synthesize elevated levels of extracellular matrix proteins in response to interleukin 4. *J Clin Invest*. 1992;90(4):1479-1485.
11. Sempowski GD, Beckmann MP, Derdak S, Phipps RP. Subsets of murine lung fibroblasts express membrane-bound and soluble IL-4 receptors. Role of IL-4 in enhancing fibroblast proliferation and collagen synthesis. *The Journal of Immunology*. 1994;152(7):3606.
12. Witherel CE, Abebayehu D, Barker TH, Spiller KL. Macrophage and Fibroblast Interactions in Biomaterial-Mediated Fibrosis. *Adv Healthc Mater*. 2019;8(4):e1801451.
13. Arango Duque G, Descoteaux A. Macrophage cytokines: involvement in immunity and infectious diseases. *Front Immunol*. 2014;5:491.
14. Darby IA, Laverdet B, Bonte F, Desmouliere A. Fibroblasts and myofibroblasts in wound healing. *Clin Cosmet Investig Dermatol*. 2014;7:301-311.
15. Stunova A, Vistejnova L. Dermal fibroblasts—A heterogeneous population with regulatory function in wound healing. *Cytokine & growth factor reviews*. 2018;39:137-150.

Burner Rig Optimization for High Temperature Materials and Coating Systems

Student Researcher: Christopher Ferguson

Advisor: Dr. Gregory Morscher

The University of Akron
Mechanical Engineering

Abstract

At the University of Akron (UA), the capability of extreme environment testing of ceramic matrix composites (CMCs) and CMC/coating systems needed to be expanded to include accurate temperature control for high temperature, high stress, and high velocity testing in a combustion environment. CMCs are traditionally used in the internal components of a jet turbine engine and will experience different stress and temperature conditions based on what stage in the cycle the aircraft is at. An automated two-axis positioner was created for the pre-existing combustion facility at UA [1] allowing for a more realistic simulation of an aircraft's typical flight cycle. This system was affordably built from two linear ball screws, two stepper motors, an Arduino, and a laptop to run the custom-built software. Flight stages include ground idle, take-off, climb, cruise, flight idle, approach, reverse thrust, and a return to ground idle [2]. Each stage requires a different temperature and stress condition that could not previously have been tested in the current facility. Automating the position of the torch allows for more complex temperature cycles, including thermomechanical fatigue tests of SiC/SiC [3] which are planned for in the future.

Project Objectives

The goal of this project is to create an automated positioner that can move the high velocity oxygen fuel (HVOF) torch both automatically, through a user created program, and manually, for simple tests, to precisely change the temperature experienced at the surface of the sample.

Methodology

As a project, the hardware, software, and validation testing are the three main stages necessary to build a reliable testing apparatus. The hardware was created first using two linear ball screws attached to custom machined aluminum plates that acted as the supports for the positioner. Two axes were chosen: one to move the torch perpendicular to the sample (Z-Axis), used to change the temperature experienced, and one parallel to the sample (Y-Axis), used to center the flame on the material.

The software of the torch positioner was split into two separate codes: an Arduino script written in C, and a desktop application written in C# through Visual Studio 2019. An Arduino is needed to communicate directly with the stepper motor drivers because it is a microprocessor that can rapidly send out step and direction signals which the desktop cannot handle alone. The C# application allows for ease of operation as all interactions between the user and system is based out of a graphic user interface (GUI).

Validation testing was conducted using a simplified square wave after the construction of the system to verify that the signals sent were followed accurately. The horizontal MTS was utilized in tandem with the positioner to induce an axial stress along with the thermal stress.

Results

The hardware was built to move the torch 176 mm in the Z direction and 112 mm in the Y direction at speeds ranging from 0.25 mm/s to 15 mm/s. 2.0 Nm stepper motors were used to provide torque to move the torch in 0.02 mm increments. That increment is based on the pitch of the ball screw (5.08 mm/rev) and the number of steps needed per revolution (200 steps/rev) for the stepper motors. The completed system is labeled in Figure 1, with most of the work in this report on the two-axis positioner located on the red frame.

Complementing the hardware is the software built in Visual Studio 2019 using the .NET Framework with Windows Form as the application builder. As seen in Figure 2, it allows for both manual and automatic control of the torch in two directions, allowing for complex programs to be built. In automatic mode, the software executes a set plan from an array of sample distance locations and dwell times. Sample distance, time, and axis location data is recorded in the "Raw Data" tab which is plotted in real time on the main page of the software. All data can be exported into a CSV file at the end of the test.

Validation testing was completed using a square wave running at a 5 mm/s torch speed, traveling from 265-125-265 mm from the sample along with an applied axial stress from 0-70-10 MPa. The test was completed in 5 minutes with 30 seconds of approaching the sample, 4 minutes to stabilize, and 30 seconds to back off the sample. The maximum temperature applied was 1230°C which occurred at 4 minutes and 30 seconds in the test after it stabilized for 4 minutes as seen in Figure 3. Temperature is not directly correlated with sample distance because the surface requires time to stabilize to its steady state condition.

Figures

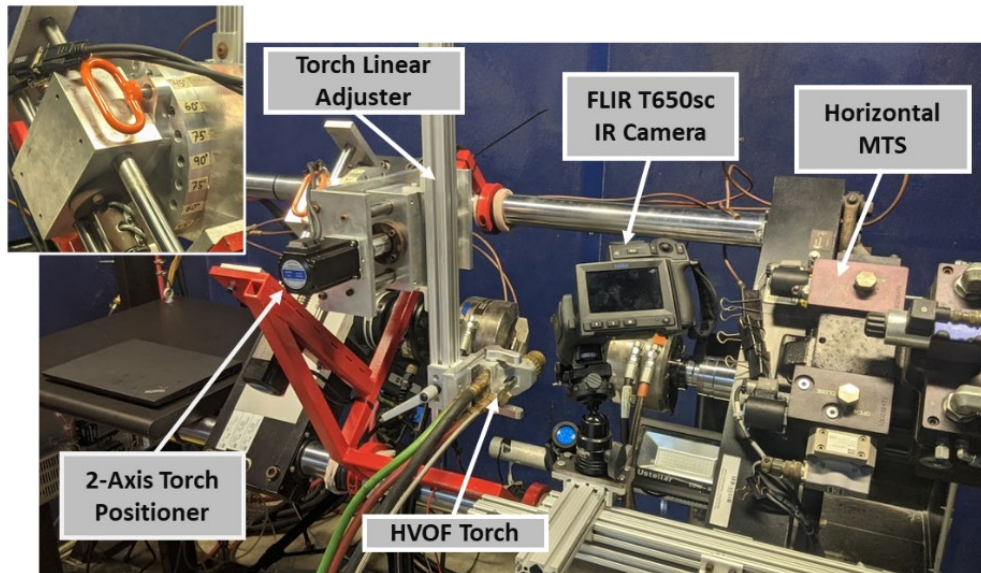


Figure 1: Current Burner Rig Hardware



Figure 2: Custom Built Desktop Application

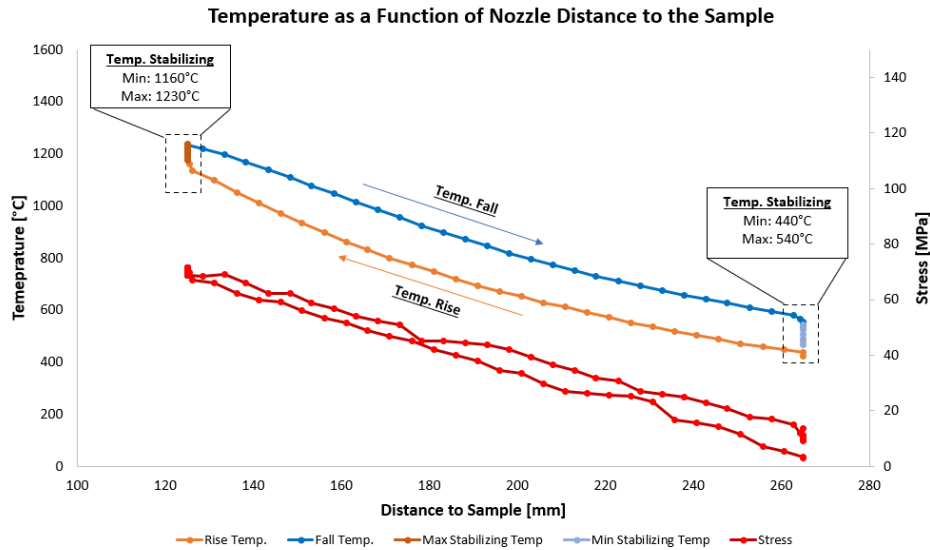


Figure 3: Validation Testing using a Simple Square Wave

References

1. G. Morscher, R. Panakarajupally, L. Hoffman, "The Versatility of HVOF Burner Rig Testing for Ceramic Matrix Composite Evaluation", J. Compos. Sci., 2021, vol 5.
2. R.C. Reed, "The Superalloys Fundamentals and Applications", Cambridge University Press (2006)
3. Panakarajupally, Ragav P., Michael J. Presby, K. Manigandan, Jianyu Zhou, George G. Chase, and Gregory N. Morscher. 2019. "Thermomechanical Characterization of SiC/SiC Ceramic Matrix Composites in a Combustion Facility" Ceramics 2, no. 2: 407-425. <https://doi.org/10.3390/ceramics2020032>

Effects of Hypoxia on Vehicle Motor Control during Matched and Mismatched Vestibular Feedback

Student Researcher: Lanna N. Klausing

Advisors: Dr. Megan Reissman and Dr. Timothy Reissman

The University of Dayton
Mechanical Engineering

Abstract

Spaceflight generates adaptations in the vestibular, sensorimotor, and cardiovascular systems due to the exposure to microgravity¹. Post-flight these adaptations manifest as deficits in spatial orientation (e.g.: tilt-translation illusions), in sensorimotor coordination (e.g.: walking, balance), and in cardiovascular function (e.g.: orthostatic hypotension). Issues impacting mission success typically arise from sensory discrepancies between visual and vestibular afferent signals, often referred to as spatial disorientation. However, the impact of spatial disorientation on motor control behaviors is less well understood since most motor control tests are conducted under stationary conditions. This study focuses on motor control of human-in-machine systems, for which motor control outputs directly impact the motion and orientation of the human/machine. This is particularly relevant to space flight as spatial disorientation during re-entry appears highly prevalent and impacts ability to complete critical motor control tasks such as vehicle landing maneuvers^{2,3}.

Project Objectives

This project seeks to advance understanding of human-in-machine motor control performance. Of particular interest is the exploration of how motor control of a moving vehicle (in this case, the motion simulator) is impacted by changes in sensory information. This is measured with regards to the participant's ability to achieve various movement tilt tasks. Studying the role of sensory input during human-in-machine movements will allow for better understanding of sensory input processing models, as well as inform pre-flight training procedures for pilots.

A secondary objective is to evaluate motor control performance as a result of oxygen level of the participant. Knowledge of motor control function during hypoxia will increase understanding of pilot risks under these conditions and inform safeguards in the case of a hypoxic environment.

Methodology

The following protocol was approved by the University of Dayton Institutional Review Board (IRB). All testing was performed in the Empower Laboratory of Raymond Fitz Hall at the University of Dayton. Data collection was divided into two sessions: Day A, in which participants completed motor control tasks while breathing ambient room air, and an optional Day B, in which participants performed tasks while breathing 10% oxygen, placing subjects in a state of hypoxia. Both sessions lasted 2 hours. All subjects (n=14 Day A) were healthy between the ages of 18-65 years old (7M 7F, 21.5±2.42 years). The physiological requirements for the study determined that participants were non-obese with normal blood pressure (<140/90 mmHg) and were not acclimated to high altitudes (>5,000 feet). Participants were also required to have natural or corrected vision to 20/20. Participants were screened to ensure they did not have a serious upper limb injury within 1 year prior to the study.

Day A Procedure (Ambient Room Air)

Heart rate (3-lead ECG) and beat-beat blood pressure (finger photoplethysmograph) were continuously monitored during Day A procedure. Participants were placed in a motion simulator (Yaw VR) controlled by a standard joystick. A neck brace was utilized to support participants' heads during the tilting motions, and a lap seatbelt was used to secure their position within the chair. A virtual reality environment was designed using Unity software (version 2020.3.22f1) to suit this study's protocol requirements, which was then displayed on a virtual reality headset (HTC VIVE Pro Eye). The environment consisted of a grassy meadow circled by naturalistic trees, which allowed for gravitational cues during the tasks, but no heading information. Participants were positioned in the center of the virtual meadow, and motor control tasks were visually presented directly in front of them. These tasks were represented by long rectangular bars, tilted from the neutral horizontal angle by $\pm 10^\circ$ or $\pm 20^\circ$. Participants were instructed to manipulate the joystick to achieve a matching tilt angle of their vehicle (the Yaw VR motion simulator). Participants indicated completion of the task by pressing the trigger button of the joystick. At this point, they received visual error feedback in the form of their current tilt angle, as well as success or failure indications to allow for performance improvement. Successful trials were arbitrarily defined as a final tilt angle within 2° of the target angle for $\pm 10^\circ$ tasks, or 4° of the target angle for $\pm 20^\circ$ tasks. The differences in success ranges for the two target angles allow both tasks to have similar task difficulties, as suggested by Fitts's Law.

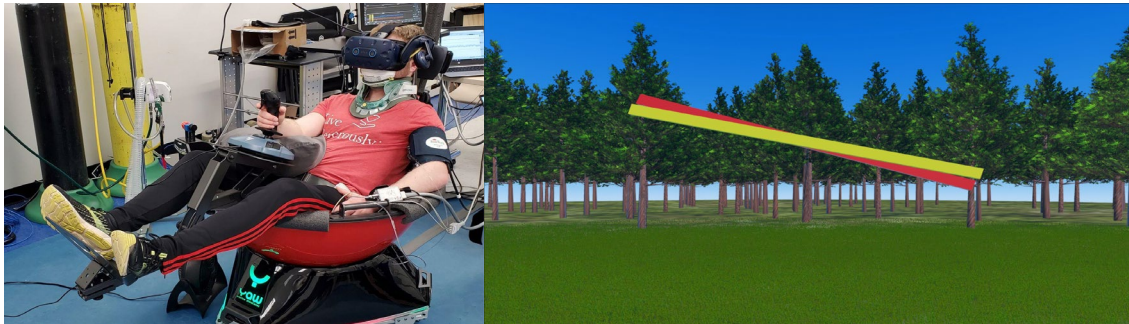


Figure 1: Experimental setup and virtual environment

These tasks were performed under four factorial condition combinations (Table 1). One of the factors was vestibular input, with levels of matched motion and no motion. "Matched motion" meant that the motion simulator chair movement matched the input of the joystick. "No motion" involved the motion simulator chair remaining stationary while the virtual environment tilted to match the joystick input, simulating a tilting motion without any physical movement. The other factor was visual target status, with the levels of solid and flashed. "Flashed" meant the red visual target appeared in the virtual environment and disappeared after three seconds. Participants were instructed not to begin flashed tasks until after the target disappeared. "Solid" indicated the red visual tilt target remained in the virtual environment without disappearing. Participants were instructed to begin solid tasks as soon as the target appeared. Participants were initially trained in each condition, and then performed two sets of each of the four conditions, with 20 tasks for each condition.

Table 1: Factors and Levels of Day A, part 1

	No Motion	Motion
Solid Visual Target	20 tasks $\pm 20^\circ$ and $\pm 10^\circ$ angles	20 tasks $\pm 20^\circ$ and $\pm 10^\circ$ angles
Flashed Visual Target	20 tasks $\pm 20^\circ$ and $\pm 10^\circ$ angles	20 tasks $\pm 20^\circ$ and $\pm 10^\circ$ angles

During the final portion of Day A protocol, participants were assessed in their ability to recognize sensory mismatch during tilt tasks. During this portion of the study, all tilt tasks were $\pm 20^\circ$ and visual error feedback was removed, as the participants were no longer being assessed in their task accuracy. Vestibular input to the subjects was manipulated by causing the motion simulator to achieve physical tilt angles that were either 7° greater than what was visually displayed during the movement, 7° less than the movement displayed through the headset, or matched to the movement displayed on the headset (table 2). Each of these three conditions were presented to the participants in a randomized set of 15 tasks, with no way of participants knowing which condition it was. Subjects were instructed to perform the tilt task as they had during the initial portion of the study and then indicate verbally whether their vestibular tilt sensation was over-tilted compared to their visual, under-tilted compared to visual, or matched to their visual. Their responses were then recorded. Participants performed 3 sets of 15 tasks with a “solid” visual target (target stayed in the environment without disappearing) and 3 sets of 15 tasks with a “flashed” visual target (target disappeared after 3 seconds).

Table 2: Factors of Day A, part 2

	Vestibular Reduced	Matched Motion	Vestibular Exaggerated
Solid Visual Target	5 tasks $\pm 20^\circ$ angles	5 tasks $\pm 20^\circ$ angles	5 tasks $\pm 20^\circ$ angles
Flashed Visual Target	5 tasks $\pm 20^\circ$ angles	5 tasks $\pm 20^\circ$ angles	5 tasks $\pm 20^\circ$ angles

Day B Procedure (Hypoxic/Normoxic Air)

Upon completion of Day A procedure, participants had the option to perform a second visit, which involved performing motor control tasks under hypoxic (10% O₂) and normoxic (21% O₂) conditions. To date, four subjects have completed Day B. Along with continuous heart rate and blood pressure, brain blood flow was measured via transcranial doppler.

During hypoxic trials, participants breathed 10% oxygen pO₂ of 76 mmHg (Hans Rudolph oro-nasal breathing mask), which is equivalent to oxygen levels at approximately 14,000ft. Subjects breathed 21% oxygen during normoxic trials, which is equivalent to ambient room air. Prior to task start subjects rested while breathing the prescribed air to allow oxygenation levels to equilibrate.

After the setup of the physiological measures, participants performed the same training tutorial completed on Day A to allow for familiarization of the tasks. The four factorial conditions from Day, previously shown in Table 1, were then performed in a randomized order while breathing the determined oxygen percentage. One set of 4 was completed under hypoxic conditions and one set of 4 was completed under normoxic conditions. Whether the hypoxic set or normoxic set came first was cross-balanced between subjects. Regardless of order, a 15 minute break was observed between the hypoxic and normoxic sets to allow for oxygenation re-acclimation.

Data Processing

MATLAB and Biomechanics Software (Visual 3D, C-Motion) were used to process the data collected from the VR environment. Data was divided into individual tasks during each of the trials. Task start was defined by the appearance of the visual target within the VR environment. A separate annotation was made to define participants were able to begin moving the joystick for the task, which was as soon as the target appeared for solid visual target conditions, and as soon as the target disappeared for flashed visual target conditions. The end of the task was defined by the participant’s press of the trigger button, or the automatic time-out of 10 seconds after the start of the trial if participants failed to press the trigger.

Absolute error was processed, with positive values defining an overshoot and negative values defining an undershoot. Statistical differences (set at $p < 0.05$) were determined using Repeated Measures ANOVA and within factors of Vestibular Input, Target Presentation, and Target Magnitude (NCSS v2021). Where indicated post-hoc Tukey-Kramer pair-wise comparisons were made to determine p values.

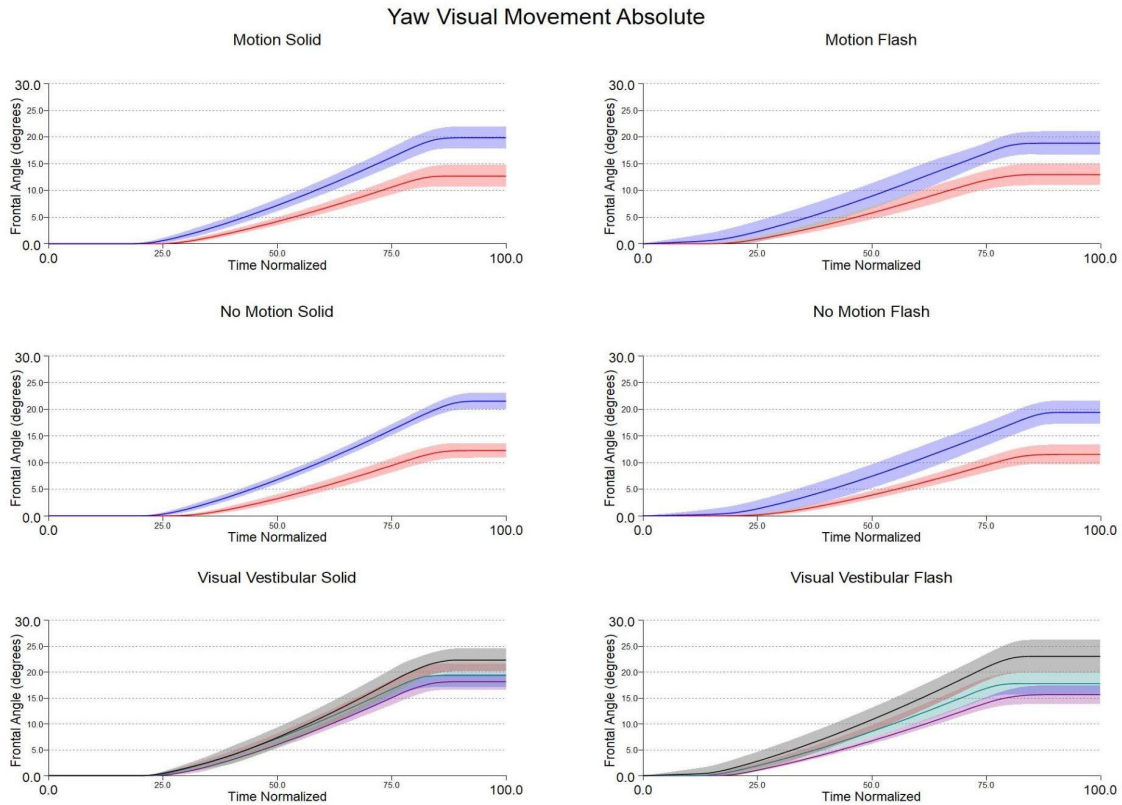


Figure 2: Angle responses over time for each vestibular condition. Blue lines represent 10° task mean and standard deviation and red lines represent 20° tasks. Black lines represent reduced vestibular input task mean and standard deviation, green represents matched vestibular input tasks, and purple represents exaggerated vestibular input.

Results

Investigation of Vestibular Input and Target Presentation- Roll Tilt Error

These results include 11 subjects from Day A protocol. Vestibular Input and Target Presentation were significant factors in final target error ($p < 0.0001$, $P = 0.99$ and $p < 0.05$, $P = 0.51$). The low power value on the Target Presentation factor suggests that further subject testing is required to correctly interpret this result. For Vestibular Input, the motion condition resulted in a mean final error of -0.33° (undershoot) and the no motion condition resulted in a mean final error of 0.45° (overshoot). For Target Presentation, the flashed target resulted in a mean final error of -0.09° (undershoot) and the solid target resulted in a mean final error of 0.21° (overshoot). Additionally, Target Magnitude was significant ($p < 0.0001$, $P = 1.00$) with the small 10° target resulting in mean error of 1.20° and the large target resulting in mean error of -1.07

These results include 11 subjects from Day A protocol. Vestibular Input and Target Presentation were significant factors in final target error ($p < 0.0001$, $P = 0.99$ and $p < 0.05$, $P = 0.51$). The low power value on the Target Presentation factor suggests that further subject testing is required to correctly interpret this result. For Vestibular Input, the motion condition resulted in a mean final error of -0.33° (undershoot) and the no motion condition resulted in a mean final error of 0.45° (overshoot). For Target Presentation, the flashed target resulted in a mean final error of -0.09° (undershoot) and the solid target resulted in a mean final error of 0.21° (overshoot). Additionally, Target Magnitude was significant ($p < 0.0001$, $P = 1.00$) with the small 10° target resulting in mean error of 1.20° and the large target resulting in mean error of -1.07° .

Investigation of Vestibular Input and Target Presentation- Task Time

Vestibular Input was not a significant factor in the time to complete the task ($p = 0.202$, $P = 0.24$). Target Presentation and Target Magnitude were significant factor (both $p < 0.0001$, $P = 1.00$). For Vestibular Input, motion gave a mean task time of 3.17 sec and no motion gave a mean task time of 3.12 sec. Flashed targets resulted in mean task time of 2.78 sec and Solid Targets resulted in mean task time of 3.51 sec. Note that Flashed targets were shown for 1 second before any movement (visual or vestibular) was allowed. Task time for Flashed targets only includes time from when the target disappears and movement is allowed. Larger Target Magnitudes took longer to complete with a mean of 2.88 sec for 10° and 3.42 sec for 20° tasks.

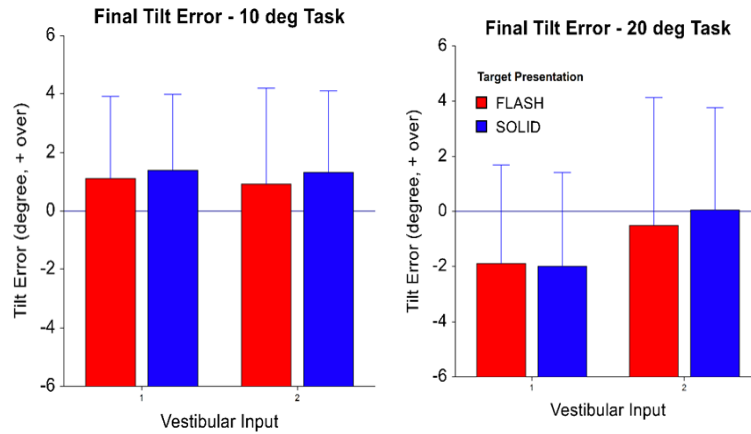
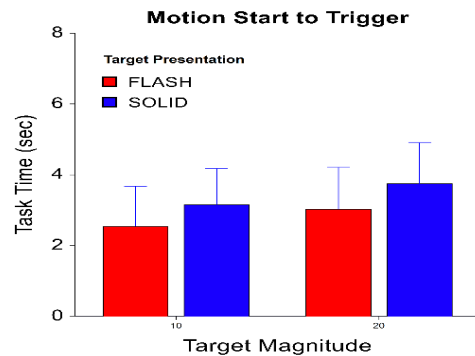
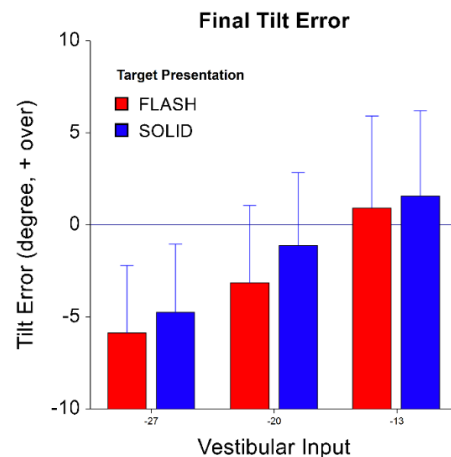


Figure 2: As the influence of Vestibular Input depended strongly on Target Magnitude, the 10° and 20° error results and shown separately. X Axis shows Motion (left) and No Motion (right). Red bars represent flashed visual targets and blue represent solid.



Investigation of Vestibular Manipulation and Target Presentation- Roll Tilt Error

Visual Manipulation was significant in Final Tilt Error ($p < 0.0000$, $P = 1.000$). Tilt error during exaggerated vestibular gain trials was significantly different from other conditions (both $p < 0.0001$). Tilt error was significantly different from each other for all vestibular gain settings. During exaggerated gain the mean error was -5.27° , indicating undershooting the visual target. When gain was not manipulated the mean error was -2.14° , again undershooting the visual target. During reduced gain the mean error was 1.26° , indicating overshooting the visual target. Target Presentation was a significant factor in tilt error ($p < 0.0000$, $P = 0.99$). Flash targets had higher error than Solid targets, specifically Flash resulted in more negative error values, indicating greater undershoot.



Investigation of Vestibular Manipulation and Target Presentation-Task Time

Vestibular Input and Target Presentation were significant factors in the time to complete the task ($p < 0.0001$, $P = 0.99$ and $p < 0.001$, $P = 1.00$). For Vestibular Input, vestibular exaggeration resulted in mean task time of 3.46 sec, no manipulation resulted in mean task time of 3.81 sec, and vestibular reduction resulted in mean task time of 3.99 sec. Flashed targets resulted in mean task time of 3.16 sec and Solid Targets resulted in mean task time of 4.35 sec.

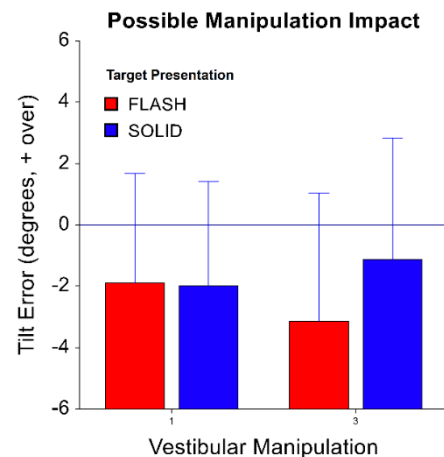
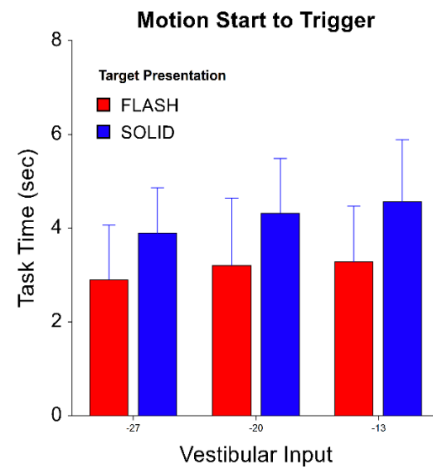
Comparison of Equivalent Tasks

To consider potential impact of the participant knowledge of the Vestibular Manipulation we compared the No Manipulation tasks from this stage of the testing with the equivalent Motion tasks at a 20° Target Magnitude. The factor of Target Presentation was significant for Tilt Error ($p < 0.005$, $P = 0.88$). Particularly, when vestibular manipulation was possible, roll tilt error when given Solid targets was significantly less than when given Flashed targets ($p < 0.001$, mean -1.2° versus -3.2°). While this had no impact when vestibular manipulations were not occurring in the session ($p = 0.92$) and error was roughly -2.0° regardless of Solid or Flashed. The factors of Vestibular Manipulation (Possible/None) and Target Presentation were both significant for Task Time (both $p < 0.0001$, $P = 0.99$). For Flashed targets task time was similar, but for Solid targets, times were significantly longer when participants knew vestibular manipulation was possible (4.41 sec) compared to when manipulations were never occurring (3.77 sec).

Discussion

The Tilt Error results in the primary study suggest that humans are more likely to overshoot a small roll tilt target, both when matched motion is present or when no motion is occurring. This may be due to reliance on visual sensory lines or relatively good perception of vestibular angle for these small changes. However, for larger roll tilt targets, participants are more likely to undershoot the target particularly when matched motion is present. As absolute error was the lowest for the no motion condition this suggests that vestibular sensory data, and the central nervous system task of integrating visual and vestibular data, may in fact reduce orientation performance. While Task Presentation was significant it did not appear to directly improve or reduce final error. This suggests that healthy humans can recall and reproduce orientation targets fairly well without continuous guidance. In the primary study, performance was similar between Flashed and Solid targets but participants spent longer on the Solid tasks. This is attributed to the fact that task direction and magnitude was randomized. For Flashed targets participants had a second to plan their movement but for Solid targets they required extra time (0.73 sec on average) to visually process their target and start moving.

In the Vestibular Manipulation study participants were instructed to perform the orientation task based on visual information and that vestibular manipulation could occur. We found that when vestibular sensory information was exaggerated, relative to the visual environment, participants consistently undershot the visual target. This suggests that when participants experienced vestibular sensation of 20°



roll tilt, they tended to stop moving despite the visual scene not yet attaining the 20° target. The opposite occurred when vestibular sensory information was reduced, participants tended to continue roll tilting the vehicle further moving slightly past the visual 20° target. Finally, when 20° roll tilt tasks under motion conditions were compared between the Primary study and the Vestibular Manipulation study, we observed that when participants knew that vestibular information might be inaccurate, they showed a larger performance difference between Flashed and Solid targets. Even though those particular tasks had no manipulation.

Conclusion

Humans can quickly learn and rapidly execute a vehicle orientation task under either matched motion or no motion conditions. However, when vestibular information is present but inconsistent error increases. This response demonstrates why astronauts may have difficulty in controlling space vehicle orientation in situations where vestibular sensory information is compromised. Both our participants and astronauts are aware that their vestibular sensory information may be inaccurate however this information clearly still influences motor control performance. Overall, the presence of continuous visual target information (Solid Targets) generally appears to reduce absolute final error which favors the use of Heads-Up-Displays where task information is superimposed on the visual field. Further hypoxic data collection is needed, however greater error and variability is expected for all conditions.

Sources

1. Clément, G. et. al, (2020) "Challenges to the central nervous system during human spaceflight missions to Mars," J Neurophysiology.
2. Paloski, W. et. al, (2008) "Risk of sensory-motor performance failures affecting vehicle control during space missions" J of Gravitational Physiology.
3. Clément, G and Ngo-Anh, J, (2013), "Space physiology II: adaptation of the central nervous system to space flight—past, current, and future studies," European J Applied Physiology.

The Effect of Active Flow Control on Far field noise in Supersonic Rectangular Twin Jets

Student Researcher: Ryan Leahy¹

Advisor: Dr. Mo Samimy & Dr. Nathan Webb

The Ohio State University
Mechanical Engineering

Introduction

In relation to axisymmetric nozzles, rectangular jets offer potential benefits that have led to renewed interest in their implementation in designs of next generation of tactical aircraft. These benefits include lower observability, simpler mechanical options for thrust vectoring, and reduced drag [1,2]. In supersonic jets, screech play an important role in the dynamics of noise generation in non-ideally expanded jets as well as jets issued from nozzles with sharp throats, even in the design condition. If two jets are located closely to one another, their screech loops can couple, and have the ability to increase near-field (NF) pressure fluctuations and far-field (FF) radiated acoustic levels [3,4]. The effect of coupling on FF and NF levels is not yet completely understood, however this is not the focus of results presented in this work. The well documented failures of nozzle flaps on the B-1A bombers and F-15E strike aircraft during the test programs are prime examples of the damage that can occur as a consequence of near field pressure fluctuations [5,6]. Far field noise has well been established to have detrimental impacts on the personnel that work on these type of aircraft on aircraft carriers [7], as well as aircraft noise having adverse health effects on the community that lives near air bases [8]. With the possible advantages that rectangular jets offer over axisymmetric jets, and the known adverse effects of twin supersonic jets (both rectangular and circular nozzles), the outcome of this research is to obtain a better understanding of the flow physics while developing an active flow control technique that can combat the undesirable effects such as increased FF noise and NF pressure fluctuations. Previous work by this research has shown the ability to have considerable control authority over the coupling the jets [9]. Results presented in this report demonstrate active control on far field noise levels.

With the implementation of any flow control technique, it is valuable to understand the flow physics that are the root of the phenomena that are the target of control. In this research, the flow physics that drive the negative effects are screech and coupling. Powell [10] first proposed a feedback closure model for screech that other subsequent models have adapted/modified [11,12], but have not altered the original feedback loop concept. Figure 1 contains a schematic that is the current understanding for screech and coupling.

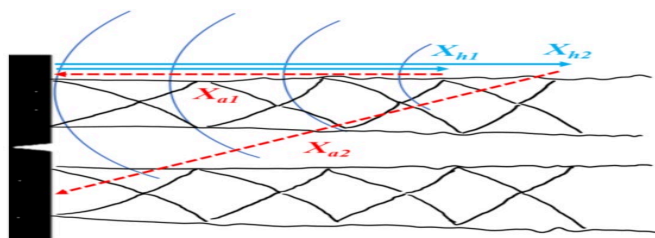


Figure 1: Schematic of twin jets (looking top-down view) displaying screech and coupling phenomena

Specifically, screech occurs when perturbations in the jet shear layer near the nozzle exit excite the Kelvin-Helmholtz (K-H) instability and generate large-scale structures (LSS) in the shear layer of the jets. The LSS

¹ Graduate Student, Aerospace Research Center, OSGC fellow

convect downstream (path of which is indicated with the blue arrows), interacting with the jet shock system. These interactions produce acoustic waves (denoted with blue curved arcs) which propagate upstream and perturb the jet shear layer (direction of these are represented as the red dashed arrows), generating more LSS and thereby completing the feedback loop. To be self-sustaining, this feedback process must occur over an integer multiple of the screech frequency period. Twin jets coupling is also connected to the screech feedback. When the screech frequency and nozzle spacing are such that feedback waves from one jet arrive at its own nozzle exit in-phase with the acoustic waves from the other jet (denoted as arrow X_{a2}), these perturbations reinforce one another and further strengthen the feedback loop. This couples the screech loops and could have the ability to increase the far-field noise levels and near-field pressure. This is currently being investigated and not presented in the results that follow.

Methodology

The active control was tested on rectangular twin jets in an anechoic test facility at Ohio State's Gas Dynamics and Turbulence Laboratory within the Aerospace Research Center. The twin jets (shown in Figure 2) consist of two rectangular jets of aspect ratio 2. The jet width is 0.95 inches (24.1 mm), and the adjacent nozzle lips are spaced 0.758 inches (19.25 mm) apart, 1 area-based equivalent diameter ($D_e = 2\sqrt{(b * h)/\pi}$), where b and h are the width and height of the nozzle exit). The nozzles are bi-conic with a sharp throat. The design Mach number is 1.5. The twin jets assembly is installed within a 6.2 m by 5.6 m by 3.4 m anechoic chamber. The flow is driven by high pressure air from two large (36 m³ total capacity) pressure vessels with a maximum pressure of about 2300 psi (16 MPa). The stagnation pressure of the flow is set by a computer-controlled valve, which can be adjusted to maintain the desired NPR. For this work, the NPR was varied from 2.97 to 5.32 ($M_j = 1.35$ to 1.75). This allowed the LAFPAS' control authority to be examined in overexpanded, design and underexpanded operating regimes

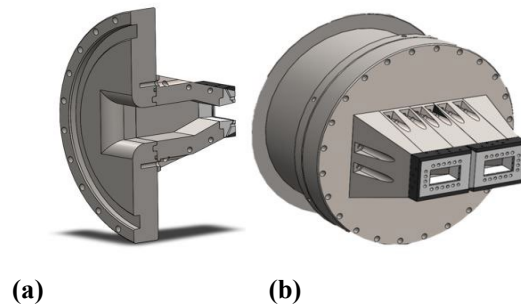


Figure 2: $M_d = 1.50$ Nozzles, (a) nozzle cutaway of 1 jet, (b) front face of the twin jet assembly

Far field acoustic measurements were carried out using the 7 Brüel and Kjær 4939 $\frac{1}{4}$ in microphones that are oriented on the minor axis of the twin jet assembly and located at polar angles (θ) ranging from 30 to 90 degrees at distances of 80 equivalent diameters (D_e) or larger away from the jet. This setup's schematic is illustrated in Figure 3.

The microphone data was recorded with a sampling frequency was 200 kHz and 25 blocks of 32,768 samples were acquired for each data point, resulting in a frequency resolution of 6.10 Hz. These signals were amplified and band-pass filtered between 20 Hz and 100 kHz, using a Nexus 2690 signal conditioner. Microphone calibrations were also performed at a set gain, using a Brüel and Kjær model 4231 acoustic calibrators. The gain value for experiments reported in the results was set to 31.6 mv/Pa. A Fast Fourier Transform code in MATLAB is used to calculate the spectra presented in the plots for each block of data and then average values were calculated from 100 blocks. The calculated Power Spectral Density (PSD) is then converted to SPL in decibels referenced to 20 μPa .

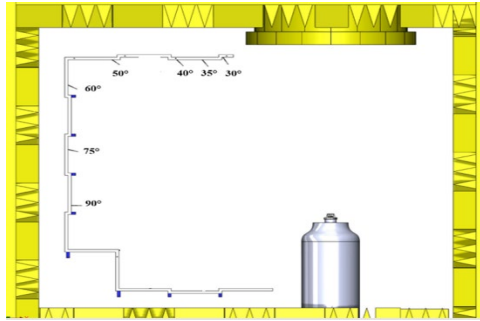


Figure 3: Schematic of Far Field microphone placement within the anechoic chamber

Localized Arc Filament Plasma Actuators (LAFPA), introduced in 2004 [13] were designed to provide instability-based flow control by providing simultaneous high-bandwidth, high-amplitude excitation. In this approach, rapid, near-adiabatic heating in the current filament, which also produces compression waves, is capable of exciting instabilities in high Reynolds number jets [13–15]. Figure 2b shows a model of the current rectangular supersonic twin jet nozzle assembly. The nozzles have thicker lips to accommodate the plasma actuators, distributed around the nozzles. There are a total of 6 actuators (a pair of electrodes for each actuator) on each nozzle (3 on the top, 3 on the bottom). The electrodes are located within a groove that is 1.0 wide and 0.5 mm deep, about 1 mm upstream of the nozzle exit. The tips of the electrodes are nearly flush with the nozzle surface. Applying high voltage across the two electrodes of an actuator causes break-down in the air in the gap between the electrodes and produces a thermal perturbation for the excitation of instabilities in the jet shear layers. LAFPAs have proven successful in various applications [15]. The work presented here is using various actuation patterns & firing frequencies (St_e) for the excitation of the jet shear layer.

Results

Before moving into the effects that the LAFPAs have on the FF acoustics, it is necessary to point out a few characteristics of the FF for jets without excitation. Baseline jets' FF noise levels at design Mach number of the nozzles ($M_j = 1.5$) are shown in Figure 4. Figure 4a shows selected line spectra of FF SPL at select polar angles. The 30-degree spectrum is not shifted, but the respective 40-, 60-, and 90-degree spectra are all shifted down by 10, 20, and 30 decibels respectively. This figure assists in viewing levels at explicit frequency ranges that give insight on the physics of the flow, some of which will be explained later. Figure 4b shows all the measured spectra stacked on top of each other for a frequency vs directionality map. This stacked spectra aids in the comparison of intensity levels of all spectra across all polar angles. One characteristic of FF noise in screeching jets is the existence of screech tones. This sharp tone can be seen in both figures below, at all polar angles, and at a frequency of $\sim 6\frac{1}{2}$ kHz. Screech is still present at this design Mach because of the sharp throated nozzle employed that still contains shock-cell train shown in that of Figure 1. Along with screech is the accompaniment of its harmonics. From the line spectra it can be observed that the 1st fundamental harmonic is registered at higher SPL levels in the sideline angles as reported in previous literature [16]. Mixing noise region of FF noise can be seen as the hump at low polar angles (blue and orange lines) and the red lobe in the bottom left hand of the stacked spectra. It is generally agreed that the dynamics of large scale structures (LSS) are responsible for the dominant portion of turbulent mixing noise [16]. Therefore, if control of these LSS can be achieved, there is great potential in the reduction of the radiated FF noise from this region.

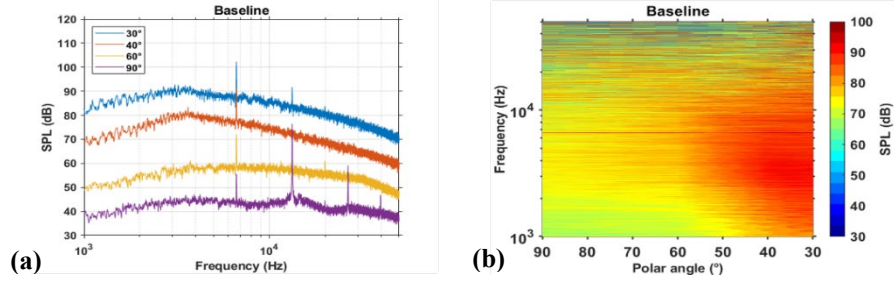


Figure 4: Baseline far field results for $M_j = M_d = 1.50$

Excitation at 4.5 kHz, lower frequency than screech ($St_e > St_s$), has shown a majority of increased SPL levels over all polar angles. Figure 5b shows the change in SPL from the baseline case to the excited. The orangish, red lobes at all low frequencies show a broadband increase in SPL levels, which is not a desirable outcome with our active control. The nonlinear interaction between the natural occurring screech and excitation also creates a large amplitude tone at an even lower frequency as seen in Figure 5b at ~ 1.3 kHz. This nonlinear interaction can be directly related to the equation $f_s - f_e = f_b$, where the frequency of this new beat tone (f_b) occurs due to the interaction of screech (f_s) and introduced excitation (f_e). This nonlinear wave interaction is similar to that has been studied in subsonic jets experimentally by Arbey & Ffowcs Williams [17].

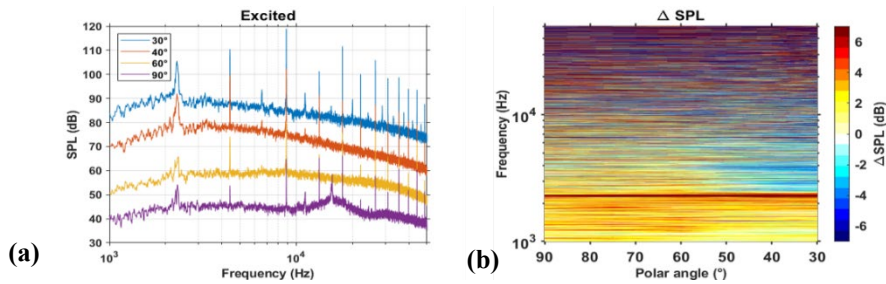


Figure 5: Excitation case: $M_j = M_d = 1.50$, $St_e = 0.20$

After demonstrating the ability to either increase (Figure 5) or decrease the FF noise (not shown) at the design Mach of the nozzle, excitation with the plasma actuators at non-ideally expanded conditions have also been performed and display advantageous results. Figure 6 illustrates the delta SPL maps of different firing patterns, with both excitation frequencies almost double screech (~ 17 kHz) at an overexpanded condition of $M_j = 1.35$. Figure 6a demonstrates firing actuators with a pattern that generates more spatially coherent structures (SCS), while Figure 6b shows the use of a firing pattern that encourages 3-dimensionality (3DS) of the turbulent structures in the flow. A comparison of the two cases shows that the 3DS pattern has a greater reduction at mid frequency content with darker blue lobes (5-6 dB reduction) and at the natural screech frequency (~ 8.5 kHz) than the SCS. The 3DS pattern displays that with more 3-dimensionality to turbulent structures, while convecting downstream, they will not be as coherent as the SCS pattern to interact with the shock cells in the flow and complete the screech loop shown in Figure 1.

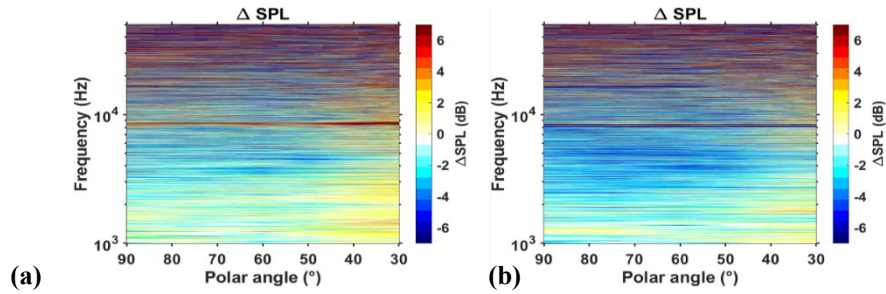


Figure 6: Excitation cases: $M_j = 1.35$, $St_e = 0.82$, (a) Firing pattern that generates spatially coherent structures, (b) firing pattern that encourages 3-dimensionality of structures

Another non-ideally expanded regime excited by the LAFPAs was the underexpanded regime at $M_j = 1.75$. The baseline, excited, and change in SPL levels can be seen in Figure 7. The excitation frequency of this case is considerably higher than that of the natural screech frequency as seen in the comparison of Figure 7a ($f_s = 5$ kHz) with Figure 7b ($f_e = 20$ kHz). These two figures also give insight to the hump that is associated with broadband shock associated noise (BBSAN) at high polar angles (purple and yellow lines) and at frequencies larger than screech. BBSAN has been noted in literature to be caused by the interaction of LSS by the shock cell system in the flow [16]. This once again shows if LSS can be controlled to a certain extent, there is a high potential to be able to control this type of noise generation in the flow. Figure 7c shows the change in SPL levels from the baseline to excitation, with an overall decrease of at least 4 dB in mid to high polar angles (40-120 deg) at low frequencies ($< f_s$). There is however a lobe located at high polar angle of 100 to 120 degree that shows an increase in BBSAN for these directions. Overall, the excitation does an appreciable job at reducing the FF noise.

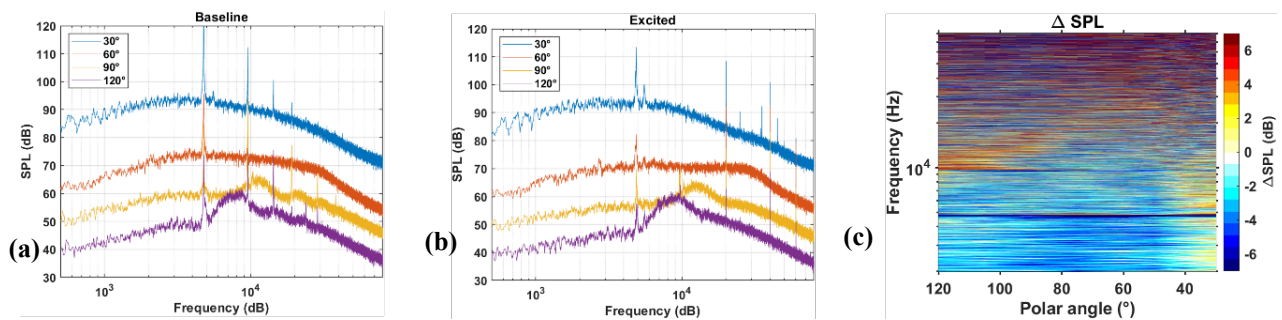


Figure 7: Excitation case: $M_j = 1.75$, (a) baseline, (b) excited case $St_e = 0.81$, (c) change in SPL (excited minus baseline)

Conclusion

The results of active flow control at design conditions and non-ideally expanded regimes show that the LAFPAs have control authority to change the far field noise characteristics in jets. FF acoustic levels for supersonic twin jets were presented and baseline noise characteristics of the jets were identified at the design Mach number of the nozzles. Most importantly it was shown that the SPL levels were able to be reduced at overexpanded ($M_j = 1.35$) and underexpanded ($M_j = 1.75$) regimes of flow while using excitation frequencies that were much higher than that of their naturally occurring screech frequencies. It is also to be noted that exciting at low frequencies, the FF noise levels showed an increase in SPL. In addition, at these low frequencies nonlinear wave dynamics were observed like those reported in the literature [17]. The next steps of this research are to develop and define a relationship (if one found)

between the coupling of the jets, FF noise and NF pressure fluctuations. Further down the road this research will characterize baseline and excited flow of heated jets.

Acknowledgments

I would like to thank my advisors Dr. Mo Samimy and Dr. Nathan Webb for their guidance on this project as well as fellow graduate student Ata Esfahani for fruitful discussions on the topic of jet noise. The support of this research by the Office of Naval Research through Dr. Steve Martens is greatly appreciated.

References

- [1] Dusa, D., Speir, D., Rowe, R., and Leavitt, L. Advanced Technology Exhaust Nozzle Development. In *19th Joint Propulsion Conference*, AIAA paper 1983-1286, 1983.
- [2] Wiegand, C. F-35 Air Vehicle Technology Overview. Presented at the 2018 Aviation Technology, Integration, and Operations Conference, Atlanta, Georgia, AIAA paper 2018-3368, 2018.
- [3] Shaw, L. "Twin-Jet Screech Suppression." *Journal of Aircraft*, Vol. 27, No. 8, 1990, pp. 708–715. <https://doi.org/10.2514/3.25344>.
- [4] Panickar, P., Srinivasan, K., and Raman, G. "Aeroacoustic Features of Coupled Twin Jets with Spanwise Oblique Shock-Cells." *Journal of Sound and Vibration*, Vol. 278, Nos. 1–2, 2004, pp. 155–179. <https://doi.org/10.1016/j.jsv.2003.10.011>.
- [5] Berndt, D. E. *Dynamic Pressure Fluctuations in the Internozzle Region of a Twin-Jet Nacelle*. Publication 841540. SAE International, Warrendale, PA, 1984.
- [6] Walker, S. H. *Twin Jet Screech Suppression Concepts Tested for 4.7 Percent Axisymmetric and Two-Dimensional Nozzle Configurations*. 1990.
- [7] Rovig, G. W., Bohnker, B. K., and Page, J. C. "Hearing Health Risk in a Population of Aircraft Carrier Flight Deck Personnel." *Military Medicine*, Vol. 169, No. 6, 2004, pp. 429–432. <https://doi.org/10.7205/MILMED.169.6.429>.
- [8] Basner, M., Clark, C., Hansell, A., Hileman, J. I., Janssen, S., Shepherd, K., and Sparrow, V. "Aviation Noise Impacts: State of the Science." *Noise & Health*, Vol. 19, No. 87, 2017, pp. 41–50. https://doi.org/10.4103/nah.NAH_104_16.
- [9] Esfahani, A., Webb, N. J., and Samimy, M. Control of Coupling in Twin Rectangular Supersonic Jets. In *AIAA AVIATION 2021 FORUM*, AIAA paper 2021-2122, 2021.
- [10] Powell, A. "On the Mechanism of Choked Jet Noise." *Proceedings of the Physical Society B*, Vol. 66, 1953, pp. 1039–1056.
- [11] Tam, C., Seiner, J., and Yu, J. "Proposed Relationship between Broadband Shock Associated Noise and Screech Tones." *Journal of Sound and Vibration*, Vol. 110, No. 2, 1986, pp. 309–321. [https://doi.org/10.1016/S0022-460X\(86\)80212-7](https://doi.org/10.1016/S0022-460X(86)80212-7).
- [12] Panda, J. "An Experimental Investigation of Screech Noise Generation." *Journal of Fluid Mechanics*, Vol. 378, 1999, pp. 71–96. <https://doi.org/10.1017/S0022112098003383>.
- [13] Samimy, M., Adamovich, I., Webb, B., Kastner, J., Hileman, J., Keshav, S., and Palm, P. "Development and Characterization of Plasma Actuators for High-Speed Jet Control." *Experiments in Fluids*, Vol. 37, No. 4, 2004, pp. 577–588. <https://doi.org/10.1007/s00348-004-0854-7>.
- [14] Utkin, Y. G., Keshav, S., Kim, J.-H., Kastner, J., Adamovich, I. V., and Samimy, M. "Development and Use of Localized Arc Filament Plasma Actuators for High-Speed Flow Control." *Journal of Physics D: Applied Physics*, Vol. 40, No. 3, 2007, pp. 685–694. <https://doi.org/10.1088/0022-3727/40/3/S06>.
- [15] Samimy, M., Webb, N., and Crawley, M. "Excitation of Free Shear-Layer Instabilities for High-Speed Flow Control." *AIAA Journal*, Vol. 56, No. 5, 2018, pp. 1770–1791. <https://doi.org/10.2514/1.J056610>.
- [16] Tam, C. K. W. "Supersonic Jet Noise." *Annual Review of Fluid Mechanics*, Vol. 27, No. 1, 1995, pp. 17–43. <https://doi.org/10.1146/annurev.fl.27.010195.000313>.
- [17] Arbey, H., and Williams, J. E. F. "Active Cancellation of Pure Tones in an Excited Jet." *Journal of Fluid Mechanics*, Vol. 149, No. 1, 1984, p. 445. <https://doi.org/10.1017/S0022112084002743>.

Self-Organization of Organic Molecules

Student Researcher: Jacob Martin

Advisor: Jessica Bickel

Cleveland State University
Chemical Engineering

Abstract

Organic semiconductors have advantages over their inorganic counterparts including low cost, flexibility, and eco-friendliness. While organic semiconductors have interesting uses in devices such as solar cells, photovoltaic cells, and even flexible electronics, they are not competitive with inorganics due to their lower conductivity. One reason for this lower conductivity is due to their amorphous structure, making it difficult for electrons to tunnel from one adjacent molecule to the next.

Methodology Used

A possible method to increase the conductivity of organic semiconductors is crystallization via self-assembly. This work computationally examines the self-organization of an organic semiconductor, pentacene, on graphene. It is expected that pentacene and graphene would stack similarly to graphite, where ABAB stacking is the lowest energy and AA stacking is the highest. Ab initio calculations were used to determine the ground-state energy of a single pentacene molecule on a graphene sheet at various orientations.

Results

Figure 1A-E shows energy maps for pentacene on graphene, where pentacene is translated in the x and y directions: A) 0°, B) 7.5°, C) 15°, D) 22.5°, and E) 30°. Only angles up to 30° were considered due to graphene's sixfold symmetry as angles of $30 \pm n^\circ$ (i.e., 0 and 60°) have the same orientation. The horizontal and vertical shifts are shown on the x and y axes, respectively, while the energy value relative to the highest energy (0 meV/pentacene atom) is shown by the color map. Each color map has notations marking the three lowest (star, circle, asterisk) and three highest (diamond, triangle, X) energies at each angle. There are several regions with similar energies: high energy (red), intermediate energy (yellow to light blue), and low energy (dark blue). The total energy range is 2.55 meV/pentacene atom (91.8 meV total), with the highest energy being 0 degrees, .5 horizontal shift, .5 vertical shift. Surprisingly, the lowest energy position is not AB stacking as expected based on graphite. It is, rather, at a rotation of 7.5°, a horizontal shift of 0.5, and a vertical shift of 0. The energy difference between these two positions is only 0.07 meV/pentacene atom and is nearly negligible. As the rotation angle of pentacene increases, the energy range decreases. High energy regions center (dark red) lower energy (orange) as the angle increases up to 30°. The resulting energy range decreases from 2.47 meV/pentacene atom at 0° to 0.85 meV/pentacene atom at 30°.

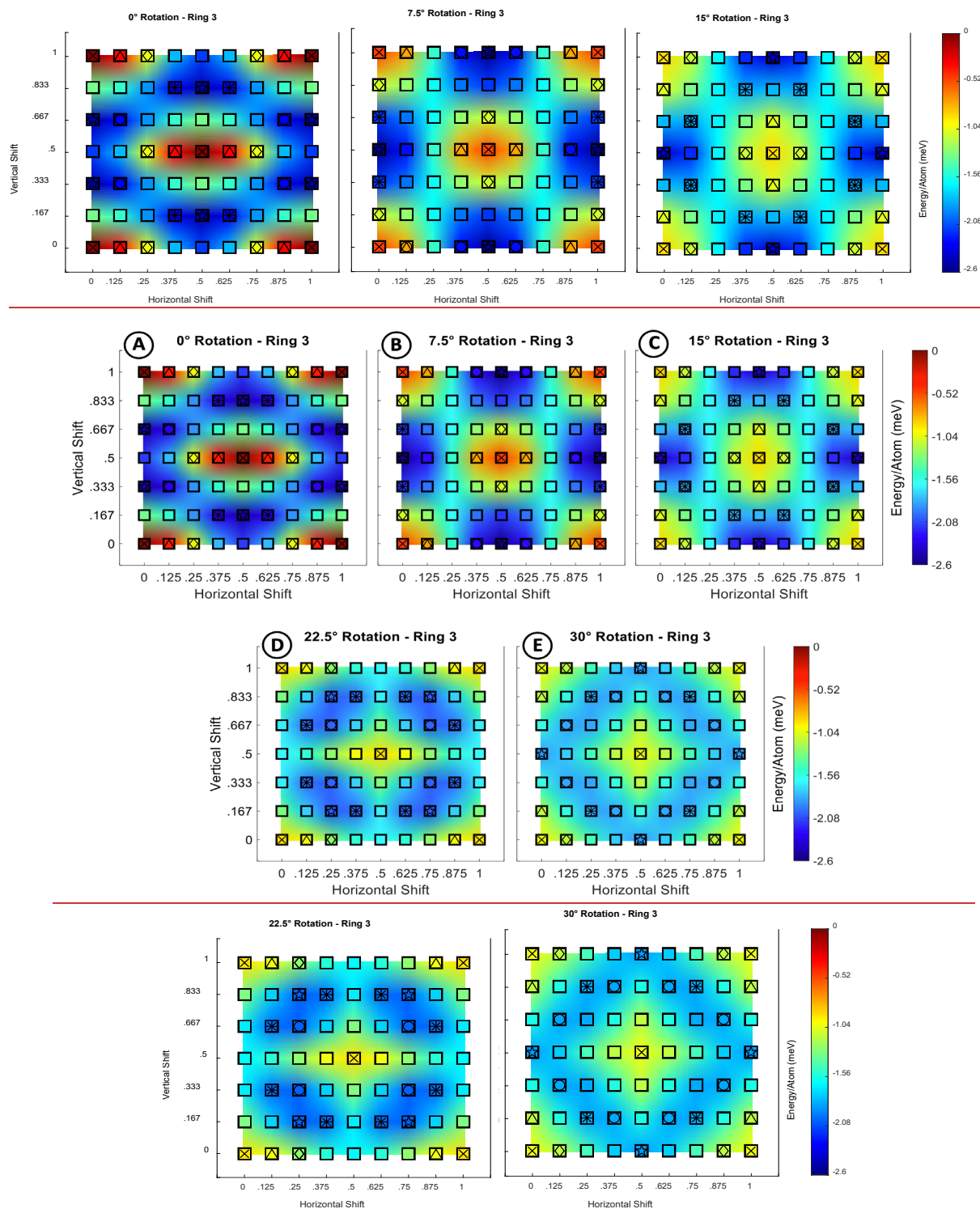


Figure 1A-E. Energy Maps for pentacene (ring 3) at A) 0°, B) 7.5°, C) 15°, D) 22.5°, and E) 30°

There are a total of 15 positions with an energy relative to the minima less than that of room temperature. This suggests that pentacene as there is not a clear, lowest energy. Rather, pentacene crystallization on graphene may be driven more through interactions between adjacent molecules.

Multimodal Environmental Sensing via Application of Heterogeneous Swarm Robotics

Student Researcher: Jacob C. O'Donnell

Advisor: Dr. Brian Trease

The University of Toledo

Mechanical, Industrial, and Manufacturing Engineering Department

Abstract

Harmful algal blooms (HABs) can be devastating to their local environment by affecting water supplies and wildlife. HAB's are often observed and measured using satellite imagery and water samples. To help prevent damage to the environment, an autonomous swarm of unmanned aerial vehicles (UAVs) and unmanned surface vehicles (USVs) can be used for locating and monitoring the harmful algae. In this study, a swarm of multiple cost-effective USVs, along with an UAV, will be developed to survey an area for HABs. Cost-effective USVs allow for a larger swarm and improving surface coverage area. To accompany the USVs, a UAV uses image processing to identify potential HABs locations, generating target areas relayed to the surface USVs for further investigation. The system functions on a centralized swarm approach with real time data transmission from the quadcopter to a designator that distributes the USV's as the quadcopter scans the area. The models are created with ROS (open-source robot control system) and Gazebo (open-source robot simulation package) to allow for simulation of controls as implemented on the actual robots. The simulations provide a test chamber for all control code that can be implemented on physical boats to be tested in the field for both ideal and realist effectiveness of this heterogeneous swarm environmental sensing method.

Project Objectives

The objectives for this project were to develop an autonomous robotic swarm that could be capable of locating algae with reduced error in algae detection. A heterogeneous swarm was desired, utilizing a quadcopter for initial detection of algae with boats on the surface to go to locations found by the quadcopter. The system needed to be designed to run centralized for the initial development, with the ability to become decentralized with future developments. For this purpose, the quadcopter needed to work as both a detector for algae and a centralized designator for the boats, but each boat should be a separate system capable of working independently of other systems in the swarm once given a target location. All of this needed to be achieved with open-source software and inexpensive parts to provide a swarm that is inexpensive to produce, maintain, replace, and expand for the desired functions.

Methodology Used

To achieve the goal of a heterogenous swarm, multiple subsystems needed developed. Previous work in the lab lead to developments for the boat design, hardware, and basic autonomous control. The boats consist of a Raspberry Pi, compass, GPS, XBee, and two waterproof brushless motors. The Raspberry Pi manages all processing and controls for the boat. All the equipment interfaces with the Raspberry Pi. The open-source Robot Operating System (ROS) is run on the Raspberry Pi to manage all internal communication and control systems. The compass is used to determine the direction of the boat. The GPS is used to determine the location of the boat. The Xbee does wireless communication to and from the boat at extended ranges. The waterproof brushless motors are used to move the boat in the water. A quadcopter using a Pixhawk 4 with four brushless motors was also set up for use with the project, but with limited testing. To get the swarm to the desired level of automation, a three-stage approach was used: (1) development of the swarm in a simulated environment to transfer assets to ROS, further develop

autonomous nature of the boats, and test all code in a simulated environment; (2) Implement ROS and the automation code on boats with a centralized designator; and (3) Implement the quadcopter into the system as a point detector and boat designator.

For the first step, all the code originally developed for the boats in Python was adjusted to run with ROS and multiple nodes. A simulation environment was set up with ROS and the open-source robot simulation environment Gazebo to develop, test, and experiment with the autonomous code for the boats. The simulated boats were set up with similarity to the physical boat to allow the control code to work in the physical and simulated environments. The boats were set up to work in an autonomous nature after receiving a target GPS location. The boat then determined a direct path to the target location based on the boat GPS location. The angle of the boat from the compass is used to determine the path angle, and as an input to the PID controller for the motors. The layout of the boat autonomous control system shown in Figure 1. Detection of points in the simulated environment rely on OpenCV BLOB Detection of circular points on the ground by a camera from above. To emulate the use of a physical quadcopter, hector quadcopter for Gazebo is used [1]. These points had a GPS location calculated by the quadcopter location and OpenCV pixel location that could then be sent to the designator. The designator algorithm outlined in Figure 1B keeps a list of the target points, determines which boats are available, determines the closest boat to the target point, and then repeats for all points in the list that have not been searched. The designator handles point selection while the boats manage autonomous movement to a designated GPS location.

The second step required implementation on physical hardware. With each boat having separate nodes all handling various aspects of the boats, the control code used by the simulated boats was put on each boat. Then, the compass, GPS, Xbee, and motor controller all have separate nodes developed. The same methodologies used for the simulated swarm were used on the physical swarm, but with modifications to be used with limited communication over an XBee mesh network. To manage designation, a laptop was used with an XBee attached to wirelessly send commands to the boats. In this stage, development started with one boat, and increased to three boats. While six total boats were produced and tested in simulations, only up to three were evaluated physically because of limitations in time and space, as well as hardware issues, but all the algorithms for designation and autonomous control were set up for expansion of the swarm.

The third step was to implement the quadcopter into the swarm. A quadcopter was set up to run in the swarm with external levels of automation through the flight controller, with the ability to implement communication with ROS by using MAVROS. Hardware and software issues with the quadcopter and flight controller prevented reliable flight, so a commercial drone was used to survey an area. The same methodology was applied to the video from the commercial drone to determine GPS location of points put on a pond with OpenCV. While this method did not follow the autonomous nature, it functioned to prove the abilities of each method.

Results Obtained

To assess the use of a swarm like this, it was analyzed if it was necessary to detect algae with both an overhead camera and a physical sample by in situ sampling. During physical detection of the points using the commercial drone, there were eight points put on the water, but ten were detected resulting in two false detections shown in Figure 2. When evaluating the swarm in simulations, it was also found that because of variation in the GPS readout and the camera angle with the ground, point detection could provide a location slightly off the true location.

Simulations provided a method of comparing quadcopter coverage time and swarm coverage time outlined in Figure 3. Settings for quadcopter and boat movement speeds were based off what the lab

equipment could do reliably. The quadcopter covered the test area of points in a 50 m by 50 m area in an average of 118.21 seconds. This included time to take off and scan the area. When using the quadcopter and having the boats check all the points, it took the swarm an average of 193.43 seconds results in a 63.63% increase in time going from the quadcopter only to using a heterogeneous swarm method. This was done with all points being required to have a boat stop at the location.

Significance and Interpretation of Results

With the physical detection having 20% of the results being false positives, it becomes beneficial to use a heterogeneous swarm to both detect and measure points with in situ sampling. As seen by the simulations results, this can result in the swarm using 64% more time than it would take to cover with the area with just a quadcopter. This time increase to perform a heterogeneous scan can counter inaccuracies in data. The testing in this project found that 20% of the points detected were false positives on the physical targets, so the number of algae would be considered higher than it is if this system were used to detect algae. To counter this, in situ sampling can be done to determine if the points found are actual algae or not, which could reduce detect to no false positives. When it comes to detecting algae which can affect many factors such as the economy [2], wildlife [3], and human health [4], a more accurate reading is beneficial to accurately combat the problem and inform the public. To do so, false negatives need minimized, while false positives can be re-examined to determine if the location has algae or not. A swarm system following the development during this project could provide a system capable of detecting algae, which can be utilized in any location at any time, as it is only dependent on user to set it in location and start the swarm. The base of the swarm developed during this project can work with other aspects to add in a machine learning model to detect algae accurately from a quadcopter and sensors on the boats to do in situ sampling for algae.

Figures/Charts

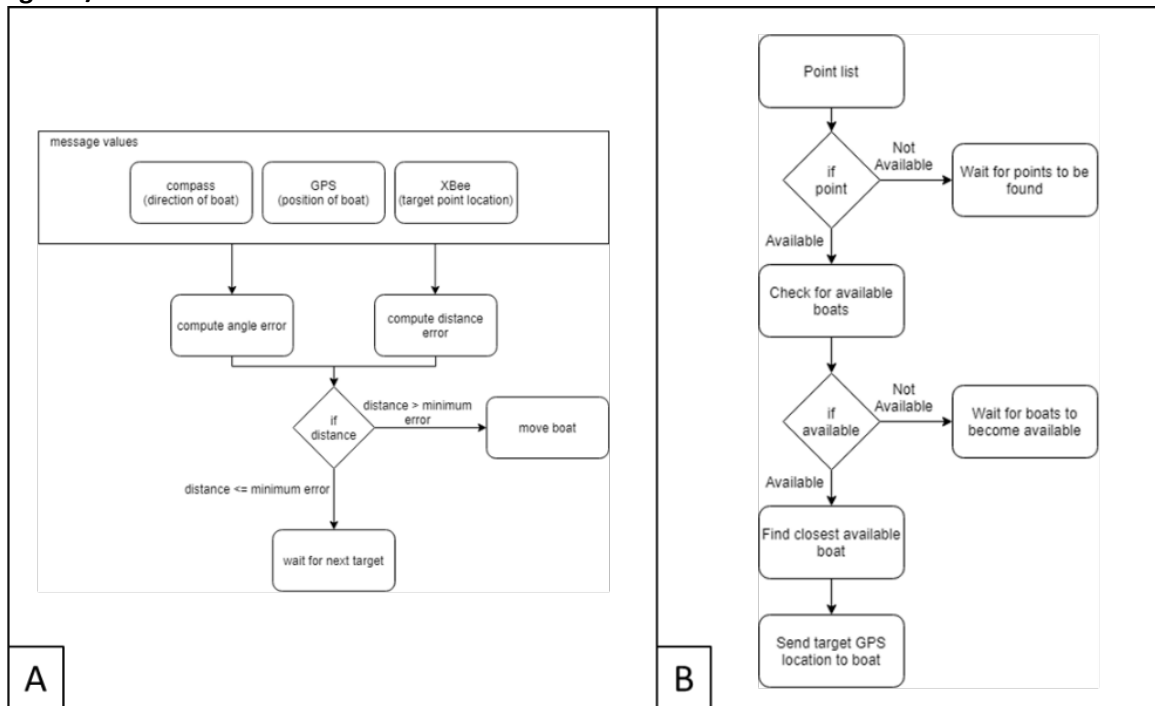


Figure 1. Code layout for boats (A) and designator (B)

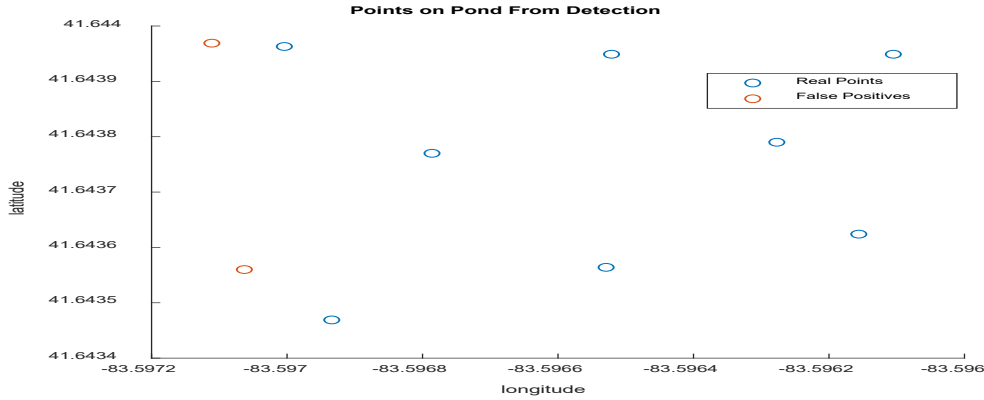
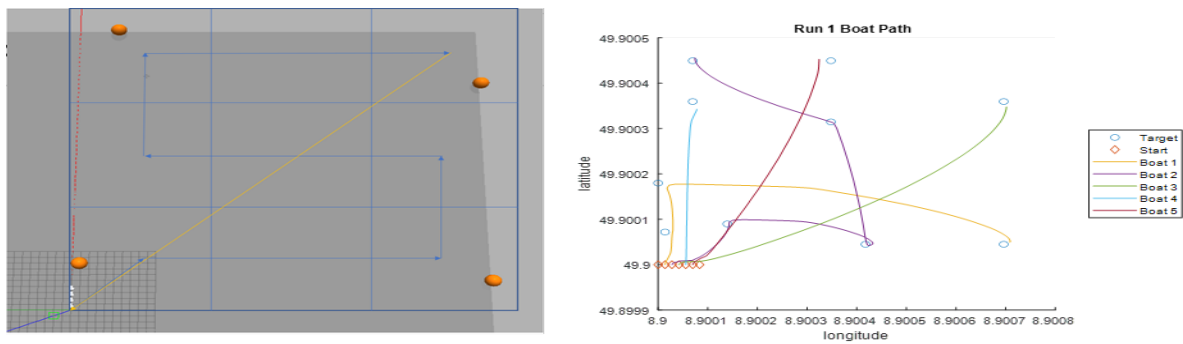


Figure 2. Points detected in physical testing with commercial drone



	Quadcopter Scan Time	Quadcopter and Boat Scan Time	Time Increase	Percentage Increase
Run 1	117.465	193.66	76.195	64.87
Run 2	119.515	194.24	74.725	62.52
Run 3	117.65	192.39	74.74	63.53
Run 4	116.545	196.225	79.68	68.37
Run 5	118.42	194.43	76.01	64.19
Average	118.21	193.43	75.22	63.63

Figure 3. Scan path of quadcopter and boats with time for each method

Acknowledgements

The author would like to thank the Ohio Space Grant Consortium for their support and his advisor Dr. Trease for his guidance throughout this work. The author is also thankful for the members of the 3MDL lab for their help with running tests and working on the hardware, as well as the UTPD and UT Rec Center for the use of test locations.

References

1. "hector_quadrotor - ROS Wiki." http://wiki.ros.org/hector_quadrotor (accessed Aug. 05, 2021).
2. "Status, causes and controls of cyanobacterial blooms in Lake Erie," *Journal of Great Lakes Research*, vol. 40, no. 2, pp. 215–225, Jun. 2014, doi: 10.1016/j.jglr.2013.12.012.
3. "Approaches to monitoring, control and management of harmful algal blooms (HABs)," *Ocean & Coastal Management*, vol. 52, no. 7, pp. 342–347, Jul. 2009, doi: 10.1016/j.ocecoaman.2009.04.006.
4. "Health impacts from cyanobacteria harmful algae blooms: Implications for the North American Great Lakes," *Harmful Algae*, vol. 54, pp. 194–212, Apr. 2016, doi: 10.1016/j.hal.2016.02.002.

Genetic Fuzzy Controller for the Homicidal Chauffeur Differential Game

Student Researcher: Lynn K. Pickering

Advisor: Dr. Kelly Cohen

University of Cincinnati College of Engineering and Applied Sciences
Department of Aerospace Engineering and Engineering Mechanics

Abstract

A fuzzy system is trained by a Genetic Algorithm (GA) to find the optimal control path of the evader relative to the pursuer in the differential game the Homicidal Chauffeur. The optimal control solution is implemented and used to generate a dataset of paths in the solution space that the GA uses to train the fuzzy system. The GA, fuzzy logic system and optimal control solution have been summarized. An average error for each path point of all the paths 0.0861 for the training data set and 0.0852 for the testing data set. Error is defined here as the sum of the error in the x and y coordinates.

Personal Objectives

The objective of this project was to train a fuzzy logic system using a Genetic Algorithm on the optimal control solution to the homicidal chauffeur game and comparing the results. The second contribution of this paper is an initial look at the effect of noise when added during the testing of the system.

Methodology Used

A genetic algorithm uses data created by the optimal control solution to train a four input, two output fuzzy system on the Homicidal Chauffeur solution space. The game was originally described by Rufus Isaacs in 1951 [2], and he published a more detailed problem description in 1965 in his book "Differential Games" [3]. The full optimal control solution for the original solution space given by Isaacs is given by Coats in [1]. The optimal control trajectories describe the relative position of the evader as it is captured. There are five trajectories in this space: primary trajectories, tributary trajectories, secondary trajectories emanating from the equivocal surface, secondary trajectories emanating from the y axis, and secondary trajectories emanating from the safe contact region. The solutions are replicated for fixed parameters of speed ratio equal to 0.5, and capture distance equal to 0.5 as well. A mesh of 800 points is laid over the solution space. Each point is the starting point of the relative position of the evader to the pursuer, and the optimal control solution is used to calculate the trajectory from each of these 800 points. These points are divided in a random 80% training - 20% test split for the training of the fuzzy system. The GA trains for 50 generations on the training data. Each generation, the GA takes a random sample of 50% of the training points to run through, so that more generations may be completed in less time. The error is the average error on a given path in a generation of training of the GA.

Results Obtained

The change in error over time during the training of the system is given in Fig. 2. The total error in x and y is per path point for both train data and test data is given in Table 1 relative to path length. To demonstrate the results on the paths, the path with the highest error per path point is plotted compared to the optimal control solution in Fig. 1.

Significance and Interpretation of Results

The trained fuzzy system performs well at developing the optimal control path for a given starting position of the evader relative to the pursuer. This is especially impressive given that the number of generations to train the FIS was only 50 generations. The training time on the author's desktop computers for these 50 generations was a total of about 16 hours. It is clear from Fig. 1 that the GA did not yet converge, and that therefore it is likely more training generations will decrease the error further. Results show that the system performs comparably on the test data to the train data, so over-fitting is not an issue here. The highest error per data point was 0.25744 which is the average of the summed x and y error at each point in the path. The average error per path data point for is 0.0861 for the train data and 0.0852 on the test data. This means, for example, if in a trajectory path the next point is [1, 2], the fuzzy system would predict, on average, the next point to be [1.085, 2.085].

Figures/Charts

	Highest Error per Path Point	Average Error per Path Point	Lowest Error per Path Point
Train Data	0.0785	0.0861	0.0494
Test Data	0.1051	0.0852	0.0479

Table 1. Highest, Average and lowest error per path point for the test and train data

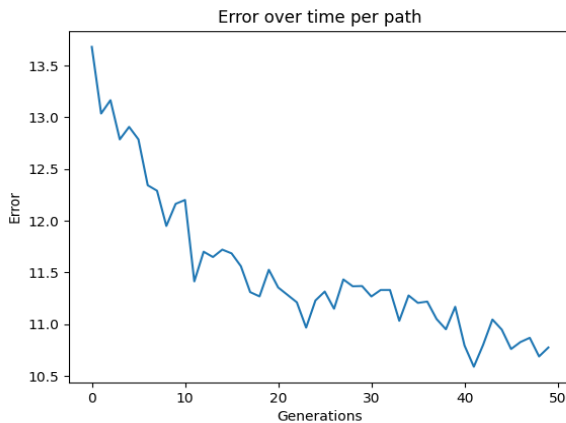


Figure 2. Error over time per path during the GA training

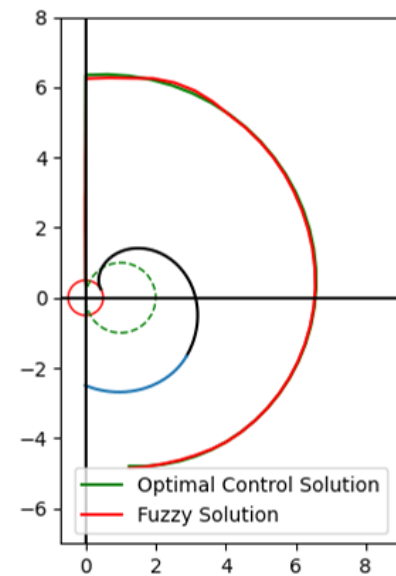


Figure 1. Path with the highest error per path point in test data set

Acknowledgements

This work would not have been possible without the support of the Ohio Space Grant Consortium and my advisor, Dr. Kelly Cohen. Thank you!

References

1. Coates, S.: An investigation of the homicidal chauffeur differential game. Tech. rep., AIRFORCE INSTITUTE OF TECHNOLOGY WRIGHT-PATTERSON AFB OH WRIGHT-PATTERSON . . . (2017)
2. Isaacs, R.: Games of pursuit. scientific report of the rand corporation. Santa Monica (1951)
3. Isaacs, R., Collection, K.M.R., for Industrial, S., Mathematics, A.: Differential Games: A Mathematical Theory with Applications to Warfare and Pursuit, Control and Optimization. SIAM series in applied mathematics. Wiley (1965). URL <https://books.google.com/books?id=gtlQAAAAMAAJ>

An Improved Method For Turbulent Flow Simulation Validation Using Surrogate Markov Models

Student Researcher: William L. Rickman

Advisor: Edgar Caraballo

Miami University

Department of Mechanical and Manufacturing Engineering

Abstract

Highly turbulent flows require a great deal of computational time to properly simulate. The study and extraction of coherent structures from turbulent flows offers the potential for a more rigorous understanding of turbulence, paired with more determinative analysis techniques than the widely used statistical approaches. Reduced-Order Models (ROMs) present a family of numerical methods for extracting these dominant structures from flow data and constructing models of the original system. These models possess fewer degrees of freedom than the original system and are thus less computationally expensive; low computational cost is desirable when modeling turbulent flows. Since ROMs are numerical methods, they require validation to ensure that they effectively model the original flow. Chabot [1] produced a framework for the objective validation of such models, in contrast to the more subjective validation methods common in this field; methods that often varied widely between research groups. This framework was constructed around the idea that a model could be scored on how similar the simulated data it produced was to that of the experimental data. These scores were generated by producing Markov models for both data sets, clustering the flow states via Gaussian mixture models (GMMs) and the k-means algorithm, and producing maximum likelihood estimates. This framework lacked generality; in that, it only explored the application of this technique to Proper Orthogonal Decomposition (POD), a specific type of ROM. Additionally, the current framework possesses a certain amount of ambiguity in how it defines outlier states. This work aims to expand the application of this framework to other ROM methods, particularly the popular Dynamics Mode Decomposition, and to improve upon its current state by increasing efficiency and refining the outlier classification process.

Introduction

Turbulence is a fluid flow phenomenon characterized by its nonlinearity, vorticity, and dimensionality; it can often be described as a chaotic phenomenon. Chaotic, in this context, means that any small change in the inlet parameters to the flow can result in significantly larger changes downstream. This chaotic nature makes it incredibly difficult to simulate highly turbulent flows using traditional CFD approximations. These limitations are to the point that extremely turbulent flows often require high mesh resolutions and the implementation of direct numerical simulation (DNS), both of which drastically increase the computational cost of the simulations. This gap in the “simulation space” is a symptom of the Navier-Stokes equations and a testament to the difficulty of the turbulence problem. This difficulty in direct calculation and simulation led to the development of the statistical methods for turbulence that are commonly used, such as RANS and LES turbulence models. Those statistical methods serve well to show how little intuition the scientific community has for turbulence as a whole. This is unfortunate, as turbulent flow is a common topic of interest in engineering; the internal flow of a turbojet engine, the

pipes that deliver drinking water, and the currents in the atmosphere and oceans are all examples of turbulent systems that are of great interest.

While turbulence is categorized as chaotic, it appears to have its dynamics dominated by structures that seem to lend it some form of order. If these structures could somehow be extracted and categorized, the analysis of turbulent flow would no longer be restricted by the limits of statistical methods or computational power. More determinative techniques could be developed and allow for a more rigorous understanding and intuition of turbulent phenomena as a whole. The field of dynamical systems analysis has offered promising gateways to isolating these structures from flow data in the form of reduced order modeling (ROM). ROMs offer a variety of different numerical methods and approaches that are well suited for extracting these dominant structures from PIV and DNS data and use them to construct models of the original system. These models have fewer degrees of freedom than the input system, earning the methods their name. This reduction in order allows for these models to predict the behavior of the flow at a much lower computational cost than traditional computational fluid dynamics. This reduction in cost is especially desirable in these highly turbulent flows, even though it is accompanied by a slight decrease in accuracy. ROM methods are numerical in nature and as such require validation to ensure that they effectively model reality.

Project Objectives

The goal of this project was to build upon the ROM validation framework built by Chabot [1]. While that thesis had effectively done what it laid out to do; demonstrate an objective method for validating low order models using classification techniques; there were a handful of loose ends left, as well as the potential to generalize the framework.

The latter is the more straightforward of the objectives in terms of explanation. Chabot focused his study on one particular method of producing ROMs, the POD method of snapshots laid out by Sirovich [2]. The snapshot method is an alteration of the original POD method that is better suited to working with Particle Image Velocimetry (PIV) data, which most of the experimental data used in the original study is. In the past decades, other forms of projection-based linear reduced order modeling methods have been developed and gained popularity, such as the spectral analysis-born Dynamic Mode Decomposition (DMD) [3,4]. Testing the rigor of this framework against another ROM method, such as DMD in particular, would be valuable in both showing its usefulness and in highlighting any weaknesses that could be rectified.

The former refers to how outlier states are defined in the original thesis. Originally, a data point was only assigned to the outlier cluster if its distance from the center of the nearest cluster was equal to or greater than some critical distance. In the clusters produced by both clustering methods, the k-means algorithm and GMM, rather arbitrary distances were selected, being some positive multiple of the largest distance between any two clusters and any two Gaussian components, accordingly. Despite this method being effective in constructing a rough idea of the outlier groups, these thresholds could be selected in a more logical manner. Doing so would not only improve the credibility of the clustering but also be better aligned with the goal of the work; to create a framework to objectively validate ROMs. In particular, as is briefly mentioned in the original thesis, the Mahalanobis distance could be used to better define the GMM clustering. A similar metric needs to be determined for the k-mean clusters, but

more work is necessary to determine what that metric would look like. Regardless of the metric chosen for either clustering scheme, the solution to this clustering problem needs to be grounded in the characteristics of the clusters themselves while remaining computationally cheap. The latter is important in ensuring that these additional features don't bog down the performance of the code as a whole.

Methodology

A literature review to become familiar with the interdisciplinary theory involved with this project was necessary to understand what was trying to be accomplished. Chabot [1] provided a solid basis of the theory currently implemented in the project. Ahmed [5] served to paint a picture of the current state of the science. All of the previously written code was written in MATLAB, something that this project does not plan on altering. Code alterations were done on copies of the original master code to ensure that any mysterious and/or catastrophic changes were not fatal.

As laid out above, the ROM method implemented was the Galerkin-projected POD method of snapshot, and the clustering was done with both k-means and GMM. As this project progresses and more new code is implemented, care will be taken to ensure that the framework remains as high-performance as possible. This may require implementing alternative methods that are more efficient than the originals, such as swapping out integration algorithms. These changes will be made to ensure that the expanded functionality does not overly compromise runtime. Additionally, exploration may be done into alternative clustering schemes that could be better suited for this application and that may remove the necessity to use two clustering schemes entirely.

Results

The literature review has been completed and an understanding of the theory has been developed. As laid out above, the codes used to develop the results described in [1] were iteratively ran and debugged until the results could be roughly duplicated. This allowed both for a good deal of familiarity to be built with the existing code, which will be invaluable as the project moves forward with its key objectives. The implementation of the improvements in outlier classification laid out in the objectives has begun. In particular, the replacement of the k-means clustering critical distance with the Mahalanobis distance has been nearly completed; unfortunately, no data on this alteration is able to be presented as of the writing of this report. There has not been much progress in terms of redefining the critical distance of the GMM clustering, however research is ongoing. Implementing the framework on DMD models will be done once the outlier clustering has been implemented. Until then work on code to produce the DMD models will continue.

Acknowledgements

The author would like to thank Dr. Edgar Caraballo, his advisor, for his guidance through this project, OSGC for facilitating its continuation, and Miami's MME department for supplying the resources to undertake it. The author would also like to thank his friends in the CSE department for their assistance in gaining an intuition for the classification techniques implemented in this project. Finally, the author would like to thank his family and friends for their companionship, support, and for reminding him that there's always clear skies on the horizon.

References

- [1] Chabot, John. *Validating steady turbulent flow simulations using surrogate Markov models*. [Master's thesis, Miami University]
- [2] Sirovich, Lawrence. Turbulence and the dynamics of coherent structures. Part I: Coherent Structures. *Quarterly of Applied Mathematics*, Volume 45(3), pp. 561-571 (1987).
- [3] Rowley, C., et al. Spectral Analysis of Nonlinear Flows. *Journal of Fluid Mechanics*, Volume 641, pp. 115-127 (2009).
- [4] Schmid, Peter J. Dynamic Mode Decomposition of Numerical and Experimental Data. *Journal of Fluid Mechanics*, Volume 656, pp. 5-28 (2010).
- [5] Ahmed, S., et al. On Closures For Reduced Order Models – A Spectrum Of First-Principle To Machine-Learned Avenues. *Physics of Fluids*, Volume 33, p. 33 (2021).

Controller for Metal Oxidation Warming System

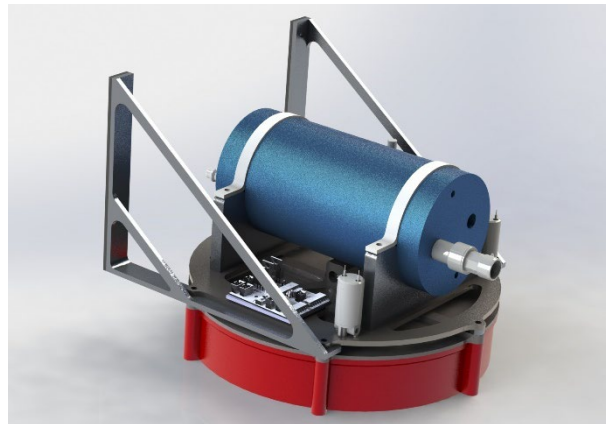
Student Researcher: Joshua Stanley

Advisor: Dr. Anju Gupta

The University of Toledo
Mechanical Engineering

Background

The lunar night lasts 14 earth days long and can reach temperatures as low as -200°C . Because of this oppressively low temperature, computer systems on board lunar landers and lunar rovers break down and are no longer operational the next lunar day. This essentially limits the duration of lunar missions to one lunar day or approximately 14 earth days. Alongside this, there are some regions of the moon that are permanently shaded. Because they never receive warmth from the sun, these areas are perpetually at these low temperatures seen throughout the lunar night. In order to increase the duration of lunar missions and to enable the exploration of permanently shaded regions, a heating system needs to be in place to keep critical components at a reasonable temperature for the duration of the lunar night. Because of the significant cost associated with sending payloads to space, the warming system would need to be as small and light as possible. The proposed solution involves using a highly exothermic reaction to generate heat to keep the critical components warm. This provides a system with a very high thermal efficiency that is much more energy dense than other warming methods like resistance heaters or thermal batteries. This system envisioned was termed the Metal Oxidation Warming System (MOWS) and is composed of a liquid reactant in a pressurized ullage tank connected via a solenoid valve to the reactor filled with the other reactant (current design shown to the right). By monitoring the temperatures and pressures of both vessels, the inlet valve can be used to deliver a precise amount of the liquid reactant to the reactor chamber initiating the oxidation reaction. Another solenoid valve acts as an outlet to vent the product of the reaction to a fuel cell to be used to generate electricity.



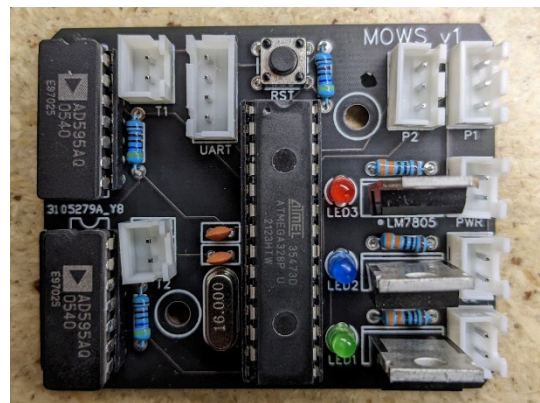
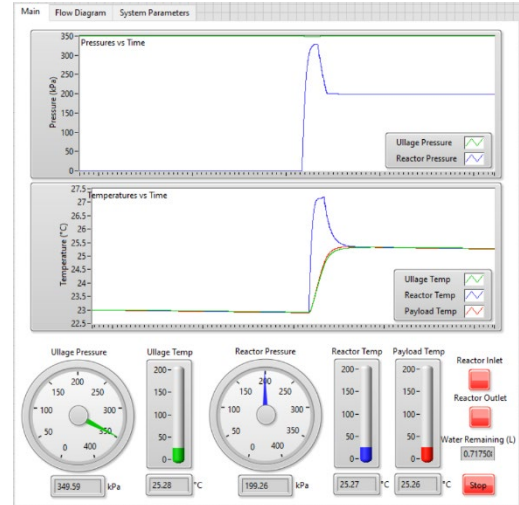
Objective

The objective of my portion of the project is to create a control system capable of monitoring the temperature of the payload as well as the temperatures and pressures present in the MOWS and determine when to open and close the inlet and outlet valves to optimally regulate the temperature of the system. This involves designing the controller itself as well as programming the logic of the controller.

Current Work

The oxidation reaction we are using was chosen because of its high energy density, but this also means that it is highly dangerous to work with. It requires specialized hardware to perform the reaction because of the corrosive and hazardous nature of the reactants. To keep experiments as safe as

possible, the first step for this project was to create a program that could accurately simulate the behavior the MOWS system. This simulation could be used for testing potential control boards instead of the actual reaction because it would mimic how the actual reaction would respond to the inputs of the system. The simulation was created in LabVIEW and accurately showed the pressure and temperature responses of the system as the inlet and outlet valves were opened (user interface shown to the right). The next step of the process was to design the control board. This required sourcing the solenoid valves, pressure sensors, and thermocouples that would be used in the system. Then electrical components were sourced for the control board including the microcontroller, the thermocouple amplifiers, and the mosfets for driving the solenoids. After all the components were obtained and tested to ensure they worked together, a custom printed circuit board was designed and created to neatly wire the components together (shown to the right). This circuit board allowed the microcontroller to interface with all of the sensors and actuators as well as a laptop. Next three different control system architectures were created to compare against one another. Each one ranges in terms of sensors required, simplicity, and adaptability. The three different control system types will be tested against one another using a hardware in the loop approach. This would interface the control board with the simulation of the system, and each of the control architectures would be compared in terms of their ability to maintain a target temperature as well as the average electrical power consumed by the control board.



Future Work

Future work for this project includes experimentally determining the current draw of the control board in each of its configurations. Then hardware in the loop testing with the control board and the simulated system will be used to evaluate and improve upon each of the different control architectures.

Multi-fidelity Analysis of Predictive Capability for Hypersonic Conceptual Design

Student Researcher: James Wnek

Advisor: Dr. Mitch Wolff

Wright State University
Mechanical Engineering

Abstract

The conceptual design process requires going through numerous design iterations. The many iterations needed to explore a design space preclude the use of time-consuming RANS CFD for all but a few combinations Mach number, angle of attack, and angle of sideslip. This research focuses on identifying the level of fidelity needed to adequately predict the aerothermodynamic characteristics of hypersonic vehicles. Three different tools with differing levels of fidelity – CBAERO, Cart3D, and Kestrel – were used to analyze the Generic Hypersonic Vehicle (GHV) at design conditions. The data gathered in this research can aid engineers in choosing an appropriate level of fidelity for different design goals. The preliminary results showed a large difference in the unstart threshold predicted by inviscid and viscous CFD, 21° vs 11.75° for $M = 5.85$. Despite that difference, the low and medium fidelity methods, CBAERO and Cart3D, can adequately predict C_L and C_D across the entire range, however the differences were magnified substantially when calculating L/D. The medium fidelity method was also capable of predicting C_M and mass capture below the unstart threshold. The high-fidelity method, Kestrel, was only necessary to predict the unstart threshold and mass capture after unstarting. Further research is still being conducted on aerodynamic heating estimates and off-design Mach numbers.

Project Objectives

This project had several objectives:

1. Analyze a vehicle geometry with a high fidelity, RANS CFD solver.
2. Compare a low and medium fidelity conceptual design tool by analyzing the same vehicle geometry and using the high-fidelity tool for reference.
3. Identify the minimum level of fidelity needed to adequately predict different aerodynamic characteristics including the lift, drag, and pitch moment coefficients, and unstart threshold.

Methodology

To accomplish the objectives of this research, CBAERO, Cart3D, and Kestrel were used to analyze the same vehicle geometry. The vehicle geometry chosen for this research was the Generic Hypersonic Vehicle (GHV), a family of integrated scramjet vehicle configurations released by AFRL in 2012 to foster collaboration with academia and industry. This research specifically uses the default configuration of a parameterized version developed by Boyd and his coauthors in 2020, which is a close approximation of the original GHV [4]. All simulations were conducted at design conditions, which for the GHV were Mach 5.85 on a trajectory with a dynamic pressure of 1500 psf.

For CBAERO, inviscid flow was chosen. This means CBAERO only makes a global estimate of viscous drag, instead of estimating the skin friction distribution. For Cart3D, adaptive grid refinement was used with functionals of $0.4C_L$ and $0.6C_D$. The functionals were chosen based on those found in literature. For Kestrel, all body surfaces were set as adiabatic, no-slip walls. The CFL number was initially set to 25 and

was reduced to 10 if the simulation didn't converge to 10^{-5} after 2500 iterations. The turbulence model used was Spalart-Almaras.

Results and Discussion

It was found that Cart3D's inviscid CFD predicts a substantially higher unstart threshold than Kestrel's viscous CFD, $\sim 21^\circ$ compared to $\sim 11.75^\circ$. The difference in unstart threshold resulted in a large difference in the mass capture. Before unstart, however, Cart3D and Kestrel both predicted very similar values of mass capture. An analysis of the density field near unstart shows a markedly different shape for the shock in front of the inlet. In Cart3D, the shock was nearly a normal shock, while Kestrel predicted an oblique shock at a much smaller angle.

CBAERO predicted smaller coefficients than Cart3D and Kestrel, however, all three methods predicted similar values of the lift, drag, and pitch moment coefficients across the entire range of angle of attack, from 0° to 25° . In contrast to the individual coefficients, each method predicted a markedly different value of L/D_{max} and a different angle of attack at which it occurred. Kestrel predicted the lowest value at $L/D_{max} = 4.4$ at 5° angle of attack. Cart3D and CBAERO both predicted a value of $L/D_{max} = 7$, however this occurred at 0° in CBAERO and 2° in Cart3D.

Significance and Future Work

The results showed that both the low and medium fidelity methods are suitable for prediction of the lift, drag, and pitch moment coefficients. Inviscid analysis was also suitable for estimating mass capture below the unstart threshold. Viscous analysis was only necessary to properly predict the unstart threshold, L/D , and the angle of attack of L/D_{max} .

Additional work is being done on heat flux calculations and extending the present analysis to off-design Mach numbers.

References

- [1] D. J. Kinney, "Aero-Thermodynamics for Conceptual Design," in *42nd AIAA Aerospace Sciences Meeting and Exhibit*, Nevada, 2004.
- [2] NASA, "NASA Selects Two Design Tools as Software of the Year," *NASA Tech Briefs*, pp. 28-29, October 2002.
- [3] S. A. Morton, D. R. McDaniel, D. R. Sears, B. Tillman and T. R. Tuckey, "Kestrel – A Fixed Wing Virtual Aircraft Product of the CREATE Program," in *47th AIAA Aerospace Sciences Meeting*, Orlando, 2009.
- [4] I. M. Boyd, R. V. Grandhi, J. Camberos, D. Sandler and R. A. Canfield, "Generic High-Speed Vehicle Configuration Modeling and Optimization," in *AIAA Aviation Forum*, Virtual, 2020.

Scholars

Surface Enhancements and Their Effects on Critical Heat Flux and Heat Transfer

Student Researcher: Madeline G. Barto

Advisor: Dr. Chirag Kharangate

Case Western Reserve University
Department of Mechanical and Aerospace Engineering

Abstract

Many new technologies, including those involved in spacecraft, have a need for a more efficient and more compact thermal management systems. Two-phase cooling systems can help meet these requirements in comparison to traditional single-phase counterparts. Additionally, surface enhancements made to the boiling surface can further improve boiling performance and heat transfer coefficients. Using the pool boiling facility in the Two Phase Flow and Thermal Management lab, various types of surface enhancements can be examined. The aim of this research is to explore the effects of different surface enhancements applied to a copper surface. Data will be collected that allows for the critical heat flux and heat transfer coefficients to be calculated and compared against each other. Additionally, images taken of the fluid while boiling will provide insight into how the surface enhancements impact the onset of critical heat flux.

Project Objectives

The objectives of this research were to examine the effects of surface enhancements on boiling performance. Water was first used to validate the experimental set up and allow the experimenter to practice the experimental procedure before moving to refrigerant. Once the set up was validated, refrigerant could then be tested and the data could be used to determine how effective the surface enhancements were.

Methodology Used

To collect data, refrigerant was pumped into the pool boiling module as shown in Figure 1. Inside of the pool are two cartridge heaters that maintain the fluid temperature at its saturation temperature. The cartridge heaters are controller by the system controller which operates a control loop with a solid state relay so that the heaters only turn on when they are needed. On the bottom of the pool is a space for the enhanced copper sample to be used as a boiling surface, and below that is a heating element to change the surface temperature of the copper. The temperature of the copper boiling surface is controlled by the experimenter by adjusting the Variac power supply.

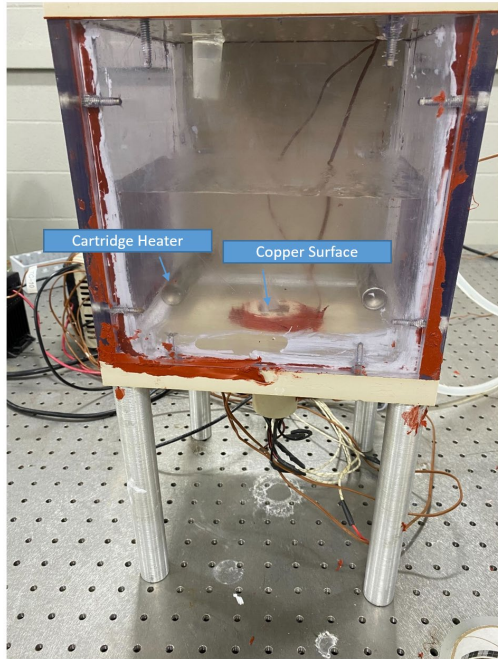


Figure 1: (left) Pool Boiling Module

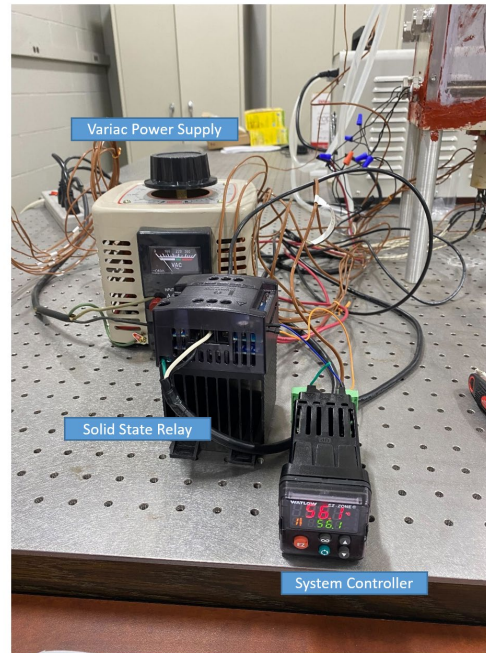


Figure 2: (right) Pool Boiling Module Control System

While running the experiment, the temperature of the fluid, the copper surface, and the heating element below the copper surface were monitored and processed with thermocouples and a LabVIEW code to report back the superheat and heat flux. The Variac power was increased in increments until the superheat and heat flux reached steady state, and after collecting data at steady state, the power was increased again. The experiment ended when the fluid reached critical heat flux.

Results Obtained

The pool boiling experiment has been performed on water with an enhanced copper surface to generate a curve of superheat and heat flux values. Preliminary data has also been collected for PF5060, but more experiments must be run before the results can be analyzed.

Significance and Interpretation of Results

The results collected for water indicate that the boiling surface does affect the boiling curve of water. The graph shown in Figure 3 is for a boiling surface with a hole pattern machined into it, and it does not follow the expected boiling curve for an un-enhanced surface. While more data must still be collected for PF5060, it is suspected that the enhanced copper surfaces will improve boiling performance compared to the expected boiling performance of the fluid for an un-enhanced surface.

Figures/Charts

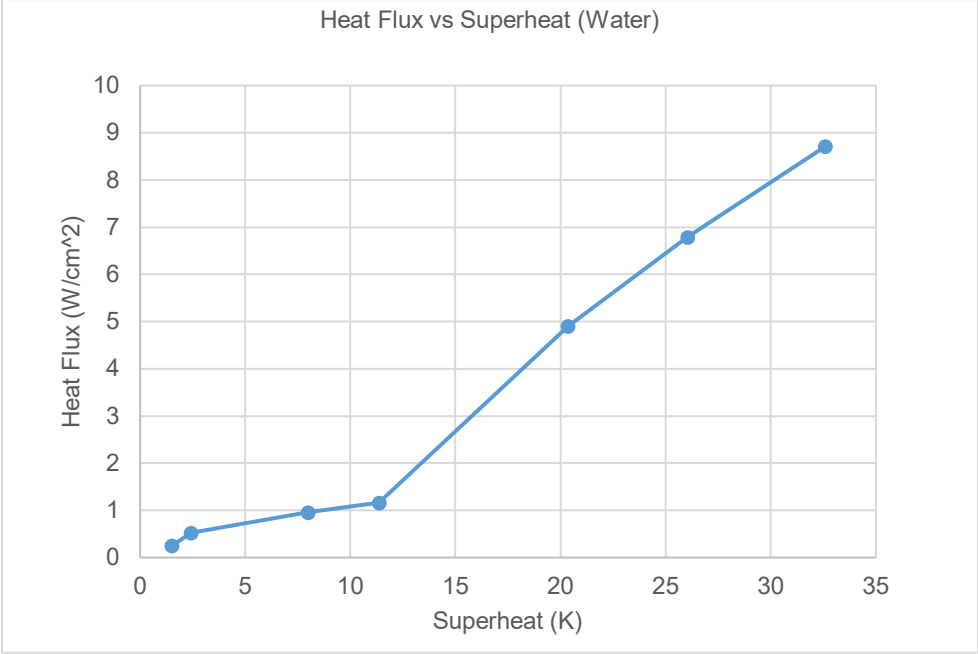


Figure 3: Sample Heat Flux vs Superheat Data for an Enhanced Copper Surface

Acknowledgments and References

The author would like to thank the Ohio Space Grant Consortium for their scholarship and support of this project. Additionally, the author would like to thank Dr. Chirag Kharangate and Chinmay Shingote for their assistance and guidance throughout the entirety of this project.

Optimization and Validation of a Digital Image Correlation System for Large Deformation Soft Materials Testing

Student Researcher: Joseph G. Beckett

Advisor: Dr. Robert L. Lowe

University of Dayton

Department of Mechanical and Aerospace Engineering

Abstract

Stereo digital image correlation (DIC) is an optical measurement technique capable of producing full-field strain and displacement maps by tracking a high-contrast pattern applied to a deforming object. These rich measurement capabilities make DIC a compelling research tool for material characterization efforts involving coupon-level specimens undergoing complex, three-dimensional modes of deformation. Soft materials, which typically exhibit large strains at fracture, present several major challenges to DIC measurements including pattern breakdown at large strains, saturated image regions from glare, and large fields of view. This research implements several cost-effective strategies to improve soft material DIC measurements by increasing DIC image quality and optimizing DIC analysis parameters. It also provides relevant proof-of-concept DIC analyses of emerging soft materials and highlights applications that would benefit from experimental validation facilitated by large-deformation DIC measurements.

Introduction and Objectives

The scope of this research is to design and implement a low-cost open-source stereo digital image correlation (DIC) system optimized for testing soft materials, a class of materials whose large elastic deformations present significant challenges to traditional DIC measurement techniques (e.g., pattern breakdown, glossy surfaces, significant deformation from reference image)¹. DIC is a game-changing optical measurement technique that analyzes a series of images to track the motion of a high-contrast speckle pattern applied to the surface of a test specimen undergoing deformation². Stereo (or three-dimensional) DIC utilizes a series of synchronized images from a *pair* of cameras to produce high-precision 3D surface strain and displacement fields³. These full-field deformation measurements are substantially richer than those obtained from traditional extensometers and strain gauges, which only provide an average strain over a given length or the strain at a single point on the body. The novel DIC system developed as part of this research effort will be used to characterize the deformation and fracture of a wide class of soft materials, including BeckOHflex, a rapidly self-healing photocurable elastomer synthesized at the Air Force Research Laboratory.

Methodology

Prior to a focused optimization of the DIC system for large-deformation soft materials testing, a low-cost open-source DIC frame was designed. In prior research, a literature review was conducted identifying best practices for design of DIC systems and current studies and limitations of DIC in large-deformation applications^{4,5}. The review along with early trials of soft material DIC in a prototype testing apparatus identified glare on the surfaces of glossy polymers, pattern delamination, and correlation issues at large strains as key concerns during system development. With these challenges in mind, the system grew outwards from the acquisition of a pair of machine vision cameras with Sony IMX267 CMOS sensors. These sensors feature a high aspect ratio 8.9 MP frame (4096 x 2160 px) that is more cost-effective at capturing

DIC images of large-deformation uniaxial tension or pure shear tests than lower aspect ratio (less rectangular) frames where a large portion of the frame would be unused. The cameras were paired with compatible high-performance 35mm fixed focal length lenses before being mounted onto a custom mounting system. A pair of LED light panels were used to provide lighting for the system. During preliminary testing, several open-source DIC codes were tested and the Digital Image Correlation Engine (DICE)⁶ was selected as the top candidate. DICE eclipsed its rivals because of its 2D and 3D DIC capabilities, excellent documentation, and its rigorous ongoing development at Sandia National Laboratory.

Results and Discussion

To begin tailoring the system for large-deformation DIC of soft materials, 3D DIC (i.e., stereo DIC) capabilities were added to the system due to their ability to account for out-of-plane motion (e.g., specimen thinning in large-deformation mechanical testing), non-planar specimen surfaces, and camera misalignment. Additionally, stereo DIC reduces errors due to vibrations and heat waves. The cameras were physically linked using GPIO cables to allow for synchronized imaging triggered on the same electronic signal. An aluminum extrusion rail was used to rigidly mount the pair of cameras. To eliminate glare resulting from unwanted spectral reflections on the surface of glossy polymer samples under powerful LED lighting, a cross polarization scheme was implemented. This affordable solution involved installing high-contrast linear polarizing film on both LED lights panels, and glass linear polarizing filters were placed on the lenses of both cameras. To ensure the high-contrast patterning remains intact on the surface of polymer samples throughout the test, inks were used to stain the surface of the polymer samples tested. StāzOn brand ink proved to be especially effective at permanently patterning a variety of rigid plastics and soft elastomers. Traditional air brush patterning using a variety of black inks proved moderately effective in early testing, however, the technique wasted relatively large amounts of ink and it required use of a fume hood. To facilitate more repeatable patterning of samples, a custom DIC patterning stamp was developed with the use of an extruded uniform dot pattern with programmed locational jitter for each dot. Using a Stratasys Objet printer, the stamp could be easily scaled during the 3D printing process and printed out of materials with varying moduli to better suit patterning of samples exhibiting a wide range of stiffnesses.

In initial validation testing, these optimization measures were extremely effective in producing 2D and 3D strain maps on 3D printed PLA tensile samples with low errors. High deformation DIC analyses conducted with the system have measured deformations as high as 280% strain on Smooth-on EcoFlex tensile specimens. These tests were conducted prior to the implementation of ink stamp patterning, cross polarization, and stereo DIC. Consequently, large portions of the gage sections of the Eco-flex samples decorrelated after exceeding 100% strain. The proximate cause of the failure was some combination of the delamination of the acrylic paint from the sample's surface and initialization issues within DICE at very large strains. Work is currently being conducted on quantifying the optimized system performance on molded samples of BeckOHflex, a novel photocurable, ultra-stretchable, self-healing elastomer.

Acknowledgments

The author would like to thank the Ohio Space Grant Consortium, the University of Dayton (UD) School of Engineering, the UD Honors Program, the UD Berry Summer Thesis Institute, the Air Force Research Laboratory, the University of Dayton Research Institute, and UES Inc. for supporting this research. The author would also like to thank Dr. Robert Lowe and the other members of the Behavior of Advanced Materials and Structures (BAMS) Lab for their support.

References

1. Tang, Z., Liang, J., Xiao, Z. & Guo, C. Large deformation measurement scheme for 3D digital image correlation method. *Opt. Lasers Eng.* **50**, 122–130 (2012).
2. Chu, T. C., Ranson, W. F. & Sutton, M. A. Applications of digital-image-correlation techniques to experimental mechanics. *Exp. Mech.* **25**, 232–244 (1985).
3. Luo, P. F., Chao, Y. J., Sutton, M. A. & Peters, W. H. Accurate Measurement of Three-dimensional Deformations in Deformable and Rigid Bodies Using Computer Vision.
4. Beckett, J. G. Overcoming the Challenges of Digital Image Correlation Measurements for Soft Materials at Large Deformations: A Review. in *Berry Summer Thesis Institute Proceedings 2021* (2021).
5. Beckett, J. G. Toward DLP 3D-Printed Soft Robots: A Stereo DIC Investigation of the Mechanics of Ultra-Stretchable Self-Healing UV-Curable Photopolymers. in *2020-2021 Annual Student Research Symposium Proceedings XXIX* (2021).
6. Turner, D., Crozier, P. & Reu, P. Digital Image Correlation Engine. (2015).
7. Jones, I. *et al.* A Good Practices Guide for Digital Image Correlation. *Int. Digit. Image Correl. Soc.* 94 (2018).
8. Blaber, J., Adair, B. & Antoniou, A. Ncorr: Open-Source 2D Digital Image Correlation Matlab Software. *Exp. Mech.* **55**, 1105–1122 (2015).

Gust Response Evaluation for Small Unmanned Aerial Systems

Student Researcher: Isabella Bidart Ferrer

Advisor: Dr. Matthew McCrink and Dr. Dhuree Seth

The Ohio State University
Mechanical and Aerospace Engineering

Abstract

This research project aims to ensure the safe use of Small Unmanned Aerial Systems (sUAS), often referred to as drones, for commercial applications such as infrastructure monitoring, agricultural missions, and small-package delivery in unpredictable gusty environment. Gust tolerance is one of the most important technical challenges for sUAS because of its relatively light weight and low-altitude operations where severe turbulence often exists, which is caused by terrain, trees, buildings and so on. However, there are no standards provided by the UAS traffic management system (UTM) on the sUAS performance evaluation of the gust tolerance. In this research, multirotor UAS will be designed to evaluate the wake responses to controlled gusts by simulating maximum velocities, and velocity gradients that are expected in wake encounters in a controlled outdoor environment. This will help in the analysis and quantitative evaluations of the severity of the gust response for a representative sUAS.

Project Objectives

To design and develop a specialized quadrotor that can be instrumented with direct thrust and torque capabilities to allow for direct assessment of the forces and the moments produced by the individual rotors. In addition, a series of crosswind fans at the Transportation Research Center (TRC) facility were used to generate free-flight gusts and wake encounters in outdoor environments to produce repeatable spatial and temporal variation in the ambient wind field. The characterization of the wind field generated by the crosswind fans is performed using ground-based ultrasonic anemometers. A controlled free flight demonstration of a highly instrumented quadrotor was made in the presence of the crosswind fans to understand the aerodynamic responses of the multirotor in gusty environment.

Methodology Used

Vehicle design

Table 1 shows the main design characteristics of the vehicle which was constructed based on the DJI S1000 design. The vehicle is constructed primarily of carbon fiber, aluminum components with aerodynamic fairing for central body. The propulsion system consists of four brushless motors arranged symmetrically about a central fuselage. These motors are powered by ESCs which modulate current to control RPM. The vehicle is instrumented to measure rotor thrust, speed, vehicle state, motor current and voltage. Each arm is equipped with load cells and strain gauges to assess the total thrust produced by each motor in flight and resulting moments. Voltage and current are monitored using a custom power distribution board. The load cells are mounted under the motors, which measure thrust. Pixhawk Gen-2 controller was used to collect vehicle state data, acceleration, velocities, position, body angular rates which are used for post flight analysis. A Raspberry Pi was used as a data acquisition system and to collect measurements from the sensors and state data from the Pixhawk. Fig. 1 shows the architecture diagram which used lower-level interface protocols such as i2c which were translated by an on-board Propeller multi-core microcontroller to interface with the Robotic Operating System (ROS) node.

Table 1. Quadcopter design characteristics

Size (L x W x H)	0.7m x 0.7m x 0.8m
Weight	4 kg
Rotors	DJI S100+1552
Rotor Pitch	0.381 m
Motors	T-Motor U7 420 kV
ESC	Castle Mukti-rotor 25
Battery	Turnigy 10,000 mAh
Flight Controller	Pixhawk V2.0
Max speed	20 m/s

Flight test

Initial flight test was performed in an outdoor environment. Succeeding tests were performed at the TRC facility where 6 crosswind fans, as shown in Fig. 2 were mounted on the ground level of the track. These fans had variable speeds and were adjusted by turning the throttle up and down. Each one is driven by a gasoline engine. They generated up to 35 mph (15 m/s or 51 ft/s) windspeeds, which simulated gusty environments. Each fan has 4 horizontal vanes and 6 vertical vanes that can be adjusted to direct the flow of air. Fan opening on the output side was 68" tall x 109" wide. Each fan has 6 blades and is 40" long (not including the cone in the center). The gust and wake profiles were characterized using ground-based ultrasonic anemometers, which allowed the atmospheric turbulence information to be collected.

Results and Discussion

To characterize the flow for the 6 crosswind fans using the ultrasonic anemometer were utilized. Fig. 3 shows the speed of the 6 crosswind fans, which was used to generate ramp up and ramp down gust profiles. Fig.4 shows the height above the ground where the anemometer was placed. 15 measurements were taken at every 5 ft for a period of 30 seconds for each point. Figure 5 shows an example of the windspeed collected by the anemometer at 0.91 m (US customary units).

Example of the flight data that was collected during free flight is shown in Fig. 6. These plots indicate the thrust, current, RPM and voltage produced for each arm. Arms 1 and 3 are in the flight direction such that arm 3 is closer to the fan. The wind from the fan was pushing the vehicle away from the fans, which lead to rolling the vehicle. Therefore, arm 1 shows higher thrust to compensate for the rolling maneuver and keep the vehicle level during the flight.

Significance

Successful flight demonstration and data gathering were performed for sUAV in gusty environments. Since this research aims to help create an understanding of the aerodynamic reactions of sUAV in gusty environments, these results can help predict these reactions and therefore ensure sUAV safe operations.

Figures/Charts

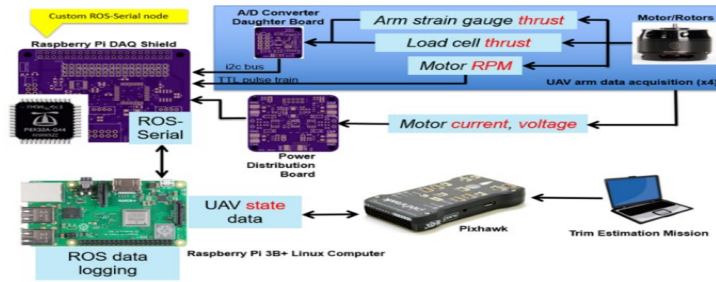


Figure 1. System architecture diagram for the quadrotor.

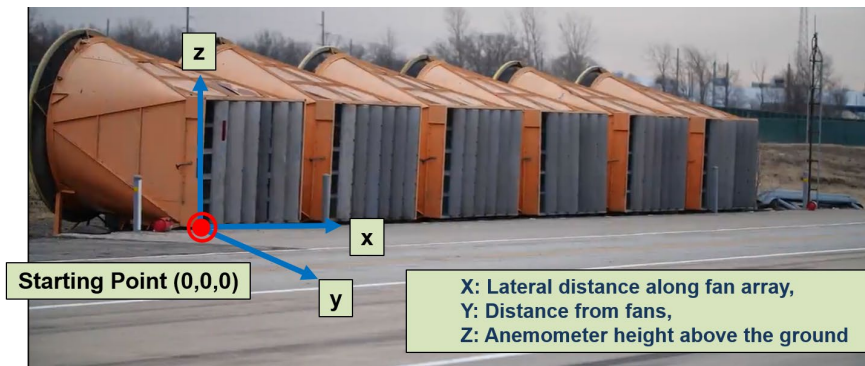


Figure 2. Crosswind fans at the Skid Pad facility at the Transportation research Center (TRC).

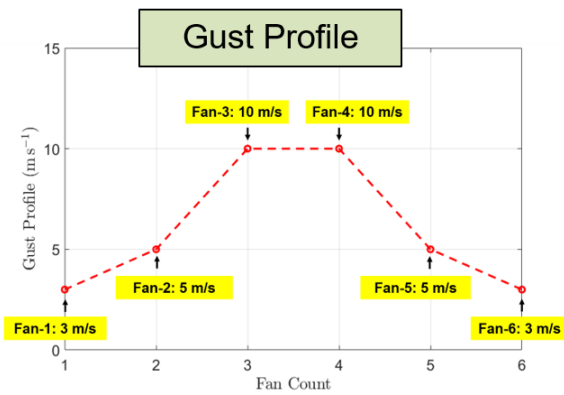


Figure 3. Gust Profile

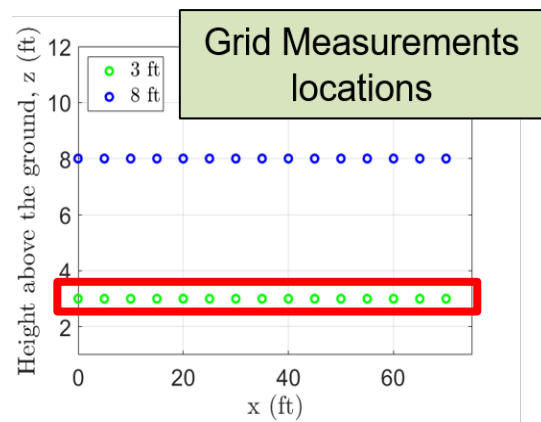


Figure 4. Grid Measurements locations

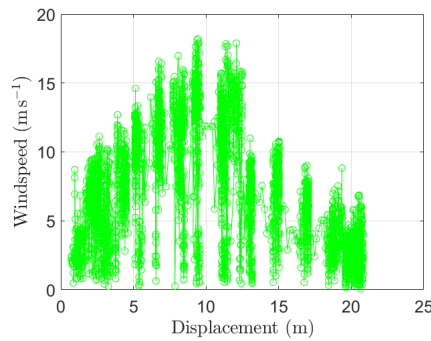


Figure 5. Windspeed measured using ultrasonic anemometer at ~4 ft.

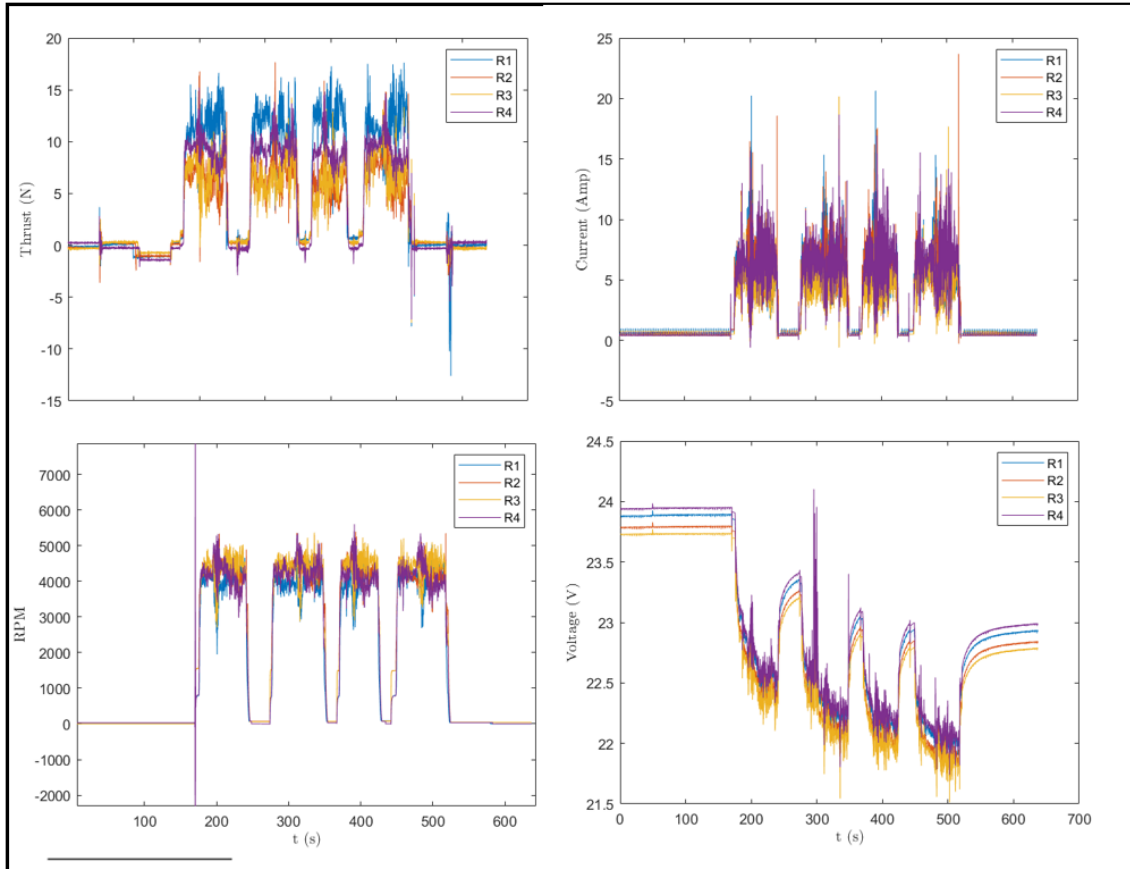


Figure 6. An example of the thrust, current, RPM, and voltage measurements made during the free flight in the presence of crosswind fans.

Acknowledgments

I. Bidart Ferrer would like to thank my advisors Dr. Matthew McCrink and Dr. Seth Dhuree for their guidance and help throughout my undergraduate research. Also, graduate students Sage Herz, Isaac Bensingor, and Ross Heidersbach who collected and processed the data used in this research paper. Lastly, I would like to thank OSGC for supporting this research project.

References:

- [1] McCrink, M., Seth, D., Herz, S., "Understanding the Aerodynamic Interactions for Quadrotor Configurations Through Flight Testing". VFS 78th Annual Forum & Technology Display, Fort Worth, TX, May 10-12, 2022 (to be presented)
- [2] McCrink, M., Seth, D., Herz, S, "Quadrotor Performance Measurement during Wake and Gust Encounters", 2022 AIAA Aviation Forum, Chicago, IL, June 27—July 1, 2022 (to be presented)

Lunabotics Rover Auger System

Student Researcher: Tyler Blackey

Advisor(s): Dr. Hazel Marie

Youngstown State University
Mechanical Engineering

Introduction

NASA Lunabotics is a collegiate competition designed to cultivate innovative designs that have potential to expand the technological capabilities of lunar exploration via autonomous rovers. The focus of this year's competition is collecting soil samples by means of aggregate mining. Competition consists of first traversing a lunar surface simulant, autonomously avoiding obstacles to reach the specified mining location. Next the rover mines soil simulant in the means a team determines, separating the desired regolith rock simulant from soil, and delivering the regolith to a specified location, where teams are then scored on quantity of material mined. Youngstown State University's Robotics' Club heads our team, which consists of computer science, mechanical engineering, and electrical engineering undergraduate students. Student's design, calculate, prototype, test, analyze, optimize, and build a functional rover to compete at this national event held at the Kennedy Space Center, FL.

Abstract

Sound engineering practices are used in conjunction with the implementation of advanced aerospace materials to meet target specification and maintain compliance with competition rules. CAD (Computer Aided Design), along with other softwares, are tools used throughout the project to reach team objectives. Objectives include but are not limited to, reducing mass, reducing complexity, partial system autonomy, maintaining reasonable serviceability of the rover, and acquiring maximum points during competition in accordance with the scoresheet. Four subsystems, auger, dumping, drivetrain, and frame were redesigned to maximize operational performance during competition and earn the top number of points in their respective categories. The design process started by analyzing the shortcomings of the 2021 rover design: excess mass, over built, unnecessary complexity, ect. The focus of this presentation is predominantly the auger or digging system. Which acts as the main collection system for the entire rover to be used in competition. Preliminary designs were drafted and put up against team and performance criteria. Prototypes of key components were first 3D printed for testing, and eventually machined.

Interpretation of Results

The final design includes on auger system that is capable of extracting and digging simultaneously through a chute fixed to the top of the system. The auger flight itself has an added taper that elevates the clogging the system is prone to undergo. Original design conception positioned the auger system behind the dumping system. This design also included a 4-pin 4 bar linkage. The idea of this orientation was for the auger system to rotate from 180 degrees to 90 degrees, dig into the BP-1 simulant and expel the material into the dumping system. The operation would end with the auger system returning to 180 degrees before the rover moves to the dumping site destination. Throughout the semester this design was modified to better perform during competition and meet competition constraints and requirements.

Conclusion

The final auger design is more about the orientation of the auger and dumping system rather than a substantial change to the auger system itself. As stated previously, the Auger and Dumping system were colinear on the rover. However, due to the design changes implemented and constraints of the mining competition, the two systems needed to be reoriented. This orientation was finalized to the auger and dumping system actuated side by side. This created a compact design and allowed the auger to reach the desired digging depth while simultaneously funneling material into the bucket.

Observing Earth's Past Climate Using Rock and Ice Core Data

Student Researcher: Alec Bollinger

Advisor: Dr. Guam

Marietta College

Petroleum and Environmental Engineering

Abstract

The concern for climate change is one of the leading issues in our world today. The consistent rise in Earth's average annual temperature over the past couple of decades has many people fearing for our future. This slow rise in temperatures has been linked to prolonged droughts, melting glaciers, and extreme weather, among other things. Many believe that the major cause of this climate shift is due to human influence. While this is no doubt concerning, Earth's climate has always been going through extended periods of warming and cooling, long before humans ever influenced the climate. Historic changes in Earth's temperatures stem from a variety of natural causes. Major events such as volcanic eruptions or meteorite impacts cause swift fluctuations in Earth's climate, while other events such as the evolution of life take much longer to impact Earth's climate. This study will analyze natural climate shifts that occurred throughout the mid to late Cenozoic Era to establish a better understanding of our current climate change. Data preserved in deep sea sediments and cores will be analyzed to interpret the conditions of these past environments.

Introduction

It has been well documented that Earth's climate has always been changing along with shifting between states of greenhouse and icehouse conditions. Evidence of these alternating climates can be traced all the way up until the beginning of the Archean some 3.8 BYA. With Earth amidst an unprecedented rise in temperature, we often look back upon Earth's previous climates to gain insight and guidance on how to handle our current situation. While we have literal billions of years' worth of climate data at our disposal, a problem with this data is the accuracy and the resolution significantly decline with time. Ice core data, for instance, is heavily relied upon to accurately measure historic CO₂ and Methane levels, but we currently only have 800,000 years' worth of data. Older periods typically rely on data obtained from either leaf stroma or isotopes of elements like Boron, Oxygen, and Strontium, (Letcher, 2015). This data is critical in climate evaluation, especially in this instance, because the warming period of the mid-Pliocene (3 MYA) has often been relied upon for our current climate projections. During this time, the poles were much warmer with lush forest covering areas that are tundra's today, with average surface temperatures estimated at roughly 2-4 °C warmer on average, (Schmidt, 2020). The driving cause for this warming period is not entirely certain, but determining the influence of certain factors, such as CO₂ concentrations, and how the Earth responded to such threats through climate models prove invaluable in understanding and predicting our current climate.

Methodology

As one of the more recent warming periods, there are many advantages when choosing to analyze the mid-Pliocene. In comparison to older periods, the organisms that occupied Earth are very similar to today's, and the amount of available core and isotope data is abundant. With today's increasing release of greenhouse gases such as CO₂ and CH₄, it is imperative that isotope data be analyzed from the Miocene to determine their levels and subsequent influence on the warming period. Additionally, by looking at varying foraminifera around the globe, we can calculate temperature ranges at different

regions around the planet. Using this, the influence of other factors, such as ocean depths and currents or vegetation levels on the warming can be more accurately determined.

Results

By studying Boron and Oxygen isotope data, as seen in Figure 1, it has been estimated that CO₂ levels from the mid-Pliocene somewhere between 330 and 400 ppm, similar to today's levels, (Vega et al, 2020). Being relatively at the same CO₂ levels, questions arise for what caused the mid-Pliocene to experience warmer temperatures. Some believe the answer has been found in the form of ocean ridges. During the mid-Pliocene, it has been predicted that the Greenland-Scotland ridges were much deeper as a result of hot spot activity, thus allowing for warm water from the equator to travel freely to the arctic, (Morello, 2011). When analyzing the mechanisms that led to the cooling events, similar questions are raised. The leading theory is that the expanding abundance of plant life led to an overall decline in atmospheric CO₂ levels, resulting in cooler conditions. This in turn, is causing aridity and turning many of the lush forest into either grasslands or tundra's, (Polly, 2009).

Conclusion

With the CO₂ levels from this warming period relatively similar to ours, it is unlikely that enhanced levels of greenhouse gases in the atmosphere were the direct cause in this warming period. The possibility exist in which elevated CO₂ levels may have triggered the event or events that ultimately caused the difference in temperature. However, the elevated temperature levels of the mid-Pliocene are likely the result of deeper ocean ridges and changes in ocean currents. Adding this variable into the equation, many of today's climate models now match much closer to the predicted environments of 3.2 MYA, adding significant amounts of confidence in extrapolating future climate trends. Earth has proven time and time again that it can self-regulating conditions prolonging life on this planet. With this in mind, it must be noted that the climate shift we face today is unprecedented, as never before has the warming been driven by human's influence. However, human influence also has the opportunity to give Earth an advantage it has never had before, an ally that can assist in maintaining temperature conditions suited for life.

Figure 1

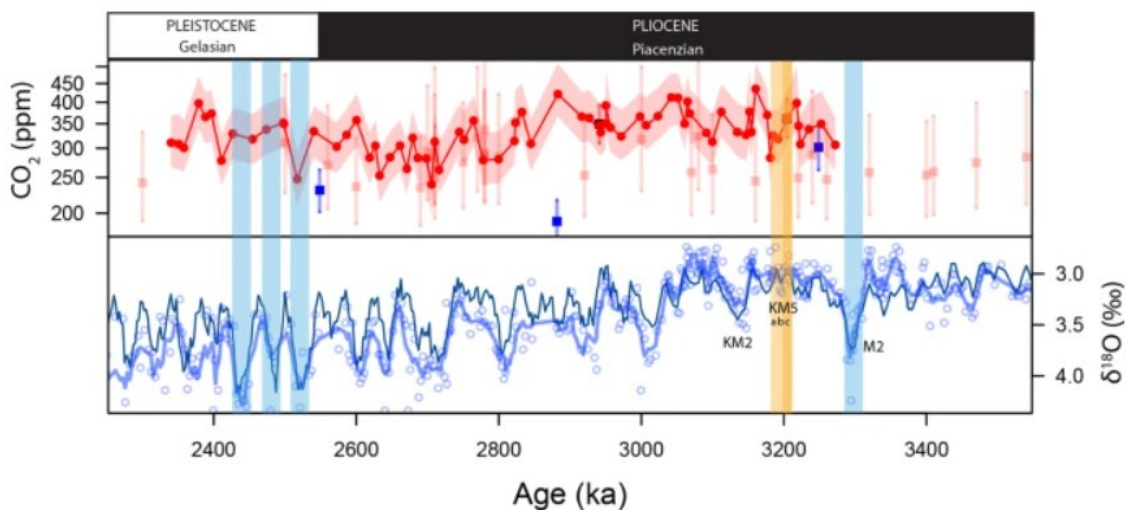


Figure 1: Pliocene and Pleistocene estimated CO₂ levels from O₁₈ isotopes provided by benthic foram (Vega et al, 2020).

References

- Letcher, T. M. (2015). *Climate change: Observed impacts on Planet Earth*. Elsevier.
- Schmidt, G. (2020). *NASA GISS: Research Features: Pliocene global warming: Page 2*. NASA. Retrieved March 23, 2022, from https://www.giss.nasa.gov/research/features/199704_pliocene/page3.html
- de la Vega, E., Chalk, T. B., Wilson, P. A., Bysani, R. P., & Foster, G. L. (2020, July 9). *Atmospheric CO₂ during the Mid-Piacenzian Warm Period and the M2 glaciation*. *Nature News*. Retrieved March 23, 2022, from <https://www.nature.com/articles/s41598-020-67154-8>
- Morello, L. (2011, February 7). *How ocean currents once warmed the Arctic*. *Scientific American*. Retrieved March 24, 2022, from <https://www.scientificamerican.com/article/ocean-currents-once-warmed-arctic/>
- Polly, D. (2009). The pliocene epoch. Retrieved March 24, 2022, from <https://ucmp.berkeley.edu/tertiary/pliocene.php>

Design and Analysis of Annular Aerospike Plug Nozzle using CFD

Student Researcher: Anthony M. Bothe

Advisor: Dr. Jed Marquart

Ohio Northern University
Mechanical Engineering

Abstract

A brief introduction to the Lockheed Martin X-33 project and Rocketdyne's XRS-2200 project is presented as well as key advantages of aerospike nozzles over conventional bell nozzles. This article details the design, preliminary analysis, and evaluation of an annular aerospike plug nozzle using the simple approximate method for plug contour design. Plug nozzle contours were developed and computational fluid dynamics analyses performed. Conclusions are drawn from the data which promote understanding of the concepts of aerospike propulsion as well as present new ideas for aerospike research.

Project Objectives

The primary objective of the paper was to pool together known mathematical formulae for designing aerospike nozzles, and create a simple methodology for creating and assessing aerospike nozzle design. This research specifically focuses on annular aerospike nozzle design. This methodology was crafted in such a way that can be easily understood and used to create new aerospike nozzle designs. This new methodology was then verified using a CFD software called Cobalt. The isentropic and numerical analyses were then compared side-by-side to check if the new methodology is reasonably accurate. The secondary objective of the paper was to present a brief history of aerospike propulsion during the 1960s as well as notable advantages of the aerospike nozzle over a conventional bell nozzle. For the paper, mission parameters were set as a start point for the design. They were as follows: Thrust = 5 kN; Combustion Pressure = 2,067.857 kPa; Exit Mach = 3.0, Specific Heat Ratio = 1.4; Atmospheric Pressure = 101.325 kPa.

Methodology

The methodology presented in this paper began with the research presented in "Approximate Method for Plug Nozzle Design," written by G. Angelino. Since the aerospike is essentially a concave version of a bell nozzle, he determined mathematical formulae that would approximate an ideal curve for Prandtl-Meyer expansion waves that formed as exhaust gases reached sonic speed at the throat line. This research has been built upon by several others which were also used to create the methodology in this paper.

Results Obtained

The resulting data from the numerical analysis showed a fairly reasonable margin of error at less than one percent. Refer to Table 1 and Figures 1-2 for the data comparison as well as the pressure contours on the plug nozzle.

Significance and Interpretation of Results

The first observation made once all the data was listed was how accurate the total thrust was from the numerical analysis when compared to the isentropic analysis. Secondly, it is easy to deduce from the pressure data that nearly 60% of the plug length was contributing very little to the overall thrust. From this, a new model was created with a 60% truncation on the spike length and simulated under the same conditions as before. The new data is shown in Table 2 and Figures 3-4. The truncated model had 1.2% reduction in total thrust from the previous simulation. This proved my hypothesis that aerospike nozzles can be made more efficient by removing useless spike length after an extensive analysis.

Figures/charts

Table 1: Comparison between Isentropic and Numerical Values (No Truncation)

	<i>Isentropic</i>	<i>Numerical</i>
Mass Flow Rate (kg/s)	3.695	3.697
Throat Velocity (m/s)	726.7	730.39
Throat Pressure (Pa)	1,092,000	1,084,920
Center-body Thrust (N)	2,141	2,101
Thruster Force (N)	2,859	2,860.09
Total Thrust (N)	5,000	4961.09

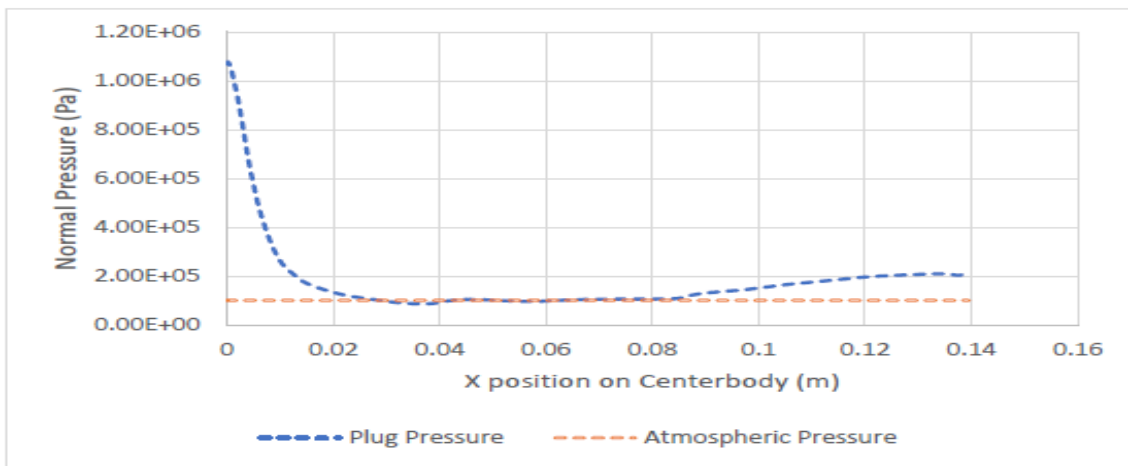


Figure 1: Plug Pressure Distribution and Comparison (No Truncation)

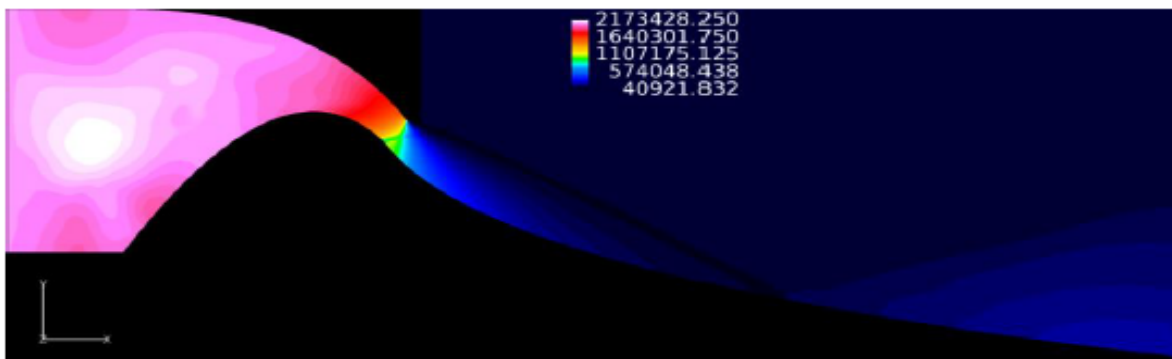


Figure 2: Pressure Contour along Plug (No Truncation)

Table 2: Comparison between Isentropic and Numerical Values for Truncated Model

	<i>Isentropic</i>	<i>Numerical</i>
Mass Flow Rate (kg/s)	3.695	3.697
Throat Velocity (m/s)	726.7	730.39
Throat Pressure (Pa)	1,092,000	1,084,920
Center-body Thrust (N)	2,141	2,040.5
Thruster Force (N)	2,859	2,860.09
Total Thrust (N)	5,000	4900.59

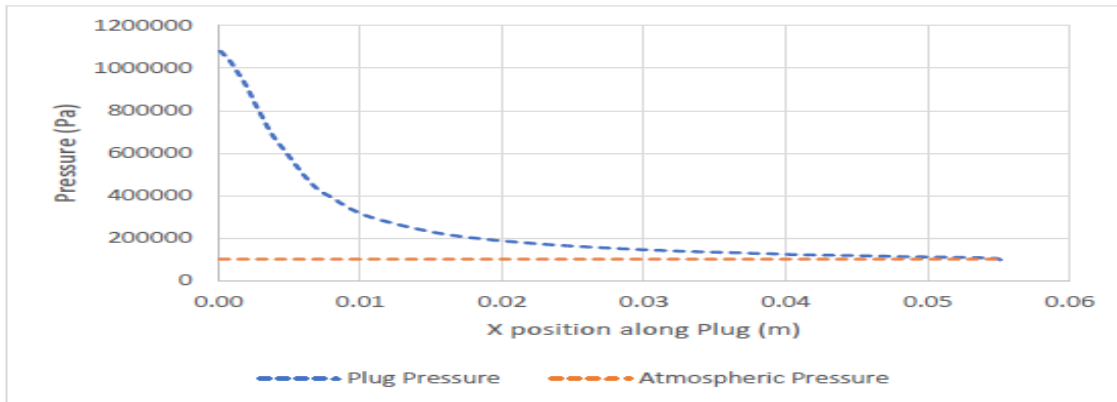


Figure 3: Pressure Data for Truncated Model

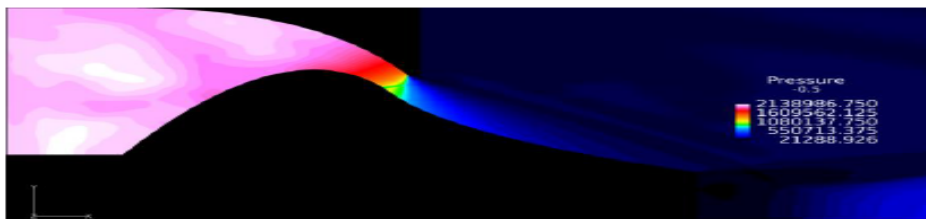


Figure 4: Pressure Contour along Plug of Truncated Model

Acknowledgements and References

This research was funded by OSGC (Ohio Space Grant Consortium). I am grateful to OSGC for providing me the opportunity to conduct this research. I also want to thank Dr. Jed Marquart, a Mechanical/Aerospace Engineering professor at Ohio Northern University, for helping me through every step of the process.

- [1]. *Cobalt Manual, Version 8*, Cobalt Solutions, LLC, Dayton, OH, 2018.
- [2]. G. Angelino, "Approximate Method for Plug Nozzle Design," *AIAA J.*, Vol. 2, No. 10, 1964.
- [3]. Eric Besnard, Hsun Hu Chen, Tom Mueller, "DESIGN, MANUFACTURING AND TEST OF A PLUG NOZZLE ROCKET ENGINE," *AIAA-02-4038*, 2002
- [4]. Mehdi Nazarinia, Arash Naghib-Lahouti, Elhaum Tolouei, "Design and Numerical Analysis of Aerospike Nozzles with Different Plug Shapes to Compare their Performance with a Conventional Nozzle," *AIAA-11*, March 2005
- [5]. Utah State University, "MAE 5540 – Propulsion Systems I"
- [6]. K Naveen Kumar et al 2017 IOP Conf. Ser.: Mater. Sci. Eng. 247 012008
- [7]. Rohanverse, "Aerospike Engine," 2010
- [8]. F-Chart Software, "Engineering Equation Solver."
- [9]. Chris Bergin, "X-33/VentureStar – What really happened," *nasaspaceflight.com*, January 4, 2006
- [10]. Jeff Scott, "Aerospike Engine," *aerospaceweb.org*, Fall 1999

Dynamic Response of Swept Wing Aerodynamics to Active Flow Control through Vortex Generating Jets

Student Researcher: Patrick Brandt

Advisor: Dr. Jeffrey Peter Bons

The Ohio State University
Aerospace Engineering

Background

On a swept wing, the stall is known to begin near the wingtip at the trailing edge and develop over the wing toward the leading edge at the wing root with increasing angle of attack. Since control surfaces such as ailerons are often placed near the location of initial stall for a swept wing, a serious safety and control problem is caused by swept wing stall. The wingtip stall also generates a nose-up pitching moment that can further decrease control authority. Since swept wings see performance enhancements in other areas of aerodynamics, as well as control and stability, stall mitigation techniques are valuable in wing integration. By reducing the harmful effects of stall, an aircraft could be safely operated in a wider envelope of flight conditions.

A proposed method for addressing the harmful effects of stall over a swept wing in a low Reynolds number flow is the use of Active Flow Control (AFC). The details of the present AFC design and implementation are given by McFadden et. al. [1]. The introduction of AFC will cause a time-varying reaction in the global forces and moments acting on the wing, and these transient conditions will have significant implications for flight controllability. Because many of the benefits of AFC are observed in flight mission profile sections such as landing and takeoff, the ability to activate AFC with safety and control is crucial for practical feasibility. The present study will seek to investigate the time-varying effects of AFC actuation on the global forces and moments acting on a swept wing.

Methodology

Experimental data is collected in two steps. The first step is to characterize the time response of AFC actuators to activation and deactivation signals sent to the AFC system. To accomplish this, hot film anemometry is used to detect air velocity exiting the AFC actuators simultaneously with the signal generation. This experiment is accomplished in a benchtop experiment. The second step is to characterize the time response of aerodynamic loadings on the wing with actuation of the AFC. This is accomplished using a load cell attached to the wing mounted in a low-speed wind tunnel. Combining both the benchtop experimental results and the results recorded from wind tunnel experiments, information can be gathered relating to the time response of the wing's aerodynamic performance as AFC is activated and deactivated. For data collection with both the hot film anemometer and the load cell, data is collected for 250 seconds while the pulse driver generates a square wave signal with 50% duty cycle and 3 second period to actuate the AFC. The data is phase averaged across all cycles to achieve the final result, a characterization of the average time response over one cycle of activation and deactivation. Additionally, the loading data from wind tunnel experiments is notch filtered to eliminate frequencies in the signal that have been identified as structural resonance frequencies of the mounting structure attached to the wing.

Results

McFadden et. al. [1] provide a comprehensive characterization of the steady-state performance of the wing in both the controlled and uncontrolled states. Figure 1 gives the time response results from both the benchtop actuation characterization and the wind tunnel aerodynamic loading characterization for 4

angles of attack in the wing’s stall regime. For comparison, the aerodynamic loading coefficients for each angle of attack are given in terms of a deviation from the steady state performance of the wing at a given angle of attack in the uncontrolled configuration. In Figure 1, t^+ is the nondimensional time for the experiment, which is normalized by the convective time for the flow. The convective time is given by the quotient between the effective chord length of the wing and the tunnel freestream velocity and is approximately 7 milliseconds for the present configuration. The blowing ratio (BR) is defined as the ratio between the velocity of air exiting the AFC system and the freestream velocity of the wind tunnel and can be considered as relating to the level of AFC actuation.

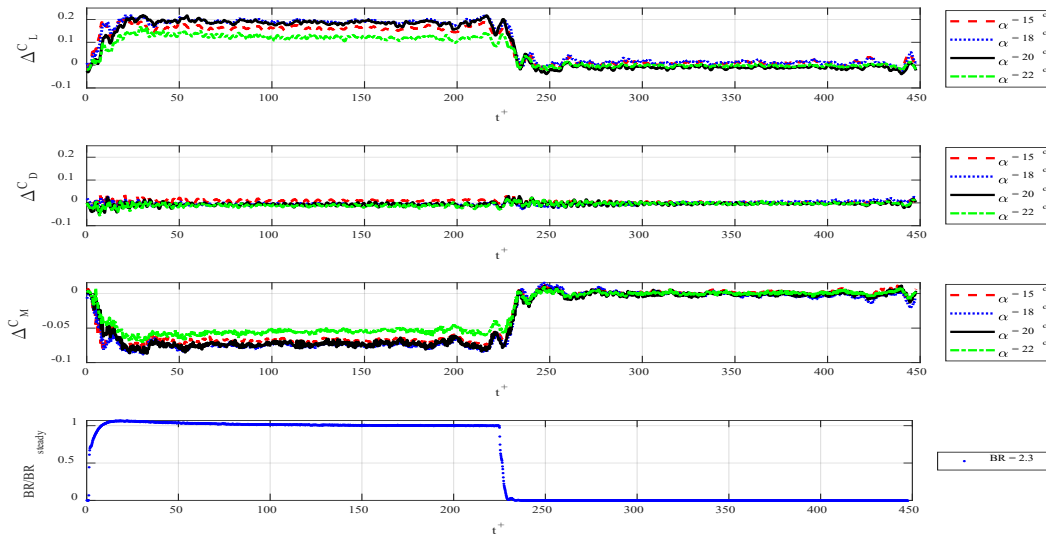


Figure 1. Time response of aerodynamic loadings to step inputs of AFC activation and deactivation
 From Figure 1, the aerodynamic lift force and pitching moment tend to lag behind the AFC actuation on the order of 10 convective time units. The drag on the wing is not strongly influenced by the AFC. Furthermore, the time response in aerodynamic loading does not seem to be a strong function of angle attack. While the angle of attack increases, the lag time between AFC actuation and aerodynamic loading response increases slightly.

Conclusion

Active Flow Control can improve the aerodynamic performance of a swept wing, and the low Reynolds number case investigated is of special interest thanks to the rapidly growing industry of unmanned aerial vehicles. In order to successfully implement AFC on a flying vehicle though, research must be conducted to fully understand the effects of AFC actuation on the dynamic problem of aircraft flight.

This project represents one of many steps required for physical understanding of the effectiveness and practical feasibility for AFC on advanced flight vehicles. The time response of a swept wing’s aerodynamic performance is characterized as aerodynamic loadings adjust dynamically in time to step inputs of AFC actuation. Developing this physical understanding is crucial for the successful design of a control algorithm to implement AFC while maintaining safe and controlled aircraft operation.

References

[1] McFadden, E. C., Brandt, P. J., and Bons, J. P., “Swept Wing Active Flow Control Using a Streamwise Row of Vortex Generating Jets,” AIAA-2022-1546, January 2022, DOI 10.2514/6.2022-1546.

A *cyp1b1* Deletion Mediates Primary Open-Angle Glaucoma Through Malformations in Schlemm's Canal and the Trabecular Meshwork

Student Researcher: Elizabeth M. Bryson

Advisors: Morris, Jaquelin Ph.D. Munroe, Karen Ph.D.

Baldwin Wallace University

Biology and Geology

Abstract

Primary open-angle glaucoma is the second leading cause of blindness and the most common type of glaucoma in adults over forty years of age, affecting one in every 10,000 people. The autosomal dominant form of the disease, juvenile open-angle glaucoma, affects one in 50,000 people from three to thirty-five years of age (Chak et. al 2014). While the mechanism of the disease is not fully understood, *cyp1b1* is thought to play an integral role in the development of Schlemm's canal and the Trabecular meshwork in the eye due to its' expression in pericytes, endothelial cells, and astrocytes (Falero-Perez et. al 2019). Each of these cells has a different role in the formation of the two important parts of the drainage system of the eye. The study I am conducting aims to use the CRISPR/Cas9 system to create a targeted deletion of *cyp1b1* to better understand the effects of a complete gene deletion on the development of primary open-angle glaucoma. Three *Danio rerio* specific oligonucleotides were created to target the *cyp1b1* gene located on exon one of chromosome thirteen. The oligonucleotides were PCR amplified and purified before undergoing in vitro transcription. Completed gene transcripts were confirmed via electrophoresis. *Danio rerio* one-cell stage embryos were then injected with Cas9 protein and the four *cyp1b1* specific gRNAs. DNA isolated from injected embryos is currently being used to confirm mutagenesis.

Methodology

The four target sequences used to design the oligonucleotides and gRNAs were chosen based on an analysis done in the CHOPCHOP program under the metrics that they have high efficacy and no off-target sites that would interfere with the CRISPR. The decision to use four target sites rather than two was made to increase the chances of a successful knockdown in case one or two of the gRNAs were ineffective. Once the oligonucleotides were designed, they were PCR amplified using two gRNA primers and a guide constant oligonucleotide in order to create the template strands. Once the PCR was complete, the DNA was run on a 2% electrophoresis gel, extracted, and purified using the Illustra GFX PCR DNA and Gel Band Purification Kit.

After purification, the DNA went through in vitro transcription and Lithium Chloride precipitation to retrieve the gRNA that would be used for injections. 200 pg of gRNA and 400 pg of Cas9 protein were put into an injection mixture along with Potassium Chloride, Phenol Red, and water. The mixture was injected into one cell stage embryos to ensure that the Cas9 and gRNA was inserted into the blastula to be incorporated into the genome of the fish. The embryos were placed in a 37° C incubator. After 48 hours the embryos were removed from their chorions and lysed to retrieve DNA. DNA from injected and un-injected embryos were again amplified via Touchdown PCR using a forward and reverse primer designed to determine mutagenesis. A second set of primers and PCR parameters are currently undergoing troubleshooting in order to send the DNA to be sequenced.

Next steps

After PCR parameters have been optimized, the DNA from the embryos injected with the gRNA mixture will be sent off to be sequenced. This will allow us to see exactly where in the genome our mutations have occurred and determine how we proceed with the project.

Figures

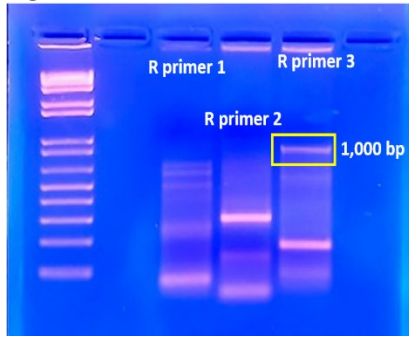


Figure 1: Testing three different reverse primers on *Danio* tail DNA to determine which one to use.

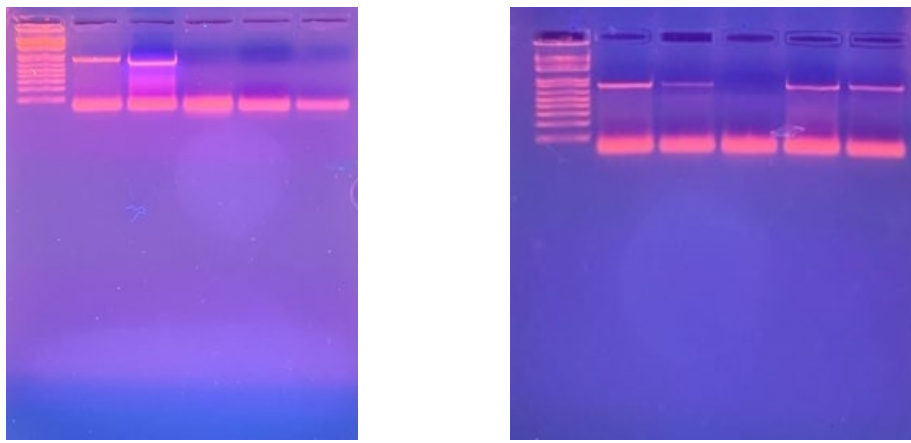


Figure 2: (left) Reactions containing the tail DNA as a comparison in lane 3, DNA from pooled embryos that had been injected in lane 4, and three sets of injected single embryo DNA in lanes 2, 5 and 6. Reactions were run using the third reverse primer from Fig. 1.

Figure 3: (right) Single embryo DNA that had been injected with the CRISPR mixture. Reactions were run using the third reverse primer from Fig. 1.

References

- Chak, G., Mosaed, S., & Minckler, D. S. (2016, May 4). Diagnosing and managing juvenile open-angle glaucoma. *American Academy of Ophthalmology*. Retrieved November 14, 2021, from <https://www.aao.org/eyenet/article/diagnosing-managing-juvenile-openangle-glaucoma-2>.
- Falero-Perez, J., Larsen, M. C., Teixeira, L., Zhang, H. F., Lindner, V., Sorenson, C. M., Jefcoate, C. R., & Sheibani, N. (2019). Targeted deletion of *Cyp1b1* in pericytes results in attenuation of retinal neovascularization and trabecular meshwork dysgenesis. *Trends in developmental biology*, 12, 1–12.

Flow Meter Calibration Apparatus

Student Researcher: Zachary Carner

Advisor: Dr. Mitch Wolff

Wright State University
Mechanical Engineering

Background

Flow meters are devices used to measure the volume or the mass of a liquid or gas. These devices measure the flow of the material that is passed through them. The greatest benefit of flow meters is that they provide a more accurate measurement of the gas or liquid that is circulated through a specific point. Researchers use flow meters to determine many different attributes of an experiment. Like all equipment, it is important to understand the uncertainty of the flow meters when they are being used in an experiment. Currently, to calibrate flow meters, they must be sent to outside companies. This circumstance prevents flow meters from being calibrated in situ. This apparatus will allow the flow meter to be calibrated in the environment in which it will be used, without sending it away. The apparatus works by accurately weighing the total amount of water, stored in a drum, that passes through the flow meter over an interval of time.

Design

The design of the apparatus (shown in Figure 1) was based on a stock drum dolly from McMaster-Carr. The cart was outfitted with four floor locks to keep the cart in a level and stationary position while the apparatus is in use.

To accurately measure the weight of the water inside the barrel, three Adam Equipment CKT 32UH scales were used (shown in Figure 2). Three smaller capacity scales were utilized in this calibration apparatus because the smaller capacity scales had higher accuracy values for the price. In comparison, the large capacity scales were not as accurate and were much more expensive. To accommodate all three scales, an 80/20 aluminum extrusion and a ¼-inch sheet of aluminum were utilized to expand the platform on which the scales were placed.

A series of pipes, fittings, and pressure relief valves were used to direct the flow of water out of the flow meter and into the tank for measurement. These pipes were attached to two Unistrut Channels and secured to the cart. This way, the weight of the piping would not be calculated with the weight of the water.

Data Acquisition

The three scales purchased used the RS-232 serial communication standard to allow for data acquisition. RS-232 was ideal for this application because it is low in cost, is widely used, is free from noise, and allows for quick data transfer. Dewesoft Data Acquisition Software was utilized to read and record the data output from the scales. Significant time and effort were spent getting the software and the scales to talk to one another properly and to accurately record the data.



Figure 1: Flow Calibration Cart CAD Model

Future Work

As a result of the COVID-19 pandemic, access to the AFRL was restricted for several months, significantly impacting and restricting the progress made on this project. Continued work involves installing the scales on the testing apparatus, calibrating the apparatus, and completing an uncertainty analysis of the testing apparatus.

Conclusions

Once complete, the flow meter calibration cart apparatus will allow researchers to calibrate their flow meters in situ. This ability will prove advantageous to the industry by saving time and money and by improving the accuracy of the calibration. Additionally, the use of stock, commercially available products will make the apparatus easily replicable for researchers across the country.

Acknowledgements

Special thanks to P.C. Krause and Associates for providing the project opportunity and for funding the purchase of the different parts required in the construction of the apparatus. I would also like to thank Dr. Tommy Baudendistel for his help and guidance on the project.

Additionally, I would like to thank the Ohio Space Grant Consortium for providing the scholarship funding that allowed me to work on this project and Dr. Mitch Wolff for guiding me through this opportunity.



Figure 2: Picture of the Adam Equipment scale utilized in the design

Smart Flying Sensor

Student Researcher: Zackry D. Cephas

Advisor: Dr. Deok H. Nam

Wilberforce University

Department of Computer Engineering

Abstract

The purpose of this project is to examine the sensors that is use on space travel to understand what we need to know that distinguishes the condition of the entryway (open or shut).A sensor, without help from anyone else Astrobotic is creating visual territory relative route (TRN) and LiDAR-based risk location to empower exact and safe planetary arrivals on the Moon, Mars, and others. They were the primary business organization to utilize TRN and peril recognition to direct a suborbital sendoff vehicle to a protected landing site. Lighting conditions on the lunar surface, for any location and time. This is especially useful for polar missions, where long, sweeping shadows can cause the lighting conditions to change dramatically. NASA's Astrobe robot to acoustically, monitor ISS systems and predict when maintenance is needed. The program is part of research collaboration between Astrobotic, NASA, and the ISS National Laboratory. SoundSee launched in 2019 and will conduct its first experiments aboard the ISS in 2020.

Project Objective

For the flying sensor what the robot uses to assemble information about its general surroundings. Cameras touch sensors are exceptionally normal, however a few robots use temperature, moistness, orindeed, even pH sensors. The smoke alarm introduced in your home uses a carbon-monoxide sensor to decide whether there is a fire in the house. A few sensors are somewhat more unremarkable, yet at the same no less significant. The switch that controls your cooler light, mounted in the entryway, is a sensor that distinguishes the condition of the entryway (open or shut).A sensor, without help from anyone else, just gives information. It is up to different pieces of the robot to as a matter of fact accomplish something with that information.

Astrobotic is creating visual territory relative route (TRN) and LiDAR-based risk location to empower exact and safe planetary arrivals on the Moon, Mars, and then some. they were the primary business organization to utilize TRN and peril recognition to direct a suborbital sendoff vehicle to a protected landing site. They keep on refining these frameworks to limit size, weight, power, and cost. Both their TRN and hazard discovery frameworks will be utilized to land NASA's VIPER wanderer at the south pole of the Moon on their Griffin lander in 2023. Smart camera for cutting edge space missions. This low size, weight, and power framework incorporates a coordinated set-up of equipment sped up PC vision calculations that empower a wide scope of in-space applications, including meeting and docking, independent meanderer route, and accuracy planetary landing. Work with capacities like TRN, visual concurrent confinement and planning (SLAM), 3D reproduction, object acknowledgment and following, and element focusing on. Programming system for multi-tangible mechanical route and planning. AstroNav will empower free-flying space apparatus to quickly investigate dim, unmapped, GPS-denied conditions like lunar bay windows and frosty moons. AstroNav has been broadly tried on Earth in caverns, passages, and magma tubes. It looks to defeat the vital difficulties of exact position assurance, advances among light and dim conditions, Luna Ray is a truly exact planetary renderer and set-up of programming apparatuses for arranging accuracy arrivals and meanderer navigate ways. It utilizes

geology and ephemeris information to create photometrically exact renderings of the lighting conditions on the lunar surface for any area and time. This is particularly helpful for polar missions, where long, clearing shadows can make the lighting conditions change drastically. LunaRay can likewise create ground station view and Earth height maps for media communications arranging. LunaRay consolidates continuous physical science based beam following and utilizes best in class photogrammetric techniques to combine high-goal DEMs from orbital pictures and LiDAR information. Astrobotic and Bosch Research have collaborated to foster SoundSee. This instrument will help crewmembers on the International Space Station (ISS) by flying through the station on board NASA's Astrobeerobot to acoustically screen ISS frameworks and foresee when support is required. Develops custom designs, sensor systems, and rovers for planetary. Surface activities such as autonomous exploration, site preparation and resource extraction astrobotic creates specially crafts, sensor frameworks, and wanderers for planetary surface exercises like independent investigation, site arrangement, and asset extraction. For instance, we are creating co-confinement innovation for groups of meanderers to empower quicker investigation and more noteworthy usefulness in future planetary missions. This innovation comprises of conservative detecting equipment and novel programming methods for groups of independent vehicles to mutually assess their positions comparative with each other, explore all the more unequivocally, and complete mission objectives all the more adequately.

Methodology

Astrobotic has created programming for arranging meanderer missions. The product gives a graphical UI to mission designers and researchers to intelligently investigate situations including different landing locales, mission spans, and security edges. Strong and productive course arranging advancement calculations consider time-shifting conditions, meanderer capacities - like climbing capacity and energy prerequisites - hazard particulars, and the sequencing of science goals. The product can likewise be applied to spatiotemporal arranging assignments on Earth in fields like mining, horticulture, and flying studying. Which also help comprises of minimal detecting equipment and novel programming strategies for groups of independent vehicles to mutually assess their positions comparative with each other, explore all the more definitively, and do mission objectives all the more really.

Development of a System for Diffuse Reflectance Spectroscopy with Variable Source-Detector Separation

Student Researcher: Boyd Colbrunn

Advisor: Dr. Karthik Vishwanath

Miami University
Department of Physics

Abstract

Diffuse reflectance spectroscopy (DRS) is an optical technique to interrogate a medium non-destructively using light. Information about the color of light backscattered from the medium is related to the optical absorption and scattering of the material, which in turn indicate its make-up and composition. [1] DRS systems use fiber optic channels to couple a light source to the medium and to capture reflected light to the detector. The distance between the source and the detector fibers is called the source-detector separation and controls the depth of light penetration in the medium. A larger source-detector separation provides for deeper penetration, though the larger the source-detector separation the lower the signal measured. DRS fiber probes used usually have a fixed source-detector separation. When measurements need to be taken at different source-detector separation distances, probes are often built with several channels, each needing individual detectors. Although the method works, it does not allow one to dynamically vary source-detector separation and the cost of a system scales with the number of channels used. The goal of this project is to develop a fiber-based DRS system with a single detector and source that are coupled to a 3D printed variable-source-detector separation fiber optic positioner.

Project Objectives

The objectives of this project are centered around creating and testing the utility of a diffuse reflectance spectroscopy system with variable source-detector separation (SDS). The system itself ideally has a measurable position and thus measurable SDS. Practicality of the system can be examined by experimenting with separation velocities and by performing sweeping DRS scans.

Methodology

Designs for the system were modeled in Autodesk Inventor, then 3D printed to be tested. Models consisted of a mount for both the source and detector, one or both of which needed to be mobile. Ideal minimum source-detector separation was 1-3mm at least, and any maximum SDS above 1cm was considered more than sufficient.

A broadband tungsten-halogen lamp source (HL2000, Ocean Optics, FL) and spectrometer (USB4000, Ocean Optics, FL) were used for verification. Reference spectra were collected from a white spectralon reflectance standard (Labsphere, New Hampshire) and a scan of ambient light in the room. The lamp and detector were coupled to the rest of the configurable system using SM600 optical fibers (Thorlabs,

New Jersey), and to the control system using SM400 optical fibers (Thorlabs, New Jersey). Integration times used for each DRS scan were 40 ms.

Results

The final system design can be seen in figure 1. A linear rail with NEMA 11 Stepper Motor was used to control the movement of the source, while the detector stayed stationary at one end of the rail. Minimum SDS is ~5mm and maximum SDS is ~80mm. Verification of the system is shown in figure 2.

Discussion

Further spectroscopic analysis must be done to draw definitive conclusions regarding the accuracy of the system. While the plots in figure 2 are notably different, future analysis must be done to interpret the data and determine measured optical properties of the standard. It is worth noting that the second figure in figure 2 features peaks in similar places for both systems, which is promising.

Future Work

Future investigation should be done to reduce the minimum SDS to 1-3 mm and to develop a more accurate method of measuring the source-detector separation. If these goals are achievable, additional work can be done to investigate the practicality of a “sweeping scan”. This type of scan would move the source across the medium while continuously collecting data. If this proves useful, more work can be done looking into the effects of varying separation velocities while holding integration time constant, and vice versa.

Figures and Tables

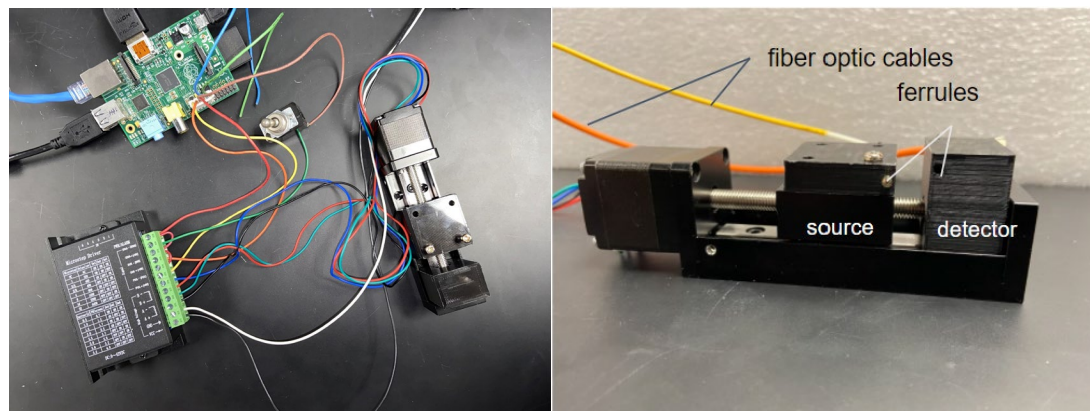


Figure 1. DRS system with variable source-detector separation. The left image is the full setup, with Raspberry Pi, stepper motor/linear rail, driver, and emergency stop switch. The right image is just the stepper motor/linear rail, with fiber optics wired in (source in yellow, detector in orange).

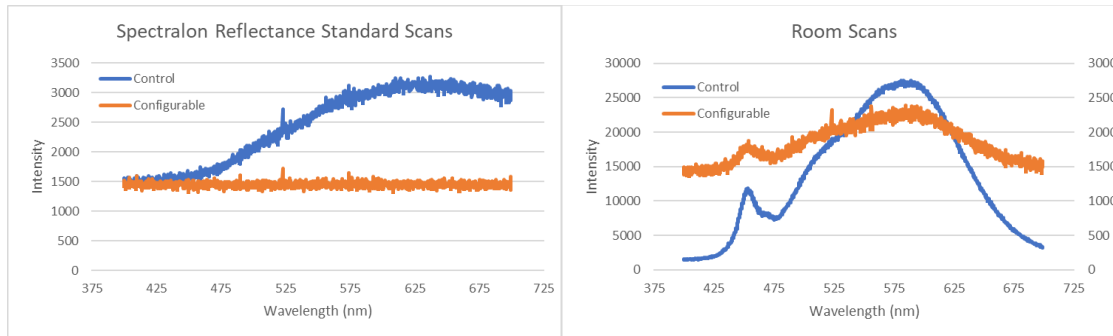


Figure 2. Verification of the system using white reference standard phantom (left) and ambient light scan (right). Blue data represents the control system and orange is the configurable system.

Acknowledgments

Thanks to Dr. Karthik Vishwanath and Mark Fisher for their support and guidance throughout this project, as well as Miami University’s Department of Physics and the Ohio Space Grant Consortium for making the project possible.

References

1. Wilson, R. H., Vishwanath, K., and Mycek, M. A. “Optical methods for quantitative and label-free sensing in living human tissues: principles, techniques, and applications,” *Advances in Physics: X*. 1(4), 523-543 (2016).
2. Vishwanath, K., Gurjar, R., Wolf, D., Riccardi, S., Duggan, M., and King, D. “Diffuse optical monitoring of peripheral tissues during uncontrolled internal hemorrhage in a porcine model. *Biomedical Optics Express*, 9(2), 569. doi.org/10.1364/boe.9.000569

Paraoxonase Regulation of Vascular Dementia

Student Researcher: Jacob A Connolly

Advisor: Dr. David Kennedy

University of Toledo
Department of Medicine

Abstract

Chronic Kidney Disease (CKD) has shown to be a possible risk factor for dementia and cognitive impairment¹. These cognitive changes often occur early in the progression of CKD and the rate of decline varies with the progression of the disease¹. Furthermore, CKD is considered to be a model of accelerated aging due to increased vascular calcification, oxidative stress, and vascular dysfunction². Around 45 percent of adults above the age of 70 are affected by CKD and that number is only expected to rise due to the increasing prevalence of hypertension and diabetes in an aging US population³. My research is conducted on the Dahl-S strain of rats, a model that exhibits premature vascular remodeling and cognitive decline⁴. Even when placed on a low salt diet, Dahl-S rats show the development of fibrosis in cardiac and renal tissue along with the development of CKD. Furthermore, genes implicated in the development of Alzheimer's disease are overexpressed in the hippocampus of these animals⁴. The family of enzymes known as the paraoxonase enzymes were originally discovered because of their ability to hydrolyze paraoxon⁵. There are three known members of the paraoxonase family: paraoxonase-1 (PON-1), paraoxonase-2 (PON-2) and paraoxonase-3 (PON-3). Previous studies on this family of enzymes have shown that they also possess lactonase and esterase activity⁵. Furthermore, PON-1 is believed to be a major protein that is responsible for the antioxidant properties of high-density lipoprotein (HDL)⁶. Studying dementia on the background of CKD can provide insights into the mechanism of the disease and how we can discover better treatments.

Project Objectives

The goal of this project was to test the cognitive ability of our novel Paraoxonase knockout animal models to determine if paraoxonase has an influence on cognitive function.

Methodology Used

In order to test the cognitive ability of our animal models, the Barnes Maze and Open Field Maze tests were performed. The Barnes Maze is a hippocampus dependent task where the animal learns the relationship between cues in the surrounding environment and the location of an escape box. The Barnes Maze I constructed is a circular table 4 feet in diameter with 20 holes evenly spaced around the perimeter (**Figure 1**). An escape box is placed underneath one of the holes while the other 19 are left open. Bright lights and open spaces are used as motivating factors for the animal to find the escape box as quickly as possible. The testing proceeded over a two-day period. On the first day, a habituation trial occurs. The habituation trial consisted of a 3-minute trial, and if the animal was unable to find the escape box within that interval it was gently guided to it. The animal then remained in the escape box for 2 minutes before returning to its home cage. 24 hours later, the testing phase consisting of 4 trials began. Each testing trial was 5 minutes in length and if the animal was unable to find the escape box in the allotted time, it was given a latency value of 300 seconds and was gently guided to the box. The animal remained in the escape box for 1 minute before it was returned to its home cage. The animal would then wait in their home cage for at least 15 minutes before the next trial. The amount of time it took for the animal to reach the escape box was recorded as latency time. Primary latency time was defined as the length of time it took for the animal to correctly identify the escape hole.

The animals were then tested using the Open Field maze (**Figure 2**). The Open Field maze consists of a square box 72 by 72 cm that is split into a grid of squares. The animal was then allowed to explore the maze for 10 minutes. During their run, tracking software was used to track their movements. Rodents show an aversion to open and brightly lit spaces and will avoid the center of the box. The anxiety level of the animal can be determined by the amount of time spent in the inner vs outer regions. Motor ability can also be assessed through values such as total ambulatory distance and average speed. The Open Field Maze analysis is current ongoing.

After completing both tests, the animals were euthanized, and their brains were examined for evidence of inflammation, oxidative stress, and vascular fibrosis using unbiased proteomic, genetic, and histologic techniques. This analysis is also currently ongoing.

Results Obtained

The Barnes Maze test has been performed on animals aged 6 and 9-months old. The Open Field Maze has also been performed on animals 6, 9 and 12-months-old. The results from the Barnes Maze test on the 6-month-old animals can be seen below in **Figures 3A** and **3B**. The results from the Barnes Maze test on 9-month-old animals can be seen below in **Figures 4A** and **4B**. Animals 12 months of age are currently being tested on the Barnes Maze. Animals aged 6, 9, and 12-months old have been tested in the Open Field Maze and the data is currently being analyzed. Brains were also collected from these animals and are currently in the process of analysis in terms of hippocampus size and the presence of fibrosis.

Significance and Interpretation of Results

The results in **Figure 3B** show that there is an increase in the area under the curve for latency time of the PON-3 Knockout Dahl-S animals versus the Wild Type Dahl-S animals. This indicates that the 6-month-old PON-3 Knockout animals have greater cognitive impairment than their age matched counterparts. The data also suggests that PON-3 Knockout males have greater cognitive impairment than PON-3 Knockout females, indicating the present of PON dependent sex differences in cognitive ability. However, there is no difference between the Wild Type Dahl-S animals and the PON-1 Knockout Dahl-S animals.

The results from **Figure 4B** show that Wild Type Dahl-S male animals have significantly worse cognitive ability than the Wild Type Dahl-S females, PON-1 Knockout, and PON-3 Knockout animals at 9 months of age. **Figures 4A** and **5A** show that as the trials progress, the animals are locating the escape box faster, indicating the presence of learning. However, the speed at which each group of animals learns is different.

Figures/Charts



Figure 1: Barnes Maze



Figure 2: Open Field Maze

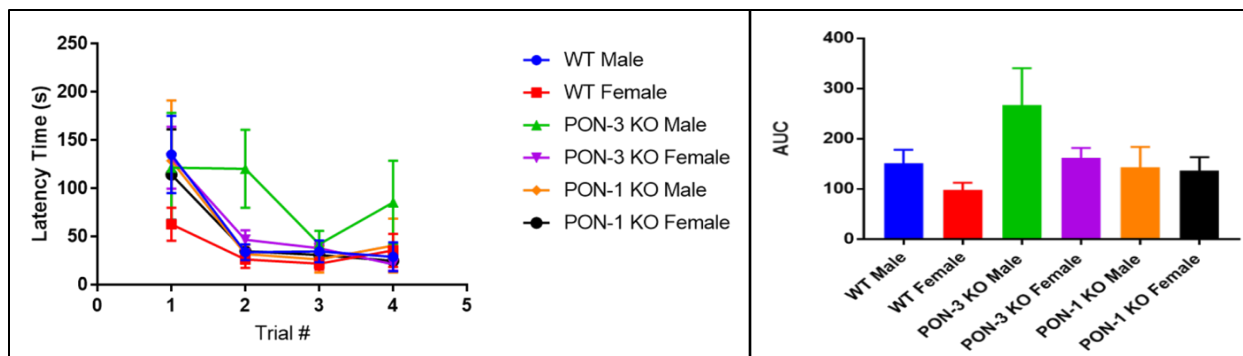


Figure 3A: Barnes Maze Primary Latency Time (6-Months)

Figure 3B: Barnes Maze Latency Time Area Under the Curve (6-Months)

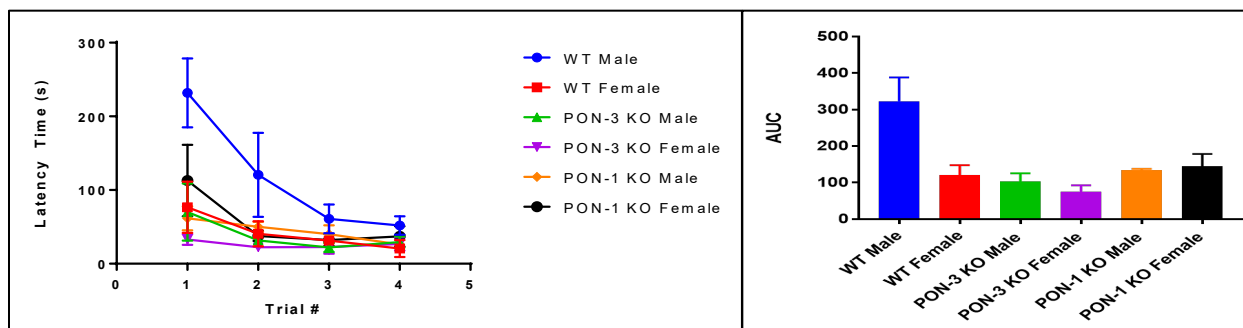


Figure 4A: Barnes Maze Primary Latency Time (9-Months)

Figure 4B: Barnes Maze Latency Time Area Under the Curve (9-Months)

Acknowledgements

The author of this paper would like to thank Dr. David Kennedy and Dr. Steven Haller for their continued guidance and all the members of the Kennedy/Haller lab for their assistance and support in this research project. The author would also like to thank the Ohio Space Grant Consortium and the Ohio Aerospace Institute for their support of this project.

References

1. Etgen T, Chonchol M, Forstl H, Sander D. Chronic kidney disease and cognitive impairment: a systematic review and meta-analysis. *Am J Nephrol.* 2012;35(5):474-482.
2. Bronas UG, Puzantian H, Hannan M. Cognitive Impairment in Chronic Kidney Disease: Vascular Milieu and the Potential Therapeutic Role of Exercise. *Biomed Res Int.* 2017;2017:2726369.
3. Coresh J, Selvin E, Stevens LA, et al. Prevalence of chronic kidney disease in the United States. *Jama.* 2007;298(17):2038-2047.
4. Fedorova OV, Lakatta EG, Bagrov AY. Endogenous Na,K pump ligands are differentially regulated during acute NaCl loading of Dahl rats. *Circulation.* 2000;102(24):3009-3014.
5. Draganov DI, Teiber JF, Speelman A, Osawa Y, Sunahara R, La Du BN. Human paraoxonases (PON1, PON2, and PON3) are lactonases with overlapping and distinct substrate specificities. *J Lipid Res.* 2005;46(6):1239-1247.
6. Mackness MI, Arrol S, Durrington PN. Paraoxonase prevents accumulation of lipoperoxides in low-density lipoprotein. *FEBS Lett.* 1991;286(1-2):152-154.

Microhardness and Fractography of Alloy 718 Additively Manufactured Samples

Student Researcher: Sabrina D'Alesandro

Advisor(s): Anna Dunn, Henry Young

Wright State University
Material Science Engineering

Abstract

Additive Manufacturing (AM) is a layer-by-layer process in which samples are built in an iterative style. AM has many benefits including low cost, quick prototyping, and low energy consumption that makes it a competitive choice for manufacturers compared to other more traditional methods. Due to the variability in thermal energy within the material during manufacturing, it produces microstructure within the material which effects it differently from other manufacturing processes. The thermal history of the material can drastically affect the structure which in turn will affect the material's performance in a created part. However, high-level analysis can be done to better understand how to avoid potential detrimental effects. Using alloy 718, the microstructure of a sample that was created using AM, will be observed by conducting image collection using SEM. Additional data will then be collected using microhardness and fractography, such as feature detection, to understand how microstructure is related to fatigue. This data will be used to gain insight into the mitigation against detrimental effects from the AM process to increase its effectiveness in industry.

Introduction

AM is a layer-by-layer process of manufacturing samples. This style has many benefits such as its low cost, manufacturability, and low energy usage. However, due to the variability in the thermal energy applied to the samples during the manufacturing process, AM samples often produce a higher rate of defects or unexpected microstructure. To create a method to mitigate against these issues, a process of failure analysis called fractography can be used in conjunction with microhardness to gain information about the material and its manufacturing process and how this will relate to fatigue. Fractography can be completed by collecting scanning electron microscopy (SEM) images and processing them with a method of image manipulation called image processing. Image processing is a tool that utilizes programming to manipulate images to gain further information about the materials that are images. In this project image processing can be used to identify certain geometries in the material images to identify features or defects in the material to aid in the fractography process. Microhardness is the second part of this project that will aid in the understanding on how AM effects the microstructure of the parts that are created. Microhardness testing is a mechanical test that applies a small load to the material, using an indent, to create a micro indent on the material surface using a specific applied load. From the depth of the indent hardness value can be assigned. Microhardness can detect changes in the material hardness on a much smaller scale than hardness tests such as Rockwell hardness testing. The ability to detect changes of hardness at the microlevel can aid in the understanding of how hardness values change from melt pool to melt pool, or by any additional variability in the materials production. In this experiment a program was created for feature detection for SEM images as well as a program to visualize hardness testing data. Using both hardness testing data and fractography will connect how hardness and material defects are related to changes in thermal energy within AM parts.

Experiment and Results

The first step of the project was to train on the microhardness tester. From this training a procedure was created to better understand the method of testing to understand how the data should be visualized. For the microhardness testing a sample is first prepped. After the sample is created and prepped, the sample can be placed on the stage of the microhardness. At this time the correct settings can be adjusted to begin the hardness test and the start button can be pressed. The microhardness data will then populate, and the data can then be used to be visualized. To visualize the data MATLAB can be used to create graphs or images showing the topography of the sample as it relates to the microhardness. From the microhardness data a X and Y value will be given. These X and Y values pertain to the location of the hardness indentation on the sample. After the X and Y values the hardness for that location will be given. To visualize this, in MATLAB the x and y values can be input along with the hardness value, and it can be plotted as a contour plot. This rudimentary method of hardness visualization will give information as to how the hardness values are changing across the sample.

To begin the SEM process samples are prepped beforehand to ensure they are clean to make sure no dust or debris is obstructing the view of the sample. Once the SEM images are collected, they can be viewed and then processed for feature detection. Common features, or defects, that are present in AM parts are cracks and pores. The notable difference visually between these 2 features are the length and roundness of the geometry. Pores are more circular in shape, while cracks are long and thin. In software, these visual differences can be differentiated by the aspect ratio. So, in order to complete feature detection, you can visually note what the feature should be and allow the code to detect the feature by noting a range that the aspect ratio should be. Pores will have a ratio closer to 1, while cracks will be further away from 1. To complete the feature detection, open-source SEM images were converted to 8-bit images. Once the images were converted, they were then made binary, and the pores or cracks were detected using the method of detection via aspect ratio. While some visual analysis is necessary, the processed image can be helpful for additional analysis. Image 1 below shows pore detection, while Image 2 shows the method of feature detection.

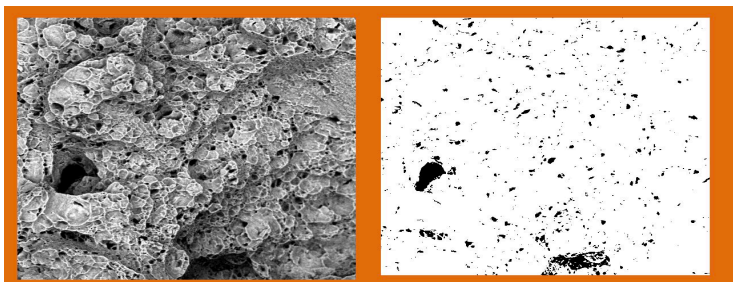


Image 1: Porosity detection using image processing. [1, Author]



Image 2: Crack detection using image processing. [1, Author]

Conducting the feature detection is crucial to connect to the AM parts performance in withstanding fatigue. Being able to detect the features is imperative due to defects being large stress concentrators. Within the material surface any cracks or pores will create a sudden change in the internal geometry. If there are only a few of these defects within the surface of the material, this may not impact the material performance at a recognizable level. However, due to the thermal history of AM parts, there is often a large amount of these stress concentrators. Being able to detect the number of defects and type of defects allows for researchers to make connections to the parameters used to build the part. Finally, more studies can be done to ensure the parameters are corrected to lessen the amount of defects impacting the part.

Conclusion

The conducted experiment focused on how using fractography and microhardness testing could obtain a deeper understanding on how thermal energy differences can affect the material on a microscopic level. While AM has many benefits, the changes in thermal history can create detrimental effects on the material and its microstructure. Using alloy 718, the microstructure of a sample that was created using AM, will be observed using SEM. Additional data was then collected using microhardness and fractography to understand how microstructure is related to fatigue. This data was then processed with image processing code to detect the features that were present within the material. These features that were detected were cracks and pores that are harmful to the material. Harmful geometry can affect how the material will withstand fatigue, and lead to the crack propagation that can cause premature failure. Using the fractography code, future defects can be understood and mitigated against. Lastly visualizing microhardness data can give insight into what the topography of the sample looks like regarding hardness values. Due to the thermal history of AM parts, many samples will show variability in microhardness values across the sample. However, using microhardness data in conjunction with fractography analysis can be conducted to better understand how to avoid these issues in the future.

Works Cited

[1] <https://www.nanoscience.com/applications/materials-science/fractography/>

Water Purification with a LED UV-C Reactor

Student Researcher: Kevin Decato

Advisor: Dr. Glenn Lipscomb

University of Toledo
Chemical Engineering Department

Abstract

Access to clean drinking water is one of the world's largest problems of our generation. As global populations tick upwards, an estimated 663 million lack access to an improved source of drinking water [2]. While of course there are a variety of water treatment methods that exist the today, the struggle has always been finding a method that consistently works in developing parts of the world, which often lack access to the requirements of these alternative methods, as well as the capital to purchase and maintain them. A UV-C photoreactor to inactivate bacteria and viruses constructed using LED bulbs addresses many of these issues.

A traditional UV-C reactor utilizes a fluorescent bulb that emits a wavelength of UV-C radiation at 254 nm. This wavelength of UV-C light inactivates the bacteria and viruses by catalyzing a reaction between amino acids that fuses their DNA together, preventing reproduction and thus preventing illness [4]. The optimal range for this process to occur is between 250-280 nm and varies between microorganisms. While the fluorescent bulb has worked to date, there are many improvements to be made around the design, especially with the development of LED lights that mimic the same UV-C output as fluorescent bulbs. LED chips offer a more robust 40-50% power efficiency compared to the 20-30% of the fluorescent tube [3]. LED chips also last 10 years compared to the 1 year of a fluorescent bulb, along with removing the complication of disposing fluorescent bulbs and the mercury within them [3]. Due to COVID-19 and a variety of factors, increased research into sanitization using UV-C light should have a positive effect on the price as demand and supply increase. The increased efficiency, longevity, and lack of maintenance makes the LED bulbs the superior choice for a UV-C reactor. A variety of 3D models were created to provide a foundation for testing.

Personal Objective

The objective is to continue developing an alternative UV-C reactor using LED instead of fluorescent bulbs. This would allow the reactor to be more durable, environmentally friendly, require less maintenance and become more efficient.

Method

Although the LED bulbs are the future, it's not as simple as just switching them out with the fluorescent bulbs. Water flowing through the reactor needs to be exposed to a minimum cumulative fluence dose to achieve inactivation of the bacteria and viruses. While the required dose is fixed at 40 mJ/cm^2 , light intensity varies with distance (normal and angular) from the bulb surface and is dependent on bulb and water flow channel design [1]. Currently, we are evaluating alternative flow channel designs that give sufficient fluid residence time to achieve the target dose. A variety of 3D models have been created on AutoCAD to model the irradiance output from the LED bulbs. One of the biggest challenges is measuring intensity as a function of distance and angle for use in design calculations. Currently all intensity information and measurements are provided by the LED supplier and other empirical research measurements. However, we have recently purchased a light meter to make measurements locally. For

example, the bulb intensity at ½ inch distance is 1.821 mW/cm² and 1 inch is .582 mW/cm², indicating a significant decrease over ½ inch distance [3]. Also, the light is confined to a 120 degree angle conical volume, meaning that if we had a 1 inch depth in our channel, the water in the bottom right corner would be exposed to a much lesser intensity than water flowing directly in front of the bulb due to the intensity fall off from distance and angle. Current design options focus on spacing the LED chips out in a manner that provides optimal distribution of light. Switching from a fluorescent tube as the light source to a light bar containing 5 LED chips means that there isn't a uniform intensity output coming from one bulb across the whole channel. Instead, we have to measure the intensity coming from 5 point sources. Proposed designs include a cylindrical flow chamber with lights on both the inner and outer wall of the chamber. Eventually, a computational fluid dynamics software will be used to evaluate cumulative fluence for different photoreactor designs (channel shape and bulb placement)[6]. A research piece also details past photoreactor trials on LED irradiance outputs[6]. Local measurements will also be made to ensure the proposed irradiance output is accurate.

Preliminary Results and Future Work

Given that this is a major improvement on an existing design, we know what fluence dose is required and the general design of the reactor. Since the relationship between intensity and distance is unknown, we cannot evaluate design parameters a priori.

For prototype development, we purchased a light bar with 5 LED chips emitting UV-C light at 276 nm which is comparable to the 254 nm light from a mercury fluorescent bulb [3]. Water that flows through the channel needs to receive a cumulative fluence dose of 40 mJ/cm². The benefit of point light sources are also evident in empirical data [5]. A fluence dose supplied by high intensity point sources over shorter amounts of time provides additional inactivation compared to the same fluence dose supplied by a low intensity, uniform source over an extended period of time[5]. Once we establish the relationship between fluence and distance from the bulb, optimal dimensions for the channel will be determined and the required residence time calculated. The results will establish the maximum water flow rate that can be treated for comparison to experimental measurements. The currently modeled 3D designs are being used as a basis going forward. A section of said designs will be tested using the light bar. However, alternative designs from Irtronix's website display a different take on the issue. They featured a flow chamber with an overwhelmingly intense set of LED bulbs near the exit that provides more and enough fluence dose for deactivation [7]. The caveat for this is lack of efficiency and increased power consumption. This design simplifies the need for equal distribution of light and all of the complexities that go with it. Further evaluation is needed to pick a suitable design that maximizes efficiency while achieving necessary fluence dose.

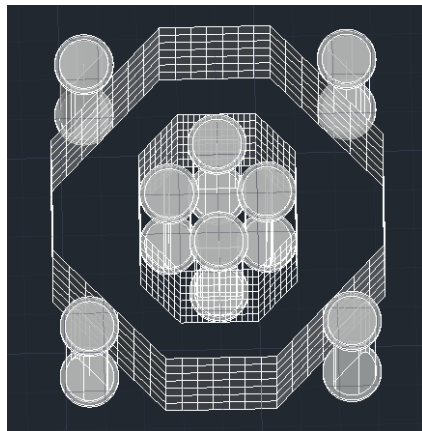


Figure 1: Proposed Flow chamber design featuring 8 light bars (40 LED chips)

Conclusion

The LED UV-C reactor offers a more efficient version of its predecessor. Although reactor designs have not been optimized, the designs are expected to be more efficient, environmentally friendly and durable than the current fluorescent bulb reactor. The longevity of the LED bulbs allows the unit to remain in place for 10 years without significant maintenance, which is a massive improvement upon the current design in which the fluorescent bulb has to be replaced annually. As the world shifts in a new direction, increased research in UV-C light being used in sanitization should reduce the overall cost of the LED chips as production ramps up and a greater demand develops. With major developments in efficiency and design, more people will be able to reap the benefits of this type of reactor.

Sources

- 1.) "UV-FAQs" IUVA, <https://iuva.org/UV-FAQs>
- 2.) "Drinking-Water." *World Health Organization*, World Health Organization, <https://www.who.int/news-room/fact-sheets/detail/drinking-water>
- 3.) "UV-C Light Bar" Irtronix, <https://www.irtronix.com/uv-bar-uv1001t>
- 4.) "UV LED Benefit: Wavelength Selection." *Aquisense*, <https://www.aquisense.com/wavelength-selection>.
- 5.) "Influence of light distribution on the performance of photocatalytic reactors: LED vs mercury lamps" *Elsevier*, https://www.researchgate.net/publication/317136901_Influence_of_Light_Distribution_on_The_Performance_of_Photocatalytic_Reactors_Led_vs_Mercury_Lamps
- 6.) "Enhanced numerical simulation of photocatalytic reactors with an improved solver for the radiative transfer equation" *Elsevier*, <https://www.sciencedirect.com/science/article/pii/S1385894720301741>
- 7.) "UV LED Water Sterilizing Reactor" Irtronix, <https://www.irtronix.com/water-sterilizing-reactor>

The Effect of Rotor Scaling on Acoustic Metrics

Student Researcher: Amanda M. Devillier

Advisor: Dr. Daniel R. Cuppoletti

University of Cincinnati

Department of Aerospace Engineering and Engineering Mechanics

Abstract

Urban Air Mobility (UAM) is a topic of increasing interest as urban roadways get more and more congested. In overpopulated areas, such as Los Angeles, residents on average spend a cumulative seven weeks a year commuting to and from work. The tops of buildings, parking garages, existing helipads, and open areas nearby population centers can be converted to VTOL hubs. The noise created by rotors used for distributed electric propulsion on Urban Air Mobility presents a unique challenge that must be accounted for in the preliminary design of such vehicles. Currently, many predictive tools use helicopter rotor data which does not accurately model noise physics at lower rotor tip speeds, characteristic of smaller rotor diameters. Disk and blade loading will also differ from helicopter rotors and smaller UAV rotors.

Project Objectives

The objectives of this research were to capture acoustic trends on rotors of various scales in the lab and to explore scaling the acoustics data up to 5x of the measured size to explore how the acoustic energy distribution may impact noise metrics. The accuracy of scaling rotor data up will also be explored in this work. The ability to accurately scale subscale rotor acoustics data will allow engineers gain a better understanding of the noise of their vehicle in preliminary design stages prior to testing full scale rotors. The methodology developed here will be useful for tailoring acoustic energy distributions by selecting the rotor size and number of rotors to minimize noise metrics.

Methodology Used

The rotor data was taken in the University of Cincinnati's hemi-anechoic chamber. The data was processed through a MATLAB code in which ensemble averaged narrowband frequency spectra were computed using a Fast-Fourier Transform with a sampling frequency of 204.8 kHz and 40,960 data points, providing a resolution of 5 Hz and 75 instances for averaging. The rotor data could be scaled up to five times its original size by shifting the energy into lower frequencies. Sound Pressure Level (SPL) and A-weighted SPL were integrated over a frequency window of 100 to 2000 Hz. This was done in order to: 1) keep the acoustic energy levels the same across different sized rotors and scales 2) keep the high frequency motor noise from impacting the SPL. While this technique does eliminate the effect of the high frequency motor noise, it is unknown if some of the mid frequency tones are from the motors. The A-weighted Sound Pressure Level was of particular interest as it places more importance on the frequencies that are perceived by the human ear.

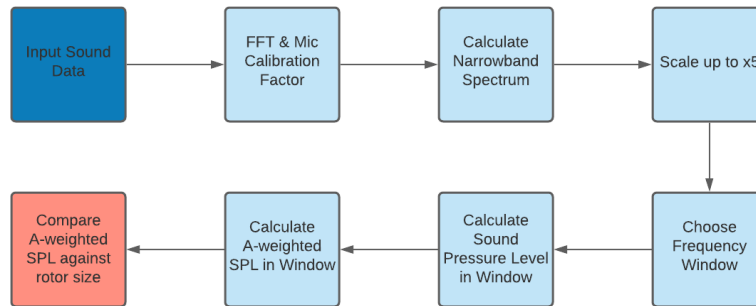


Figure 1. Data Process Flowchart

Results Obtained

Figure 2 compares the A weighted sound pressure level for raw microphone data and the same data scaled by 5. This is for Mach numbers of 0.25 and 0.45. On the left the effects of scaling drops large groupings of tones closer to 1000 Hz where the human ear is most sensitive so the A-weighted SPL goes from 47 to 52. On the right the effects of scaling moves several very large tones away from the sensitive frequencies so the A-weighted SPL drops from 70 to 59.

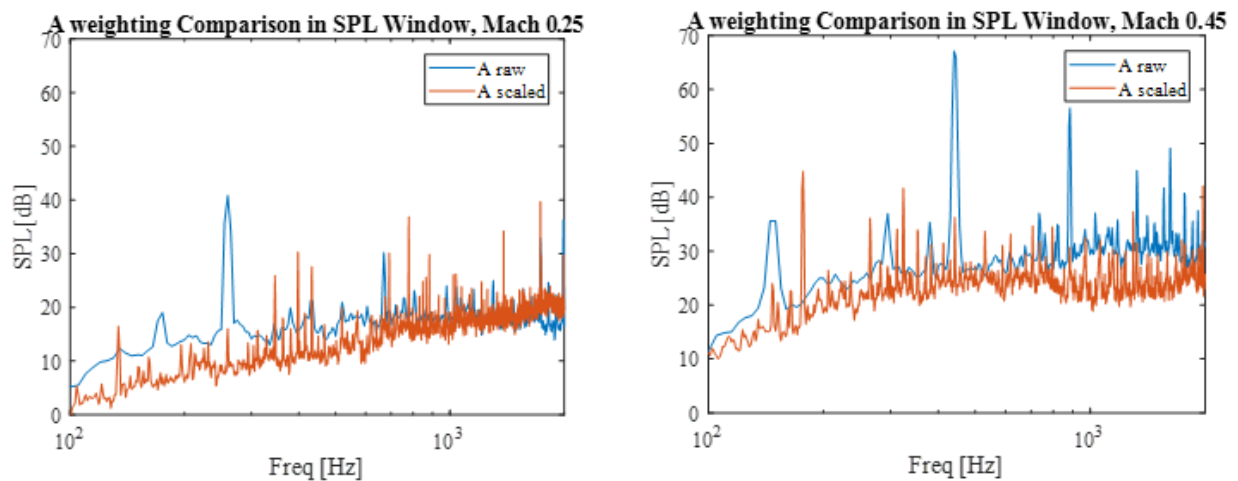


Figure 2. Comparison of A-weighted Raw data vs A-weighted Scaled data

Figure 3 shows a direct comparison of 30.5" diameter blades vs 12.5" diameter blades at Mach 0.25, both scaled to approximately the same size of 60". It can be clearly seen that the two spectra show some significant differences, the 12.5" blades are ~10 dB lower than the 30.5" blades. This difference could possibly be due to the flow over the 12.5" blades being more laminar than that of the 30.5" blades. This possible change in flow over the blades with increase in size is not accounted for when scaling the data.

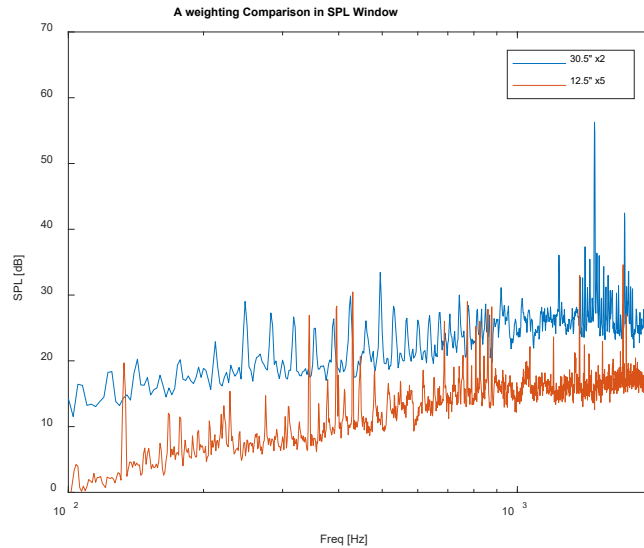


Figure 3. Comparing sets of data scaled to same size

Significance and Interpretation of Results

From the data taken, several conclusions can be made. The proximity of tones to 1000 Hz will greatly impact how the Overall Sound Pressure Level is perceived by listeners. The scale of rotor chosen in preliminary design will vary by the mission/thrust required for daily use of UAM (shift tones away from lower frequencies). The ability to scale data is made complex by the change in flow (laminar, turbulent, or transitional) over different diameter blades.

Acknowledgments and References

Thank you to the Aerospace Department at University of Cincinnati and the OSGC for funding this research. Thank you to Dr. Cuppoletti for the guidance on this work.

Geometric and Heat Transfer Optimization of Radiative Fins for Small Spacecraft Applications

Student Researcher: Natalie Douglass

Advisor: Dr. Rydge Mulford

The University of Dayton

Mechanical Engineering

Abstract

Radiative fin technology is used in a wide variety of applications and is particularly applicable to spacecraft. However, much of the previous optimization of radiative fins only analyzes the thickness profile of such fins. This work analyzes radiative fin thickness profile in tandem with the planar shape to achieve the most optimized radiative fin geometry. These results informed the investigation of a novel dynamic spacecraft radiator system. Currently, all satellites have passive radiators that reject heat at a constant rate to counteract heating by the Sun. However, once the satellite moves in orbit to the cold, shaded region of Earth, heaters are turned on to maintain proper operating temperature. An actuating dynamic radiator may prove useful to reducing the number of on-board survival heaters to maintain operating temperature. This work analyses and optimizes radiative fins for a particular actuation method for CubeSat applications.

Methodology

The geometric optimization of radiator panels involved the development of both Python and SolidWorks models. The numerical Python model was used to optimize fin planar and thickness geometries as a function of mass, fin tip temperature, and fin efficiency. Then, analysis was performed on fins with constrained volume but different planar geometries to assess fin tip temperature and fin efficiency. This was repeated for restrained length and varying volume. Next, a model was developed in SolidWorks of a CubeSat with radially actuating radiative fins (Fig. 1). Annular fins are chosen due to the heat coil actuation method for this novel system. Using SolidWorks computational thermal analysis feature, the model was used to assess fin efficiency and minimum fin tip temperature of three different thickness profiles: uniform, tapered, or step-thickness; and at four actuation angles: 0, 30, 60, and 90 degrees. The SolidWorks model serves as a validation of the results obtained in the Python model by metrics of tip temperature comparison, fin efficiency, and turndown ratio.

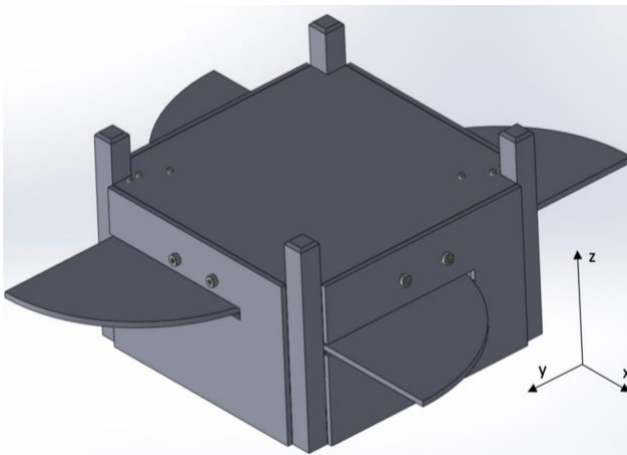


Figure 1: A model of the novel dynamic radiator system aboard a CubeSat with fully extended, uniform thickness fins

Significance and Interpretation of Results

Fin Optimization - It is found that a triangular thickness profile is most critical for heat rate maximization. A fin with a triangular thickness profile increases heat rate by 38.8% when compared to a fin with identical planar geometry and volume, but with a uniform thickness profile. Planar shape is also found to influence fin performance. A fin with a rectangular planar geometry has a 6.8% increase in heat transfer as compared to a fin with a triangular planar geometry and identical thickness profile and volume. Additionally, it is also found that triangular thickness profiles produce the maximally efficient fins. Following these results, a novel design for a dynamic spacecraft radiator with annular geometry and varied thickness profiles is presented. It is found that turndown ratios of 3.33 are capable with the novel system. Furthermore, it was found that fins with tapered thickness profile have the highest efficiency and turndown ratio. Finally, it was shown that turndown ratio and fin efficiency decrease as operating temperature increases.

CubeSat Modeling - Figure 2 shows a comparison of the minimum temperature SolidWorks and Python results for uniform, tapered, and step thickness fins with a matching constant temperature boundary condition. On average, the temperature values differed by 1.57% from the Python model to the SolidWorks model. The step thickness fin was closest to the SolidWorks results (0.67% difference) while the tapered thickness fin was the most inaccurate (2.68% difference). The net heat rate of each fin was also compared between the SolidWorks model and the Python model. The average difference between models was 6.97% with the step thickness fin being most accurate (2.01% difference) and tapered fin being least accurate (12.71% difference). Across all comparisons of the results, the Python model differed from the SolidWorks model by an average of 2.94%. The difference may arise in the simplified geometry of the CubeSat in the Python model as compared to the SolidWorks model. The Python model assumed the satellite to be an isothermal box whereas, the SolidWorks model considered conduction and radiative losses from the fully featured, exposed spacecraft surfaces shown in Figure 1. As such, an error of approximately 3% was assumed between models and is sufficient for this study.

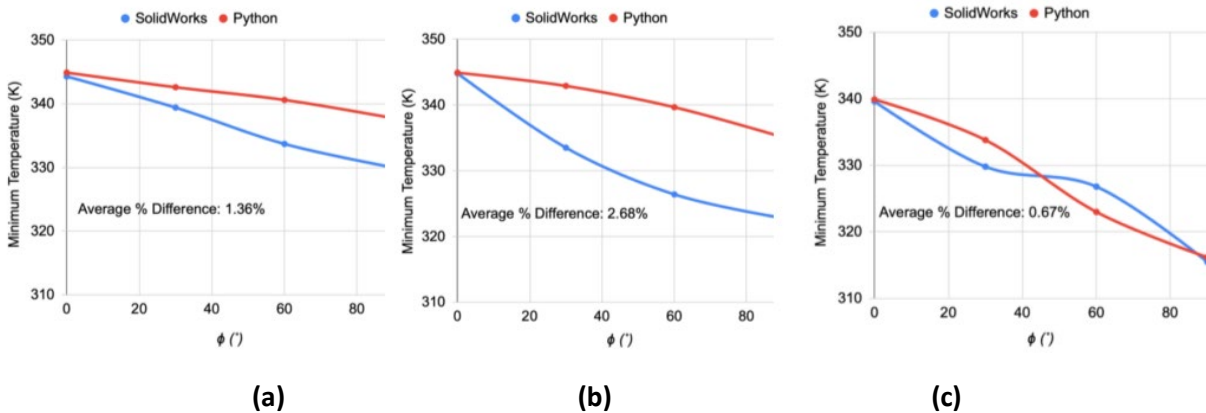


Figure 2: Comparison of SolidWorks and Python results for minimum fin temperature with a constant temperature boundary condition for (a): uniform thickness fin, (b): tapered fin, (c): step-thickness fin

Conclusion

This work aimed to address optimization of both planar geometry and thickness profile of radiative fins, a topic missing from thermal control literature. The results of this work can serve as a guide for further development of the studied design, as well as to inform other novel dynamic spacecraft radiator designs. This study's results show several trends which apply to both the novel design presented, as well as to dynamic radiators in general. First, it is shown that tapered fins achieve best fin efficiency, best turndown ratio, and highest heat rate as compared to other designs with identical base temperatures. Furthermore, if an isothermal fin is desired, tapered fins have the lowest change in temperature for all actuation angles. Despite this, tapered fins may not be the optimal choice due to difficulty in manufacturing². Thus, a uniform thickness fin may be considered as the better option, as it has proven to have similar turndown ratio and fin efficiency.

The novel design of an actuated radiative fin can be advantageous to spacecraft applications for several reasons. First, the fins in this design do not irradiate one another and multiple fins act as a means for redundancy. Also, the proposed actuation is passive, which is advantageous to small spacecraft application where space for other electronics is essential. Finally, it is beneficial that any portion of the fin inside the spacecraft still absorbs heat radiatively, thus increasing fin performance.

References

- [1] Zirbel, S. A., Lang, R. J., Thomson, M. W., Sigel, D. A., Walkemeyer, P. E., Trease, B. P., Magleby, S.P., and Howell, L. L., 2013, "Accommodating thickness in origami-based deployable arrays," *Journal of Mechanical Design*, Vol. 135, pp. 111005.
- [2] Arslanturk, Cihat. "Performance Analysis and Optimization of Radiating Fins with a Step Change in Thickness and Variable Thermal Conductivity by Homotopy Perturbation Method." *Heat and Mass Transfer*, vol. 47, no. 2, 2010, pp. 131–138.

Report on Artificial Neural Network (ANN) for Modeling Policy Effects on COVID-19 Infection Rates

Student Researcher: Kevin Du

Advisor: Professor Lei Zhu

Case Western Reserve University

Applied Mathematics

Objective

The purpose of this project was to create an ANN that considered COVID-19 policy in predicting infection rates. Secondary goals of the project include being able to use the ANN as a tool to predict the effect of hypothetical policies on infection rates and better understanding the benefits and limitations of ANNs. The result of the project was the successful completion of the primary goal; the researcher was able to create an ANN that incorporated COVID policy information that is more accurate than a comparable ANN from a referenced paper. However, the researcher is not confident in the utilization of the model to predict the effect of hypothetical policies, as the ANN is not trained to predict the effects of hypothetical policies and is overall unreliable for extrapolation. The biggest critique of ANNs the researcher discovered was the lack of usefulness of the ANN in any application other than the one it was trained on; the ANN takes very little understanding of the data to create, and it provides little understanding of the data after training.

Introduction

There are two big sections to the project: the first section is the infection rate and policy datasets used to train the ANN, and the second is the ANN itself. The infection dataset used is the public Johns Hopkins University Infection Rate Dataset. This dataset was chosen due to its reliability and the number of research papers that cited it. A paper related to the ANN structure used the JHU dataset, so it also had the benefit of being easy to integrate into the ANN for this project.

The policy dataset used is called “Statistically Validated Indices for COVID-19 Public Health Policies”, which is a numerical synthesis of the CoronaNet COVID-19 Government Response Event Dataset and the Oxford COVID-19 Government Response Tracker. This resource was chosen because it is a mathematically grounded numerical representation of policy severity, and the researcher was already familiar with the data from CoronaNet from previous experience. Artificial neural networks (ANNs) are a type of machine learning and more specifically a type of neural network. ANNs were chosen for this project due to their establishment in the intended use of infection rate prediction and their ease of application for numerical data.

Methodology

The researcher selected Python due to its Tensorflow neural network package for the execution of this project for its robust documentation. All code related to this project was coded in Jupyter notebooks and is publicly available on Github. The structure for the ANN was based on the ANN from a paper called “Neural network powered COVID-19 spread forecasting model.” Wiczorek, et al. in accordance with standard procedure. The paper’s network was also reconstructed as a baseline for comparison to the ANN integrating the policy information.

After changes to the ANN structure, the researcher preprocessed the infection rate and policy data; this included normalization of the data, grouping by time steps, vectorization, and separation of the data into training and test sets. Finally, after bug fixing the code, the researcher went through cycles of analysis and hyperparameter tuning to improve the ANN structure; that is to say, trial and error until the network produced reliable and satisfactory results.

Results

The researcher was able to create an ANN that was overall more accurate than the baseline ANN from the referenced paper; representative training cycles produced test losses of 3.1 E-5 and 5.2 E-5, from the created ANN and reference ANN, respectively.

Conclusion

The primary goal of this project, to create an ANN that takes policy information into account to predict infection rates, was achieved. The results support that the created ANN produced more accurate results than the referenced paper's comparable ANN. One secondary goal of this project, to make the ANN useful in predicting hypothetical policy effects on infection rates, was not completely achieved; testing of the ANN suggested unreliability in its use for extrapolation. Since the ANN does not understand context, it does not differentiate between correlation and causation; if used to extrapolate the effects of policies, the result could easily be due to an overvalued correlation rather than causation. The secondary goal, to learn more about the benefits and drawbacks of ANN, was achieved as follows; the primary benefit and drawback of an ANN is the lack of context required to train one. The training process required almost no understanding of the input data or the expected results to produce satisfactory results. However, this lack of deeper understanding makes the ANN very poor at extrapolation, especially in manners that it isn't explicitly trained on.

Sources

- Dong E, Du H, Gardner L. An interactive web-based dashboard to track COVID-19 in real time. *Lancet Inf Dis.* 20(5):533-534. doi: 10.1016/S1473-3099(20)30120-1
- Kubinec, R., Barceló, J., Goldszmidt, R., Grujic, V., Model, T., Schenk, C., ... Thorvaldsdottir, S. (2021, May 1). "Cross-National Measures of the Intensity of COVID-19 Public Health Policies". <https://doi.org/10.31235/osf.io/rn9xk>
- Michał Wieczorek, Jakub Siłka, Marcin Woźniak. "Neural network powered COVID-19 spread forecasting model." *Chaos, Solitons & Fractals*, Volume 140, 2020, 110203, ISSN 0960-0779. <https://doi.org/10.1016/j.chaos.2020.110203>.
- Syrowatka, et. al. 'Leveraging artificial intelligence for pandemic preparedness and response: a scoping review to identify key use cases.' *Nature*. (2021) <https://doi.org/10.1038/s41746-021-00459-8>

All code available at <https://github.com/mountain07/COVID-19>

Design and Testing of a Heated Plasma Flow Reactor for Plasma Assisted Combustion Studies

Student Researcher: Trevor A. Dundore

Advisor: Dr. Igor Adamovich

The Ohio State University

Department of Mechanical and Aerospace Engineering

Abstract

A supersonic flow wind tunnel is coupled with a heated plasma flow reactor to study chemical reactions that occur during combustion of hydrocarbon fuels, at extreme “fuel-lean” conditions. In the reactor, which serves as the wind tunnel plenum, the fuel-oxidizer flow is diluted in argon is heated by passing through a thermal energy storage system (a container filled with ceramic beads and placed in a tube furnace), and then expanded through a converging-diverging nozzle into a supersonic test section. Between the thermal storage and the nozzle, there is an electric discharge section, to generate reactive radicals not present in the fuel-oxidizer reactant mixture. The heated and reacting flow excited in the plasma is expanded through the nozzle into the supersonic test section. This wind tunnel / heated flow reactor will be used by graduate research assistants, to measure the reaction products in the supersonic test section using laser diagnostics.

Project Objectives

There is limited knowledge on the kinetics of radicals and the intermediate species formed during the combustion of hydrocarbon fuels at extreme “fuel-lean” conditions. Therefore, the aim of this project is to develop a deeper understanding of these phenomena, using a new experimental facility where these species are generated in the flow by an electric discharge plasma, and measured spectroscopically after a supersonic expansion. This facility will be used in several research projects at the Nonequilibrium Thermodynamics Laboratories (NETL). The potential outcomes of these projects include the improved jet engine performance, improved supersonic combustor performance, and the development of safe and efficient plasma assisted combustion methods. The main objective of this project is the design, development, and testing of the new facility, a heated plasma flow reactor combined with a supersonic test section for in situ spectroscopic diagnostics.

Methodology

At the Nonequilibrium Thermodynamics Laboratories, there have been previous projects where nonequilibrium plasmas were combined with supersonic expansion flows, to study energy transfer and chemical reactions in the flow. As an illustration, Fig. 1 shows a photograph of a nonequilibrium flow plasma wind tunnel, used previously for the laser diagnostic measurements of excited species generated in the plasma [1]. Fig. 2 [1] shows a schematic of the plasma wind tunnel and the laser diagnostic used in this project. This work served as a starting point for the present heated flow reactor. The key difference between the previous work and the present heated flow reactor is the heat addition to the flow using a thermal storage system. The analysis of energy storage, heat transfer to the flow, and variation of the flow parameters in a supersonic expansion was used to assess the feasibility of the heated reactor. The design of the reactor, shown schematically in Fig. 3, is based on the results of this analysis. Figure 4 shows a photograph of the overall view of the actual reactor. The flow through the reactor is argon gas mixed with a small fraction of oxygen, 1-2%, delivered from high-pressure cylinders via a 1-inch diameter supply line, at a pressure of $P = 0.5\text{-}1.0$ atm. Argon is utilized as a neutral buffer, to prevent a significant temperature rise in the flow during the reaction with the fuel, which would result in ignition.

A small amount of hydrocarbon fuel, 0.1-0.2%, is added to the supply line in a tee connector (see Fig. 3). The fuel is mixed with the argon/oxygen flow in an in-line static mixer, placed downstream of the injection point. The mixture then enters a thermal storage unit, which is manufactured from a 3-inch diameter stainless steel tube 38.5 inches long, filled with ~30,000 alumina ceramic beads 1/5 inch in diameter and placed into a tube furnace (ThermCraft) heated to $T = 600-900$ K (see Fig. 3). The heat transfer analysis showed that this thermal storage system is sufficient to heat the flow close to the furnace temperature, at the flow rate of up to 10-20 g/s. Once heated, the flow enters the electric discharge section, shown schematically in Fig. 3. The purpose of the plasma sustained in the electric discharge section is to generate highly reactive radicals, mainly O atoms, out of relatively non-reactive O_2 molecules in the mixture. This will be done in a high peak voltage (25-30 kV), nanosecond pulse duration (5-10 ns), high pulse repetition rate (up to 100 kHz) discharge. This approach produces a volume-filling diffuse plasma, as has been shown in previous work at NETL [1]. The production of these radicals initiates chemical reactions with the fuel, such as occur in conventional combustion.

Some of the species taking part in these reactions, such as (CH_4 , C_2H_4), reaction intermediates (HO_2 , CH_2O , CH_3O_2 , $C_2H_5O_2$), and reaction products (CO , CO_2 , and H_2O) can be measured in the flow using laser diagnostics, such as absorption spectroscopy. For these measurements, it is critical to expand the flow to low temperatures and pressures. The expansion effectively “freezes” the chemical reactions and greatly simplifies the identification of different species, since the spectral lines become narrow and do not overlap. The expansion has to be rapid, such that the target species would not have time to decay. In the present work, the expansion occurs in a converging-diverging nozzle, designed for $M=4$, followed by a straight diagnostic section and a supersonic diffuser, shown in Fig. 5. The flow heated in the thermal storage unit and excited in the plasma passes through the nozzle, test section, and diffuser, before exhausting into 750 ft³ vacuum tank evacuated by a 300 cfm vacuum pump (United Vacuum). The design calculations predict that the steady-state run time of the facility is approximately 10 seconds. This is consistent with the previous results obtained using an unheated nonequilibrium flow supersonic wind tunnel [1]. After the entire system, including thermal storage, electric discharge, and nozzle / diffuser is tested, the diagnostic section will be equipped with arms with optical access windows or high-reflectivity mirrors for laser diagnostics. This work is outside of the scope of this project and will be done by a graduate research assistant.

Results

Following the thermal storage unit / heat transfer / supersonic flow design calculations, the entire flow channel, including the flow delivery lines, in-line mixer, tube furnace, thermal storage unit, electric discharge section, supersonic nozzle, diagnostic section, and supersonic diffuser has been assembled. The overall view of the experimental facility is shown in Fig. 4. The flow channel is equipped with 3 pressure ports and pressure gauges for the measurements of the plenum pressure and static pressures at two different locations in the supersonic test section. The pressure gauges are connected to digital readouts to monitor the pressures during the run. The flow channel is also equipped with a thermocouple for the plenum temperature measurements. The leak tests of the flow channel have been completed. The supersonic flow tests, with and without flow preheating in the thermal storage unit, are currently underway.

Summary

A supersonic flow wind tunnel is coupled with a heated plasma flow reactor to study chemical reactions that occur during combustion of hydrocarbon fuels, at extreme “fuel-lean” conditions. In the reactor, which serves as the wind tunnel plenum, the fuel-oxidizer flow is diluted in argon is heated by passing through a thermal energy storage system (a container filled with ceramic beads and placed in a tube

furnace), and then expanded through a converging-diverging nozzle into a supersonic test section. Between the thermal storage and the nozzle, there is an electric discharge section, to generate reactive radicals not present in the fuel-oxidizer reactant mixture. The heated and reacting flow excited in the plasma is expanded through the nozzle into the supersonic test section. The rapid supersonic expansion “freezes” the chemical reactions in the flow, such that the reaction products can be analyzed spectroscopically. This wind tunnel / heated flow reactor will be used by graduate research assistants, to measure the reaction products in the test section using laser diagnostics.

References

1. E.R. Jans, I. Gulko, D.C.M. van den Bekerom, T.A. Miller, and I.V. Adamovich, “Measurements of Metastable $N_2(A^3\Sigma_u^+, v)$ Molecules in Nonequilibrium Supersonic Flows”, *Journal of Thermophysics and Heat Transfer*, vol. 36, 2022, p.196



Figure 1. Unheated nonequilibrium flow supersonic wind tunnel (Mach 5) used for laser diagnostic measurements of excited species generated in the plasma sustained in the plenum or in the throat [1].

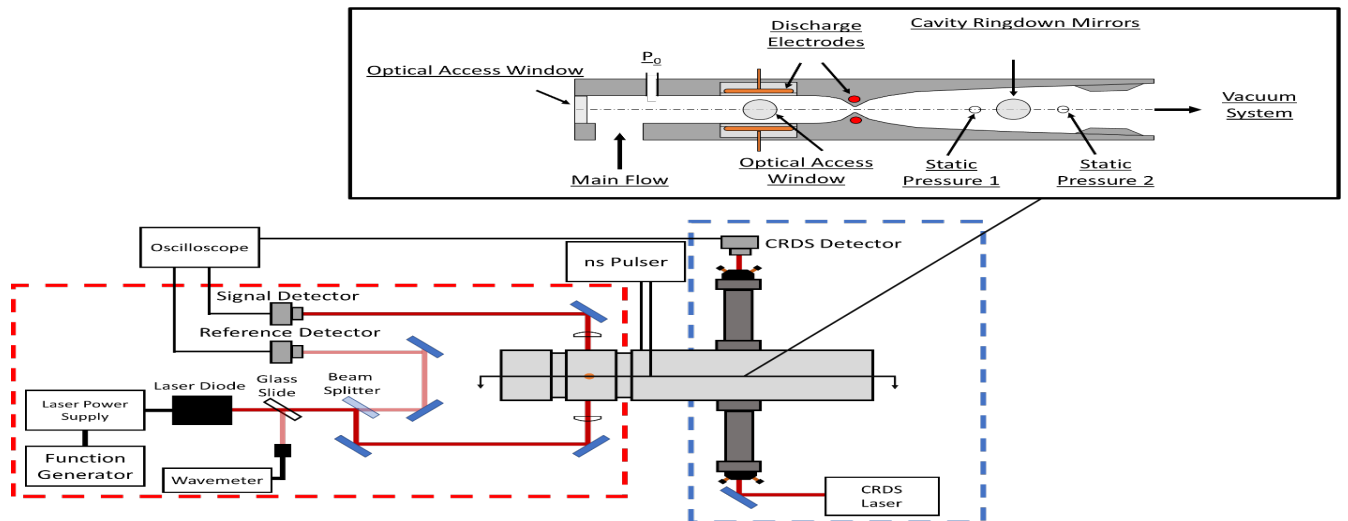


Figure 2. Schematic diagram of Cavity Ring Down Spectroscopy diagnostic used in the plasma wind tunnel shown in Fig. 1 [1].

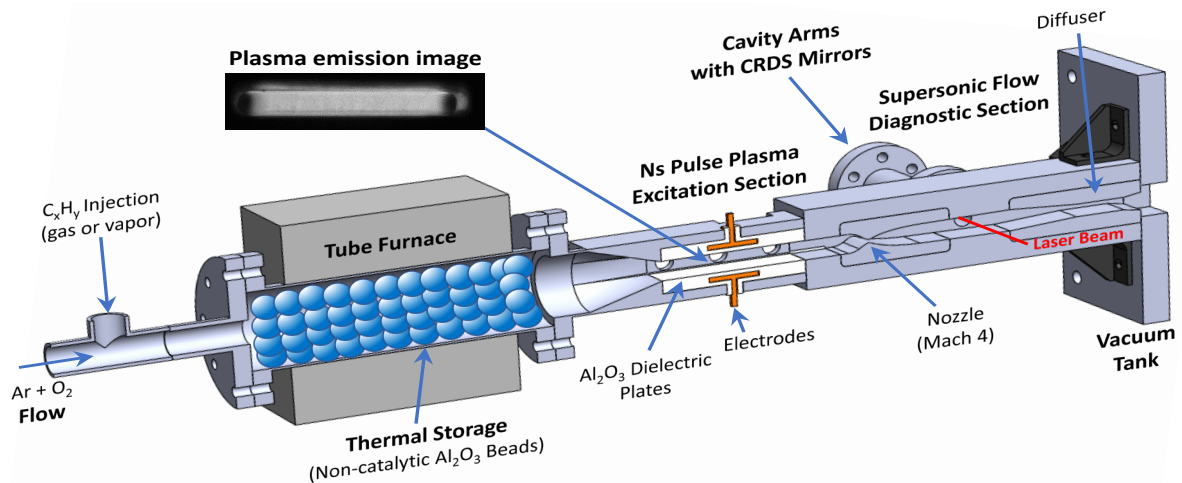


Figure 3. Schematic diagram of the heated plasma flow reactor developed in the present work.



Figure 4. Overall view of the heated plasma flow reactor (Mach 4) developed in the present work.



Figure 5. Mach 4 nozzle, supersonic flow diagnostic section, and supersonic diffuser. Flow direction is left to right.

Characterization of Skin-Like Elastomers for Improving Accuracy of Radial Pulse Pressure Measurements

Student Researcher: Miranda Eaton

Advisor: Dr. Jeong-Hoi Koo

Miami University

Department of Mechanical and Manufacturing Engineering

Abstract

Blood pressure (BP) is a major indicator of multiple health risks. Hypertension, or high blood pressure, can damage the heart, kidney, and many other organs. Thus, accurate measurements of blood pressure and its continuous monitoring are extremely important for personal health care. In general, invasive BP measuring is desirable for continuous and accurate readings. However, invasive BP measuring is not practical for everyday use due the inability of easily and continuously monitoring BP. Thus, noninvasive BP measuring is desired for everyday use. Yet, the accuracy of noninvasive BP measurements is low due to the effect of skin. The location of the skin between the artery and the BP measuring device affects the sensor measurement, meaning the BP on the outside of the skin is different than the BP in the artery. This research looked at investigating the effect age-dependent skin has on BP measurements.

Project Objectives

The primary goal of this project is to study the effect of age-varying skin on radial pulse measurements.

More specific objectives of this project are to:

- Fabricate silicone skin samples which represent a wide range of human skin properties
- Experimentally characterize skin samples using a dynamic mechanical analyzer (DMA)

Methodology

Various skin samples were created by using a silicon base resin called Ecoflex. Furthermore, magneto-rheological elastomers (MREs) were added to a handful of samples. Properties of each sample were varied by changing the base resin of the sample (such as Ecoflex30 or Ecoflex50), amount of MRE within the sample (based on weight percent), thickness of the sample (1 to 3 layers), and the applied magnetic field (0mT-110mT). Applying a magnetic field to the samples containing MREs would alter the properties of the sample. Thus, four variables were investigated in this research. Once samples were created, they were placed under a dynamic mechanical analyzer (DMA) to conduct indentation testing. Data was collected from the DMA to determine the modulus of elasticity (E) and hysteresis loop (area within loop, A) for multiple samples under various conditions and parameters. The mechanical properties were then compared against each other to determine the effect of each parameter.

Significant Results Obtained

Figure 1a shows the effect of sample thickness on modulus of elasticity (E) and hysteresis loop (area within loop, A)

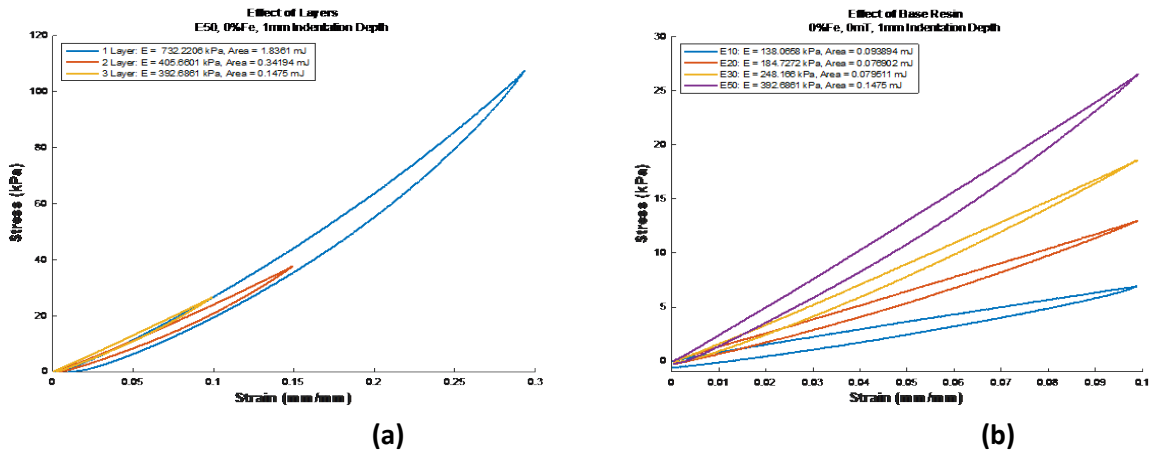


Figure 1. Effect of sample thickness (a), effect of base resin (b)

Sample thickness increased from 1 to 3 layers, with each layer approximately 3mm. Testing showed that an increase in sample thickness decreases modulus of elasticity and the hysteresis loop or damping. Figure 1b shows the effect of base resin, increasing from Ecoflex10 to Ecoflex50. Data showed that an increase in base resin leads to an increase in both modulus of elasticity and hysteresis loop (except for E10). The increase in modulus of elasticity was expected as a stiffer material would exhibit a higher E. However, an increase in hysteresis loop was unexpected because younger skin did not exhibit this property. Younger skin resulted in a decrease in the area of the loop, not an increase. This means that based on our testing, the stiffer the skin sample, the more energy is dissipated. In other words, the sample does not bounce back as one would expect.

Figure 2a shows the effect of adding iron or MREs to each sample (based on weight percent). Experimental data has consistently shown that an increase in iron content leads to an increase in modulus of elasticity and area of hysteresis. This is the same unexpected phenomenon that is experienced with an increase in base resin. Figure 2b is a graph indicating the effect of applied magnetic field on the sample. The overall trend is that an increase in magnetic field will lead to an increase in E and A. However, other data has shown some discrepancies with the claim. Sometimes an increase in magnetic field would lead to a decrease in E and A. Therefore, more testing will be conducted to truly understand the effect of a magnetic field.

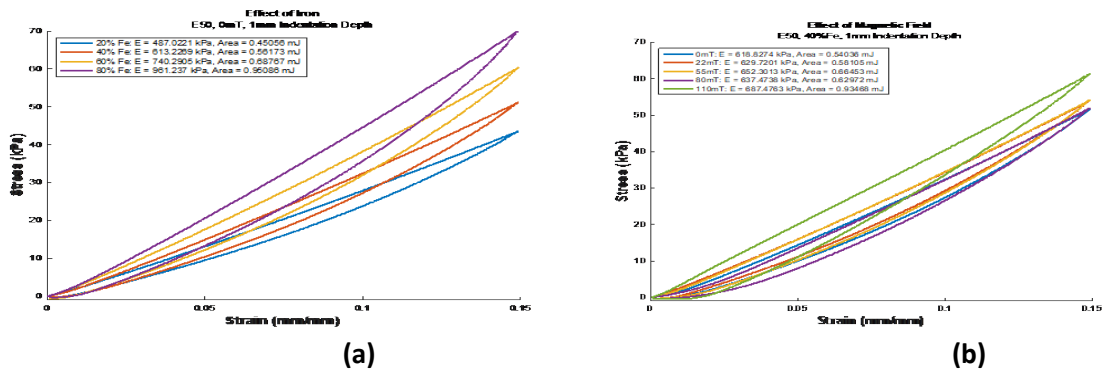


Figure 2. Effect of iron (a), effect of magnetic field (b)

Conclusion and Future Work

This semester we were able to determine the effect each variable has on skin properties. In summary, we found that, overall, increasing the base resin, iron content, and magnetic field all result in an increase in stiffness and hysteresis loop. As mentioned before, an increase in both E and A was not expected as a stiffer material would intuitively result in a smaller hysteresis loop, but that was not the case with these results. Therefore, further skin samples will be created and tested to explain the results. We determined that we will be able to represent age dependent properties by changing the base resin of the sample, the iron content, or the applied magnetic field. Moving forward, additional testing and fabrication will lead us to the creation of an artificial skin sample that will better replicate the properties of real human skin. We hope that our work here will help wearable non-invasive blood pressure measuring devices become more accurate.

Waste to Energy: Catalytic Gasification of Household Recyclables

Student Researcher: Rebecca Ellis

Advisor: Dr. Jorge E. Gatica

Cleveland State University
Chemical Engineering Department

Abstract

Waste buildup is quickly becoming a serious global problem, one that negatively impacts quality of life and damages ecosystems. While a variety of methods of reducing waste exist, their environmental impact is rapidly becoming an issue. Thus, developing a waste management method that does not further harm the environment is a necessary next step in pollution control and sustainability. Via the process of gasification, recyclable plastics can be converted into syngas (gasified), which in turn can be converted into fuel. The low-temperature catalytic gasification of Polyethylene Terephthalate (PET) is the focus of this project. Research was centered on comparison of thermal properties of PET recovered from household recyclables and laboratory-grade PET. Thermal analysis completed in a research-grade Differential Scanning Calorimeter (DSC) yielded heat of formation values of 24.99 J/g and 27.33 J/g for pure PET and household-recovered PET, respectively. Mixing patterns of a multi-phase reacting media in a laboratory-scale stirred tank reactor were predicted using a finite-element method (FEM) based computational fluid dynamics (CFD) platform. The results suggested satisfactory mixing within the reactor and flow patterns were recovered to study simultaneous mass transport and reaction phenomena in a particulate (catalyst and polymeric particles in a fluid media) system.

Project Objectives

The scope of this project began with waste produced by astronauts while in space. However, since its conception, the project has grown to examine waste on a global scale. Plastic waste makes up 12% of the total waste produced. The most common plastics found in waste are Polyethylene, PET, Cellulose, and Nylon. Of the many types of plastic waste produced, Polyethylene Terephthalate (PET) is the material of focus for this project. Via the process of catalytic gasification, PET can be converted into a gaseous form at a low temperature. This process is outlined by a series of reactions that reduce waste byproducts and result in methane which is a type of fuel. Thus, the plastic waste is reduced to a gas via a process with minimal harmful emissions and then repurposed into a usable fuel.

Methodology

All experiments were performed with a Differential Scanning Calorimeter and recorded with the associated software. Disposable aluminum dishes were used to hold the samples. The machine operated under a user – defined program listed as such: Equilibrate at 45°C, Isothermal for 0.50 min, Ramp 8°C/min to 270°C, Isothermal for 0.5 min, Ramp 8°C/min to 45°C, Isothermal for 0.50 min.

Results and Discussion

Thermal analysis completed in a research-grade Differential Scanning Calorimeter (DSC) yielded heat of formation values of 24.99 J/g and 27.33 J/g for pure PET and household-recovered PET, respectively. The relatively small differences between house - hold recovered PET and lab - grade PET tells that there are few impurities in the recovered sample, thus making the recyclable plastic a good contender for the objective of this project. Though it is important to note that only clear house - hold recovered samples of PET are being tested as dyed plastic samples have not yet been evaluated.

For the next portion of the project, modeling the reactor was done digitally in COMSOL. Following the digital rendering of the reactor was a study of the velocity profile. For this portion of the simulation, a controlled study was pieced together to map the magnitudes and vectors of the field inside the reactor which can be seen in Figure 1 and Figure 2. Areas of lighter color are indicative of increased motion. As such, the hues of yellow and red surrounding the impeller blades are to be expected.

Figures

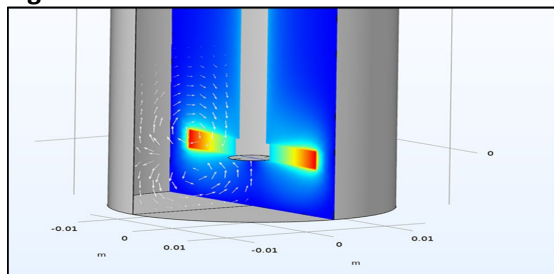


Figure 1 - Study of Velocity Field within Reactor

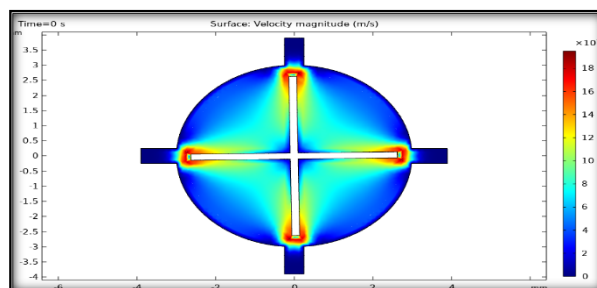


Figure 2 – Top View of Velocity Field within Reactor

Acknowledgments

The author would like to thank the Ohio Space Grant Consortium, and the Cleveland State University Washkewicz College of Engineering. The author would also like to thank Dr. Jorge E. Gatica for support and supervision on the project.

References

1. Atassi, L. "From waste to watts: Cleveland's controversial pursuit of trash conversion technology," The Plain Dealer (June 17, 2012).
2. Jarboe-McFee, M. "With waste-to-energy project, Forest City and Quasar Energy Group chart renewable course," The Plain Dealer (July 07, 2012).
3. Reyes, K.M., N. Plentovich, M.J. Lang, and J.E. Gatica "Catalytic Gasification of Polyethylene As an in-Situ Resource Utilization (ISRU) Alternative," 2020 National AIChE Annual Meeting, November 16-20 (2020).
4. Lang, M.J. and J.E. Gatica "Catalytic Gasification – a Critical Analysis of the Water-Gas-Shift Reaction on Ru and Pt-based Catalysts," International Journal of Chemical Reactor Engineering, submitted (2022).
5. Lange, E.M., B. DeMattia, and J.E. Gatica "Catalytic Gasification – A Critical Analysis of Carbon Dioxide Methanation on a Ru/Al₂O₃ Catalyst," International Journal of Chemical Reactor Engineering, 16 (7), pp. 20180008 (2018).
6. Santiago-Maldonado, E., J. Captain, R. Devor, and J. Gleaton, "Creating Methane from Plastic: Recycling at a Lunar Outpost," AIAA 2010-1551, 48th AIAA Aerospace Sciences Meeting, Orlando, FL (January 2010).
7. American Polymer Standards Corporation, 17 December 2018. www.ampolymer.com/SDS/PolyethyleneTerephthalateSDS.html. 1 March 2022.

The Martian Moons eXploration (MMX) Mission: Investigating the Composition of Phobos using Neutrons

Student Researcher: Emily Etheridge

Advisor(s): Dr. Andrew W. Beck

Marietta College
Planetary Science

Abstract

In this project, neutron behavior was examined to find the predicted composition of the martian moon Phobos if it is of a Mars-like composition. We must first simulate fast neutron flux and thermal neutron absorption in both compositional types in order to interpret MEGANE data and test the two hypotheses, being asteroid capture and giant impact. This project has constructed the compositional dataset, which will then be utilized to simulate neutron flux.

Methodology

The methods used to construct a bulk geochemical data set were taken and altered to fit this project from the work Dr. Andrew Beck completed in Beck et al. 2015. This study was centered on the asteroid 4 Vesta and were altered to study Phobos and Deimos. We used this to determine thermal neutron absorption that would result from this through calculations in Prettyman et al. as well as high-energy gamma rays using Peplowski and Lawrence et al. Further work at Johns Hopkins University APL will consist of simulating fast neutron counts using the Monte Carlo N-Particle Transport Code (MCNPX). MCNPX will use the data set that we have created to simulate fast neutron production on the surface of an airless planetary body (such as Phobos) with a given radii through the bombardment of high-energy gamma rays. The simulations will take multiple days to complete once started and will reveal a fast neutron flux count. This count can be used alongside the neutron absorption and high-energy gamma rays to predict and constrain the surface compositions of Phobos and Deimos.

In order to complete the necessary work this year to prepare for the simulations that will be conducted summer 2022, we will started by identifying elements on the surface of Phobos and Deimos that are critical to neutron absorption. To determine this, an analysis of elemental concentrations across Martian meteorites and volatile-rich carbonaceous chondrites to determine which elements are primary contributors to thermal neutron absorption was conducted. The atomic thermal neutron absorption cross section of the element (Prettyman et al) and its concentration in rock petrology determines the contribution to thermal neutron absorption. The elements determined to contribute to this will then be ranked on the basis of their contribution, ordered from high contribution to low contribution. This makes it necessary for multiple bulk chemistries of the same meteorite to be ordered and averaged into a single, representative chemistry for the specified meteorite.

Interpretation of Results

The final step in the research that was conducted this summer was to calculate thermal neutron absorption and high-energy gamma ray flux with methods in Prettyman et al. 2013 and Peplowski and Lawrence 2013 based on the chemistries collected from the literature that have been averaged and ranked. We will then examined the results, analyzing trends between meteorite petrology and these neutron parameters. The completed data set will then be used to simulate fast neutron flux in the summer of 2022, as previously outlined.

We found that the shergottite group, consisting of 22 of the 28 examined meteorites, fell in the middle of the pack when graphing the thermal neutron absorption and the iron abundance against the average atomic mass. The chassignite group, only having two, seemed to fall higher than the shergottites. The nakhlite group was the lowest of the three groups.

Flexural Properties of Carbon Fiber Reinforced Onyx

Student Researcher: Gregory Fetter

Advisor: Dr. Muhammad Jahan

Miami University

Department of Mechanical and Manufacturing Engineering

Abstract

Polymer reinforced composite materials are known for their strength and low cost, but with new materials being implemented, it is still a field that requires further research to understand the material properties. One such polymer reinforced composite is carbon fiber reinforced onyx, which has comparable strength to aluminum and carbon fiber has one of the best strength-to-weight ratios compared to other reinforcing materials. This material can benefit multiple industries because it is possible to 3D print at a significantly decreased amount of time and cost compared to ordering new custom aluminum parts or 3D printing aluminum parts. With companies like Markforged supplying 3D printers that use Continuous Fiber Reinforcement (CFR), which have the capability to reinforce materials like onyx with other materials such as kevlar and fiberglass, it is important to understand what changing the different variables of how these materials are printed effect their mechanical properties.

Project Objectives

Markforged uses Eiger software to allow users to change different variables of the part that is being printed. Each of these variables can be changed using a range of options displayed in the software, which present the question of what happens to the mechanical properties when these variables are changed. Markforged has done their own studies on the flexural properties of carbon fiber reinforced onyx, but these studies do not specify the variables used. Using the Markforged Mark Two 3D printer and the accompanying Eiger software, this study examines how the changes in the infill pattern, fill density, and fiber angles effect the flexural properties of carbon fiber reinforced onyx, and how it compares to the results of the Markforged study. The design of experiment (DOE) created with respect to the range of parameters presented by the Eiger software and its recommendations, called for each of the three variables to be changed three times. The three infill patterns used were triangular, hexagonal, and rectangular, the fill densities used were 29%, 42%, and 55%, and the fiber angles used were (0°, 90°), (0°, 45°, 90°, 135°), and (45°, 135°). Completing this study requires at least 27 test specimens, but in compliance with ASTM D 790 Standard Test Methods for Flexural Properties of Unreinforced and Reinforced Plastics, the standard used by Markforged, and ASTM D 7264 Standard Test Method for Flexural Properties of Polymer Matrix Composite Materials, stated that five specimens must be used for each test condition. So, 135 test specimens must be printed to be compliant with the ASTM standards. Once these parts are tested, there will be more insight into the strength, stiffness, and load/deflection behavior of carbon fiber reinforced onyx and companies will be able to confidently print a part, and know its flexural properties.

Results Expected

One third of the specimens that will be tested are set to the Eiger-recommended properties, so they should have equivalent results to the Markforged study. Given the properties of carbon fiber, it will significantly increase the flexural properties when reinforcing onyx, as shown in Figure 1 and 2. With

regards to the infill pattern, the triangular pattern is the strongest, the rectangular pattern can achieve 100% density, and the hexagonal pattern has the highest strength-to-weight ratio. The fill density of the specimen does not have a significant impact on flexural properties, but it does have a slight effect on the print time and the mass of the part, with 29% having the lowest print time and mass, and 55% having the highest print time and mass. When the fiber angles are (0°, 90°) and (45°, 135°), the results of the testing should be the same, but it can be expected that when the fiber angles are (0°, 45°, 90°, 135°) the specimen will be able to better handle forces in different directions. Considering these facts, it can be hypothesized that if a high strength-to-weight ratio is desired, then a hexagonal infill structure, 29% fill density, and (0°, 45°, 90°, 135°) fiber angles are the optimal settings. It can also be hypothesized that if a high strength is desired, then a triangular infill pattern, 55% fill density, and (0°, 45°, 90°, 135°) fiber angles are the optimal settings.

Future Work

Using the ASTM D 7264 as stated, four test specimens have been printed with a span-to-thickness 38:1, which is same as the Markforged study, with a conditioning process of unconditioned and an unknown moisture content. These specimens, along with the 131 other specimens that have yet to be printed, will be subjected to a three-point bending test that will provide data similar to the data collected by Markforged and shown in Figure 1 and Figure 2. The data then needs to be analyzed to examine the specific print variables required for different industry needs. Once these are completed, further tests can be conducted such as compression, fatigue, and tension tests which will also require a certain number of specimens for it to be ASTM compliant. These tests will provide a full picture of the material properties of carbon fiber reinforced onyx.

Figures and Charts

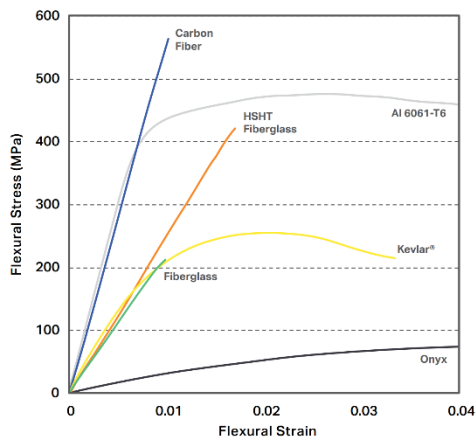


Figure 1. (left) Markforged data on the flexural stress vs the flexural strain of the polymer reinforced composites available.

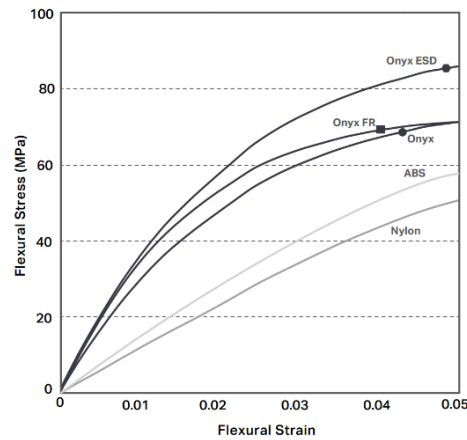


Figure 2. (right) Markforged data on the flexural stress vs flexural strain of composites available.

References

1. Liu, Wenfeng, et al. "Maximizing Mechanical Properties and Minimizing Support Material of PolyJet Fabricated 3D Lattice Structures." *Additive Manufacturing*, 2020, <https://doi.org/10.1016/j.addma.2020.101257>.
2. "MATERIAL DATASHEET Composites - Markforged." Markforged.com, 1 Aug. 2021, <http://static.markforged.com/downloads/composites-data-sheet.pdf>.
3. Mishra, Pradeep Kumar, et al. "An Investigation to Study the Combined Effect of Different Infill Pattern and Infill Density on the Impact Strength of 3D Printed Polylactic Acid Parts." *Composites Communications*, vol. 24, 2021, <https://doi.org/10.1016/j.coco.2020.100605>.
4. Wang, Kui, et al. "Effects of Infill Characteristics and Strain Rate on the Deformation and Failure Properties of Additively Manufactured Polyamide-Based Composite Structures." *Results in Physics*, vol. 18, 2020, <https://doi.org/10.1016/j.rinp.2020.103346>.

Detonation Quenching and Re-initiation Behind an Obstacle Using a Global 4-Step Combustion Model

Student Researcher: Grace Floring

Advisor: Dr. Brian Maxwell

Case Western Reserve University
Mechanical and Aerospace Engineering

Abstract

The ability to predict the deflagration-to-detonation transition (DDT) can have impacts on mitigating industrial explosions, many of which involve hydrocarbon fuel vapors. Detonation attenuation and re-initiation following its interaction with obstacles exhibits the same features seen in the final stages of DDT, and can be studied to elucidate the key mechanisms involved in the process. While past experiments have at least provided a qualitative insight into the process, numerical simulation is required to gain quantitative insight. However, there is also a need to develop a numerical strategy that finds balance between accuracy and computational efficiency. In this study, a 4-species, 4-step combustion model is coupled to an adaptive mesh refinement (AMR)-enabled compressible flow Euler simulation framework to simulate detonation attenuation and subsequent re-initiation following interaction with a half-cylinder obstacle in stoichiometric methane-oxygen mixtures. This investigation focuses on capturing different regimes of detonation behavior. Six distinct categories of outcomes were identified: detonation quenching, critical ignition without detonation re-initiation, critical detonation re-initiation, critical detonation re-initiation without transverse detonation, critical transmission, and unattenuated detonation transmission. It has been concluded from these simulations that the transverse detonation wave plays an important role in the re-initiation events of a quenched detonation, as it is present most of the time for critical detonation re-initiation. Only rare cases, both experimentally and numerically, show re-initiation without a transverse detonation. Some cases exhibit a pocket of unburned gas, but it is not a necessary feature for re-initiation to occur. This study demonstrates the suitability of a 4-step combustion model to capture multiple outcomes of detonation re-initiation behavior, including the transverse detonation wave feature, which has not been captured by previous simple chemistry models. Therefore, a model that responds appropriately to the thermodynamic state behind complex shock wave interactions is required for accurate representation of detonation re-initiation.

Project Objectives

The goals of this project include to demonstrate and validate the abilities of a 4-species, 4-step combustion model to accurately simulate different regimes of detonation behavior in stoichiometric methane-oxygen after encountering a half-cylinder obstacle when compared to past experiments. Namely, this includes capturing the transverse detonation wave seen in critical detonation re-initiation. The 4-step model was originally developed by Zhu for acetylene combustion,¹ and has since been developed and validated in-house for other mixtures, including stoichiometric methane-oxygen.^{2,3} This project also has the goal of using the simulations to investigate the roles that shock collisions, burnout of pockets of unburned gas, and local hot-spots have on the formation of transverse detonation waves. And finally, to evaluate the role that the transverse detonation has on re-initiation.

Methodology Used

A numerical setup, which can be seen in Figure 1, to mimic the experiments done by Bhattacharjee in 2013⁴ was simulated using the 4-step combustion model. The model is an Euler Model and uses Adaptive Mesh Refinement (AMR) to resolve the grid. In order to observe different regimes of detonation behavior,

the initial pressure of the mixture was varied. The left wall was placed 40 mm behind $x = 0$ so that a Taylor wave would help the detonation stabilize before hitting the obstacle. An overdriven ZND solution (the structure for a detonation wave) was placed at $x = 0$ m and the leading edge of a 150 mm radius half-cylinder obstacle was placed at $x = 500$ mm.

Results Obtained

Six distinct regimes of detonation behavior was observed in the simulations, which can be seen in Figures 2 and 3. The first is *detonation quenching*, where the detonation dies out after clearing the obstacle. The *critical ignition* regime shows significant burning of the gas behind the Mach stem, but a detonation does not re-establish. *Critical detonation re-initiation* is the regime that experimentally saw transverse detonation waves, and the 4-step model was successful at capturing these transverse detonations. *Critical detonation re-initiation without a transverse detonation* was also observed some of the time, but it was a rare result both experimentally and numerically. *Critical transmission* showed the detonation front experiencing areas of partial quenching, and *unattenuated detonation transmission* showed no major areas of quenching, and the cellular structure was maintained throughout the channel. The detonation quenching, critical ignition, and critical detonation re-initiation with and without a transverse detonation compare both qualitatively and quantitatively well when compared to the experiments. The last two regimes were not observed experimentally.

Significance and Interpretation of Results

These results are significant because the 4-step model has demonstrated that this is the minimal combustion description (with both 4-species and temperature dependent heat capacities) that is necessary in order to accurately capture critical detonation re-initiation, which is important in scenarios like this one that contain complex shock dynamics. Also, the mechanisms and sequence of events for re-initiation has been clarified through these numerical simulations. First, a reflected transverse shock triggers an explosion event. This explosion event results from shock focusing on the burned/unburned gas interface. The outward explosion triggers a transverse detonation and/or the Mach stem, the transverse detonation propagates through shocked/unburned gas, and finally a self-sustained detonation front is re-established. Sometimes, the transverse detonation is triggered directly from the reflected transverse shock, and the remaining steps are the same. Another important conclusion from this work is that re-initiation does not occur due to turbulent mixing in the pocket of unburned gas, which is contrary to what was speculated with the experimental studies. Instead, the pockets are consumed by their own deflagrative burning or the passing of a transverse detonation wave.

Figures

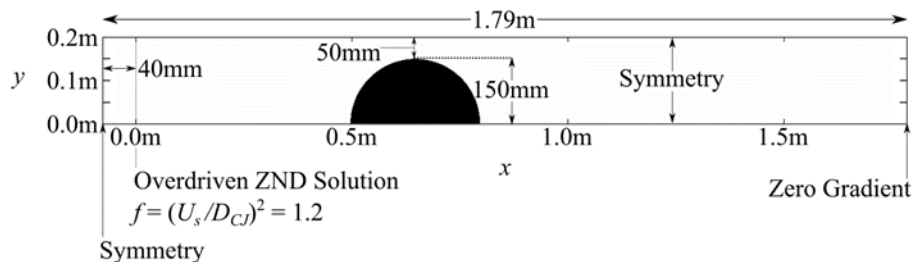


Figure 1: Numerical domain.

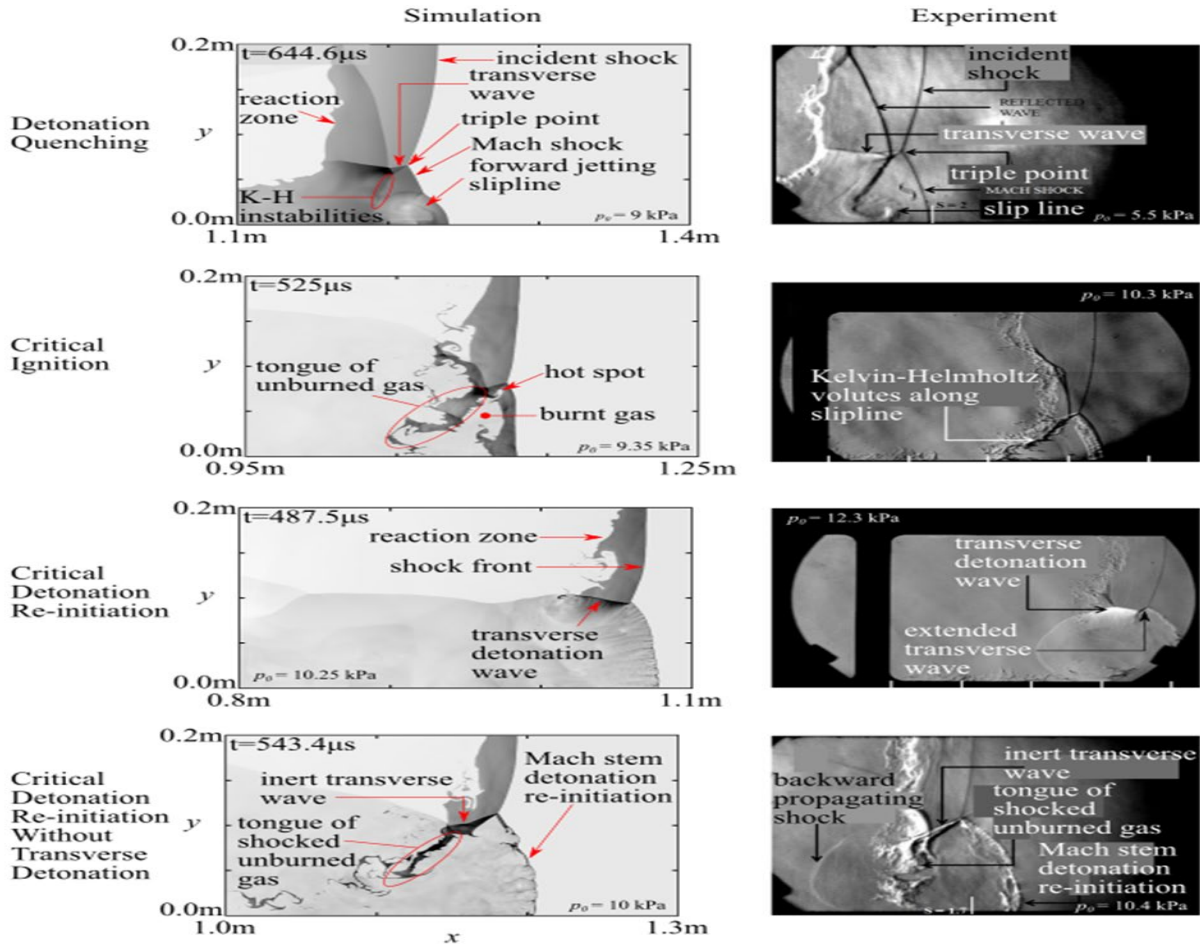


Figure 2: The first four regimes of detonation behavior observed with the 4-step model, compared to experiment.⁴ The simulation is plotted with density.

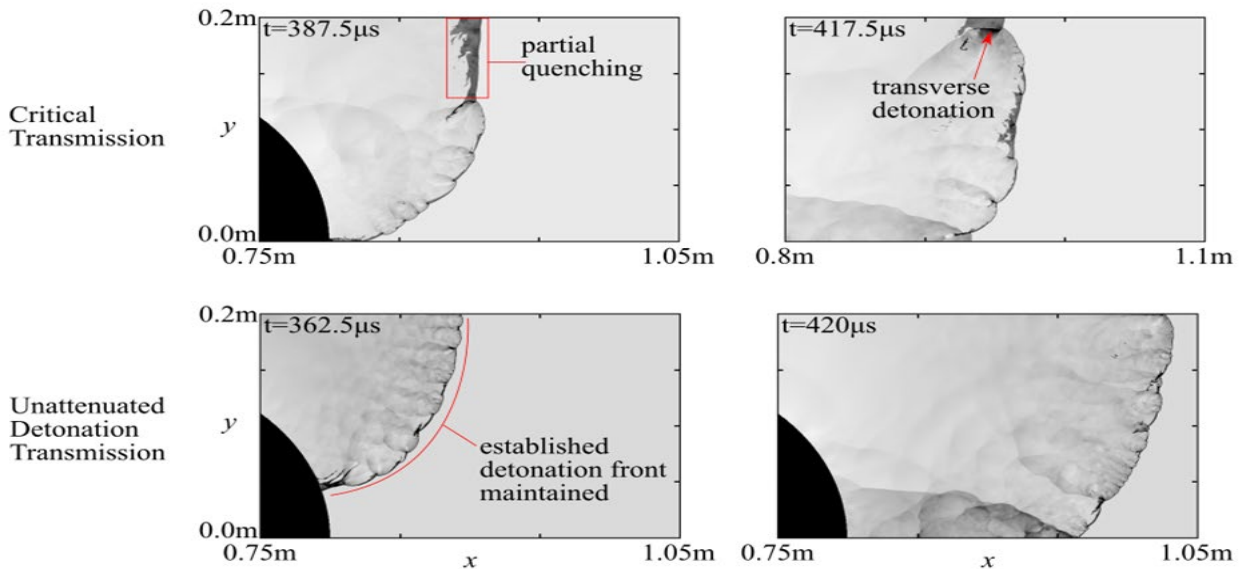


Figure 3: The last two regimes of detonation behavior observed with the 4-step model, plotted with density. These regimes were not observed experimentally.

References

- [1] Y. Zhu, J. Yang, and M. Sun. A thermochemically derived global reaction mechanism for detonation application. *Shock Waves*, 22(4):363–379, 2012.
- [2] M. Peswani and B.M. Maxwell. On using a simple 4-step combustion model to recover the universal χ parameter and Zel'dovich number in reactive hydrocarbon mixtures. 12th U.S. National Combustion Meeting, 5 2021.
- [3] M. Peswani and B.M. Maxwell. Performance of a Generic 4-Step Global Reaction Mechanism With Equilibrium Effects for Detonation Applications. Volume 11: Heat Transfer and Thermal Engineering of ASME International Mechanical Engineering Congress and Exposition, 11 2020. doi:10.1115/IMECE2020-23786.
- [4] R.R. Bhattacharjee. Experimental investigation of detonation re-initiation mechanisms following a mach reflection of a quenched detonation. Master's thesis, University of Ottawa (Canada), 2013.

Rocket Propulsion Systems – The Past and The Future

Student Researcher: Olivia F. Galigher

Advisor: Jed E. Marquart, Ph.D., P.E.

Ohio Northern University
Department of Mechanical Engineering

Abstract

Rockets are a crucial component of space exploration and without their propulsion system, they'd never leave the ground. The goal of this research is to understand how rocket engines work and how technology in this field has advanced beginning in the thirteenth century until present day. Understanding what has and hasn't worked in the past, will provide pertinent information to allow for predictions of what to expect in the future.

There are plenty of different types of engines, but for rockets, two main types are used: solid-propellant and liquid-propellant. A comparison of the two engines, with both advantages and disadvantages addressed, will create a deeper understanding of this technology, and allow for engineers to make the best possible choice to meet the needs of each rocket they design, build, and test.

Project Objectives

The following goals were set for this project:

1. Analyze the different types of rocket propulsion systems, specifically liquid rocket engines and solid rocket engines
2. Explore the history of rocket engines and how technology has changed over the years
3. Predict the future of rocket propulsion systems

Results Obtained

All aircraft utilize thrust to move but the main difference between airplanes and rockets is the working fluid. In turbine engines or propeller powered aircraft, air is the working fluid; however, rockets cannot utilize the same type of engine because in outer space, there is no atmosphere. In rocket engines, there is a combustion process that produces hot exhaust, and this is what is used as the working fluid. In a combustion chamber, fuel and oxidizer is mixed and exploded. The hot exhaust this chemical reaction produces is funneled through a nozzle to accelerate the flow of the fluid and this produces thrust. In a solid-propellant rocket engine, fuel and oxidizer are mixed and packed into a solid cylinder and only explode when ignited by a heat source. Whereas, in a liquid rocket engine the propellants are liquids and stored in their respective tanks. There are pumps that pump the liquids into the combustion chamber [1].

The earliest rockets originated in the thirteenth century when the Mongols and Chinese were at war and the Chinese launched fire-arrows. These were the first form of a simple solid-propellant rocket historians are aware of. Over the next couple of hundred years, rockets spread through Europe increasing in range due to advancements in gunpowder. Johann Schmidlap of Germany was a fireworks maker who invented the step rocket in the 1700s, which is a large rocket that carries a smaller one and once the larger one is burnt completely, the smaller one continues to increase in altitude. This is the same principle idea used in rockets that travel to outer space. Another significant contributor is Konstantin Tsiolkovsky who was a teacher in Russia. He is known as the father of modern astronautics

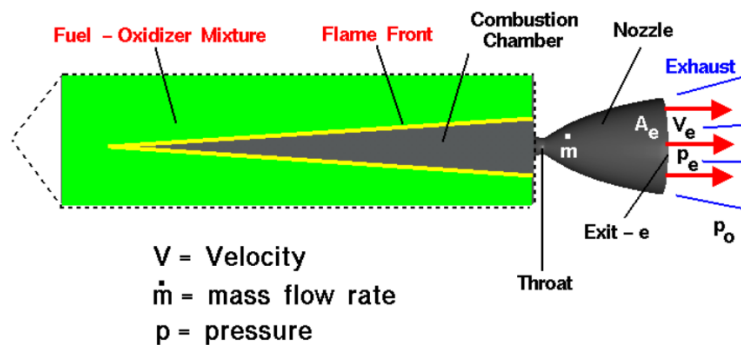
because of his ideas of using liquid propellants to take rocket propulsion to the next level and was the first to propose the idea of using rockets to explore outer space in 1898. American Robert H. Goddard is called the father of modern rocketry because after performing experiments with solid-propellant engines, he became convinced that liquid fuel would be a better option and became the first to successfully design a liquid-propellant rocket in 1926. During World War II, German engineers were designing and assembling the most advanced rockets and missiles at that time. With the fall of Germany, these rocket scientists scattered to the United States and the Soviet Union. This led to both countries beginning to experiment with using rockets as weapons for their respective militaries; this aided in both the Cold War and the Space Race [2].

Significance and Interpretation of Results

Solid-propellant rocket engines are mainly used in air-to-ground and air-to-air missiles, model rockets and boosters for satellite launchers [3]. This type of engine is the simplest form and because of the compactness, it takes up less space than a liquid rocket engine [4]. It can also sit for a very long time before it is used and is much easier and safer to handle. The biggest disadvantage of a solid-propellant engine is once ignited, there is no way to stop the combustion process from happening [1]. Liquid-propellant rocket engines are used on almost all rockets that go into orbit, including the space shuttles and un-manned missiles carrying satellites [5]. This type of engine requires a complex setup and process of pumps and containers, taking up a lot more space and adding additional weight to the rocket, therefore requiring even more thrust to be produced. However, it is the best option for any type of rocket going into orbit because of its thrust control ability. Thrust can be controlled by the amount of propellant entering the combustion chamber at a given time. Thrust control is crucial because too much thrust or thrust at the wrong time can place it in the wrong orbit or send it too far, but too little can cause it to fall back out of space. Complex rocket flights require the engine to be started and stopped many times throughout the entire process and liquid engines can do this easily [4].

In present day, solid-propellant rocket engines are still used in military missiles, model rockets, and rockets going just outside the Earth's atmosphere. However, most of the new technology being developed with space exploration, the missions to the moon, and commercial spaceflight utilize liquid-propellant rocket engines. Given all the research collected, it is predicted that solid-propellant rockets will still be used for specific applications due to their reliability and simplicity, however with the direction that space exploration and commercial spaceflight is headed, liquid-propellant rocket engines will be the primary engine type in rockets moving forward.

Figures/Charts



$$\text{Thrust} = F = \dot{m} V_e + (p_e - p_0) A_e$$

Figure 1. Schematic of a solid-propellant rocket engine with labels and corresponding thrust equation [3]

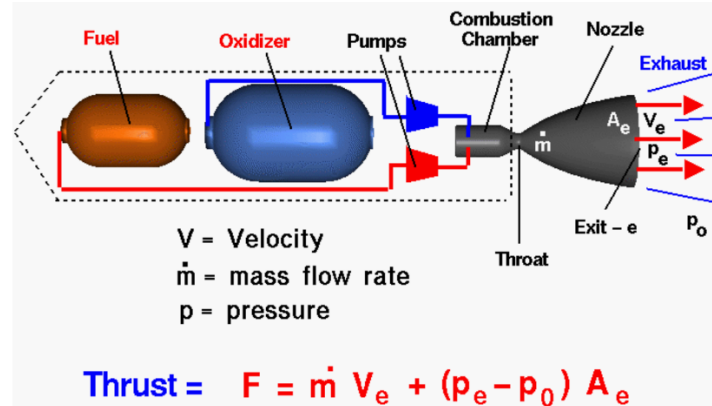


Figure 2. Schematic of a liquid-propellant rocket engine with labels and corresponding thrust equation [5]

Acknowledgements and References

- [1] N. Hall, "Rocket Propulsion," NASA, 13-May-2021. [Online]. Available: <https://www.grc.nasa.gov/www/k-12/airplane/rocket.html>.
- [2] T. Benson, "Brief History of Rockets," NASA, 13-May-2021. [Online]. Available: https://www.grc.nasa.gov/www/k-12/rocket/TRCRocket/history_of_rockets.html.
- [3] N. Hall, "Solid Rocket Engine," NASA, 13-May-2021. [Online]. Available: <https://www.grc.nasa.gov/www/k-12/airplane/srockth.html>.
- [4] T. Benson, "Practical Rocketry," NASA, 13-May-2021. [Online]. Available: https://www.grc.nasa.gov/www/k-12/rocket/TRCRocket/practical_rocketry.html
- [5] N. Hall, "Liquid Rocket Engine," NASA, 13-May-2021. [Online]. Available: <https://www.grc.nasa.gov/www/k-12/airplane/lrockth.html>.

Aft Imaging of Hollow Rotating Detonation Engines

Student Researcher: Peter Glaubitz

Advisor: Ephraim Gutmark

University of Cincinnati
Aerospace Engineering

Introduction

A rotating detonation engine is a type of pressure gain combustion system that harnesses a continuous detonation which rotates around the wall of the combustion chamber. Rotating detonation engines offer the potential for significant gains in efficiency over conventional combustors. The gain in efficiency is from the shift from the Brayton cycle to something closer to the Atkinson cycle. Additionally, the continuous nature of the detonation in the engine eliminates many of the issues inherent in using similar systems such as the need for an ignition source.

RDE Test Facility

The RDE test facility at GDPL consists of a centerbodyless rotating detonation engine with a 6-inch diameter running on gaseous hydrogen and compressed air. The engine can run at oxidizer flow rates from 0.3-0.5 kg/s with equivalence ratios from 0.6 to 1.2. The engine is ignited with a predetonation tube which injects a detonation wave normal to the exit plane near the perimeter of the engine. A high-speed camera is placed directly downstream of the engine protected by a flat plexiglass shield and is aligned with the engine visually to image the exit plane of the combustor. The camera records black and white video at 45000 frames per second with exposure times between 5 and 10 μ s. Each hot fire test lasts approximately 0.4 seconds. The camera is triggered to record based on a signal from the engine's control computer and captures the injection of the detonation wave, the engine operation, and end of the test.

Wave Angle Finding Program

The processing code was written in MATLAB. The code imports the highspeed footage and then identifies the center point and outer perimeter of the RDE in the frame. The code then crops the high-speed footage to center the RDE in the frame to allow each frame to be rotated without translating the RDE in the frame. The cropped footage is then rotationally stabilized to make allow for the identification of the wave front and subsequent measure. This stabilization also serves the double purpose of identifying the direction of the detonation wave's rotation. The applied rotation to each frame uses interpolation to try and better preserve the shape of the wave. A reference image is then manually selected. A frame that clearly shows the wave front. Using the chosen reference frame, the program then calculates the 2-D correlation coefficient between the reference image and each frame. Images with high correlation coefficients (typically > 0.90) are retained while the other frames are removed. This provides a collection of frames on which the computer has relatively clear images of the wave. Through the use of a binary filter, the wave shape is isolated from the frame, and the edge of the wave is then detected. The points of the wave front are used with a linear regression to calculate the detonation wave front in each frame.

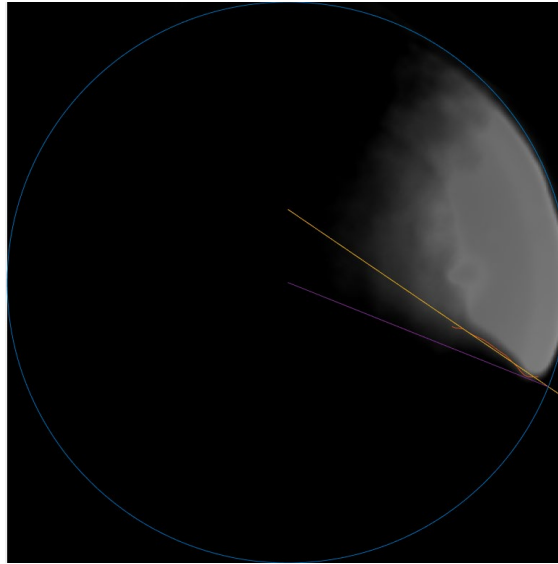


Figure 1: Processed wave image, with RDE perimeter in blue, RDE engine radius in purple, calculated wave front in yellow, and detected wave front in orange

Results

The code was applied to multiple experiments performed on the same day with the same engine configuration. The mean wave angle for each test showed a back swept wave angle with angle measures ranging from approximately 70° to 89° . The angle measures had large standard deviations of around 3.77° on average. There were generally no trends found across mass flow rates or across equivalence ratios.

Conclusion

The code created is a first step in trying to use aft high-speed imaging of an RDE to provide usable verification for simulations of CRDEs. The high degree of variability in the wave front angle could be a result of the low resolution of the wave images. In all footage used, the resolution did not exceed 400 pixels for the diameter of the engine. This gives only 67 pixels per inch. This severely limited the resolution of the wave, and it is likely small changes in the wave shape were amplified due to the low resolution. Future use of this program may benefit from higher resolution imaging.

High Altitude Ballooning with Raspberry Pi For Ozone Detection

Student Researcher: Devin Grant

Advisor(s): Dr. Augustus Morris and Dr. Marvin Reid

Central State University

Department of Manufacturing Engineering

Project Objective

The objective of this project is to create a fast, inexpensive, and innovative way to understand the ozone layer at the highest level of concentration in comparison to NASA ozone missions using pico high altitude ballooning.

Engineering Standards and Regulations

The pico balloon is considered an unmanned free balloon because it is radio-controlled and carry meteorology instruments. The engineering standards and regulations for the impact of the design project are stated on FAA Standards FAR-101 restrictions.

Equations

The equations that were used for the design:

Okay The Archimedes Rule which states that the upward buoyant force that is exerted on a body immersed in a fluid, whether fully or partially, is equal to the weight of the fluid that the body displaces. Archimedes' principle is a law of physics fundamental to fluid mechanics.

$$F_b = \rho gV$$

Where F_b = the buoyant force, which can be calculated from the payload mass; ρ = fluid density or for this case, the atmospheric density; g = acceleration due to gravity; and V = volume of gas inside of the helium. This calculation accounts for helium needed for the floating state of the balloon once it reaches the desired altitude.

Ideal Gas Law where the state of an amount of gas is determined by its pressure, volume, and temperature.

$$PV = nRT \quad pV = nRT$$

Where p = pressure of the gas; V = volume of the gas; n = the number of moles of helium; R = the ideal gas constant; and T = temperature. This equation was used to derive the pressure required to fill the balloon.

The Combined Gas Law which combines the three gas laws: Boyle's Law, Charles' Law, and Gay-Lussac's Law. It states that the ratio of the product of pressure and volume and the absolute temperature of a gas is equal to a constant.

$$\frac{P_1V_1}{T_1} = \frac{P_2V_2}{T_2}$$

Materials

Mylar material is what the balloon will be constructed of. Pico balloons, although small in size, are still super pressurized balloons and the material strength of mylar will limit the balloon from popping due to pressure differences. For the balloon launch a count of two balloons will be used to accommodate the required volume needed for the lifting force of the payload.

The ozone sensor that was selected for this project was the Taidacent Low Concentration Qualitative Detection MQ131 Ozone Air Qualitative Monitoring gas sensor. This is an analog signal output sensor that

requires to be preheated for at least 24 hours for accuracy. This sensor has a long service life and reliable stability as well as high sensitivity, and suitable for environmental gas detection and ozone gas detection. This ozone sensor was selected for this design project because of its beginner friendly installation and testing set up process. The testing concentration range of this ozone sensor is 10-1000 ppb whereas the projects mission will require to test ozone at its highest level of concentration, at 80,000 ft above earth's surface, the ozone concentration is about 11 ppm. This sensor will measure the ozone concentration to its max range and then will measure any discrepancies in the ozone at its highest concentrations to predict depletion. The ozone sensor measures the concentration of ozone by its analog output voltage, with a range of 5-5 volts, and concentration of a linear relationship between the need to convert the analog voltage into the resistance ratio, and then convert the analog voltage into the resistance ratio the to a logarithmic relationship to calculate the specific concentration value..The ozone sensor was received without a load adjustment knob. The load adjustment knob (RP3) is just a potentiometer composed of the sensors load resistance for the parallel relationship stated above. To accommodate, a 2.2 MΩ potentiometer was soldered onto the RP3 pins.

For this design, it was intended to select the LightAPRS-W(+WSPR) tracker to track the pico flight as it circumnavigated but the tracker was not available in the timeframe to purchase the design materials. As an adjustment, the LightAPRS tracker without the WSPR feature was selected for this design project; the WSPR feature would have accounted for reporting data and farther ranges including across large bodies of water. The lightAPRS tracker can report location, altitude, temperature and pressure to the internet (APRS-IS) or direct to an amateur radio once a minute with a solar panel/super-capacitor or just 4xAAA batteries. This tracker was selected because it is the most affordable, smallest, lightest, powerful and one of few open source APRS trackers available. Its radio operating frequency is 144-146 MHZ and is in the 2-meter radio band.

The Raspberry Pi Pico was implemented for this project because it has GPIO pins that receive and control input from other electronic devices such as the LightAPRS tracker and the Ozone Sensor. The Raspberry Pi Pico was selected rather than the regular Raspberry Pi due to its size and weight.

Power requirements:

Raspberry Pi kit: 3.3 V_{max} output current ≤ 300 mA

Ardurcam Camera: Analog 2.8V digital 1.2 V

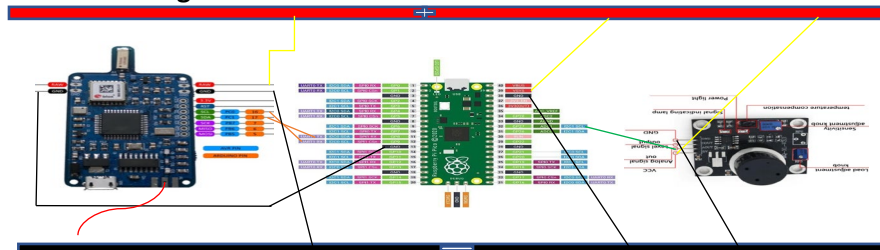
Ozone Sensor: 900mW= 5VDC * 180mA

Transmitter: 1W aprs= 3.3 V ; 300 mA

Power Supply ≥ 3.9 W

A battery pack was made from four (4) AAA coppertop batteries soldered together to accommodate the power consumption of all hardware. A single AAA battery has 1.5 volts and a current of 1000 mAh, with four batteries, the power supply is equivalent to 6 volts, 4000 mAh, consequently producing 24 volts which is more than enough power.

Electrical Design



The design project pin layout and connection read as follows:

Ozone Sensor Pins:

- VCC is connected to the power source of the breadboard
- Analog signal output which sends out the measurement of ozone concentration in voltage is connected to pin GP27 of the Raspberry Pi Pico
- Ground is connected to the ground source of the breadboard

Raspberry Pi Pico Pins:

- VSYS (pin 40) is the main system input voltage which can carry a range from 1.5-5.5 V and by the on-board SMPS can generate the 3.3 V needed for power consumption
 - GND (pin 38) is connected to the ground source of the breadboard
 - ADC1 (pin 32, GP27) is the A/D converter that is connected to the Analog signal output of the ozone sensor and turns the analog data into digital readable data
 - Pins I2C0 SDA and I2C0 SCL are interfaced with the LightAPRS tracker through I2C which requires a 2-wire interface for low-speed data transfer from the Raspberry Pi Pico to the LightAPRS tracker, whereas the Raspberry Pi Pico is the slave
 - o SCL (pin 17) is a clock
 - o SDA (pin 16) is the data
 - GND (pin 3) is connected to the ground pin of the Light APRS tracker
- LightAPRS Tracker Pins:
- RAW pin is the raw voltage and is connected to the power source of the breadboard
 - GND is connected to the ground source of the breadboard
 - SCL and SDA pins are I2C pins that are connected to the Raspberry Pi Pico to retrieve the data it gets from the MQ131 ozone sensor where the LightAPRS Tracker is the master
 - A1 middle pin is the 50 cm antenna wire

Testing Evaluation

A series of three tests were conducted for this project. The first test studied the balloon, the second test observed the ozone sensor, and the last test verified the signal of the Light APRS tracker. A test was performed on the 35" mylar balloon for leaks and temperature constraints. The procedure of the test was 1. Fill the mylar balloon up with air. 2. Retrieve the balloon weight filled with air. 3. Place the balloon into a refrigerator on the lowest temperature setting and allow the balloon to remain in the refrigerator for at least the projected flight duration time. 4. Retrieve the balloon from the refrigerator and measure the weight of the balloon. 5. Report any observations.

Once opening the refrigerator, an observation was made of the balloon compression due to the temperature. As the balloon was weighed it also was expanding back to its original form due to the temperature difference. Once weighed, it was concluded that there was not a significant loss of air from the balloon. The loss of air was from the self-sealing valve. From the balloon tests it is concluded that the self-sealing valve does not completely close, additional support is needed to seal the balloon. The balloon will be sealed with masking tape or a clamp for the final launch. Also, the refrigerator accounted for the temperature difference the flight will endure and it is expected that the balloon will compress at altitudes with lower temperatures. To test the flight conditions are constraints a mock launch was implemented. This launch consisted of the two (2) Mylar balloons which is required for the final launch, the fishing line which connected the two (2) mylar balloons, the payload, and the banister that the balloon will be tied to. This test will mock the flight characteristics of the final launch.

The mock balloon launch helped understand the flight characteristics of the final launch. The weather during the balloon launch was as follows: 82 ° F, 45% humidity with a dew point of 57°, and 17.4 mph

wind speeds. The wind was so strong during the mock launch, the two mylar balloons ripped from the string and floated away. The objective of the mock launch was to test how a real flight would go with the constraints such as, weather conditions, wind speed, and the payload. Overall, the mock launch was successful, but it was concluded that the balloons should not have been tied to the railing with such high wind speeds.

With the Raspberry Pi Pico connected to the Ozone sensor on the bread board it was able to send the code from the pico to the sensor being powered by the USB. To test the MQ131 ozone gas sensor and be sure it could detect ozone concentration, a can of WD-40 which is an aerosol spray was sprayed in proximity of the sensor to see if it could not only detect the concentration, but to also see if the pico could retrieve the information and display the result on Arduino IDE.

The results were given in PPM, PPB, mg/m³, ug/m³

Once the ozone sensor was connected to the Raspberry Pi Pico and the WD-40 was sprayed, the data was collected on Arduino IDE. The objective was to see if the data would come back every 60 seconds and it did consistently. Overall, this test was remarkably successful in retrieving the data. To test the LightAPRS tracker, the tracker was placed on a small breadboard and connected to the constructed battery pack. The constructed breadboard was then transported to the nearest iGATE in Beavercreek, Ohio so that the trackers data packages can be picked up seen on APRS.fi.

The results from the LightAPRS Tracker test were successful. Once the constructed breadboard was transported to the nearest iGATE it took over an hour for the data package to be seen on APRS.fi. The LightAPRS Tracker may be a real time reporter but APRS.fi has many complaints that the data packets are available for viewing at an offset time. For the final launch, it is recommended to wait till launch until the first data report is seen on APRS.fi which will help account for data during the launch afterwards

Conclusion and Recommendations

In conclusion, the design project did not get completed due to numerous amount of factors. During the first session of the project, the focus was primarily on research and getting the report drafted. The process for ordering materials began at the end of the first semester when it became aware that the items needed for the design were out of stock. Due to the items being out of stock for such an extended period of time, it pushed the time back the receiving time, on top of waiting for the shipment of the items. Once all the materials arrived, the focus shifted to conducting tests, programming, and assembling the payload. Another factor during this project that slowed down the process was the programming. Programming the Raspberry Pi Pico using Arduino IDE was conflicting. However, there were still issues with interfacing everything. After much wiring, soldering, and programming, it was concluded that the design did not need the Raspberry Pi Pico after all. The LightAPRS tracker already had Arduino IDE in its software system for the Ozone Sensor. By the time this became apparent, the project time had concluded.

For this design project two recommendations would assist in improving time management for completing this design project. The first recommendation is to have a rigorous Gantt chart that will include the necessary time for delays while also enough time to finish the project. Also, it is recommended to account for time such as research, shipping, programming, and even small tasks such as soldering and filling the balloon with helium.

For the launch of the balloon to finish the design projects mission it is recommended that the design excludes the raspberry pi pico. As stated before, the LightAPRS tracker has capabilities to receive the MQ131 ozone sensor output through its SCL port; this port will act as an A/D converter. If the code for the ozone sensor that is on raspberry pi pico is transferred to the LightAPRS using Arduino IDE.



Characterization and Modeling of Hydrogen Fuel Cells for Thermal Management

Student Researcher: Amy R. Gravenstein

Advisor: Dr. Edward Evans, Dr. Chelsea Monty-Bromer

The University of Akron
Chemical and Biomolecular Engineering

Abstract

The focus of this project is to model the performance of a hydrogen fuel cell system in order to optimize the thermal management. Green hydrogen offers many capabilities in heavy weight transportation and specifically in aviation. The nature of hydrogen causes it to have higher safety risks which is why the integration of fuel cells can be more complex. In aviation applications, weight optimization is a high priority. Characterization of the fuel cell includes modeling and predicting hydrogen and air consumption, water production, power production, and efficiency. These fuel cell characteristics can be used to predict cooling requirements during operation and allow for creative solutions to optimize performance. A MATLAB code was created to calculate fuel cell characteristics and heat production for a hypothetical fuel cell operation. The code is adaptable and can be used to model various fuel cells. Further advancements should include experimental verification of heat integration designs. This research can be used to strengthen the foundation for hydrogen power in aviation.

Project Objectives

The objective of this model is to quantify heat production of various fuel cells in order to propose thermal management solutions. When using fuel cell systems in aviation, minimizing the weight of the balance of plant is specifically important. Thermal management solutions can be provided to optimize fuel cell performance while minimizing the overall system weight.

Methodology Used

This model utilizes basic mass and energy balances of a hydrogen fuel cell to determine the inlet and outlet flow rates of hydrogen, oxygen, air, and water. Enthalpies of the reactants and products can be determined and used to calculate the heat generated from the reaction. From this value, the flowrate of coolant can be determined and thus the balance of plant can be designed to provide the necessary heat transfer.^{1,2,4,5} Figure 1 displays some of these equations used in the MATLAB code. Testing with the Ballard 600W fuel cell was used to verify the theoretical flow rates as seen in Figure 2. This testing included replicating difference power profiles to characterize overall fuel cell performance.

In addition to the Ballard fuel cell, a 25kW Powercell stack and the 2017 Toyota Mirai fuel cells were modeled with the MATLAB code as well. An example of the results found from the Toyota Mirai stack indicated that there was an excess of heat amounting to roughly 95kW present in the coolant line.^{3,6,7,8} A potential solution for the utilization of this heat can be seen in Figure 3. In application with liquid hydrogen fuel tanks, this option allows for the some of the excess heat to be repurposed for liquid hydrogen vaporization and water ballast vaporization. A solution such as this allows for better on board weight management and weight reduction in the balance of plant design.

Significance and Future Work

The MATLAB code developed is a versatile tool that can be used to predict heat produced while operating a hydrogen fuel cell under various conditions. Thermal integration efforts can utilize this information to design an efficient balance of plant for the fuel cell, and these efforts can also allow for innovation within other systems. Experimental efforts with the Ballard 600W fuel cell verified the code was accurate at a small scale. Future work will focus on verifying the results seen from the Toyota Mirai fuel cell and other large-scale fuel cells.

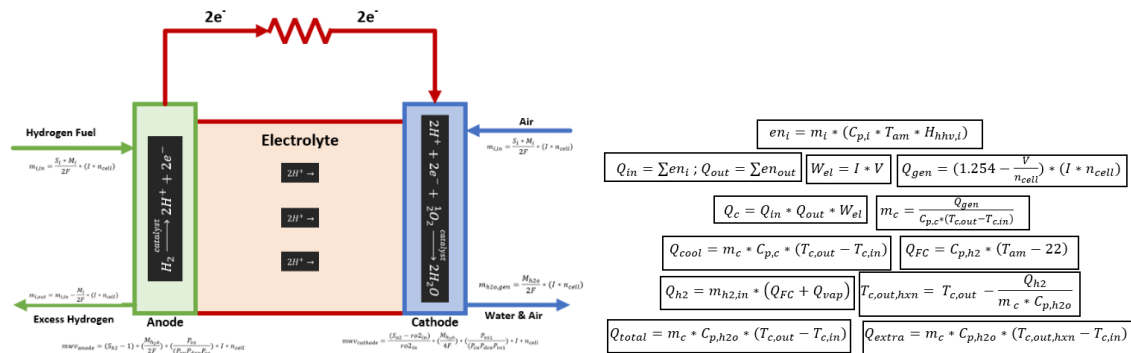


Figure 1: The left image shows a hydrogen fuel cell diagram with general mass balances. The right image displays key equations used to predict heat in the coolant lines of a hydrogen fuel cell system.

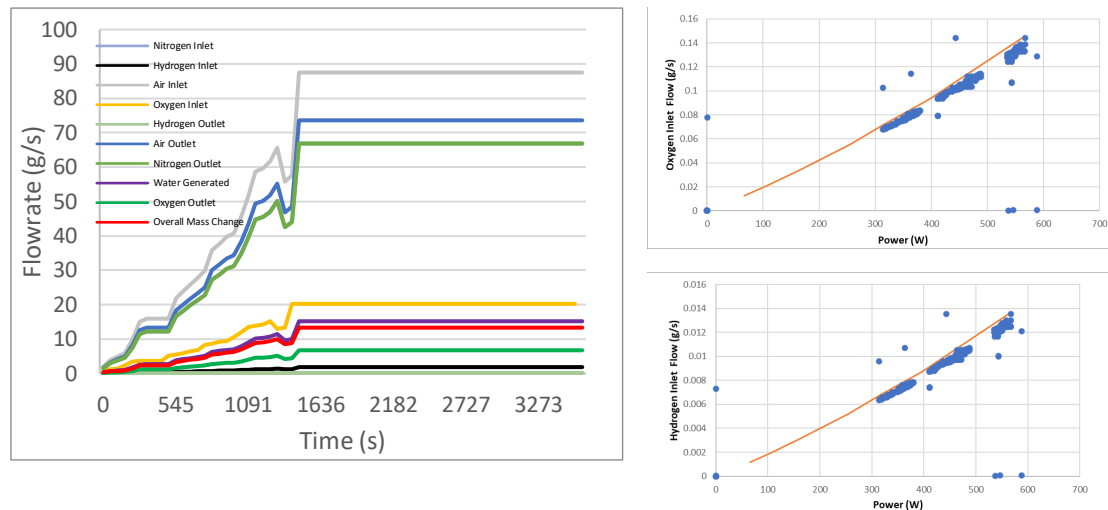


Figure 2: The Left image displays theoretical mass flow rates for 2017 Toyota Mirai fuel cell system. The right images display the oxygen inlet flow (top) and hydrogen inlet flow (bottom) experimental results from testing the Ballard 600W fuel cell along with the theoretical flow rate predictions.

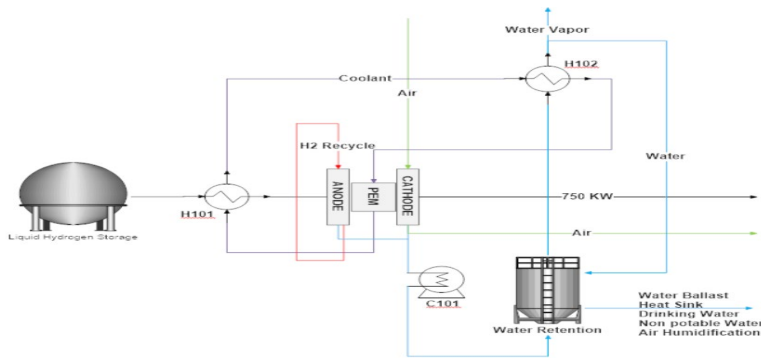


Figure 3: This image displays a potential solution for utilizing the excess heat present in the coolant line of the 2017 Toyota Mirai fuel cell. Excess heat would first be used to vaporize the liquid hydrogen draw from a tank. The water ballast or retention tank can then be used a heat sink. Water vapor produced from this could also be a means of weight management.

Work Cited

1. Guandalini, Giulio, et al. "Simulation of a 2 MW PEM fuel cell plant for hydrogen recovery from chlor-alkali industry." *Energy Procedia* 105 (2017): 1839-1846.
2. Ko, DaeHo, et al. "Non-isothermal dynamic modelling and optimization of a direct methanol fuel cell." *Journal of Power Sources* 180.1 (2008): 71-83.
3. Lohse-Busch, H., Duoba, M., Stutenberg, K., et al., "Technology Assessment of a Fuel Cell Vehicle: 2017 Toyota Mirai," 2018. Argonne National Laboratory. <http://www.anl.gov/D3>.
4. Spiegel, Colleen. *PEM fuel cell modeling and simulation using MATLAB*. Elsevier, 2011.
5. Swedenborg, Samuel. "Modeling and simulation of cooling system for fuel cell vehicle." (2017).
6. Tomi, N., Hasegawa, S., Farnsworth, J., Imanishi, H. et al., "Development of Air Supply Controller for FCV Based on ModelBased Development Approach," SAE Technical Paper 2021-01-0742, 2021, doi:10.4271/2021-01-0742.
7. Yahashi, H., Yamashita, A., Shigemitsu, N., Goto, S. et al., "Development of High-Pressure Hydrogen Storage System for New FCV," SAE Technical Paper 2021-01-0741, 2021, doi:10.4271/2021-01-0741.
8. Yoshizumi, T., Kubo, H., and Okumura, M., "Development of High-Performance FC Stack for the New MIRAI," SAE Technical Paper 2021-01-0740, 2021, doi:10.4271/2021-01-0740.

Evaluation of the Hydrological Effectiveness of Rain Gardens on Baldwin Wallace's Northern Parking Lots

Student Researcher: Jude Hagerman

Advisor(s): Dr. Annette Trierweiler, Dr. Carrie Davis Todd

Baldwin Wallace University
Department of Biology and Geology

Introduction

Rain gardens are a common solution to the increased runoff caused by urbanization. They have been successfully implemented across the country, gaining popularity as an efficient way for the control of runoff, along with the removal of pollutants picked up as rainwater runs off roads, parking lots, and sidewalks (Schuster *et al.*, 2017). College campuses have become increasingly modernized, as the paved surfaces allow for large amounts of sediment-rich runoff to concentrate into local waterways, causing contamination and flooding. The implementation of bioretention basins, such as rain gardens, help to increase the lag-to-peak time and reduce sediment pollution (Bratieres *et al.*, 2008). These rain gardens often require yearly maintenance and upkeep to ensure the drains and curb cuts are clear of debris, the soil and hydrophytic vegetation is maintained, and the hardscape responsible for drainage is graded properly (Winston *et al.*, 2016).

This case study focuses on the two rain gardens present on Baldwin Wallace University's campus, located in Berea, Ohio. To date, there has been no quantification of the garden's abilities to control runoff, sediment pollution, and nutrient pollution, despite yearly maintenance. While it is important to have these facilities to help prevent sediment and nutrient pollution, it is equally important to continue to ensure that they are still controlling runoff to an acceptable degree. This case study aims to assess how efficiently the Baldwin Wallace rain gardens are performing their designated hydrologic role of runoff storage and control by assessing the soil properties, hydrologic properties, plant life, and water quality of the two gardens present on BW's north campus.

Methodology

Rainwater was collected utilizing a Teflon funnel on top of a nearby building, while runoff was collected by hand. Groundwater samples were collected via two lysimeters at 18 and 36 inch depths. I collected soil samples from each garden. Their texture and color were described. I also extracted nutrients from the soil samples. Nutrient content of soil and water samples was determined using methods from Doane *et al.* (2003) to measure NO_3 and Weatherburn *et al.* (1967) to measure NH_4 concentration using a plate reader. A subset of the soil samples and plant samples were shipped to Jen Latimer's lab at Indiana University of Fort Wayne to quantify metal concentrations via XRF Analysis to determine metal concentrations.

Runoff was modeled using the rational method equation. Precipitation data was sourced from the Cleveland Hopkins Airport Monitoring Station (KCLE). The drainage area was measured using ArcMap. For the Telfer North rain garden calculation, only impermeable surfaces were considered. For each garden, the rational method quantified the lag-to-peak time and peak discharge.

Results and Discussion

The prominent findings in this case study were from our observations of runoff from precipitation events: the majority of the runoff in the Telfer parking lot was being directed away from both rain garden inlets. While we found the soil properties of the rain garden appropriate for their role (Table 1), the structural landscape around the gardens reduced the discharge into the gardens. Due to this disconnect between utility and design, the surrounding landscape does not allow the garden to perform its role in storing excess runoff.

Table 1: Soil Properties of Telfer Parking Lots

Site	Soil Type	Soil Color	Peak Discharge (cfs)	Infiltration Rate (in/hr)	Water Quality Volume (ft ³)
Telfer West	Loamy Sand	5YR 2.5/1	0.082-0.093	13	418
Telfer North	Sand	5YR 3/1	0.054-0.061	7.75	1045

The gardens themselves were constructed using soils with high infiltration rates, allowing for any absorbed water to be moved quickly into the storage sublayer then out through the underdrains. The soil consisted of loamy sand mix, which is the most efficient for infiltration, capture, and prevention of overflow into the storm drain (Bratieres *et al.*, 2008).

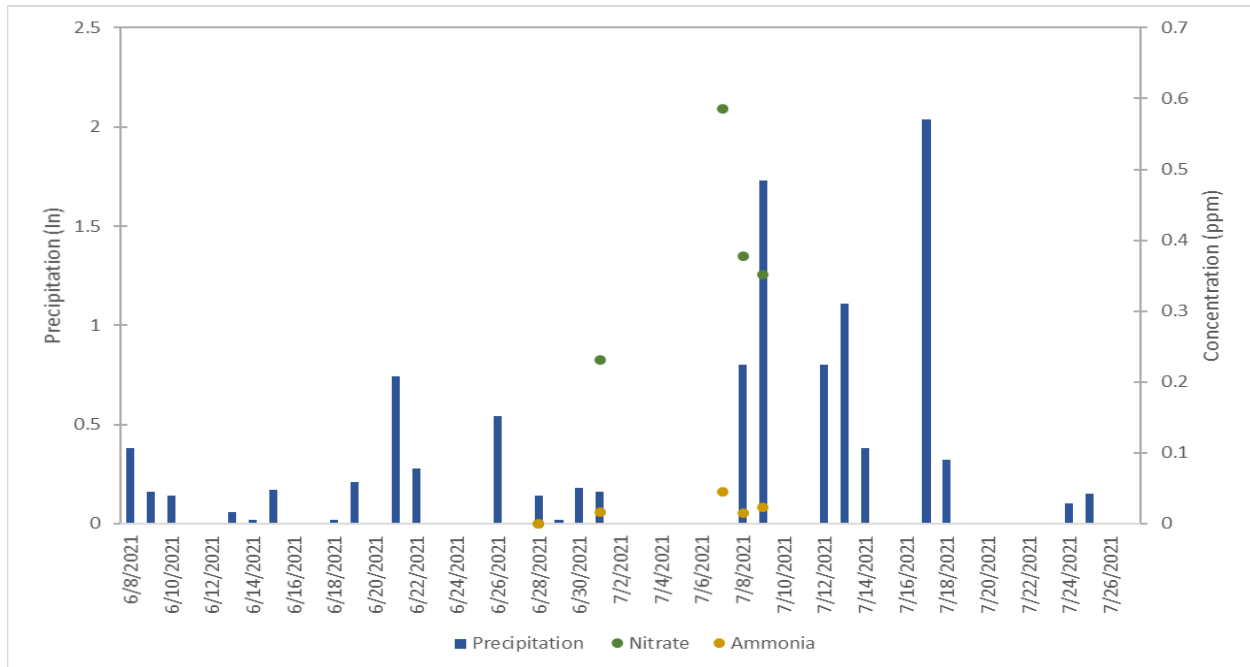


Figure 1: Precipitation and groundwater nutrient concentrations (nitrate and ammonium) over the study period. Sampling took place over the course of 4 weeks and was heavily dependent on precipitation events.

Soil and water chemistry were tested for over a 4 week period and compared to the precipitation events and intensity during the time period, the nutrient data returned was inconclusive due to the nature of the collection timeframe (Figure 1). We found common vehicular metals, such as Si, Fe, Ca, Na, Mg, Al, and K, were within normal bounds in all soil samples (Hjortenkrans, 2008; Kim *et al.*, 2005).

As this is a short-term case, future studies of these rain gardens would benefit from multiple seasons of data and in-situ measurements via the usage of a measurement flume. As this study is precipitation dependent, studies in this region may take multiple seasons to provide conclusive and concrete results surrounding hydrology and water chemistry.

References

- Bratieres, K., Fletcher, T. D., Deletic, A., & Zinger, Y. (2008). Nutrient and sediment removal by stormwater biofilters: A large-scale design optimization study. *Water Research*, 42(14), 3930–3940. <https://doi.org/10.1016/j.watres.2008.06.009>
- Dietz, M. E., & Clausen, J. C. (2005). A field evaluation of rain garden flow and pollutant treatment. *Water, Air, and Soil Pollution*, 167(1-4), 123-138.
- Doane, T.A. and W.R. Horwath. 2003. Spectrophotometric determination of nitrate with a single reagent. *Analytical Letters* 36: 2713-2722.
- Fletcher, T. D., Andrieu, H., & Hamel, P. (2013). Understanding, management and modelling of urban hydrology and its consequences for receiving waters: A state of the art. *Advances in Water Resources*, 51, 261–279. <https://doi.org/10.1016/j.advwatres.2012.09.001>
- Hjortenkrans, D. (2008). *Road traffic metals -sources and emissions*. <http://www.diva-portal.org/smash/get/diva2:15019/FULLTEXT01.pdf>
- Kim, L.-H., & Lee, S. (2005). Characteristics of Metal Pollutants and Dynamic EMCs in a Parking Lot and a Bridge during Storms. *Journal of Korean Society on Water Environment*, 21(4), 385–392. <https://www.koreascience.or.kr/article/JAKO200510103482983.page>
- Shuster, W. D., Darner, R. A., Schifman, L. A., & Herrmann, D. L. (2017). Factors contributing to the hydrologic effectiveness of a rain garden network (Cincinnati OH USA). *Infrastructures*, 2(3), 11.
- Weatherburn, M.W. 1967. Phenol-hypochlorite reaction for determination of ammonia. *Analytical Chemistry* 39: 971-974.
- Winston, R. J., Dorsey, J. D., & Hunt, W. F. (2016). Quantifying volume reduction and peak flow mitigation for three Bioretention cells in clay soils in northeast Ohio. *Science of the Total Environment*, 553, 83-95.

Fuzzy Logic Based Approach for Autonomous Vehicle Decision Making at Roundabouts

Student Researcher: Daniel R. Heitmeyer

Advisor: Dr. Kelly Cohen

University of Cincinnati

Aerospace Engineering

Introduction

The introduction of Autonomous Vehicles (AVs) proposes a solution to reducing traffic congestion, emissions, collisions, and human errors. AVs may also allow for faster reaction times and consistent decision making compared to human drivers. These benefits are especially desired at roundabouts which can present a difficult scenario for unfamiliar drivers. To achieve these, a fuzzy logic system controlling the vehicle's acceleration and lane changing decision was implemented within a SUMO simulation. A similar genetic fuzzy system using the SUMO simulator has been shown to provide benefits in throughput of traffic in a highway merging scenario [5]. These systems balance a trade-off between performance and safety to improve traffic conditions while preventing collisions.

Reductions in emissions, energy, and fuel consumption are found from avoiding sudden changes in acceleration, road conditions, or traffic conditions. Improvements in these fields have been shown with an increase in AV usage dependent on the aggressiveness of the model [3]. Aggressive AV models were shown to have positive effects on travel time at the cost of increased emissions, while defensive models showed nearly no changes when compared to human drivers. Positive effects on both have been shown at roundabouts with an increase in the percentage of AVs at the cost of increased collision numbers [2]. The trade-off between collisions and traffic performance is affected heavily by the spacing between vehicles [1]. Small spaces are often used by aggressive models to obtain better performance, but may not be acceptable to human drivers. Driver acceptance may be affected by psychological factors such as driving style, trust in automated driving, and overall acceptance of AI technology [4]. To make AV usage acceptable while human drivers are still in the loop, larger spacings may be required.

Methodology

A fuzzy logic controller that outputs the vehicle acceleration and decision to change lanes based on vehicle positions and speeds was developed. Contrary to binary logic, fuzzy logic provides a degree of membership to certain groups to be assigned. For example, spacing values between cars is translated into memberships to the negative far, negative close, zero, positive close, or positive far away groups. This then allows for the simple linguistic rule base that associates the input to output groups. These rules can be crafted from expert knowledge of the system or, in this case, be trained by an optimization technique such as genetic algorithms. An example rule is as follows:

**"IF spacing is positive close AND velocity difference is positive big
THEN acceleration is positive big"**

After all rules have been applied, the output groups are aggregated and a defuzzification method is used to output a number where the centroid method was used in this paper. An example of the fuzzy inference process is seen in Fig. 1.

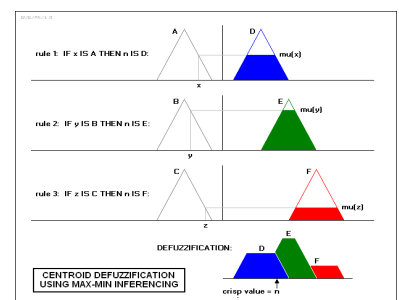


Figure 1: Fuzzy Inference Process

A Genetic Algorithm (GA) was created to optimize the rule base of the fuzzy logic controller set in place. Each controller is represented by a chromosome which contains a list of integers that each represent an If-Then rule to be used. The controllers are created from this chromosome and tested to determine a fitness score. This score is used to promote desired controllers for selection as parents to create the next generation. The score aimed to maximize average travel speed and maintain a minimum distance between vehicles during the simulation.

The selection of parents is done by a roulette wheel method, where controllers with large fitness values have a proportionally larger chance of being selected. The lists of integers describing the parents then go through crossover which swaps sections of the list at two points. Each integer is then subject to a small probability of being mutated. This simply replaces the integer with another random integer. A number of the best controllers are immediately passed onto the next generation, and the rest are determined randomly while encouraging larger fitness scores.

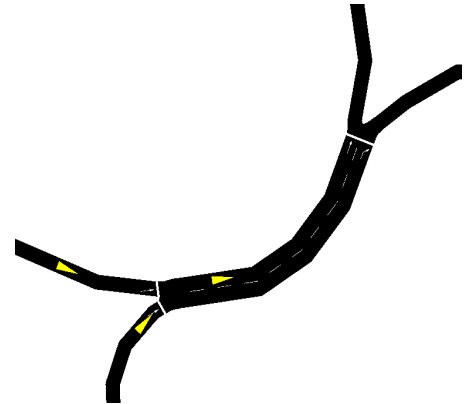


Figure 2: Simulated Roundabout Merging

A simple roundabout network with a speed limit of 35 mph, one AV, and two human drivers was created in SUMO as seen in Fig. 2. Human simulated cars entered from the main line that the AVs merge into. The TraCI client was used to collect all relevant traffic information and control the AV through a Python script using the fuzzy controller. This info was used for both the vehicle control and the resulting fitness score after simulation.

Results and Future Work

The fuzzy system was trained by the GA and tested on two scenarios. The first scenario featured one human driver and one AV merging, where an increase in average speed, max speed, and minimum distance was found. The second scenario had two human drivers, where a less noticeable increase in key metrics was found as seen in Table 1b. Both scenarios found an increase in emissions due to the aggressive nature of the fuzzy controller developed through training. Notable metrics of the emission increase can be seen in Table 1a. Future work includes extending the scenarios to a continuous flow of traffic with more variety in vehicles and road network configurations. Emission data may also be used in the future for the controller's fitness score.

Emissions	NOx	CO2	Fuel Consumption
Human Control	21.7	52044	22.3
Fuzzy Control	26.7	60691	26.1
Percent Increase	23%	17%	17%

Table 2a: Emissions During 1v2 Merging

Performance	Avg. V	Max V	Min. Dist.
1v1 with AV	31.1 mph	35.0 mph	27.8 m.
1v1 with Human	24.3 mph	27.8 mph	16.7 m.
1v2 with AV	27.4 mph	28.7 mph	8.8 m.
1v2 with Human	21.3 mph	24.4 mph	8.4 m.

Table 1b: Performance Data

Collaboration between vehicles may introduce game theory to create a more optimal system. More inputs such as blinker light status and road information may be implemented easily at the cost of computation time in both training and evaluation.

References

- [1] Apostolos Anagnostopoulos and Fotini Kehagia. "CAVs and roundabouts: research on traffic impacts and design elements". In: *Transportation Research Procedia* 49 (2020), pp. 83–94. DOI: <https://doi.org/10.1016/j.trpro.2020.09.008>. URL: <https://www.sciencedirect.com/science/article/pii/S2352146520307298>.
- [2] Aleksandra Deluka Tibljaš et al. "Introduction of Autonomous Vehicles: Roundabouts Design and Safety Performance Evaluation". In: *Sustainability* 10.4 (2018). ISSN: 2071-1050. DOI: 10.3390/su10041060. URL: <https://www.mdpi.com/2071-1050/10/4/1060>.
- [3] Laura García Cuenca et al. "Machine Learning Techniques for Undertaking Roundabouts in Autonomous Driving". In: *Sensors* 19.10 (2019). ISSN: 1424-8220. DOI: 10.3390/s19102386. URL: <https://www.mdpi.com/1424-8220/19/10/2386>.
- [4] Yujie Li et al. "Tradeoffs between safe/comfortable headways versus mobility-enhancing headways in an automated driving environment: preliminary insights using a driving simulator experiment". In: *Frontiers in Engineering and Built Environment ahead-of-print* (Sept. 2021). DOI: 10.1108/FEBE-05-2021-0025.
- [5] Anoop Sathyan, Jiaqi Ma, and Kelly Cohen. "Decentralized Cooperative Driving Automation: A Reinforcement Learning Framework Using Genetic Fuzzy Systems". In: *Transportmetrica B* (July 2021). DOI: 10.1080/21680566.2021.1951394.

Investigation of Surface Finish and Applied Force on the Tribological Performance of High-Performance Polymers

Sarah C. Herbruck

Advisor: Mark A. Sidebottom

Miami University

Department of Mechanical and Manufacturing Engineering

Abstract

Polymeric-based lubricants are useful for use in aerospace situations. With the use of a flat-on-flat tribometer, the relationship between counter surface roughness and tribological performance (friction and wear) of high-performance polymers is evaluated. Wear rates improved as surface roughness decreases. Samples lose less volume when counter surfaces are smooth and well machined.

Project Objectives

High performance polymers are typically stronger than tradition engineering polymers, are suited for high-temperature applications, maintain integrity in high compression situations, resist against aggressive media, and provide a low coefficient of friction. Due to these key characteristics, high performance polymers are useful in applications such as turbofan jet engines. By testing the friction and wear properties of high-performance polymers under different conditions (contact pressure and surface finish), this study aims to allow for better machine and material design choices. These improvements may lead to longer maintenance intervals, higher engine temperature (higher performance), and improve combustion output in turbofan engines.

Methodology Used

Before testing began, the dimensions of each sample were taken using a caliper with resolution of 0.01mm. The initial mass of each sample was recorded using a 10 μ g resolution scale (Mettler Toledo XS205). Using these two values, the density for each sample was calculated. The experiments were conducted on a flat-on-flat tribometer. This machine clamps a test sample in a stable position, contacting a counter surface, and moves the counter surface against the sample. The tests conditions and details are included in Figure 1. The normal force, frictional force, volume lost, and distance traveled were all recorded to calculate the friction coefficient (Eq. 1) and wear rates (Eq. 2) of each sample.

Results Obtained

Two tests were run for each combination of pressure and surface finish. Each test's results were reviewed for possible outliers and variation within the experiment. For each set of test conditions, the test with the least number of outliers and smallest deviation was chosen to represent the representative behavior of high-performance polymers at those conditions. The volume lost and coefficient of friction versus the distance of the tests for each testing condition are presented in Figures 2 and 3.

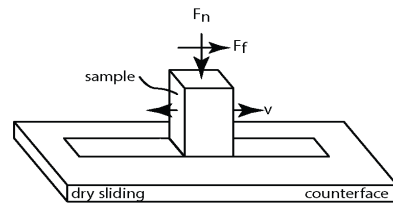
Significance and Interpretation of Results

Through observation of the data provided on the graphs, a few trends in the wear and friction performance of high-performance polymers can be observed. As seen in figure 2, the friction coefficient vs the sliding distance for all samples, the samples organize themselves, with rougher surfaces resulting in higher friction coefficients. The roughest counter sample, surface roughness of 210 micro-inches, produced a total volume loss of 12.35 mm³. The smoothest counter sample, the polished mirror

sample, produced a total volume loss of 3.33 mm³. This means that when placed against surfaces with rough surface characteristics, the polymers lose more material, providing support for smoother surfaces improving engine efficiency when used in contact with bushings.

Figure 3 provides data collected on the friction coefficient generated between the high-performance polymers and their respective counter samples. The friction coefficients roughly increase when surfaces become rougher. The highest friction coefficient, 0.3797, corresponds to the second most rough counter surface. The lowest coefficient of friction, 0.2377, corresponds to the polished mirror counter surface. The lower coefficient of friction indicates a smoother movement between the bushings and their contacting surfaces, providing additional support for smoother surfaces improving engine efficiency when used in contact with bushings.

Figures/Charts



materials
 pin: Vespel-SP21
 counterface: 304 L Stainless steel
 experimental conditions:
 $F_N = 28 \text{ N (0.69 MPa), } 280 \text{ N (6.9 MPa)}$
 $V = 100 \text{ mm/s}$
 $d = 50 \text{ mm/cycle (500k cycles, 25 km total)}$
 environment: dry (lab air)

$$\mu = \frac{F_f}{F_n} \quad (1)$$

$$\kappa = \frac{V_{Lost}}{F_n * d} \quad (2)$$

$$V_{Lost} = \frac{m}{\rho} \quad (3)$$

Figure 1. Experimental

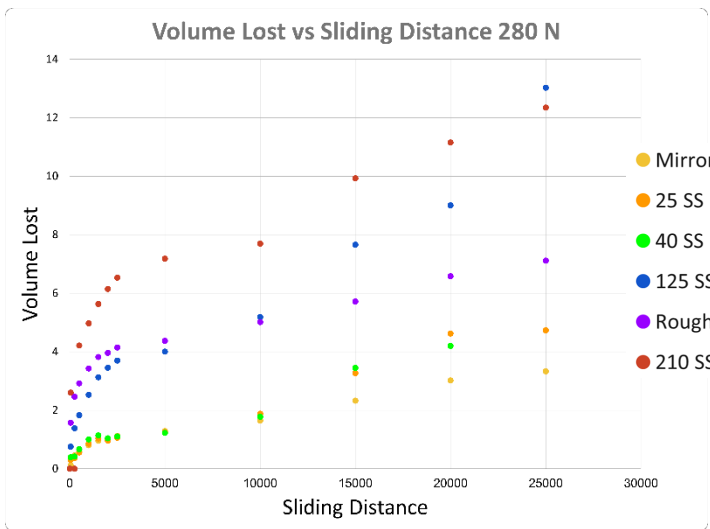


Figure 2. Volume Loss Results

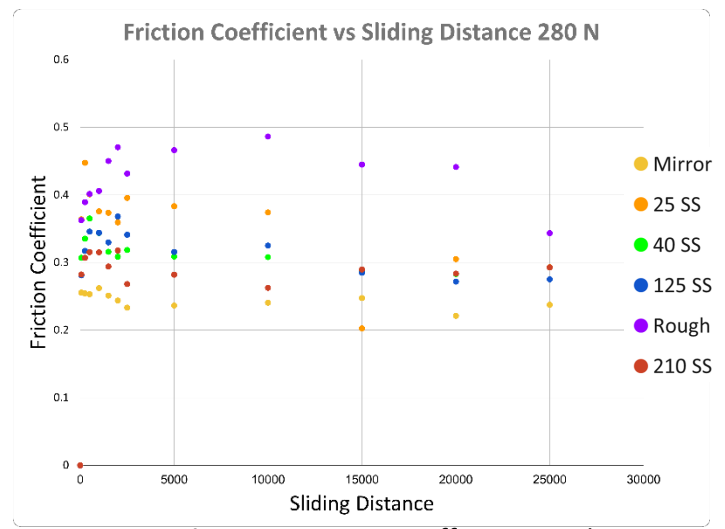


Figure 3. Friction Coefficient Results

Acknowledgments and References

I would like to express my gratitude towards Miami University graduate student Faysal Haque for their guidance and assistance in running tribometer tests. Thanks are extended to Brad Martin for facilitation in machining samples of and Karl Reiff for facilitation in machining counter samples. I would like to express my special gratitude and thanks to DuPont for supplying high-performance polymer samples for testing.

Wearable Body Smart Wireless Sensor Networks Through Implanted Communication System

Student Researcher: Allayah C. Hughes

Advisor: Dr. Deok H. Nam

Wilberforce University

Department of Computer Engineering

Abstract

Wearable body smart wireless sensor networks are revolutionizing the involvement of both doctors and patients in the modern healthcare system by extending the capabilities of physiological monitoring devices. The rapid advancement in ultra-low-power RF (radio frequency) technology enables invasive and non-invasive devices to communicate with a remote station. The purpose of this project is to provide an overview of current developments and future direction of research on wearable and implantable body area network systems for continuous monitoring of astronauts at the mars. This study shows the important role of body sensor networks in astronauts' activities and health conditions at the mars by In-body and On-body communication networks with a special focus on the methodologies of wireless communication between implanted medical devices with external monitoring equipment and recent technological growth in both areas.

Project Objectives

Body sensor network frameworks can help individuals by giving medical care administrations like clinical checking, memory improvement, control of home apparatuses, clinical information access, and correspondence in crisis circumstances. Ceaseless checking with wearable and implantable body sensor organizations will increment early identification of crisis conditions and sicknesses in danger patients and furthermore give a wide scope of medical care administrations for individuals with different levels of intellectual and actual disabilities.

Methodology

The significance of incorporating huge scope remote media transmission advances like 3G, Wi-Fi Mesh, and WiMAX, with telemedicine has effectively been tended to by certain analysts. There are as of now a few applications and models for this reason. For instance, some of them are considered for consistent observing of individuals experiencing intellectual issues like Alzheimer's, Parkinson's or comparative infections. A few papers center around fall discovery, act identification and area following, while others utilize natural and ecological sensors to recognize patients' wellbeing status. There is likewise a huge examination center around the improvement of minuscule remote sensor gadgets, ideally coordinated into textures or other wearable substances or embedded in the human body. The scope of wearable and implantable biomedical gadgets will increment fundamentally before long, on account of the enhancements in miniature electro-mechanical frameworks (MEMS) innovation, remote interchanges, and advanced hardware, accomplished as of late. These advances have permitted the improvement of ease, low force, multi-useful sensor hubs that are little in measure and can convey over brief distances, and small sensor hubs, which comprise of detecting, information handling, and imparting parts, and to exploit the possibility of sensor networks dependent on community exertion of an enormous number of hubs.

The associations with leads and links utilized in most current checking gadgets present clear downsides in that they limit the portability of patients and, what's more, they may cause skin disturbances or diseases, and accordingly add to crumbling of medical issue. Sensor networks consequently address a critical improvement contrasted with ordinary sensors. In spite of the way that a remote association isn't a prerequisite for physiological boundary checking with embedded sensors, the issue referenced above is one of the primary inspirations for this pattern to utilize remote innovation in current biomedical embedded frameworks. Instances of physiological information assortment stages with remote connections incorporate a wide scope of biomedical applications. For instance, have portrayed a framework for ceaseless remote intracavitary pressure observing of the bladder, while different creators have collected neural prosthetic gadgets.

One gadget will want to assemble a WSN with an enormous number of hubs, both inside and outside the human body that might be either predefined or irregular, as per the application. This vision must be applied using basic correspondence conventions for remote sensor organizations. The normalized equipment and programming structures can uphold viable gadgets, which are relied upon to essentially influence the up-and-coming age of medical care frameworks. A portion of these gadgets would then be able to be joined into the remote body zone organization (WBAN), giving new freedoms to innovation to screen wellbeing status.

Results

The ending result of obtaining a WBAN will increase the health care on a strategic pace providing more assistance to doctors, nurses, or anyone in assistance.

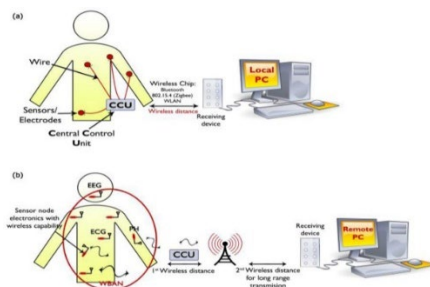


Figure 1

Acknowledgments

The author is grateful to the supervisor Dr. Deok H. Nam at Wilberforce University for his valuable support, encouragement, and guidance. I also thanks to Ohio Space Grant Consortium (OSGC) for the academic scholarship program. Special thanks to Mr. Robert Romero and Mr. Timothy Hale of OAI for OSGC Program.

References

- [1] S. Ullah, H. Higgin, M. Arif Siddiqui, and K. Kwak, "A Study of Implanted and Wearable Body Sensor Networks," arXiv:0911.1546v3, KES-AMSTA 08, LNAI 4953, Inha University, Korea, pp. 464 - 473. In [\[0911.1546v3\] A Study of Implanted and Wearable Body Sensor Networks \(arxiv.org\)](#)
- [2] G. Appelboom, et al. "Smart wearable body sensors for patient self-assessment and monitoring," Archives of Public Health 2014, 72:28, in <http://www.archpublichealth.com/content/72/1/28>
- [3] A. Darwish, and A. Hassanien, "Wearable and Implantable Wireless Sensor Network Solutions for Healthcare Monitoring," Sensors 2011, Vol. 11, pp. 5561-5595

Propulsion Systems for Future Hypersonic Flight

Student Researcher: Karli T. Katterle

Advisor: Dr. Jed E. Marquart

Ohio Northern University
Mechanical Engineering

Abstract

The next step for commercial flight is hypersonic flight, defined as traveling through the atmosphere at speeds greater than Mach 5. The propulsion system used in hypersonic flight will be similar to that seen in a rocket. However, different challenges will need to be met. Current challenges that are being seen in hypersonic flight include reducing shockwaves and disturbances. To determine what is being done currently, the NASA supersonic aircraft initiative will be examined. This research is intended to summarize the current challenges in hypersonic flight, potential solutions, and what is currently being done.

Project Objectives

The objective of this project is to better understand the challenges of reducing shockwaves and disturbances during hypersonic flight. By looking at the success of NASA's X-43A hypersonic flights at different Mach numbers, the results brought to light the possibility of using scramjet engines in hypersonic flight. They also showed challenges that need to be addressed in order for it to be successful.

Methodology Used

The process used to conduct this study included analysis of articles on the challenges in reducing shockwaves during hypersonic flight and the potential solutions that have been studied, as well as the impact X-43A's successful hypersonic flights had on the research for hypersonic vehicles.

Results Obtained

A milestone for scramjet engines occurred in 2004 when NASA's X-43A was successfully tested with a scramjet engine with hydrogen as fuel [1]. The goal of X-43A was to test and validate the performance during a hypersonic flight of a scramjet propulsion system [2]. Three X-43A vehicles with scramjet engines were tested: two at Mach 7 and one at Mach 10. The first flight at Mach 7 experienced a failure, whereas the second flight, at Mach 7, and the third flight, at Mach 10, were considered successful. The third flight of the X-43A proved that scramjet engines can work at flight conditions up to a Mach number of 9.68 [2]. This project gave confidence that hypersonic vehicles could be designed and flown successfully [2]. However, there was some behavior that occurred during the third flight at Mach 10 that showed that there is more flight research needed in order for hypersonic flight to be successful. The three test flights of the X-43A proved that scramjet engines can be successful and used in hypersonic flight. However, two issues were discovered during this test. The first issue was the acceleration of the X-43A during the test flight. At Mach number 7 the acceleration was very small, and by the time the Mach number was 10, the acceleration was zero [1]. The second issue is the discovery of a shock wave in the scramjet inlet. This shock wave can result in inlet unstart and unstable engine operation [1]. For development in hypersonic flight as well as a successful engine used in hypersonic flight, these two issues need to be considered.

There is a critical operation point for any scramjet engine under certain inflow conditions. If a scramjet is operating with a heat release over the critical operation point, compression waves traveling upstream will continue to get stronger and create a shock wave [1]. This is what is occurring during scramjet engine testing under conditions that they would be experiencing in hypersonic flight. In order for the shock waves to be reduced, the inflow Mach number needs to match the heat release reaction [1].

Additionally, the inlet flow Mach number needs to be greater than a specified Mach number (the critical Mach number) to prevent a shock wave from traveling into the inlet and causing unsteady combustion and engine surging [1]. The critical Mach number varies with the equivalence ratio. The equivalence ratio is the ratio of actual fuel to air ratio divided by the stoichiometric fuel to air ratio. However, even with varying the equivalence ratios, the critical Mach number still tends to be higher than 3 for hypersonic propulsion [1]. This makes it difficult for scramjet engines because they are typically designed to have inlet flow Mach numbers between 2.5 and 3.5 [1]. This is what is most likely causing unstable combustion and shock waves traveling upstream at inlet entrances in scramjet engines. To maintain stable combustion, low equivalence ratios are chosen; this is not acceptable for hypersonic flight. With low equivalence ratios, the engine thrust is significantly reduced [1]. A proposed engine that has the potential to work during hypersonic flight is the sodramjet engine, also called the standing oblique detonation (SOD) engine. The sodramjet engine is considered ramjet-based hypersonic propulsion but behaves differently due to its high thermo-efficiency, simple combustor structure, low inflow compression loss, and stable engine operation [1]. A design parameter of the sodramjet engine is having an inlet flow Mach number higher than the critical Mach number [1]. By keeping the Mach number for the inlet flow above the critical Mach number, shock waves will not travel upstream into the inlets, and a stable and self-sustainable standing oblique detonation can be generated. [1].

Significance and Interpretation of Results

Even though both scramjet engines and sodramjet engines have the potential to be used in hypersonic flight, sodramjet engines have more advantages. Compared to the scramjet, the sodramjet engine has better thermal efficiency. The sodramjet thermodynamic process is nearly constant volume compared to the scramjet thermodynamic process, which has constant pressure. A constant volume cycle has a 50% higher thermal efficiency than a constant pressure cycle [1]. The second advantage is the sodramjet engine has a smaller combustor size, which reduces the drag force acting on the combustor walls [1]. The third advantage is the sodramjet engine has a lower inlet flow compression loss compared to the scramjet engine. Because sodramjet engines need an inlet flow Mach number greater than 5 compared to the scramjet engine needing an inlet flow Mach number between 2.5 and 3.5, the inlet flow compression loss is reduced greatly in the sodramjet engine [1]. Another advantage of the sodramjet engine is the thermal load reduction on the combustor. The shorter combustor of the sodramjet engine reduces the thermal load as well as prevents heat loss from the combustor [1]. For hypersonic flight to be successful, there are still challenges that need to be overcome, however, from the success of the hypersonic flight of X-43A using a scramjet engine to the sodramjet engine that has most recently been proven to be successful in hypersonic flight, hypersonic vehicles can be designed successfully.

Acknowledgments and References

- [1] Z. JIANG, Z. ZHANG, Y. LIU, C. WANG, and C. LUO, "Criteria for hypersonic airbreathing propulsion and its experimental verification," *Chinese Journal of Aeronautics*, vol. 34, no. 3, pp. 94–104, Mar. 2021.
- [2] L. Marshall, C. Bahm, G. Corpening, and R. Sherrill, "Overview with results and lessons learned of the X-43A mach 10 flight," *AIAA/CIRA 13th International Space Planes and Hypersonics Systems and Technologies Conference*, 2005.

An Affordable Way to Simulate and Test Space Robots in Virtual Reality

Student Researcher: Conrad M. Kent

Advisor: Catharine L. R. McGhan, Ph.D.

The University of Cincinnati

Department of Aerospace Engineering and Engineering Mechanics

Abstract:

This project developed a method that allows robots to be displayed and controlled in virtual reality (VR) using ROS+Gazebo, a robot simulation platform, OpenVR API, and consumer grade, affordable hardware. This project leveraged prior work by UC's AS4SR lab to get ROS+Gazebo to work with Vrui and OpenCV for an older single-display headset on a single desktop system running Ubuntu Linux, and ongoing work to expand this to using OpenVR and newer dual-display VR headsets. The project then focused on making an example scenario which simulates the user working alongside robots in VR. The user is able to give robots waypoints to travel, control them directly, and pass equipment back and forth to them.

The developed package can be easily adapted to other robot simulations in ROS by other research or educational organizations, as it largely consists of free and open source code (OpenVR, ROS+Gazebo, and Ubuntu Linux). It can also be used to perform human factors testing or other space robotics research, for the cost of a commercial VR headset and a single VR-capable desktop computer. The package for this new project is called `openvr_headset_ros` [1].

Project Objectives:

The goal of this project was to allow for VR headset and controller tracking and the proper scene display of simulated space robotic systems in a Gazebo environment, by modifying and updating the original AS4SR lab code to work with SteamVR for Linux (via the OpenVR API) and newer dual-display headsets under Ubuntu with newer versions of ROS+Gazebo; this baseline functionality was achieved by the end of Summer 2021. The project then continued on into the fall, post-funding, as part of an undergraduate research course at UC, with a focus on making more advanced example scenarios that allow the user to work alongside simulated robots in VR. The goal was to make the user be able to interact with the robots in several different modes, designing and implementing several VR controller-based button and menu schemes, including the ability to give up to three robots waypoints, control them directly (VR controller tracking and inputs piped to ROS), and pass modeled equipment back and forth to simulated rovers from the human's "hand" (complex interactions with the robot models and scenes). These extended objectives were achieved by the end of the fall semester.

Methodology Used:

In 2018, Zhenyu Shi, an AS4SR lab grad student, completed the `vrui_mdf` package for ROS Kinetic+Gazebo in native Ubuntu Linux 16.04 for the HTC Vive, using Vrui with the early SteamVR beta [2]. The basics of the old `vrui_mdf` package were reused for this project (mainly code for positioning a stereoscopic camera in the Gazebo simulation and receiving a feed of images from that simulated camera to display in the VR headset). However, Vrui only supports single-display headsets, and with the only single-display commercial headset being the old HTC Vive (no longer available for purchase), there needed to be a move away from using Vrui in order to support modern VR headsets. This prompted a shift to using OpenVR with SteamVR; all use of Vrui was removed, and all other outdated ROS code was

updated from Kinetic to Noetic and the newest version of Gazebo for Ubuntu 20.04. This move away from using Vrui required a massive rewrite of the code for the image pipeline, as well as learning about not only how VR hardware works, but also how to use several software libraries to support hardware interfacing and interactive control and display (ROS, Gazebo, OpenCV, OpenVR). Code for tracking the position of the VR headset and controllers was also heavily modified to work with the OpenVR libraries, instead of Vrui. (Some code from `openvr_ros` was referenced as a helpful model for OpenVR position tracking [3], but `openvr_ros` did not include examples for the display of images to the headset.) This use of OpenVR allows the package to be used with a wide variety of headsets, under any operating system supporting OpenVR/SteamVR and ROS+Gazebo. An existing scenario was also updated from `vrui_mdf` to `openvr_headset_ros`, which allowed the user to control a simple rover by teleporting it, commanding waypoints to travel to, and controlling its velocity and turn rate directly by moving the VR controller.

After the basic package was finished, more interaction scenarios, and a menu system and several new input mappings for the VR controllers, were created during the fall semester, including control of a quadcopter in valley terrain, control of multiple rovers, and interaction with models in the simulation environment (passing an object to the rover).

Results Obtained:

A desktop system with an 8 core AMD Ryzen 7 2700x Processor, AMD Radeon RX 5700XT graphics card, and 32GB of RAM was used for all simulations. Performance in all scenarios tested (up to the three-robot simulation) had high enough framerates to be comfortable to view through the VR headset, although the quadcopter and rover models used are not particularly demanding. All aspects of viewing and interaction with the robots are functional; the control methods are currently basic and simple for ease of use, but could be further refined [1].

Significance and Interpretation of Results:

Both the HTC Vive and Vive Pro headsets are verified to work with this codeset, as well as the Lighthouse 1.0 and 2.0 tracking units. Adaptation of the headset configuration files to support other SteamVR headsets should be straightforward. The code is open-source, well commented, and can quickly be adapted to visualize existing ROS robot simulations in VR. While the scenarios tested in this project were simple, they should provide an easy toolchain for adapting other robots and simulations in ROS for VR use. (A lunar surface model was tested, but requires a more capable rover for traversal.) Extending the interaction and control functionality to other robots would be slightly more work, requiring a remapping of the current controller UI and buttons to the specific ROS topics for that robot. Future work will also involve testing `openvr_headset_ros` in more computationally-intensive scenarios to assess its performance, and possibly find ways to improve the framerates and resource use.

Figures/Charts

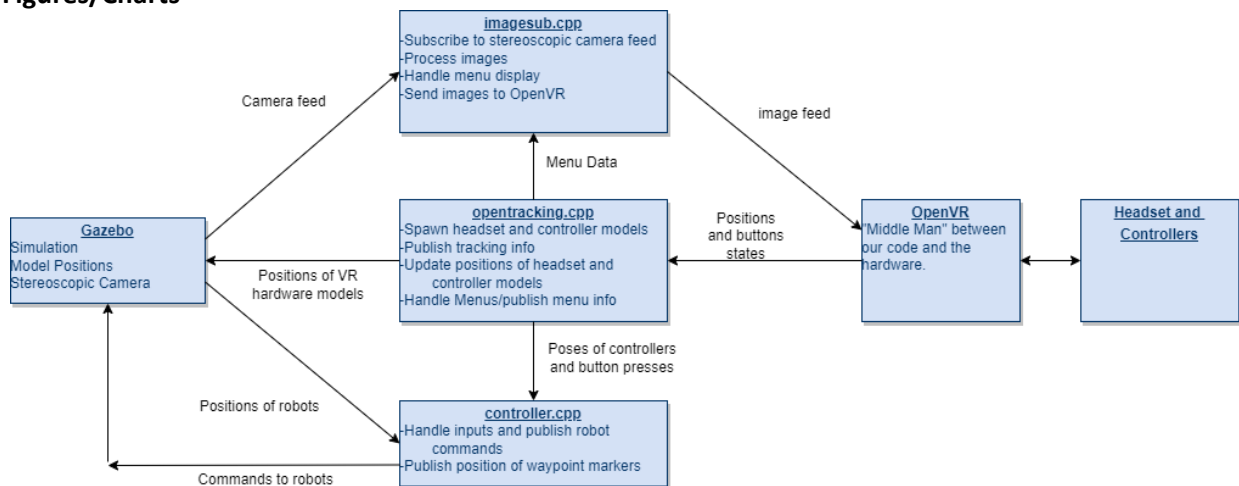


Figure 1: A diagram of how the code works.



Figure 2: A screenshot from a simulation of three controllable robots in VR.

Acknowledgements

I would like to thank my advisor, Dr. Catharine McGhan, for her support, as well as Zhenyu Shi for the original vrui_mdf, and the teams which created the open source code that I referenced.

References:

- [1] Kent, C., "openvr_headset_ros", code repository for this project, Dec 7, 2021. https://github.com/ConradKent/openvr_headset_ros
- [2] Shi, Z., "vrui_mdf", code repository, Apr 6, 2020. https://github.com/zhenyushi/vrui_mdf
- [3] Sharif, M., "openvr_ros," code repository, Nov 19 2019. https://github.com/sharif1093/openvr_ros

Lindenmayer System Renderer and Parser

Student Researcher: Zion Klinger

Advisor: Dr. Chad Mourning

Ohio University
Computer Science

Introduction

Lindenmayer Systems (L-Systems) were first suggested as a method for generating 3-dimensional models of herbaceous and arboreal plants by Prusinkiewicz, Lindenmayer, and Hanan in 1988. This work was inspired by Lindenmayer's previous work developing L-Systems for modeling the development of filamentous organisms. L-Systems were a significant departure from previous work on modeling plant geometries as they focused on the development of the plant's geometry by a series of discrete rules rather than attempting to create the model in one monolithic step (Prusinkiewicz et al.). An important characteristic of L-Systems is their generality and ability to create many different pseudo-fractal structures such as the Highway Dragon (Tabachnikov) or Sierpinski triangle (Mandelbrot). Genetic Algorithms are a class of algorithms which take inspiration from the biological mechanisms of mutation, crossover, and selection (Mitchell). Typical genetic algorithms work by simulating a "population" which are individually run through a "fitness test" where they are rated based on their fitness. The best performers are allowed to pass down their algorithmic genes to the next generation, with random mutations added in to increase diversity. This process repeats until a certain fitness score is achieved or a specified number of iterations have been run (Mitchell).

Abstract

This project aimed to create a genetic algorithm that utilizes an L-System grammar as its genome and takes environmental factors such as light and gravitational effects on the growth of woody trees into account to generate plausible tree species that could evolve from Earth plants in a terraformed Martian environment. When implemented, this algorithm would repeatedly generate trees using a set of L-System Genomes and then rate them based on the amount of net "energy" they have collected for seed production. This metric would be calculated as the difference between the amount of light energy that the tree is able to collect with its leaves and the energetic cost of growing its branches and leaves. Trees that are more reproductively successful would make up a larger portion of the subsequent generation. Each generation would also introduce random mutations to the L-System Genomes, and apply a small reproductive penalty to genomes that have remained dominant for multiple generations. These will add variation to the gene pool and prevent a "cheap" and "safe" genome from dominating for more than a few generations respectively. The implementation of this genetic algorithm depends on the development of an L-System parser and renderer which is where the majority of the development time was spent.

Methodology

Lindenmayer systems produce a string of characters, both Edge characters and Control characters, which are used as a set of instructions for a Turtle Graphics renderer. L-systems are described as a context aware parallel rewriting grammar, which means that they satisfy several specific requirements (Prusinkiewicz et al). Context aware implies that when rewriting an edge we must take into account the surrounding edges. Parallel indicates that the order of the rewrites does not affect the resulting string which then implies that rewrites may be executed simultaneously and still resolve to the same string which is useful for performance optimizations. Any given L-System consists of three components: the Alphabet (V), the

Axiom (ω), and the Productions (P) (Prusinkiewicz et al). The Alphabet consists of the set of all of the possible edges represented by capital Latin Alphabet characters (F, G, L, P, Q, etc.) (Prusinkiewicz et al). The Axiom is the initial string which is iteratively rewritten (Prusinkiewicz et al). Finally the Productions are the rules that take a context unaware edge or a context aware edge plus its context and map them to a successor string (Prusinkiewicz et al). In addition to the Alphabet there are several control characters which only appear in successor strings and are ignored by the parser (Prusinkiewicz et al). These control characters exist to provide the turtle renderer with rotation, stack, and diameter manipulation instructions (Prusinkiewicz et al).

During each iteration every edge is first inspected to see if there are any context aware rules that might apply to it (Prusinkiewicz et al). If there are no context aware rules applicable we check the context unaware mapping for an appropriate successor to the edge (Prusinkiewicz et al). If there are no context aware or unaware rules, the edge remains the same (Prusinkiewicz et al). A production "G -> BB" would transform the string "GG" to the new string "BBBB" as each edge "G" is mapped to the edges "BB" (Prusinkiewicz et al). The production "AC -> FF" indicates that "B" will be rewritten as "FF" when its left context is "A" and its right context is "C" (Prusinkiewicz et al).

The result of these rewriting iterations is a string of instructions that the turtle renderer will utilize to create a 3-Dimensional model (Prusinkiewicz et al). The string generated by an L-System is utilized as a set of instructions for a Turtle Graphics renderer (Prusinkiewicz et al). The turtle is a simple state machine with that and holds information about current heading, previous and next branch diameters, and branch length (Prusinkiewicz et al). The "turtle" takes directions from the string one at a time. Edges result in a branch segment being created according to the state of the turtle (Prusinkiewicz et al). Control characters do not result in a drawn branch, but change the appearance or orientation of the subsequent branch segments by altering the state of the turtle (Prusinkiewicz et al). Opening Brackets cause the state of the turtle to be saved to a stack. Closing brackets overwrite the current state with the state from the top of the stack without drawing a branch (Prusinkiewicz et al). This is what facilitates the branching structures required for trees.

Results

Although this project is still a work in progress we were able to create a renderer that is able to parse and generate geometry for L-Systems. This revealed a number of characteristics about L-Systems that will be helpful in our future work on this topic. Since Lindenmayer systems are able to produce arbitrary pseudo-fractal structures it is likely to be very difficult to guarantee that a given grammar will produce a tree-like structure without parsing and generating its geometry. We then also have the difficulty of verifying that an arbitrary mesh is a tree structure. Finally, L-Systems have the property that they are very sensitive to starting conditions with a single character change in a successor string potentially resulting in a markedly different result.

Future Work

In the future I intend to continue my work on the Genetic algorithm and generating L-System genomes. Adding features to the L-System generation that facilitate small adjustments to the final mesh will be essential for creating a system of mutations. Additionally, the rating mechanisms for determining the reproductive success of a tree will need to be implemented.

References

- Lindenmayer, Aristid. "Mathematical Models for Cellular Interactions in Development II. Simple and Branching Filaments with Two-Sided Inputs." *Journal of Theoretical Biology*, vol. 18, no. 3, Mar. 1968, pp. 300–315, 10.1016/0022-5193(68)90080-5.
- Mandelbrot, Benoît. *The Fractal Geometry of Nature*. New York, W.H. Freeman And Company, 2006.
- Mitchell, Melanie (1996). *An Introduction to Genetic Algorithms*. Cambridge, MA: MIT Press. 9780585030944
- Prusinkiewicz, Przemyslaw, et al. "Development Models of Herbaceous Plants for Computer Imagery Purposes." *ACM SIGGRAPH Computer Graphics*, vol. 22, no. 4, Aug. 1988, pp. 141–150, 10.1145/378456.378503
- Tabachnikov, Sergei. "Dragon Curves Revisited." *The Mathematical Intelligencer*, vol. 36, no. 1, 20 Dec. 2013, pp. 13–17, www.personal.psu.edu/sot2/prints/DragonCurves.pdf, 10.1007/s00283-013-9428-y. Accessed 26 Mar. 2021.

Thermally Conductive and Lightweight Composite Materials Designed with Hexagonal Boron Nitride Nanosheets

Student Researcher: Tanner Larson

Advisor: Geyou Ao, Ph.D.

Cleveland State University
Department of Chemical and Biomedical Engineering

Abstract

Hexagonal boron nitride (hBN) nanosheets are lightweight (density $\approx 2.12 \text{ g/cm}^3$), two-dimensional nanostructures that are mechanically robust and have superior thermal and chemical stabilities.[2] These properties are desirable for many applications, such as developing advanced composite materials for equipment protection and efficient heat management. Particularly, the high thermal conductivity of hBN nanosheets (i.e., $360\text{-}600 \text{ W/mK}$),[1] which is similar to that of copper (ca. 390 W/mK), coupled with its electrical insulating property is unique for developing certain thermal management applications that require thermally conductive and electrically insulating materials. To be able to utilize the superior properties of hBN nanosheets, high quality dispersions within a wide range of solvents are necessary. In this work, we have developed methods to produce hBN dispersions with improved quality and yield in various solvents, such as water, alcohol, and acetone, through ultrasonication with the assistance of DNA and natural polysaccharides such as pectin. hBN dispersions are characterized by UV-vis absorption spectroscopy and Tyndall effect that demonstrates distinct light scattering by suspended colloids.[3] Solid hBN assemblies of films and fibers can be fabricated through liquid phase processing. This project will lead to the design and manufacturing of strong and thermally conductive films and composite materials, which can be potentially utilized in high temperature and hazardous environment as well.

Project Objectives

Due to the poor dispersibility of nanomaterials, the objective of this project was to create high quality dispersions of boron nitride nanosheets (BNNSs) using a noncovalent surface modification approach by combining the optimal solvents and dispersing agents. These dispersions will subsequently be employed to construct assemblies with improved thermal properties for effective heat management. To achieve this goal, I have tested the dispersion of BNNS using natural DNA and pectin in various solvents including deionized water, alcohols, and acetone. Alcohols include methanol (MeOH), ethanol (EtOH), and isopropyl alcohol (IPA). The dispersion methodology developed in this work can be extended to the processing of one-dimensional boron nitride nanotubes (BNNTs) as well.

Methodology Used

1 mL dispersions of BNNSs were created using hBN powder (AC6004, Momentive Performance Materials) with natural DNA (D3158, Sigma-Aldrich) and pectin from citrus peel (P9135, Sigma-Aldrich), respectively. The initial concentration of hBN in each dispersion was kept constant while varying the hBN:dispersant mass ratio. Each sample was probe tip sonicated (model VCX 130, Sonics and Materials, Inc.) for 1 hour at a power level of 8 W. The supernatant was collected after centrifugation of BNNS dispersions. Each dispersion was characterized by Tyndall effect and UV-vis absorbance measurements (model V-760, Jasco Inc.).

Results Obtained

Figure 1a shows the light scattering effect (i.e., Tyndall effect) that indicates a stable colloidal suspension of BNNs. Additionally, UV-vis absorbance spectra for each sample was measured (Figure 1b). The dispersion quality of each sample was characterized by observing the BNNs absorption peak at 205 nm wavelength.[4] DNA was shown to produce the optimal dispersion quality when compared to pectin and was able to produce stable dispersions in various solvents including water, acetone, and methanol. As shown in Figure 1c, pectin stabilized BNNs dispersions were further explored by determining the dispersion quality at different initial mass ratios of hBN:pectin. It was found that although pectin can potentially be an effective dispersion agent for hBN, increasing the starting concentration of pectin in dispersions did not result in increased dispersion yield and quality of BNNs. Further experiments using BNNs provided much more promising results regarding dispersibility in aqueous solution using pectin.

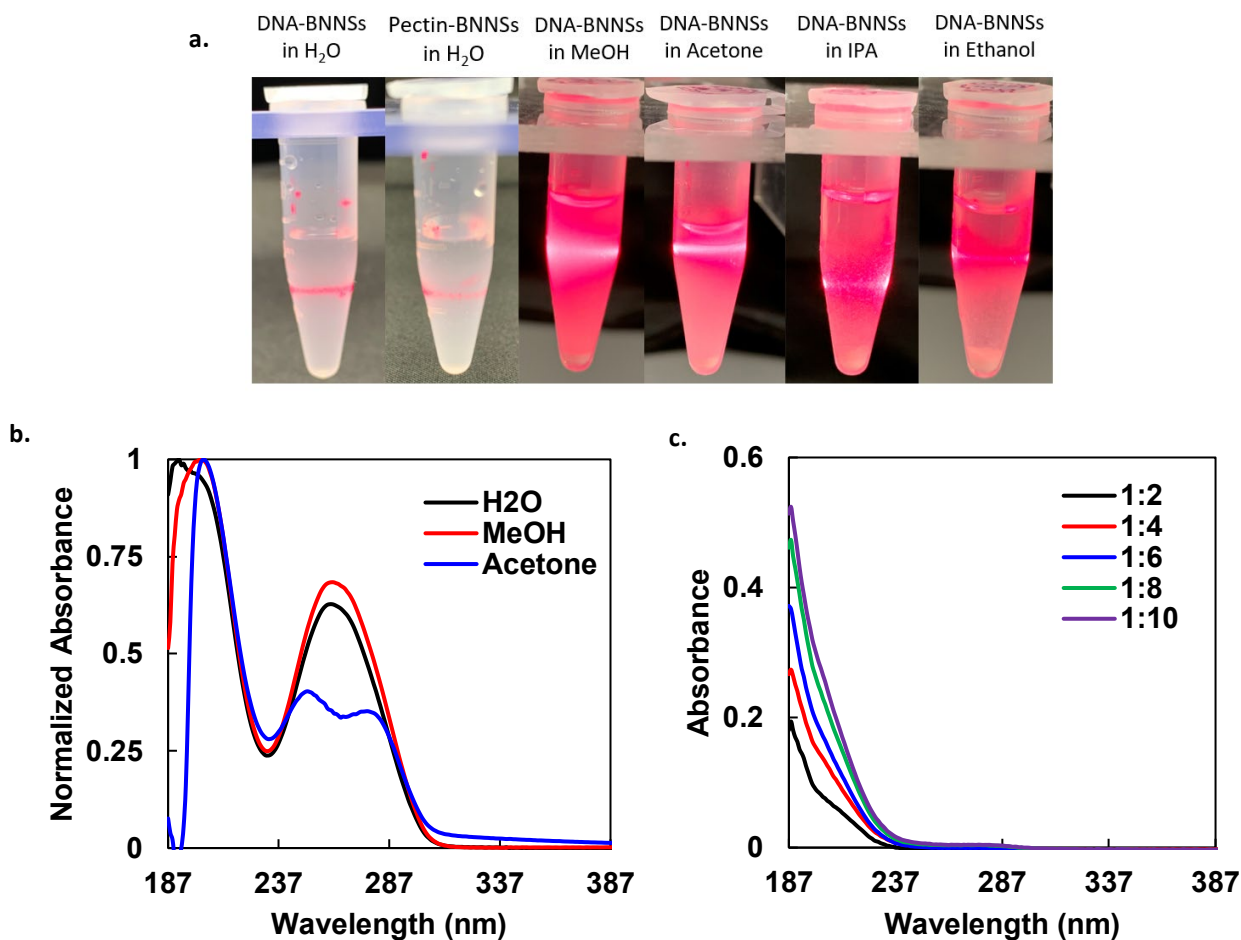


Figure 1. Characterization of BNNs dispersions. (a) Tyndall effect of BNNs dispersions stabilized by DNA and pectin, respectively, in various solvents. Absorbance spectra of (b) DNA-coated BNNs in water, MeOH, and acetone and (c) pectin-coated BNNs in water at different hBN:pectin mass ratios.

Significance and Interpretation of Results

Our results demonstrate that DNA and pectin can potentially disperse hBN effectively in aqueous solution. Stable dispersions of DNA-BNNSs can potentially be obtained in MeOH as well. This is evident by the characteristic 205 nm absorption peak of BNNSs and the light scattering effects of dispersions. With a stable BNNS dispersion, further work can be conducted to develop thermally conductive films and other composite materials.

Acknowledgements and References

I would like to acknowledge the Ohio Space Grant Consortium for the Undergraduate STEM Scholarship that contributed to furthering my education and making this project possible. I would also like to express my deepest gratitude to Dr. Ao for her support, guidance, and for continuing to spark my curiosity.

- [1] Jo, I., Pettes, M. T., Kim, J., Watanabe, K., Taniguchi, T., Yao, Z., & Shi, L. (2013). Thermal conductivity and phonon transport in suspended few-layer hexagonal boron nitride. *Nano Letters*, *13*(2), 550–554. <https://doi.org/10.1021/nl304060g>
- [2] Nag, A., Raidongia, K., Hembram, K. P. S. S., Datta, R., Waghmare, U. V., & Rao, C. N. R. (2010). Graphene analogues of BN: Novel synthesis and properties. *ACS Nano*, *4*(3), 1539–1544. <https://doi.org/10.1021/nn9018762>
- [3] Kraemer, E., & Dexter, S. (2002). The Light-Scattering Capacity (Tyndall Effect) and Colloidal Behaviour of Gelatin Sols and Gels. *Journal of Physical Chemistry*, *645*(1910).
- [4] Kode, V., Thompson, M., McDonald, C., Weicherding, J., Dobrila, T., Fodor, P., Wirth, C., & Ao, G. (2019). Purification and Assembly of DNA-Stabilized Boron Nitride Nanotubes into Aligned Films. *ACS Appl. Nano Matter*, *2*, 2099–2105.

Quadcopter Stability Varying Arm Dihedral and Motor Twist

Student Researcher: Sebastian J. Lemieux

Advisor: Dr. Kelly Cohen

University of Cincinnati
Aerospace Engineering

Abstract

Many commercially available Unmanned Aerial Systems (UASs) incorporate some amount of angle on their motor arms to improve dynamic stability in varying flight conditions. To improve the stability and yaw authority of a conventional multirotor, this research seeks to make discrete changes in motor position by varying motor twist and motor arm angle relative to the main multirotor body. This will change the thrust vector of each motor relative to the quadcopter body to allow for greater control authority in roll, pitch, and especially yaw. The small UAS used in this research will utilize a custom designed aluminum arm mount that allows for 5-degree angle changes to the angle of the platform's tube arms up to 15 degrees. Both the angle of the motor arms on the quadcopter and twist of the motors on each arm will be changed in a design of experiments to evaluate the combined effects on stability and controllability. First, Ardupilot's autotune is used in each configuration to obtain an optimal tune of the flight controller. Next, autonomous evaluation flights are flown to gather stability data in as consistent flight conditions as possible. Gyro data, accelerometer data, and desired versus actual rates are then compared from each flight log and used to quantify both the stability and the level of controllability of the UAS. The results of this research may hopefully provide insight to the effects of these changes on a quadcopter's motor position and be implemented to create a UAS with more robust stability.

Project Objectives

The goal of this project is to evaluate the effects that arm angle and motor twist changes have on the flight stability of a multirotor UAS. This project seeks to use discreet 5-degree angle changes of a UAS's arm angle and discreet angle changes to the motor twist to measure the stability and tracking error effect on a controlled flight of the UAS. This data would be used in a design of experiments to determine the optimum arm angle for this UAS as well as correlate arm size and motor angle to predict optimum angle and twist values for UASs of different sizes. This will require a well-constructed data collection method to quantify the stability of the multirotor UAS and compare across combinations of motor twist and arm angles.

Methodology Used

A custom UAS nicknamed "Archimedes" (Figure 1) was used as the primary testing platform in this project. This UAS was a 2.27 kg platform with 4 motors set in a standard quadcopter configuration. This multirotor used a custom aluminum arm mount that allowed each arm to be changed from -15 to +15 degrees of tilt in 5-degree increments (Figure 2). This arm mount clamped to a carbon fiber tube arm where each brushless motor was mounted. The tube mount of each brushless motor allowed for free rotation in plane with the body frame (Figure 3). This applied each motor with a thrust vector in the yaw direction, giving greater yaw authority than a conventional yaw control from the counterrotation force of each motor. The rotation of each motor was measured with an angle finder and changed in one-degree increments.

Once the desired arm angle and motor twist angles were set the multirotor would go through an Ardupilot autotune flight to obtain the optimum values for the PID controller on the Pixhawk flight controller. This flight sends the UAS through varying roll, pitch, and yaw maneuvers and changes the PID tuning values on the Pixhawk based on the UAS's response. Once this was complete, the multirotor would go through an autonomous evaluation flight in an hourglass and rectangular waypoint mission (Figures 4 and 5). This flight path included altitude changes along the waypoint path to maximize the variation in flight conditions during evaluation. The gyro data, accelerometer data, and desired versus actual position/rates were recorded. This data was pulled from the flight log of the Pixhawk flight controller and parsed using a MATLAB script to gather the necessary data on performance. A post flight analysis was done within the MATLAB script to derive the FFT of the flight gyro data, waypoint tracking error along, attitude tracking error, and a mean absolute deviation, as shown below, of each error as a quantified metric of controllability and stability of the platform.

$$\frac{1}{n} \sum_{i=1}^n |x_i - m(X)|.$$

This data was combined with basic weather, pilot, and flight condition information input in a google spreadsheet filled out via a QR code on the UAS. The MATLAB script pulled the error and flight data results into this spreadsheet so flight data at varying arm angles and motor twists could be compared.

Results Obtained

The initial mean absolute deviations of the system (Figure 6) were limited to 1.0 to 1.5 degrees of deviation, which has been shown to be an acceptable level of deviation for a stable system using PID control [1]. However, in order to autotune the UAS to obtain these deviation results, the flight time of the UAS needed to be increased significantly, from an average 6-8 minutes to 15-16 minutes. This was done through a combination of battery improvements and motor changes to a 750 kv KDE brushless motor and 20,000 mah battery. The larger motor and battery combination did create some yaw instabilities during the autotune flights, shown in the command yaw vs. actual yaw deviation values. These were still within our acceptable range of deviation with a maximum mean absolute deviation of 1.319, but further work will need to be done to mitigate these yaw instabilities.

Initial flights along the 2 waypoint paths were obtained and showed the UAS "Archimedes" was able to remain within the stability range for each flight path. This was done in the original arm configuration of the system at 2 degrees on arm angle and 0 degrees of motor tilt. This showed promise for moving forward with the custom arm mounts. Unfortunately, due to some challenges in manufacturing the main aluminum body connections of the arm mount we were unable to obtain results varying in a combination of arm angle and motor twist. Further alterations are underway to create these mounts for Archimedes and allow for an appropriate range of testing conditions.

Significance and Interpretation of Results

These results show promise for the multirotor "Archimedes" to conduct this research and test the effects of arm angle and motor twist on multirotor UASs. Further tuning is needed to consider this platform ready for strenuous testing of varying flight configurations. The test methodology and data collection method of this research will remain unchanged as they prove proficient in providing data to quantify controllability and stability in multiple flights of Archimedes. The results of this research show that changes in motor size and propeller size in conjunction with arm angle and motor twist have a greater effect than originally anticipated on the stability of the platform. These variables will need to be

considered when predicting an optimal motor twist and arm angle configuration for UAS's outside the scope of "Archimedes".

The results of this research may hopefully be implemented on future UASs to create improved multirotor arm designs that provide better stability and controllability for a wider range of flight conditions.

Figures/Charts



Figure 1. Archimedes Platform



Figure 2. Custom Arm Mounting Bracket

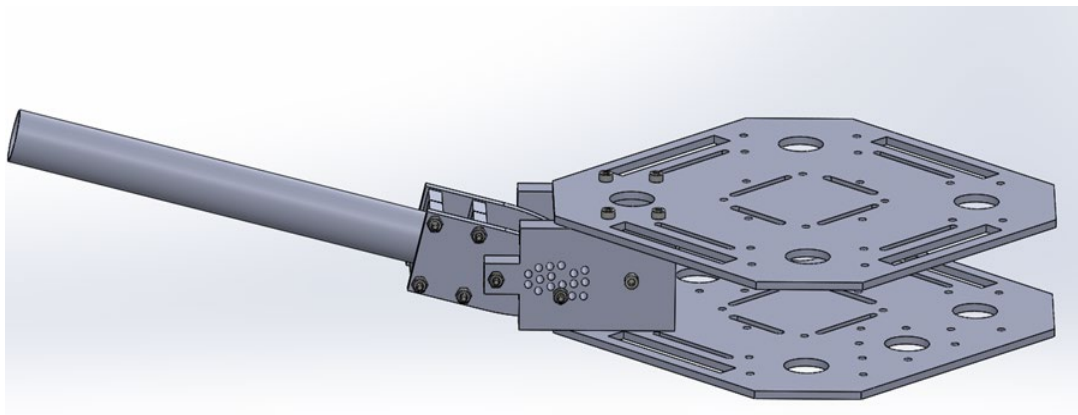


Figure 3. Arm Bracket on Archimedes Plates



Figure 4. Square Waypoint Mission

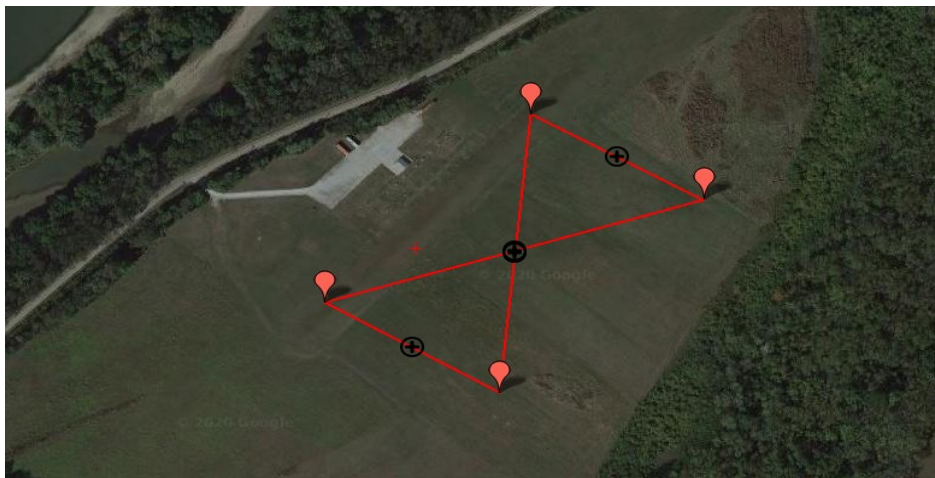


Figure 5. Hourglass Waypoint Mission

	Flight				
Mean Absolute Deviation	1	2	3	4	5
Command Roll Vs Actual Roll	0.7605442442	0.6607687537	0.5912619411	0.580201614	0.3160057419
Command Pich vs Actual Pitch	1.109487847	0.5747793461	2.633200525	3.043792276	0.40637696
Command Yaw vs Actual Yaw	5.629751621	3.353592107	2.688473317	2.621853592	7.17442149

Figure 6. Stock Archimedes Deviation Results

Acknowledgments

My thanks go to Dr. Kelly Cohen for his help and guidance, Heath Palmer for his thesis research work that directs and guides this project, and to the Ohio Space Grant Consortium who made this possible.

References

1. Mardan, Maziar, et al. "Attitude and Position Controller Design and Implementation for a Quadrotor." *International Journal of Advanced Robotic Systems*, vol. 14, no. 3, 18 Nov. 2016, pp. 1–11., doi:10.1177/1729881417709242.

A 3D Visualization of Errors in GNSS Constellations

Student Researcher: Daniel Lipec

Advisor: Dr. Chad Mourning

Ohio University
Computer Science

Abstract

This project aimed to create a 3D depiction of the accuracies of multiple Global Navigation Satellite System (GNSS) constellations. This data visualization allows the comparison of four major constellations (GPS, Galileo, GLONASS, and BeiDou) and allows the user to immediately compare the accuracies of each constellation. The data visualized will consist of the errors in the positions produced by these constellations, i.e., the difference between the data received and the surveyed position of the receivers. The visualization also highlights the maximum error so far in the dataset visually as well as displaying the current error distance in text. The user can select to hide certain constellations and adjust the playback speed of the recorded data.

Objective

The visualization of GNSS errors is important because it allows the immediate comparison of the accuracies in these constellations, not all constellations are created equal, and most modern devices use multiple constellations to provide accurate data. Modern survey equipment uses all four of these constellations to find positioning data, and most modern phones have receivers for these four constellations and others. Accurate GNSS data is used for a variety of other applications, including precision agriculture and defense systems. The visualization of these errors allows industry professionals as well as interested users to see at a glance how these systems are performing. This becomes especially useful in the case of atmospheric events such as solar flares; the comparison will make it easy to see how each constellation handles anomalies and may facilitate the progression of positioning technology. This project can also be used as an educational tool to teach how the constellations work and the general accuracy of GNSS constellations.

Methodology

The data used for the visualization comes from the receivers used for gnssperformancemonitor.com, a project overseen by Dr. Michael Braasch. This system consists of four ublox GNSS receivers located at Stocker Center at Ohio University. This system has been collecting data since December 2018 and collects one data point from each constellation every second. The error data comes in the form of ENU coordinates relative to the actual position of the receivers.

Results

The current version of the project includes all the features mentioned in the abstract, but currently only runs on recorded data. In the future, this project will be expanded to include live data as it is received from the GNSS receivers in real time. The visualization of data from known atmospheric anomalies will also be incorporated in the future. This will allow the direct comparison of how these constellations respond to sub-optimal conditions. The incorporation of dilution of precision (DOP) data is also planned. DOP values estimate the reliability of the positions received from the constellations based on factors such as the geometric position of the satellites in the sky. The addition of these data points to the visualization will allow the user to see how accurate DOPs are at estimating the accuracy of the data.

Trustworthy Analysis of Recent Debris Cloud Conjunction Events Using an Adaptive Monte Carlo Forecasting Platform

Student Researcher: Alexandra P. Mangel

Advisor: Dr. Mrinal Kumar

The Ohio State University
Aerospace Engineering

Abstract

Every untracked, inactive, or unfamiliar object in Earth's orbit poses a risk to satellites and rockets that wish to safely navigate through space. Objects of this nature, known as "space debris", will remain in orbit without deliberate intervention. The purpose of this project is to perform a highly accurate retrospective analysis of a certain outstanding close-approach event (also known as a conjunction event) that occurred in the geostationary belt. It is expected that the successful completion of this work will result in a trustworthy prognostics tool that can help minimize, or even eliminate, such risk in the future. Events related to candidate resident space objects were considered, and the 2016 Briz-M rocket body explosion was chosen as the particular event of interest. By appropriately modeling the motion of such candidates through astrodynamics analysis and adjusting the initial conditions to reflect sensor precision, a recently developed Adaptive Monte Carlo method, a MATLAB-based forecasting platform, can be employed to propagate a particle cloud representing the object's orbit over time. The completion of this project will validate the methods used, while simultaneously reducing the risks of collision and damage in similar events in the future.

Project Objectives

More than 27,000 objects are currently being tracked by the Space Surveillance Network, but the quantity of orbital debris continues to grow. It is infeasible to continuously monitor all tens of thousands of these resident space objects (RSOs) to ensure a particular orbiting body has a safe path forward for its operational lifetime. Space Situational Awareness (SSA) is the intersection between analysis within the space domain and surveillance of satellites and their surrounding environment [1]. SSA includes methods used to guide autonomous systems through potentially hazardous environments by determining the likelihood of risk, particularly of collision with other objects. The Adaptive Monte Carlo (AMC) platform has been used to create trustworthy SSA by successfully capturing the motion of objects in orbit with this controlled level of accuracy [2].

The focus of this research is an analysis of a particular event of interest in GEO, namely the 2016 Briz-M rocket body breakup. The goal is to determine the probability of collision between the fragments resulting from the explosion. The strategy is to utilize the AMC platform, coupled with an appropriate quantity of interest (QoI), to propagate the orbits of the Briz-M pieces to determine their closest approach in space.

The significance of this project is the completion of a robust and highly accurate orbital forecasting of the Briz-M rocket body and its largest pieces of debris. By being able to predict the path of these objects, future conjunction events can be avoided, and the risk of creating more debris minimized.

Methodology Used

First, initial condition data for the Briz-M rocket body and the debris resulting from the explosion was obtained [3], and the orbits for these RSOs were propagated to determine closest approach between each pair of objects. It was determined that the objects labeled “3” and “4”, i.e., the first two pieces of debris, were the only pair with a noteworthy conjunction risk of less than 10km. The orbits for all RSOs are shown in Figure 1.

Objects 3 and 4 were then further analyzed using the adaptive Monte Carlo platform. AMC is a collection of MATLAB algorithms that use ensemble-based simulations to create a cloud of particles to probabilistically represent the state of an object of interest and the uncertainty in its predicted path over time. AMC produces an evolved state-uncertainty for the object by taking a randomized distribution of particles from the underlying probability space and propagating each particle forward using the system dynamics. Choosing a QoI is essential to getting a precise evaluation of the AMC performance. The covariance matrix is a representation of the variability between each pair of elements within a random vector, making for a good comparison of the position of an element over time. Thus, the trace of the position covariance matrix is chosen as the QoI for this investigation, creating an upper bound for the ensemble uncertainty.

Results Obtained

The AMC simulations were performed starting six hours before the conjunction event for a total of three days. Figure 2 depicts the position of the two RSOs in their respective orbits at the time of conjunction. A user-defined accuracy of 10^{-3} , a bootstrap sampling size of 10,000 particles, and a 3000-particle starting size for the ensemble resulted in the ensemble development pictured in Figure 3, visualizations of the particle cloud at each timestep in the simulation. Figure 4 is a good visual of how the ensemble cloud grows with uncertainty, with only four timesteps shown. Figure 5 shows the intersection of the ensemble clouds for the two objects at the time of conjunction.

After obtaining the ensemble results, probability of collision can be computed by discretizing the domain of conjunction into a grid and determining there are particles for both objects’ ensembles present within that convex hull volume. This result is quantified using equation 1:

$$P_c = \frac{\sum_{i=1}^N \min(m_i, n_i)}{\sum_{j=1}^N \min(m_j, n_j)}$$

(Equation 1)

The AMC result determined that probability of collision is minimal.

Significance and Interpretation of Results

The initial condition data resulting from the 2016 Briz-M explosion showed that probability of collision between the rocket body and its largest pieces of debris is minimal. Specifically, the analysis was performed on the two objects that were determined to have the highest collision risk through preliminary investigation of their dynamics via orbital propagation. This event can be further explored by performing the same level of conjunction analysis on all object pairings to get a more complete picture of the scenario. Additionally, all user-defined conditions, including required level of accuracy and starting ensemble size, can be refined to increase the reliability of the results. Another way to deepen

this investigation is to compare the AMC results to a non-adaptive version of the Monte Carlo platform, or another uncertainty forecasting platform altogether, to get a better sense of AMC's reliability.

Figures/Charts

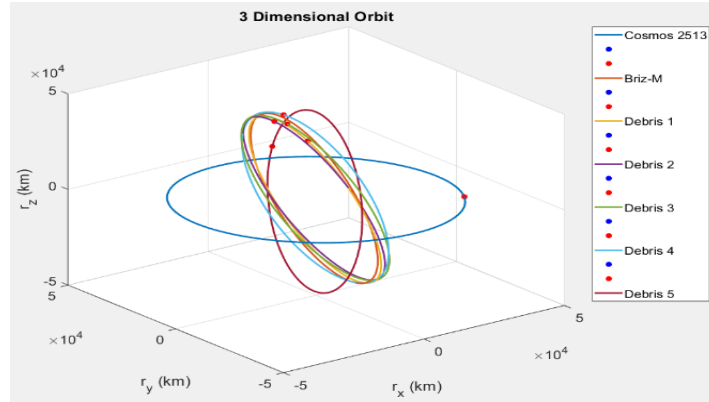


Figure 1: Propagated Orbits of All RSOs Concerning the Briz-M Event

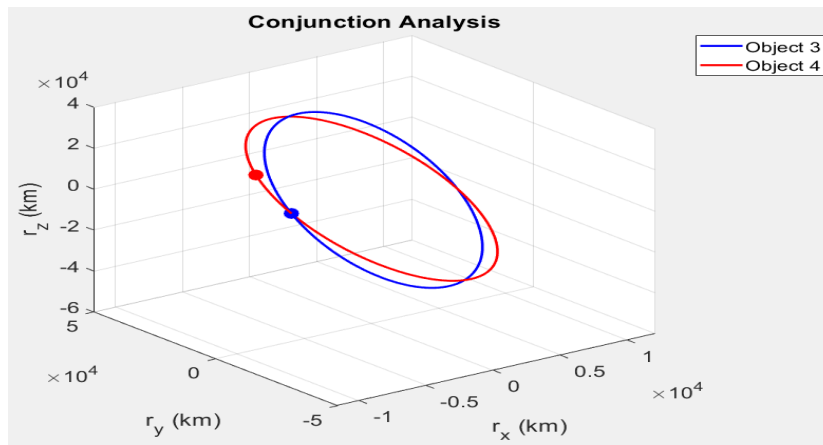


Figure 2: Orbits of Objects 3 and 4 at Time of Conjunction

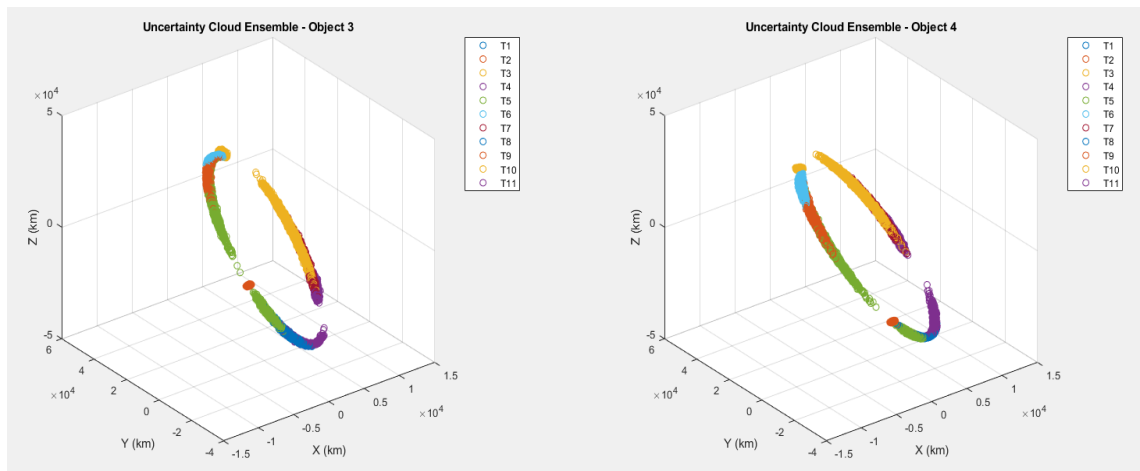


Figure 3: Development of Ensemble Cloud, Objects 3 and 4

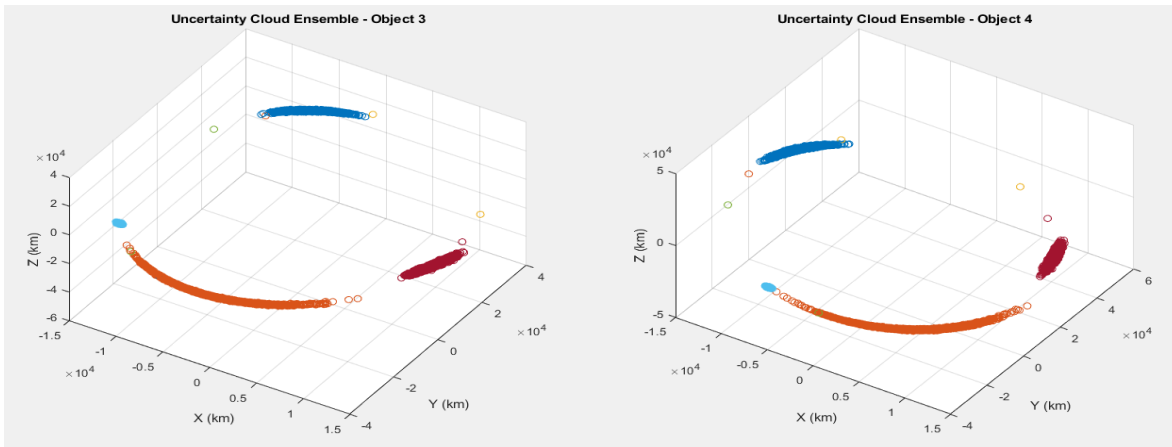


Figure 4: Ensemble Cloud at T_0 , T_3 , T_5 , and T_{10} , Objects 3 and 4

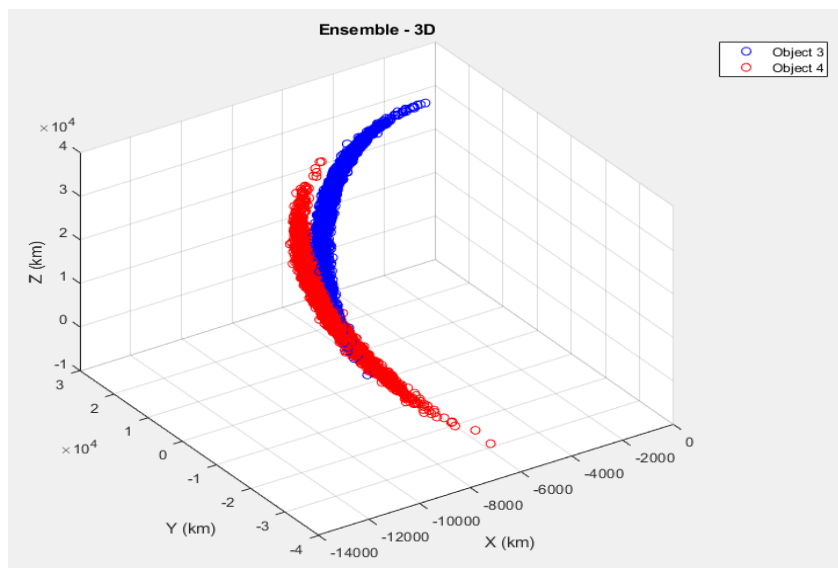


Figure 5: Ensemble for Objects 3 and 4 at Time of Conjunction

Acknowledgments

The completion of this thesis would not be possible without contributions from my advisor, Dr. Mrinal Kumar, as well as Ph.D. student Andrew VanFossen. I would like to thank the Ohio Space Grant Consortium for sponsoring this work and featuring it in their 2021-2022 Student Research Symposium Proceedings.

References

- [1] VanFossen, A., Mangal, A., Kumar, M., "Efficacy of Parallelization in Adaptive Monte Carlo for Forecasting in GEO", AIAA Sci-Tech Forum, 2022, 3-7 January.
- [2] Yang, C., and Kumar, M., "Closed-Loop Adaptive Monte Carlo Framework for Uncertainty Forecasting in Nonlinear Dynamic Systems." Journal of Guidance, Control, and Navigation, June 2019.
- [3] <https://celestrak.com/NORAD/elements/gp.php?INTDES=2015-075>

Correlations between Alcohol Preference and Hormone Profiles after Roux-en-Y Gastric Bypass Surgery in a Cafeteria Diet-Fed Female Rat Model

Student Researcher: Jacob G. Mansell

Advisor: Clare Mathes, Ph.D.

Baldwin Wallace University
Department of Neuroscience

Abstract

Even though women are more prone to obesity than men and 80% of patients receiving bariatric surgery are female, most studies feature only male model organisms. Here we sought to characterize the impact of Roux-en-Y gastric bypass (RYGB) surgery on some metabolic, reproductive, and behavioral profiles of female rats. At weaning, female rats were provided either with chow only (n=12) or with chow and access to high-fat + high-sugar supplements (a “cafeteria diet”; n=24). By 20 weeks of age, the cafeteria diet induced weight gain and blood glucose imbalances but did not alter estrous cycling profiles. RYGB surgery (n=8) decreased body weight and fasting glucose levels of cafeteria diet-fed rats and blunted their responsivity to a glucose challenge compared to their sham-operated sisters (SHAM, n=11). RYGB did not independently alter cyclicity, although estrus profiles unexpectedly changed pre- to post-surgery in both surgical groups. The operated rats as well as unoperated female rats fed chow only (n=8) were then given ad libitum access to ethanol (2-8%) alongside water; intakes were measured across multiple days and preference calculated. The ethanol preference of female RYGB rats did not differ from that of SHAM female rats, which contrasts with previous results in male rats but corroborates with previous results in female rats. We seek to explore the mechanism of this behavior by correlating alcohol preferences with serum levels of acylated ghrelin, a “hunger” hormone increased after RYGB surgery and that is positively correlated with desire for alcohol.

Project Objectives

The overarching study addresses a female rat model’s physiological, behavioral, and neurohormonal changes induced by Roux-en-Y gastric bypass (RYGB) surgery. This weight loss surgery is currently the most effective therapy employed to treat obesity and its associated complications (e.g., 3). However, in contrast to its benefits, the RYGB procedure can increase alcohol consumption (e.g., 1,11). The majority (80.7%) of people who undergo this procedure are women (e.g., 12). However, most of the mechanistic research on this topic uses male model organisms, and so know little about how the surgery may impact female-specific physiology. Studies assessing alcohol intake after RYGB surgery with male rats replicate the human condition (i.e., after RYGB surgery, rats drink more alcohol; 2,4), but only one group has examined this in female rats and found increased alcohol intake but no differences in preference (8,9). Therefore, here we sought to expand understanding in a female rat model by using a surgical procedure very similar to that used on humans and a clinically relevant obesigenic diet. Why individuals – male or female – who receive RYGB surgery are more likely to develop alcohol use disorder is not currently understood. One contributor may be the hormone ghrelin, which is produced by the stomach when it is empty and signals “hunger” when it travels through the blood to the brain. In humans, intravenous administration of ghrelin increased craving for alcohol intake (e.g., 6). In male rats, ghrelin increases after RYGB and may facilitate the increased preference for alcohol seen following RYGB surgery (4). Thus, in the third part of the project, I

hypothesize that a) we will see higher ghrelin levels in female rats given RYGB than in female sham-operated rats, and b) ghrelin levels will positively correlate with the alcohol preference displayed by the female rats.

Methodology Used & Results Obtained

The first project of our study series aimed to assess if 14 weeks of high-fat and high-sugar diet-feeding (starting at weaning) would induce obesity, metabolic disturbances, and disruptions of reproductive cycling (e.g., 10), and if RYGB could correct this physiological profile. To note, a high-fat and high-sugar diet is commonly called a “cafeteria diet” and is meant to model the “western diet,” which includes large amounts of “junk food” or “empty” calories in addition to a less palatable but full-nutrition diet. In the second part of the study series, we hypothesized that cafeteria diet-fed female rats given RYGB would show a higher preference for low concentrations of alcohol when offered ad libitum alongside water than cafeteria diet-fed female rats on which a sham operation had been performed, which is what has been seen in male (e.g., 3,4) and female (9,10) rats. We also included in this assessment a group of chow-fed control rats on which no surgery had been performed to assess the role of diet in ethanol preference as obesity may have protective effects against ethanol overconsumption (e.g., 5).

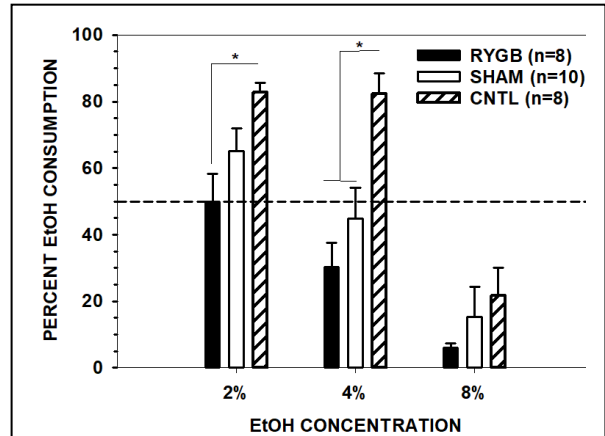


Figure 1. M +/- SE Percent ethanol preference (ethanol intake divided by total intake) calculated from the average of the last 3 days of access of female rats fed chow only (CNTL) or fed a cafeteria diet and on which RYGB surgery or SHAM surgery had been performed. Primary and follow-up ANOVA and t-tests revealed that CNTL rats preferred 2% and 4% ethanol more than either RYGB or SHAM rats.

Our cafeteria diet regimen successfully induced weight gain in (a difference on average of 39 g) and a dampened ability to respond to an injected glucose challenge. It did not, however, alter the amount of time that rats spent in the estrous phase of their reproductive cycle as assessed via cytological examination of daily vaginal lavage. We conducted RYGB and sham surgeries (as per 7) on the cafeteria diet-fed female rats and found, as expected, that RYGB in these rats decreased body weight (a difference on average of 33 g) and restored glucose metabolism. While the amount of time that the rats spent in estrus decreased after surgery, this occurred in both surgical groups and was not specifically due to RYGB. We then found that the preference of female rats given RYGB (n=8) did not differ from that of female rats given sham surgery but that maintenance diet strongly influenced ethanol preference as unoperated rats fed chow only preferred ethanol to a much higher degree than cafeteria diet-fed rats given either operation (Figure 1).

We then euthanized the cafeteria diet-fed female rats on which RYGB and sham surgeries had been performed and took blood via cardiac puncture. The blood was mixed with an anticoagulant and centrifuged, and the serum retained, mixed with a protease inhibitor, and stored at -80°C. We plan to assess levels of total and acylated ghrelin in these samples using an enzyme-linked immunoassay. We will then correlate these hormone levels to alcohol preferences assessed in the previous study aspect.

Significance and Interpretation of Results

These data suggest that alcohol preference may not change after RYGB surgery in a female rat model as previously reported in male rats. Our upcoming analyses of ghrelin may provide insight as to why our results differ from those previously reported in the literature.

Acknowledgements

Alyssa Palumbo and Devon Stewart co-led these projects, and we were aided by Gregg DiNuoscio, Lily Gabriel, Sarah Kettleberger, Sydney Klingshirn, Melanie Mavroidis, Dave Revta, and Kristen Sperber. Funding for this study was provided in part by the Baldwin Wallace Faculty Development Committee (CMM), the Summer Scholars Program (AP & CMM), and the Ohio Space Grant Consortium (JM).

References

1. Briegleb, M., & Hanak, C. (2020). Gastric Bypass and Alcohol Use: A Literature Review. *Psychiatra Danubina*, 32(Suppl 1), 176–179.
2. Davis, J. F., Tracy, A. L., Schurdak, J. D., Magrisso, I. J., Grayson, B. E., Seeley, R. J., & Benoit, S. C. (2013). Roux en Y Gastric Bypass Increases Ethanol Intake in the Rat. *Obesity Surgery*, 23(7), 920–930.
3. Fisher, B. L., & Schauer, P. (2002). Medical and Surgical Options in the Treatment of Severe Obesity. *The American Journal of Surgery*, 184(6), S9–S16.
4. Hajnal, A., Zharikov, A., Polston, J. E., Fields, M. R., Tomasko, J., Rogers, A. M., Volkow, N. D., & Thanos, P. K. (2012). Alcohol Reward Is Increased after Roux-en-Y Gastric Bypass in Dietary Obese Rats with Differential Effects following Ghrelin Antagonism. *PLoS ONE*, 7(11), e49121.
5. Kleiner, K.D., Gold, M.S., Frost-Pineda, K., Lenz-Brunsmann, B., Perri, M.G., & Jacobs, W.S. (2004). Body Mass Index and Alcohol Use. *Journal of Addictive Diseases*, 23(3), 105–118.
6. Leggio, L., Zywiak, W. H., Fricchione, S. R., Edwards, S. M., de la Monte, S. M., Swift, R. M., & Kenna, G. A. (2014). Intravenous Ghrelin Administration Increases Alcohol Craving in Alcohol-Dependent Heavy Drinkers: A Preliminary Investigation. *Biological Psychiatry*, 76(9), 734–741.
7. Mathes, C. M., Letourneau, C., Blonde, G. D., le Roux, C. W., & Spector, A. C. (2016). Roux-en-Y Gastric Bypass in Rats Progressively Decreases the Proportion of Fat Calories Selected from a Palatable Cafeteria Diet. *American Journal of Physiology. Regulatory, Integrative and Comparative Physiology*, 310(10), R952-959.
8. Orellana, E. R., Nyland, J. E., Horvath, N., & Hajnal, A. (2021). Vagotomy Increases Alcohol Intake in Female Rats in Diet Dependent Manner: Implications for Increased Alcohol Use Disorder After Roux-en-Y Gastric Bypass Surgery. *Physiology & Behavior*, 235, 113309.
9. Orellana, E. R., Piscura, M. K., Horvath, N., & Hajnal, A. (2021). Differential Response in Ethanol Behaviors of Female Rats Given Various Weight Loss Surgeries. *Alcohol and Alcoholism*, 56(5), 599–604.
10. Roberts, J. S., Perets, R. A., Sarfert, K. S., Bowman, J. J., Ozark, P. A., Whitworth, G. B., Blythe, S. N., & Toporikova, N. (2017). High-Fat High-sugar Diet Induces Polycystic Ovary Syndrome in a Rodent Model. *Biology of Reproduction*, 96(3), 551–562.
11. Suzuki, J., Haimovici, F., & Chang, G. (2012). Alcohol Use Disorders After Bariatric Surgery. *Obesity Surgery*, 22(2), 201–207.
12. Young, M. T., Phelan, M. J., & Nguyen, N. T. (2016). A Decade Analysis of Trends and Outcomes of Male vs Female Patients Who Underwent Bariatric Surgery. *Journal of the American College of Surgeons*, 222(3), 226–231.

Experimental Determination of Convective Velocity through Wavenumber Analysis

Student Researcher: David Marshall

Advisor(s): Prof. Mo Samimy and Dr. Nathan Webb

The Ohio State University
Mechanical and Aerospace Engineering Department

Abstract

Advanced tactical aircrafts are increasingly using non-axisymmetric, often rectangular, twin supersonic jets due to many advantages they provide over axisymmetric designs such as minimizing drag (since aft bodies are typically non-axisymmetric) and reductions in weight. However, one disadvantage of twinjet configurations is that they can lead to significant increases in near-field pressure fluctuations that can potentially result in structural fatigue and failure. As such, the over-arching purpose of our research is to better understand the physics behind these pressure fluctuations and establish active flow control over the twin supersonic jets using localized arc-filament plasma actuators (LAFPAs) to perturb the flow in such a way as to mitigate these fluctuations. One step in establishing active flow control is to construct an analytical model that predicts certain parameters which will be used to both model the system's response given certain inputs and provide better understanding of the flow physics. An important parameter that we need to find to corroborate our model's predictive accuracy is the screech frequency. Given that the flows are supersonic and shocks are present (meaning the nozzles are not ideally expanded and have sharp throats) there will also be the presence of jet screech which are caused when the large scale structures (LSS) shed from the jet nozzle interact with the shock cells, thus forming feedback waves which trigger the formation of more structures. The focus of this study is to empirically determine the convective velocity of the LSS since convective velocity is an important parameter of the model used to predict the system's response to particular control conditions. To empirically determine convective velocity, we generated St-k plots from experimental schlieren images of the flow at Mach numbers ranging from 1.25 to 1.90. This study resulted in the empirical determination of the convective velocities from all tested Mach number cases.

Project Objectives

The overall objective of this project is to empirically ascertain the normalized convective velocities (U_c/U_j) of the LSS from experimental schlieren images taken of closely spaced twin rectangular supersonic jets experiments run at Mach numbers ranging from 1.25 to 1.90.

Methodology

Using the experimental data we had, a method observed in the literature for U_c/U_j determination was to construct St-k plots [1] because both St, which is the Strouhal number corresponding to the normalized temporal frequencies of the data, and k, which is the wavenumber corresponding to the normalized spatial frequencies of the data are directly related to U_c/U_j through the dispersion relation shown in Equation 1 (where the equivalent diameter D_e is 0.01925 [m]):

$$\frac{U_c}{U_j} = \frac{2\pi St}{D_e k} \quad (eq. 1)$$

We can get U_c/U_j from St-k plots by procuring the slope of the best fit line through the maximum wavenumber peaks of every Strouhal number, as shown in Figure 1. The best fit line is the line that if all wavenumber peaks it passed through were added together would have the largest magnitude amongst all generated lines. One potential issue with this methodology was that if there were the presence of noise with comparable magnitude to the wavenumber peaks (in the case of our experiments most likely acoustic waves), then the best fit line could potentially be determined by our code to be a line that fits through noise rather than the maximum wavenumber peaks. To combat this potential issue, we also visually inspect the generated St-k plots and qualitatively assessed the degree to which noise may have interfered with the best fit line.

To construct the St-k plots, we swept through a multitude of measurement lines that either ran along the top or bottom of the shear layer (see Figure 2 for example of a measurement line on a schlieren image). We then ran two more sets of lines, horizontal and slanted lines, each run at differing y-offsets which moved the lines up by 10 pixels or down by 80 pixels in increments of 10. The wavenumber spectrum of each measurement line was determined through taking a temporal FFT of the line and then a spatial FFT at all frequencies [2]. We then plotted the wavenumber spectra stacked together to get the St-k plots. To determine the optimal position and orientation of the measurement line we checked two parameters. The first was the best fit line on the St-k plots for all measurement lines. Ideally, the line with the highest total magnitude (summation of wavenumber peaks passed through) would be the best line since it effectively passed through all the peaks the best. Next, we qualitatively inspected the St-k plot from the optimal measurement line for each Mach number to determine whether it was inhibited by noise and not a valid line. Finally, with all U_c/U_j 's we would determine the average U_c/U_j and check whether it conforms with values often obtained in literature.

Results Obtained

All generated St-k plots and U_c/U_j 's for $M_j \geq 1.5$ yielded results that were consistent with the literature and uninhibited by noise. For example, as can be seen from Figure 3, the St-k plot generated using the analytically determined optimal measurement line at $M_j = 1.85$ exhibited minimal intrusive noise and matched those of the St-k plots from the literature. The slope of the best fit line (in black) was the U_c/U_j for this case and was 0.73. Additionally, it was determined that for all cases, the optimal measurement line was a slanted line on the bottom shear layer.

However, for cases run at $M_j < 1.5$ there was an issue with the St-k plots which rendered the best fit lines generated from our code incorrect. The issue can be more aptly illustrated from Figure 4, which is the St-k plot generated using the 'optimal' measurement line at $M_j = 1.30$. From the figure we can qualitatively determine that the region that the best fit line needed to be fit through was obfuscated by noise (possibly acoustic waves), meaning the 'optimal best fit line' as calculated by our code wasn't optimal since it would be fit to pass through as much noise as possible.

So, we instead ascertained the U_c/U_j for all M_j 's < 1.5 by first picking the St and k values from the small region at the screech frequency from every St-k plot (using measurement line placements of slanted lines on the bottom shear layer as determined from $M_j \geq 1.5$ cases). Then, we plugged in the values of St and k into Equation 1 to get U_c/U_j .

Finally, we plotted, as shown in Figure 5, all the U_c/U_j values from all the optimal measurement line case for all M_j s along with the U_c/U_j values from measurement lines nearest the optimal, which would be the lines offset in the y direction by ± 10 pixels (assuming there was one since some optimal measurement lines were at the highest or lowest y -offset). Adding in the U_c/U_j values from adjacent measurement lines gave the final plot of U_c/U_j vs. M_j plot greater confidence in the measurement's precision and general trends and the average value across all cases of 0.72, which is consistent with the range of U_c/U_j often found in the literature.

Figures

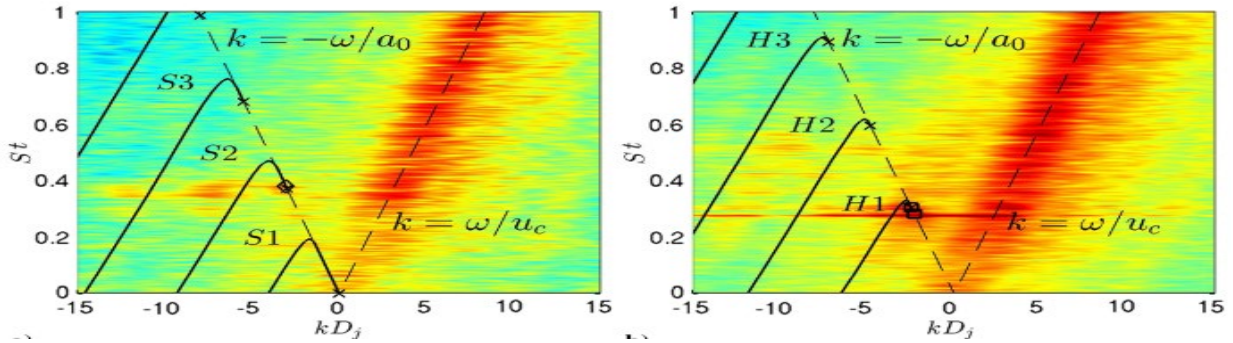


Figure 1: Examples of St-k Plots from Literature (see [1])

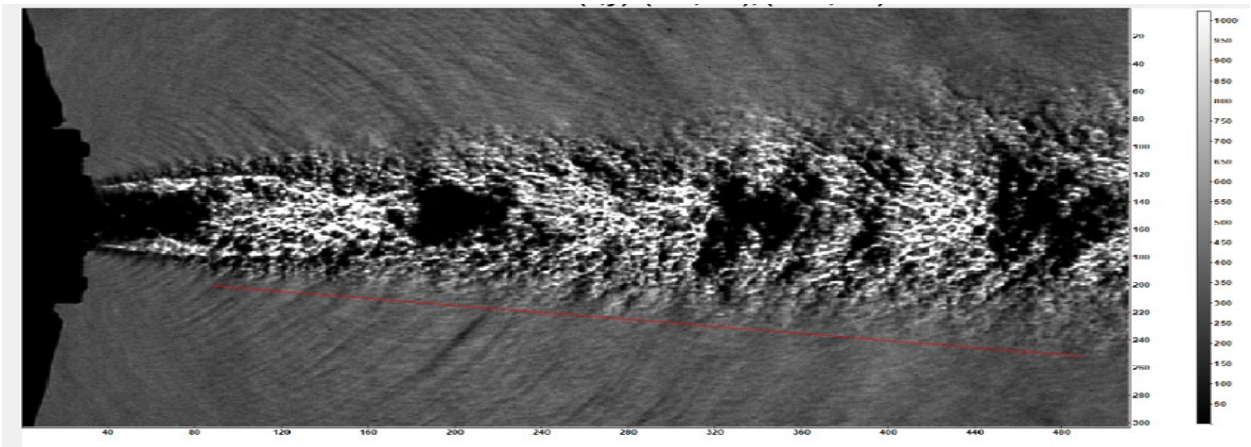


Figure 2: Data Selection

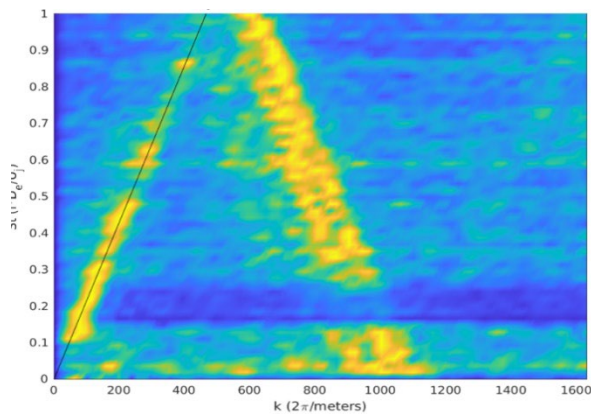


Figure 3: St-k plot for $M_j = 1.85$ (where black line is best-fit to peaks)

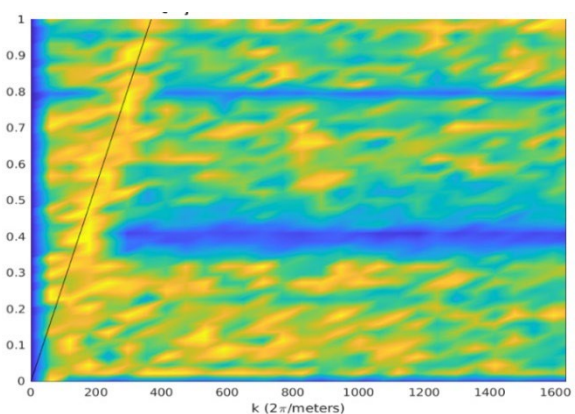


Figure 4: St-k plot for $M_j = 1.30$ (where black line is 'best-fit' to peaks)

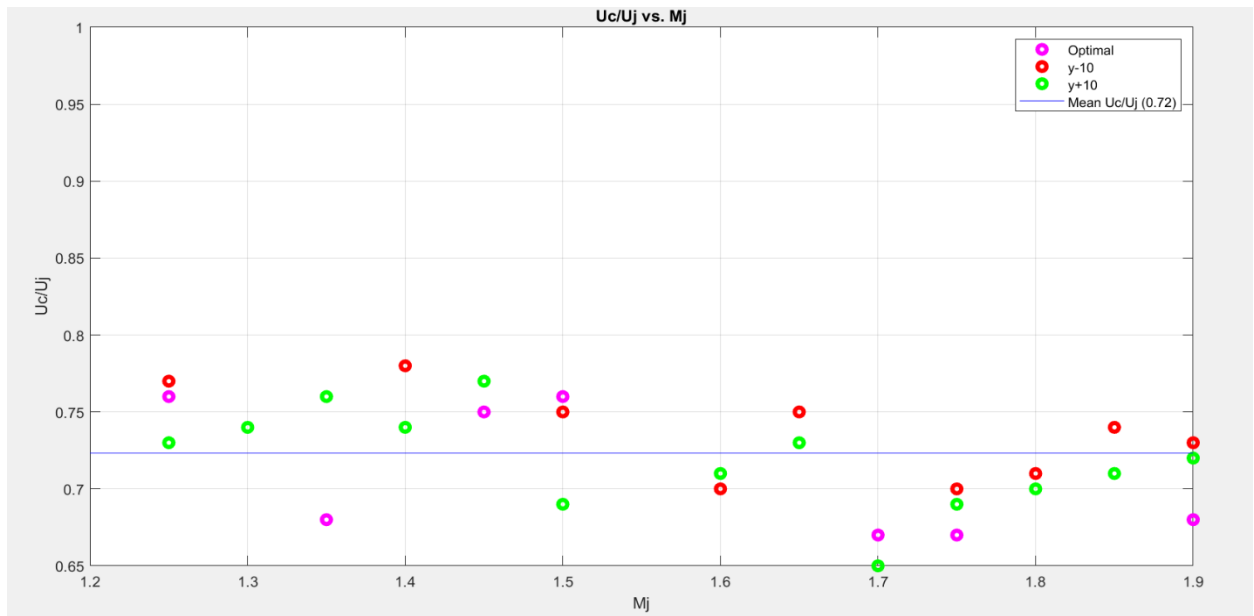


Figure 5: U_c/U_j vs. M_j Plot

Acknowledgement

The author would like to thank Dr. Nathan Webb and Prof. Mo Samimy. Their guidance and work were instrumental in completing this research. The author would also like to thank the Ohio Space Grant Consortium (OSGC), the program manager at the Office of Naval Research Steve Martens and The Ohio State University for providing both the opportunity and funding that made this research possible.

References

- [1] Gojon, Bogey, Mihaescu (2018). "Oscillation Modes in Screeching Jets." *AIAA Journal*, Vol. 56, No. 7, pp. 2918-2924.
- [2] Mercier, Castelain, Bailly (2017). "Experimental Characterization of the Screech Feedback Loop in Underexpanded Round Jets." *Journal of Fluid Mechanics*, Vol. 824, pp. 202-229.

Substrate Effects of Lead Halide Perovskites: Rapid Aging and Electron-Beam Irradiation Tests for High-Performance Perovskite Solar Cells

Student Researcher: Derek McGee

Advisor: Dr. Jennifer Williams

Wilberforce University
Electrical Engineering

Abstract

Thin-film perovskite photovoltaic (PV) devices have the potential to reduce the cost of space ready PV cells 100-fold. To date perovskite solar cells (PSC) have reached power conversion efficiencies (PCE) exceeding 25%,¹ while newer tandem perovskite devices have PCEs that surpass commercially available silicon photovoltaic devices, currently at 26%.¹ Furthermore, inexpensive perovskite liquid precursor inks, paired with simplified deposition techniques and flexible substrates illuminate the potential for full automation and in-space fabrication of solar materials. Several challenges remain before commercial use. Herein, fabrication methods used to develop PSCs are evaluated to determine the process of perovskite degradation. Six different commonly used perovskite substrates coated with popular perovskite precursor ink, MAPI (methyl ammonium lead iodide) were produced and degraded via extreme temperature and e-beam irradiation experiments. It is hypothesized that the use of e-beam excitation via Scanning Electron Microscopy (SEM) can yield a qualitative/quantitative effect of ⁶⁰Co gamma irradiation.² Analysis of MAPI thin films pre and post irradiation will be essential to unveil the mechanism of degradation of perovskite solar cells.

Objective

The project is to improve the durability of perovskite based solar cells and ultimately implement them as a means of solar electric propulsion in space missions and aid in solving the enormous power consumption problems plaguing our planet as natural fossil fuel reserves continue to be depleted. The project also dissected and duplicated various aspects of the perovskite fabrication process. The development of concise experimental protocols that are readily reproducible for perovskite solar cells is fundamental to the development of PSC stability. With the surge in revelations about the intrinsic nature of PSC devices, the potential to revolutionize the methods through which solar energy are harvested grows increasingly. Continued efforts in simulating lower earth orbit radiation exposure to quantify perovskite degradation will be beneficial for various aerospace applications. In addition to the fabrication of MAPI thin films on several different substrates, irradiation experiments to degrade these films are currently inconclusive. Variations in exposure limits will be necessary to elude the degradation mechanism.

Methodology

General Studies for this project were conducted primarily at the Materials for Opto/electronics Research and Education (MORE) Center and the SCSAM Center (Swagelok Center for Surface Analysis of Materials) at Case Western Reserve University. For Clean Glass Substrates, microscope grade glass slides were measured and cut prior to cleaning. different types of substrates were labeled and labeled. Soda Lime microscope slides, ITO, FTO, borosilicate and silicon substrates were prepared. Quartz substates were not received in time for this study and replaced with HF-etched soda-lime slides. These slides were etched to increase roughness/surface topography via a process developed by Dr. Kyle Crowley. All substates then underwent the sonication cleaning process. Alcanox soap solution prepared with 1 drop of soap per 200ml of DI water was prepared and heated to 25°C. The container holding the submerged slides was then

sonicated for 15 minutes. The slides were then dunk rinsed in fresh DI water 2x prior to being submerged in fresh DI water and further sonicated for an additional 10 minutes. The slides were then dunk rinsed in fresh DI water 2x and transferred into a solution of acetone. The container holding the submerged slides in acetone was then sonicated for an additional 10 minutes and each slide was then dried with compressed Nitrogen gas. Dry slides were then submerged in methanol and sonicated for 10 minutes and dried again with compressed Nitrogen gas. After drying, the slides were then submerged in isopropyl alcohol and sonicated for 10 minutes, followed by drying again with compressed Nitrogen gas. Substrates were then transferred to the Novascan PSDP-UV8T ozone cleaner and set to clean for 10 minutes at 75°C. Clean slides were then transferred to individual petri dishes, covered and transferred into a nitrogen filled glove box. For Spin Coating Perovskite Precursor (Anti-solvent method), The process of spin coating involves applying a solution to a substrate spinning at a set rotations per minute (rpm) speed to produce a uniform, defect-free film on the substrate surface. A Laurell WS-650-23 spin coater located in the glovebox was used to process substrates with perovskite precursor, methylammonium lead iodide purchased from Sigma-Aldrich. Using the spin-coater preset "Program F" (5 sec at 500 rpm, then 60 sec at 4000 rpm), 30µl of MAPI ink was added to the stationary sample to evenly coat the substrate. Once spinning was initiated at 500 rpm for 5 sec, 1.5 ml of an antisolvent, trichlorobenzene, was then injected onto the spinning substrate, 5 seconds after the increased RPM initiated 60 sec at 4000 rpm). All samples before were coated first, and collectively transferred to a hotplate preset to 110°C and annealed simultaneously for 10 minutes. For SEM Irradiation Testing and Hot Plate, the SWAGELOK Center is equipped with a Helios NanoLab 650 field emission SEM (FESEM) affixed with focused ion beam (FIB) technologies. Once prepared, the 6 classes of MAPI-deposited substrates/samples were glued to SEM sample holding studs with carbon black tape, device side up. Samples were prepared in the glove box and sealed with parafilm in an air-tight sample holder. Immediate transfer from the MORE Center to the SWAGELOK Center and into the SEM instrument with limited exposure to air, prior to returning under vacuum inside the instrument. Voltages and currents varied during experimentation, not to exceed 30keV exposure over a 5 minute time frame. Once irradiation experiments and imaging was completed, samples were then fully degraded at the laboratory benchtop, using a hot plate set at 150 °C.

Results

While this study focused on the perovskite precursor, MAPI (methyl ammonium lead iodide), substrate preparation procedures were also successfully duplicated, and the effect of substrate preparation was observed. Substrates that were not sterilized immediately before precursor deposition showed more irregularly coated perovskite thin films. The process of labeling samples should also be completed prior to initiating the substrate cleaning process, to minimize particulates. Various depositions techniques including physical vapor deposition, chemical vapor deposition and spin coating have successfully been completed to further perfect the skills necessary for successful cell processing. Deviations to the spin-coating recipe included the addition of an anti-solvent (trichlorobenzene) that has led to more uniformity in grain sizes, ranging from roughly 50-170 nm in diameter. Applying this anti-solvent successfully with the perovskite precursor via a drop-coating technique is also visibly noticeable by the naked eye, resulting in dark-blackish, shiny sample surfaces, post annealing. Without proper antisolvent application, however, samples appeared a dark-gray in color, with a matte-finish, post annealing, which has been associated with less uniformity and undesirably produced films.

References

- [1] Chopra, K.L.; Paulson, P.D.; Dutta, V. Thin Film Solar Cells: An Overview. *Prog. Photovolt: Res. Appl.* 2004; 12:69–92 (DOI: 10.1002/pip.541).
- [2] Suzuki, A.; Okada, H.; Oku, T. Fabrication and Characterization of CH₃NH₃PbI_{3-x-y}Br_xCl_y Perovskite Solar Cells. *Energies* 2016, 9(5), 376; <https://doi.org/10.3390/en9050376>.

Bobcat-1 CubeSat Management

Student Researcher: Austin McKibben

Advisor: Dr. Sabrina Ugazio

Ohio University
Computer Science

Abstract

Bobcat-1 is a 3-unit CubeSat developed at Ohio University's Avionics Engineering center. Its main goal is to measure the performance of Global Navigation Satellite System (GNSS) inter-constellation time offsets from Low Earth Orbit (LEO). It was launched on October 2, 2020 and was deployed from the ISS on November 5, 2020. It has been in orbit up to the time of writing and has collected over 2 GB of data. Each GNSS system has its own method of timekeeping, and as a result introduces another unknown value in a multi-GNSS PVT solution. Improved solutions could be possible if this time offset were precisely calculated, something valuable to users with limited visibility.

Project Objectives

One solution to this problem is a LEO Space Vehicle (SV) that measures this offset and provides the solution to users. A short orbit period enables an SV to see many GNSS satellites, multiple times per day. Combined with no tropospheric error and a low multipath error, this may provide more accurate time offset estimates for GEO and HEO satellites so that they may have a nearly continuous position solution. Bobcat-1's mission was to experiment with this approach, downlinking to a ground station and performing post-process analysis to determine the feasibility of this method.

Methodology Used

My involvement has been related to mission control, antenna calibration, data collection, and data organization. Bobcat-1 may perform about 15 orbits per day, but not all those orbits pass over our ground station at optimal angles. Bobcat-1's pass predictor uses a TLE to forecast Bobcat-1's orbit 48 hours in the future. The pass predictor works with a pass planner to automatically execute commands on Bobcat-1. The mission manager ensures a reliable data link to Bobcat-1, and downlinks or uplinks data whenever possible. The mission manager will run autonomously so that all possible passes are not wasted.

Bobcat-1 orbits the Earth about 15 times per day, several of which pass over the OU ground station well enough to communicate with the satellite to send and receive messages.

Results

Our ground station is maintained by a GomSpace GS100 as a transceiver and manages two UHF antennas on the Stocker Center roof. Our ground station computer uses the transceiver to configure collections and receive that collected data from Bobcat-1.

Bobcat-1 has four main types of collections, each one taken at the discretion of the Bobcat-1 team: time offset collections, antenna collections, and spectrum collections. Time offset collections contain information pertaining to the relative time offsets of different GNSS constellations. Antenna collections contain information in environmental that can affect antenna readings. Spectrum collections contain information related to the frequency spectrum over a time.

One of the unique features is the crowdsourced data enabled by SatNOGS, or Satellite Network of Open Ground Stations. SatNOGS is an open-source project by the Libre Space Foundation that allows universities, amateur radio operators, and libraries to operate a registered ground station and send its data across their network. The SatNOGS dashboard website that allows users to upload beacon data they have collected and organizes it into a user-friendly interface. Bobcat-1's beacons have been collected by many users around the world and allows the bobcat-1 team to monitor the status of bobcat-1 even when it isn't in view of our ground station.

Data management has also been an important factor in analysis. Bobcat-1 messages have a specific file format, closely related to NovAtel message formats. Bobcat-1's file format takes the NovAtel receiver output and discards any unneeded data, parsed into a custom log format. All desired data is stored in the same format and precision as raw NovAtel messages. MATLAB scripts were developed to translate raw binary data into plain text csv's. This makes files much larger, but easier to implement into programs like MATLAB for easy analysis.

This massive accumulation of data from Bobcat-1's extended lifetime will provide a more robust data set for the continued research into GNSS time offsets, as well as other fault monitoring applications for GNSS.

Electrochemically Responsive Drug Delivery Systems with Ferrocene-Containing Polyelectrolyte Complex Hydrogels for Controlled Release

Student Researcher: Victoria Messuri

Advisor: Dr. Byung-Wook Park

Youngstown State University
Chemical Engineering

Abstract

Chronic wounds are a major issue with millions of individuals being affected annually, and the current treatment is costly. This study was conducted to design a smart wound dressing made up of a polyelectrolyte complex (PEC) hydrogel composed of ferrocene-branched chitosan (CHI) with alginate (ALG) to develop a novel drug delivery system. The ferrocene allowed for enhanced drug release kinetics so it could be responsive to the needs of the wound site. The Ninhydrin test, turbidity measurement, gel content, and swelling behavior were performed to characterize the electrochemical responsive hydrogel. The diffusion rates on the phantom skin surface were estimated with the drug release kinetics of the model drugs. To design the smart wound dressing, the PEC hydrogels were fabricated. The developed wound dressing can be integrated with an enzyme-based biosensing element that detects biomarkers produced by the body.

Objectives

In order to find a solution for chronic wounds, the development of a smart bandage is being studied. The goal of the bandage is to be responsive to the wound's needs, being stimulated by biomarkers in the body and using a redox pathway to administer the release of the drug to the wound site. In order to create the electrochemically responsive hydrogel, the optimum amount of the chemical that will allow for the redox reaction needs to be found and selected. This chemical will then be incorporated into a hydrogel that will hold the drug, which will be between two custom electrodes. The hydrogel incorporated in the bandage will be able to release the drug by providing an on-demand release [4]. The patch will hopefully be useful for astronauts and soldiers for on the go treatment solutions, as well as common individuals.

Methodology

Ferrocene is a well-known organometallic redox couple (ferrocenium/ferrocene, Fc^+/Fc) mediator, which undergoes a one-electron oxidation at a certain potential [7, 9]. The ferrocene is bound to chitosan, which is one of the two polyelectrolytes creating the hydrogel, the other being alginate. Both of these materials are abundant and biocompatible. The hydrogel self-assembles after polymerization [3]. Different amounts of ferrocene in the hydrogel were composed and run through several tests. The Ninhydrin test, turbidity test, FTIR, swelling behavior, and gel contents were conducted and measured.

Results

The Ninhydrin test is a chemical reaction that allows the agent in the solution to bind to free amine groups. The Ninhydrin solution is originally neon yellow in color, and changes to a deep purple once the reaction has occurred. The absorbance is then measured. The Ninhydrin test results gathered proved that changing the amount of ferrocene in the chitosan polyelectrolyte had a direct relationship to the amount of free amines; the more ferrocene in the sample, the less free amines available, which makes sense since the ferrocene binds to the chitosan by attaching to its amine groups. The percent

conjugations of the ferrocene in the chitosan were found to be about 30%, 40%, and 56% with respective decreasing ferrocene amounts, with pure chitosan being a control at 100%. Additionally, the peaks in the sample's FTIR showed a difference in absorbance with varying amounts of ferrocene. The absorbance of the amides in pure chitosan was dramatically higher than the highest sample of ferrocene tested, with the other amounts fitting in between, respectively.

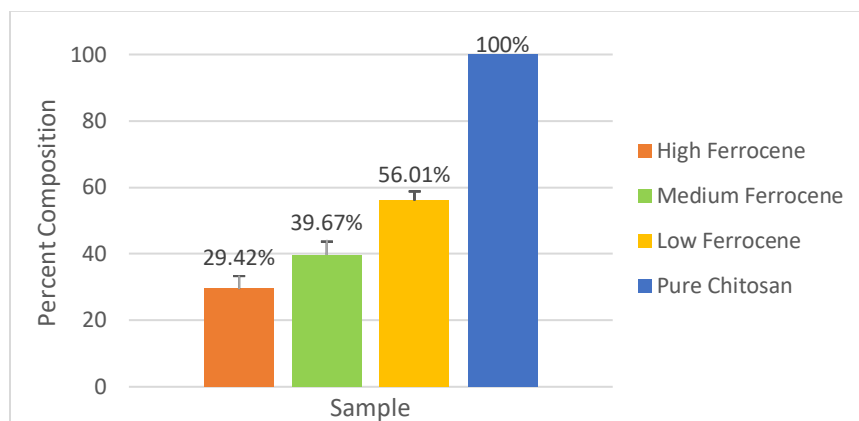


Figure 1: Ninhydrin Test Results

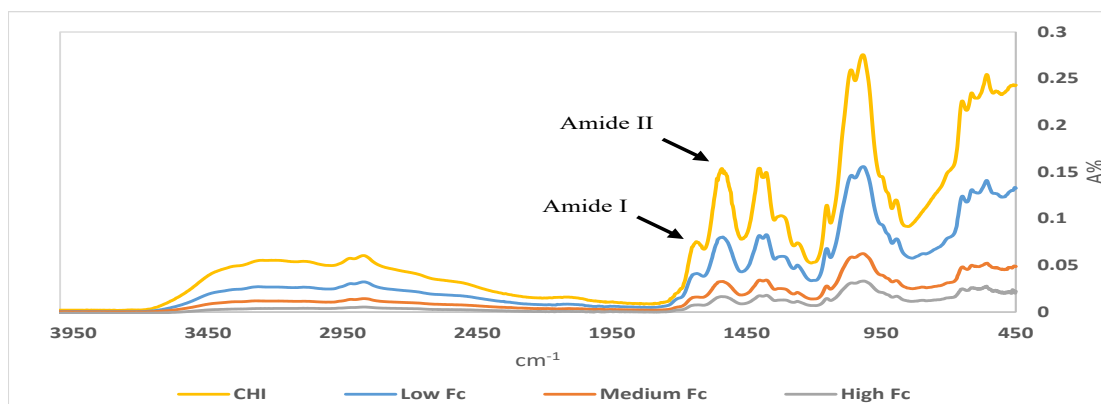


Figure 2: FTIR

Sample	Amide I (cm ⁻¹)	Absorbance	Amide II (cm ⁻¹)	Absorbance
CHI	1636	0.075	1542	0.154
Low Fc	1634	0.041	1539	0.080
Medium Fc	1634	0.016	1538	0.033
High Fc	1634	0.008	1538	0.017

Table 1: FTIR Calculations

Next, the turbidity test was conducted. The turbidity test shows what can be thought of as the strength of the hydrogel. The turbidity test measures the absorbance, which is the light that can pass through a sample. With a higher NTU value, there are more interactions between the positive and negative polyelectrolytes, with more interactions showing a more stable and homogeneous gel [5, 6, 8, 10]. The

peak of the graph in Figure 3 gave the best sample, which was the lowest concentration of ferrocene tested with a ratio of 20% ferrocene-chitosan to 80% alginate. Chitosan and alginate bond to each other in a stoichiometric ratio of 1 to 1. The turbidity test also showed that the potential of the highest ferrocene-chitosan sample being tested should be eliminated, because it had much weaker interactions than the medium and high, showing the hydrogel was not as strong.

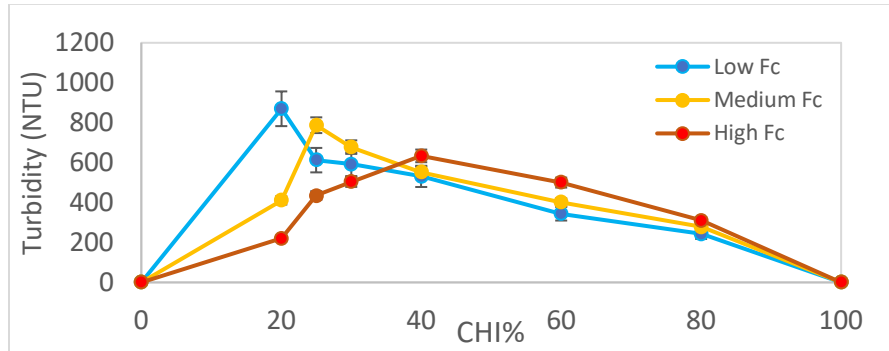


Figure 3: Turbidity Test

After the turbidity test was performed, the hydrogels were lyophilized, weighed, and incubated in PBS solution. The gel contents and swelling behaviors were then calculated. The results showed about 100% gel contents for both of the tested samples (medium and low ferrocene), suggesting that the gels were stable and balanced in charges [1]. The positive ions in the chitosan were therefore almost perfectly bonded to the negative ions in the alginate, allowing the hydrogel to have a neutral charge, so no one charge dominated the gel to give it an electrostatic phenomenon. The swelling percentage was over 4000 for the medium ferrocene sample and right below 4000 for the low ferrocene sample when comparing the beginning mass to the ending mass after incubation, suggesting that a large amount of drug could be incubated in the hydrogel without leaking or damaging the gel [2].

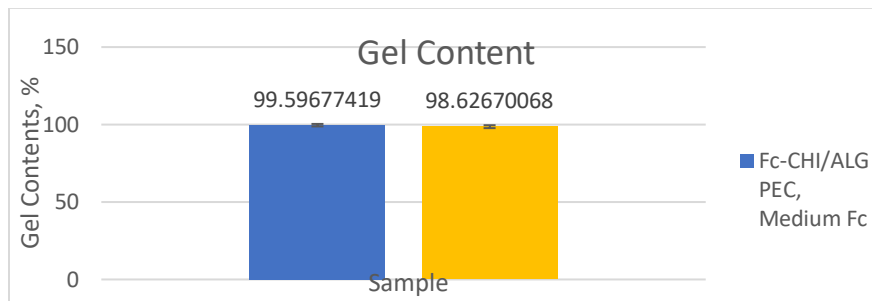


Figure 4: Gel Contents Results

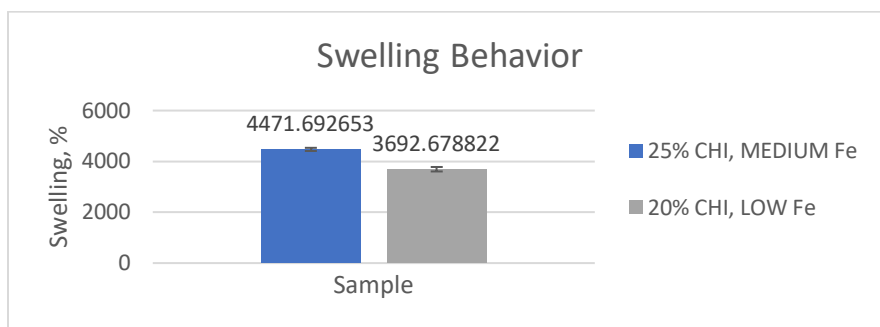


Figure 5: Swelling Behavior

Discussion

This work paves the way for the rest of our project of developing a smart wound bandage. The different samples of ferrocene chitosan have different amounts of free amine groups as shown by the Ninhydrin test. The 20% ferrocene-chitosan PEC with the lowest concentration of ferrocene is the most mechanically stable and chemically functional hydrogel according to turbidity testing. The medium concentration of ferrocene was the best hydrogel according to swelling behavior, suggesting it can encapsulate a drug 400 times its mass. More testing should be performed to further find the best amount of ferrocene, and perhaps samples with less than our lowest tested should be prepared and tested. The next step is to see how the hydrogels respond with active and passive drug release kinetics, in both solution and on agarose gel to model human skin. In-vitro experiments can then be performed.

Acknowledgement

The author would like to thank the Ohio Space Grant Consortium (OSGC), University Research Council Grants at YSU, and Assured Digital Microelectronics Education & Training Ecosystem (ADMETE) for their financial supports. The author also acknowledges Asma Allababdeh, Prakriti Dhungana, Cassidy Lyons, Anthony Romeo, Kyle Duke, Dr. Pedro Cortes, Dr. Vigil Solomon, Dr. Bhargavi Mummareddy, Ray Hoff, and especially my advisor Dr. Byung-Wook Park for their support, contributions, and help with my studies.

References

- [1] Chalitangkoon, J., M. Wongkittisin, and P. Monvisade, *Silver loaded hydroxyethylacryl chitosan/sodium alginate hydrogel films for controlled drug release wound dressings*. International Journal of Biological Macromolecules, 2020. 159: p. 194-203.
- [2] Dai, M., et al., *Chitosan-alginate sponge: preparation and application in curcumin delivery for dermal wound healing in rat*. Journal of Biomedicine and Biotechnology, 2009. 2009.
- [3] Haidari, H., et al., *pH-Responsive "Smart" Hydrogel for Controlled Delivery of Silver Nanoparticles to Infected Wounds*. Antibiotics, 2021. 10(1): p. 49.
- [4] Jiang, H., et al., *A pH-regulated drug delivery dermal patch for targeting infected regions in chronic wounds*. Lab on a Chip, 2019. 19(13): p. 2265-2274.
- [5] Meka, V.S., et al., *A comprehensive review on polyelectrolyte complexes*. Drug discovery today, 2017. 22(11): p. 1697-1706.
- [6] Potaś, J., et al., *Tragacanth Gum/Chitosan Polyelectrolyte Complexes-Based Hydrogels Enriched with Xanthan Gum as Promising Materials for Buccal Application*. Materials, 2021. 14(1): p. 86.
- [7] Qiu, J.-D., et al., *A label-free amperometric immunosensor based on biocompatible conductive redox chitosan-ferrocene/gold nanoparticles matrix*. Biosensors and Bioelectronics, 2009. 25(4): p. 852-857.
- [8] Strand, A., et al., *In-situ analysis of polyelectrolyte complexes by flow cytometry*. Cellulose, 2018. 25(7): p. 3781-3795.
- [9] Yılmaz, Ö., et al., *Chitosan-ferrocene film as a platform for flow injection analysis applications of glucose oxidase and Gluconobacter oxydans biosensors*. Colloids and Surfaces B: Biointerfaces, 2012. 100: p. 62-68.
- [10] Zhang, Y., et al., *The influence of ionic strength and mixing ratio on the colloidal stability of PDAC/PSS polyelectrolyte complexes*. Soft Matter, 2015. 11(37): p. 7392-7401.

Improvements in Airbreathing Propulsion Systems

Student Researcher: Brooke N. Meyer

Advisor: Dr. Jed E Marquart

Ohio Northern University
Department of Mechanical Engineering

Abstract

Airbreathing propulsion is commonly used in jet engines where air enters at the front and is pushed out of the back of the engine to create thrust. The air that enters the engine is compressed by a fan, combined with fuel, and combusted. This is then pushed out of the back of the engine as a high-speed exhaust creating thrust [1]. There are many areas for possible improvement in airbreathing propulsion systems. These areas include improving efficiency, noise reduction, reducing cost, lessening emissions, and improving performance. Airbreathing propulsion is also used in hypersonic jets, rockets, and other high speed aircraft, however, this research specifically focuses on improving airbreathing propulsion in jet engines used for flight by aircraft. Many ways to improve airbreathing propulsion systems involve altering the overall design of the engine and system itself. While this can lead to a more efficient engine and other benefits, it is easier said than done. In order to avoid altering the jet engine design, the fuel being used to power the engine can be altered to improve the operation of the jet engine. Airbreathing propulsion can be improved by using biofuels to power the systems which ultimately results in lower emissions [2].

Project Objectives

The goal of this research is to analyze airbreathing propulsion and look at different methods to improve airbreathing propulsion for future vehicles. Possible improvements of this method involve efficiency, noise, cost, emissions, and performance. This research looks deeper into the use of biofuels to power airbreathing propulsion systems and the benefits and disadvantages of them. The use of biofuels in jet engines is a rather recent concept in comparison to the typical use of Jet fuels or highly refined kerosene which can be further classified as Jet A or Jet A-1 [3]. The comparison between Jet fuel and biofuels is to be discussed and the advantages and disadvantages of each is also analyzed. A discussion of the future of biofuels in powering airbreathing propulsion is also included.

An Overview of Biofuels

Biofuel is fuel produced from renewable sources. In the automotive industry, corn ethanol and biodiesel are commonly used. However, Sustainable Aviation Fuel (SAF) is the biofuel of the aviation industry. SAF provides similar performance to normal jet fuel, however it produces less emissions [4]. Biofuels are produced using biomass or feedstock which can include: algae, oil seeds, corn grain, agricultural residue, wet waste, etc.

SAF vs. Standard Jet Fuel

Jet fuels such as Jet A and Jet A-1 are typically used in powering jet engines in commercial aircraft. Jet fuel is a mixture of various hydrocarbons and is petroleum or kerosene based with additives such as corrosion inhibitors and metal deactivators [3]. While jet fuel offers great performance for airbreathing jet engines, the carbon emissions produced from the use of them are high. When flying, commercial jet aircraft produce contrails due to the hot exhaust from the jet engines mixing with the cool air, forming ice crystals and creating a foggy or cloudy appearance. Sometimes these contrails can stay for long

periods of time, possibly even developing into cirrus clouds, and can have negative effects on the earth's environment. Contrails can also be worsened by the soot that is emitted by the jet engines when using typical jet fuel. However, many biofuels or SAFs used in jet engines also possess fewer aromatic compounds which would allow for the fuel to burn cleaner in jet engines. By using biofuels mixed with typical jet fuel to power jet engines in commercial aircraft, the particle emissions can be reduced by a maximum of 50 to 70 percent [2].

Possible Challenges

Some biofuels that have been manufactured as alternatives to jet fuel for airbreathing engines have been discovered to be poor lubricants inside of the engine, resulting in the escalated wearing of parts [5]. However, studies regarding the anti-wear properties of these fuels show that fuel mixtures with rapeseed-oil biocomponents actually improve the anti wear properties of normal jet fuel. Therefore, while some alternatives to traditional jet fuel may increase wear on the engine, some do the opposite and are more advantageous to the lifespan of the engine and its components. The production of SAFs can also be quite daunting. Many systems and processes go into the production of this sustainable fuel and would require large biorefineries and infrastructure and methods to produce the biofuel in the quantities that would be required.

The Future of SAFs in Aviation

SAFs are likely to become the new, typical jet fuel in the future. Emissions from aviation make up about 9 to 12 percent of the U.S. transportation's greenhouse gas emissions. By switching to SAFs this number would be dramatically reduced. The United States has launched a government-wide goal to enhance SAFs, reduce their overall costs, and expand the use and production of them, with the main goal being to supply and use SAFs for 100% of jet fuel demands by the year 2050. The use of biofuel as a substitute or supplement for typical jet fuel in airbreathing jet aircraft has benefits beyond burning cleaner and therefore resulting in lower emissions. In regards to not just the aircraft or system itself, biofuel production would also provide extra revenue for farmers and could help with other environmental issues such as requiring extra crop production which could reduce erosion and reduce pollution of wet waste [4].

Acknowledgments and References

I would like to thank OSGC for this scholarship. I would also like to thank Dr. Jed Marquart and the department of Mechanical Engineering at Ohio Northern University for providing me with many opportunities to learn and making my education possible.

[1] B. Dunbar, "Types of air-breathing engines," *NASA*, 05-Nov-2003. [Online]. Available: https://www.nasa.gov/audience/forstudents/k-4/home/F_Types_of_Airbreathing-Engines.html. [Accessed: 02-Mar-2022].

[2] K. Northon, "NASA study confirms biofuels reduce jet engine pollution," *NASA*, 15-Mar-2017. [Online]. Available: <https://www.nasa.gov/press-release/nasa-study-confirms-biofuels-reduce-jet-engine-pollution>. [Accessed: 03-Mar-2022].

[3] Wexler, P., "Encyclopedia of Toxicology," Academic Press, Elsevier, ISBN 978-0-12-386455-0, 2014.

[4] "Sustainable aviation fuels," *Energy.gov*. [Online]. Available: <https://www.energy.gov/eere/bioenergy/sustainable-aviation-fuels>. [Accessed: 02-Mar-2022].

[5] Yakovlev, A.V., Boichenko, S.V., Lejda, K., Vovk, O.A., Kuszewski, Kh., "Antiwear Properties of Plant Mineral-Based Fuels for Airbreathing Jet Engines," *Chemistry and Technology of Fuels and Oils*, v 53, n 1, p 1-9, March 2017, doi:10.1007/s10553-017-0774-x.

Frost Deposition on Flat Plates

Student Researcher: Tyler Motzko

Advisor: Dr. Mitch Wolff

Wright State University
Mechanical Engineering

Abstract

The icing phenomenon is commonly experienced in heat exchangers and the wings of an airplane. In both cases, icing is a negative phenomenon; therefore, icing must be understood so that it can be compensated for or prevented. A key part of this is understanding how the frost layer grows on a surface and the density of the frost layer. Expressions for these are presented in several publications found throughout literature. Having these expressions in an easy-to-use program, like MATLAB, would be extremely beneficial. This MATLAB program could be used to predict frost deposition. The program inputs can be changed depending on the experiment parameters. This allows for more accurate predictions which can be used in various design considerations, like heat exchangers or airplane wings, where the predictions may be useful.

Introduction

According to Leoni, icing is the process of water vapor turning directly into frost through desublimation. This occurs when the surface temperature drops below the freezing point of water. Frost build-up has two main effects: the frost layer acts as a thermal insulator, and the air flow over the surface is significantly reduced [1].

Over the passed decades, research has been conducted to try and understand the frost deposition phenomenon. A database was created of experimentally obtained data points of frost deposition on a flat plate over time. The database contains 382 data points of frost thickness and 149 data points of frost density [1]. Researchers have then tried to fit empirically derived equations through these data points with the goal of creating a model that could accurately predict frost deposition. These empirical equations try and account for the physical properties that drive frost growth. This can include the ambient air temperature, the surface temperature, Reynold's number, relative humidity, and many more properties. Empirical equations are never able to predict a phenomenon with full accuracy. This is because they are only attempts of understanding the physics behind the phenomenon. Without knowledge and understanding of all the variables that drive a particular phenomenon, it is impossible to predict it with high accuracy. Therefore, it is not uncommon to consider an error of 15% acceptable when it comes to empirical predictive models. Such models are used as a guide when designing a system. They should be used as a starting point. Designs should always be over engineered compared to the model to ensure a safe and reliable design.

Purpose

The purpose of this project is to recreate frost deposition equations found throughout literature in MATLAB. These equations can then be used to predict frost deposition for different project parameters, such as temperature, air speed, and relative humidity.

Methodology

The equations that were recreated in MATLAB were found in the review paper: *State-of-the-art review of frost deposition on flat surfaces* [1]. This paper summarized several proposed equations from previous researchers. The original sources of these equations were then reviewed. All the necessary information to recreate the equations accurately were presented in the original papers. The equations are only considered accurate within a specified range of application; therefore, the range of valid temperatures, air velocity, relative humidity, time, etc. were recorded. Plots of the equations were also found in a majority of the original papers. These plots were used to validate the MATLAB equations. If the plots did not compare well with each other, the MATLAB code was troubleshooted until the error was found and then fixed.

Results and Discussion

For the frost thickness, only the Schneider [2] and Hermes [3] equations were recreated. Lee et al. and Hermes et al. were solved analytically. These equations were not recreated because they were beyond the mathematical scope of this project. Figure 1 shows a comparison between the original plots for the Schneider equation and the MATLAB recreation. The recreation matches well with the original plot; therefore, the equation is validated. Figure 2 shows a comparison between the original plot for the Hermes equation and the MATLAB recreation. There is noticeable error between the original plot and the MATLAB plot. This error could be from the MATLAB code, or a miscommunication from the author of the original equation. The errors are within ± 0.5 mm.

For the frost density, the Hermes et al. [4], Yang [5], and Leoni [1] equations were recreated. The original papers for Hayashi et al. and Hosoda were not accessible, and the Kandula equation was solved analytically, so it was not recreated in MATLAB. Figure 3 shows the comparison between the Hermes et al. equation and the MATLAB recreation. The plot presented in Hermes et al. has the density of frost over the density of ice along the y-axis and the square root of time in seconds. Hermes et al. presents this density ratio for various Jakob numbers, which is the main parameter in the equation. The MATLAB equation lines up well with the original plot; therefore, the MATLAB equation is validated. Figure 4 shows the comparison between the Yang equation and the MATLAB recreation. As there is no plot given in the original paper, the plot from Leoni was used. The plots agree with each other; therefore, the MATLAB equation is validated. Leoni presented their own equation for frost density. This equation is shown in Figure 5 and is compared to the MATLAB recreation. The Leoni equation is called "Present correlation" in the legend. The two plots agree with each other; therefore, the MATLAB equation is validated.

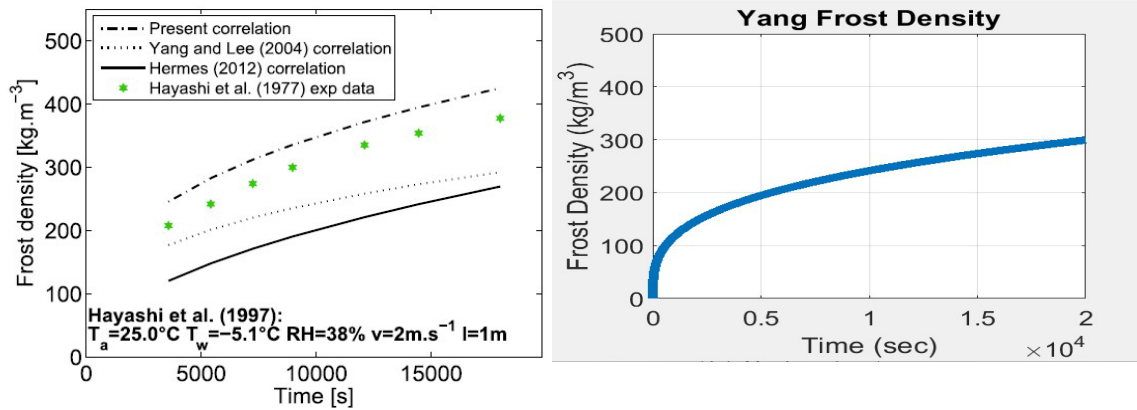


Figure 4: Yang Equation

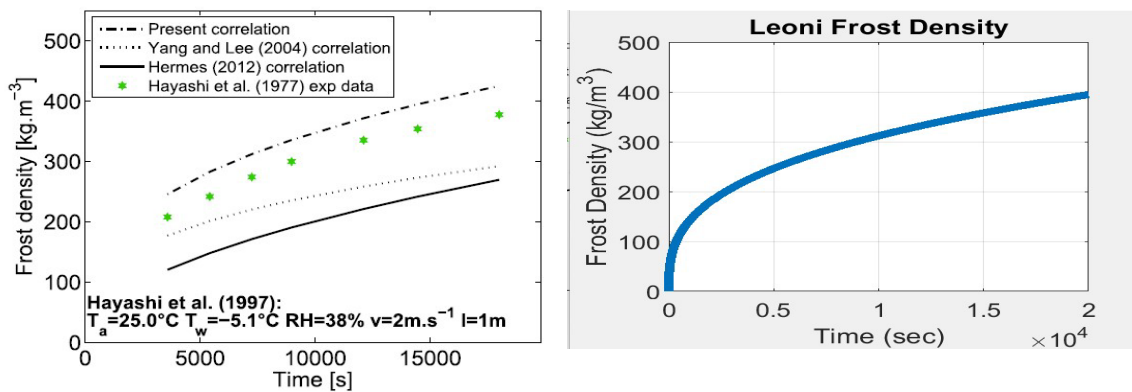


Figure 5: Leoni Equation

Acknowledgements

The author would like to thank OSGC for making this research possible, as well as Dr. Mitch Wolff and Danielle Masse for all the help and support given throughout this project.

References

- [1] Aurélia Léoni, Michèle Mondot, François Durier, Rémi Revellin, Philippe Haberschill. "State-of-the-art review of frost deposition on flat surfaces". *International Journal of Refrigeration*, Vol. 68, pp. 198 – 217, 2016. DOI: 10.1016/j.ijrefrig.2016.04.004.
- [2] Schneider, H. W. "Equation of the Growth Rate of Frost Forming on Cooled Surfaces". *International Journal of Mass Transfer*, Vol. 21, pp. 1019-1024, 1978. DOI: 0017-9310/78 0801-1019
- [3] Hermes, Christian J.L. "An Analytical Solution to the Problem of Frost Growth and Densification on Flat Surfaces." *International Journal of Heat and Mass Transfer*, Vol. 55, pp. 7346-7351, 2012. DOI: 10.1016/j.ijheatmasstransfer.2012.06.070
- [4] Hermes, Christian J.L.; Loyola, Felipe R.; and Nascimento, Valter S. Jr. "A Semi-Empirical Correlation for the Frost Density." *International Journal of Refrigeration*, Vol. 46, pp. 100-104, 2014. DOI: 10.1016/j.ijrefrig.2014.02.008
- [5] Yang, Dong-Keun and Lee, Kwan-Soo. "Dimensionless Correlations of Frost Properties on a Cold Plate." *International Journal of Refrigeration*, Vol. 27, pp. 89-96, 2004. DOI: 10.1016/S0140-7007(03)00118-X

Development of Static Test Stand for NASA Student Launch Team

Student Researcher: Stuart Nowery

Advisor: Dr. Timothy Ward

Cedarville University
Mechanical Engineering

Abstract

In this project, a test stand capable of securing the Cedarville NASA Student Launch Team's competition rocket was designed, manufactured, and analyzed with several techniques for finding effective stress to verify the stand's safety.

Project Objectives

The goal of this development was to create a static testing stand for the forerunning Cedarville Student Launch Team at minimal cost and capable of holding the rocket without causing damage as well as endure repeated use under max load of the rocket engine motor. The structure provides a means for current/future design teams to perform testing on the rocket.

Methodology

For design of the stand, a minimal and radially symmetric stand was preferred for easier modeling, analysis, and lower cost. All of the modeling work was done in SOLIDWORKS and the stress analysis was done both in SOLIDWORKS and in TKSolver. To manufacture the final design, equipment and tools were provided by Cedarville University's manufacturing lab to cut, turn, and tig weld the structure into its final state. The final design in SOLIDWORKS and real-world are shown in Figures 1 and 2.

Two methods for finding the effective von Mises stress in the stand were performed, one in simulation and one analytical to verify the simulation.

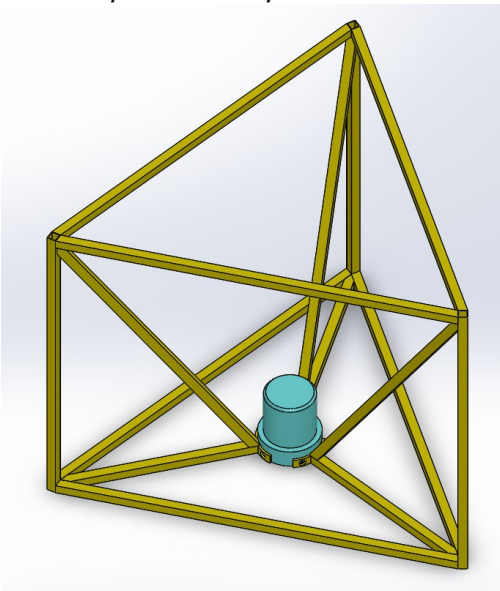


Figure 1. Final Test Stand Iteration



Figure 2. Completed Real-World Test Stand

Expected Results

By modeling the stand in SOLIDWORKS, applying the integrated finite element analysis (FEA) simulation could be performed with constraints like where the stand would be supported and the maximum force output of the rocket motor on the stand. The results of the simulation are shown in Figure 1 where the effective von Mises stress was 758.2 psi and the smallest factor of safety in the stand was 12.58. Von Mises method for effective stress was used as it correlates well with experimental data for ductile materials like the material used, mild steel.

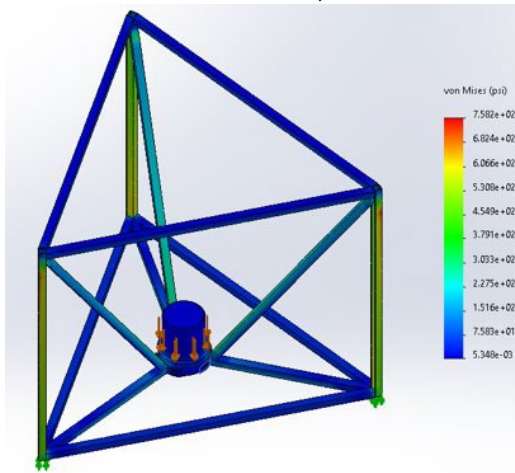


Figure 3a. Stress Distribution for Applied Load of 371 lb.

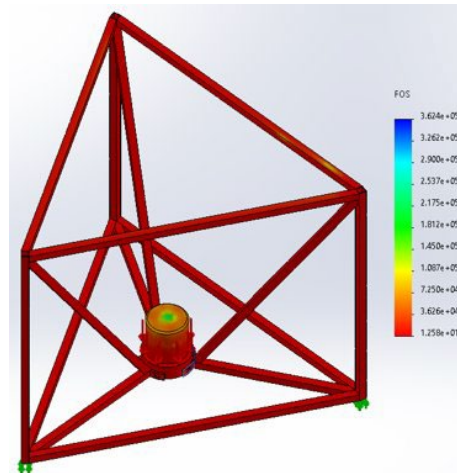


Figure 3b. FOS Distribution for Applied Load of 371 lb.

As an attempt to verify the results from SOLIDWORKS FEA, a statics method of nodal analysis was used and the free-body diagram for this investigation is shown in Figure 2. The resulting minimum safety factor was 56.443.

Significance of Expected Results

The results of the FEA simulation appeared to be reasonable, however they were not able to be verified with the analytical solution. The nodal analysis used in the analytical solution had a major oversight in that it assumed that there was zero moment about each respective node. In reality, the moment caused at each junction of members results in the limiting factor of the structure. For this reason, the safety factor given by the analytical solution was much too high to be realistic. This could have been prevented by making each joint a pin joint.

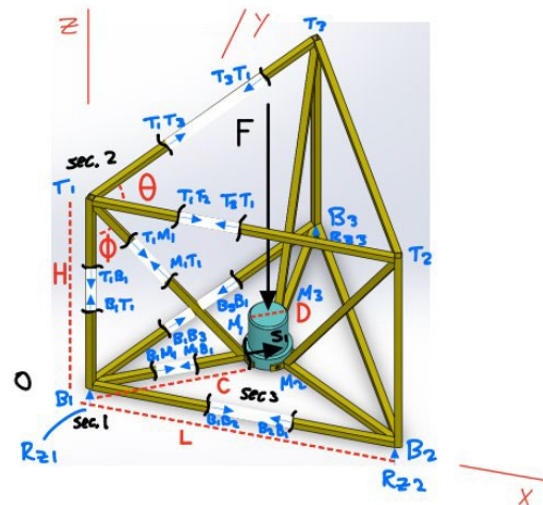


Figure 4. Free-Body Diagram of the Test Stand for Nodal Analysis

Acknowledgements

I'd like to thank OSGC for the opportunity to research, learn from, design, and manufacture this stand as a member of Cedarville's Student Launch Team

Design of Single Lap Adhesive Joints Using Machine Learning Approaches

Student Researcher: Natalie S. Richards

Advisor: Dr. K.T Tan

The University of Akron
Mechanical Engineering

Abstract

Adhesive bonded joints have an advantage in having the ability to join dissimilar engineering materials due to them having high structural efficiency and being lightweight. These joints are either between two opposite laminates or between a composite laminate and a metal structure. The aerospace and automotive industries have seen an increase in utilizing these adhesive joints in their engineering applications. Joint strength along with the failure mode (adhesive failure, delamination failure, etc.) is the most important parameter to evaluate when understanding the capability of the adhesive joint. In this paper, a regression and a classification machine learning (ML) model are utilized to predict the failure load and the failure mode of single lap adhesive joints. 103 single lap joint samples with different geometry parameters and material parameters were compiled from journal papers to build the ML tools. An Artificial Neural Network (ANN) model and a Random Forest (RF) model were developed to accurately predict the failure load and the failure mode of the joint. These models allow us to explore the complex, mathematical relationship between the input design parameters and the output.

Methodology

To generate the data set for training and testing ML models, 103 data points were congregated from other journal papers that experimentally found the strength of adhesive joints by varying the input parameters. The data set consists of 8 geometrical input design parameters and 2 output parameters. The input parameters are Adherend 1 and 2 elastic modulus (GPa), Adherend 1 and 2 thickness (mm), Adhesive Shear Modulus (GPa), Bondline Thickness (mm), Bondline Width (mm) and Bondline Length (mm). The outputs in the dataset are Failure Load (kN) and Failure Mode.

Artificial Neural Network

An ANN is a network of artificial neurons that can be trained to map nonlinear trends between multiple inputs and outputs. They were created to simulate the way biological brains work composed of "neurons". An ANN includes a large number of neurons that work together to process information and generate meaningful results. It consists of 3 layers; an input layer, hidden layer(s), and an output layer. The ANN learns the patterns of the data and stores that information in the weights of the neurons [1]. In this study, the ANN is applied to reveal the hidden information and relationship between 8 geometrical joint parameters and the failure load and mode of single lap adhesive joints. The input layer has 360 parameters, the first hidden layer has 1025 parameters, the second hidden layer has 260 parameters and the output layer has 11 parameters. As a result, there are 1,656 total trainable parameters.

Random Forest

The RF algorithm can handle continuous and categorical variables, making it applicable to solving the problem of predicting the numerical failure load output and categorical failure mode. A RF model is a white-box model, meaning it explicitly shows the relationship of the input variables with the output. The final prediction of the model can be fully explainable. This is critical in order to understand the reason behind the models decisions and to be able to defend the results of the model.

A RF is an ensemble of decision trees that are trained with the “bagging” method. The idea of this bagging method is that a combination of learning models increases the overall result of the model. A RF is built off a combination of multiple Decision Trees (DT) and merges them together to create a more accurate and more stable prediction [2,3]. The RF in this research consists of 7 DT in order to make its classification predictions on the failure mode.

Results and Discussion

Regression Model Results: The regression model accuracies can be extracted from a plot of predicted test values versus true test values along a linear slope. The ANN has high prediction accuracies across the 3 different random states of RS=26, 38 and 48 with corresponding R^2 values of 0.92, 0.925 and 0.988, respectively. The testing results of the 3 different random states based on the RF model and the corresponding R^2 values are 0.62, 0.81 and 0.83. Comparatively to the RF model, the ANN has a higher predicting accuracy for the test set in the regression model. This is a result of the random forest methods having a disadvantage due to their ability to predict discontinuous responses. ANN is able to handle more complex, nonlinear mathematical relationships due to its high flexibility in its ability to tune hyper-parameters to plot on a regression curve, to solve this specific problem. The ANN’s utilization of backward propagation allows for the ANN to train until the desired result is achieved.

The main question the regression model needs to answer is whether ML is able to capture the mechanics of the adhesive joint based on the patterns it learned from the input parameters. The results show both of these ML models can accurately predict the strength of a single lap adhesive joint with the geometrical input parameters.

Classification Model Results: The classification model accuracies are extracted from confusion matrices, displaying the correlation between the predicted test values versus the true test values. The accuracy of the random forest for the classification model is 100%. The classification ANN model is 94% accurate. This matrix is showing the ANN is incorrectly classifying delamination failure. The model is predicting one of the delamination failure modes to be cohesive failure mode. This is a consequence of the high amount of cohesive failure occurring in the dataset. The classification results can be seen in Figures 1 and 2.

Design Parameters: From the correlation matrix produced in the model and classification mode RF model, the bondline length was found to be the most important parameter in correlation with the failure load of the single lap joint. To study the relationship of the bondline length versus the failure load, four combinations of adherends were studied across the ANN and RF model: Aluminum + Composite Adherends, Aluminum only Adherends, Composite only Adherends, Green Composite only Adherends. The bondline length was measured from 10-55mm in 5mm increments. In both models, each plot shows an increase in strength as the bondline increases, regardless of the adherends. The result of the Aluminum + Composite Adherends can be seen in Figure 5. The failure modes were also gathered from the RF and ANN model with varying the bondline from 10-55mm in 5mm increments. It was shown that with each adherend combination, a failure mode reigned consistent. The parameter difference between the different adherend combinations occurs in the adherend elastic modulus. The results of failure mode gathered indicate the adherend material is a key indicator on the failure mode of that joint, rather than the varying in bondline length. These results can be seen in Figure 6.

Figures and Charts

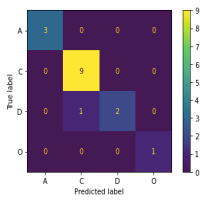


Figure 1: (left) Classification Model ANN prediction results Aluminum + Composite Adherends

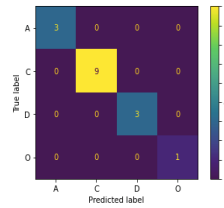


Figure 2: (right) Classification Model RF prediction results

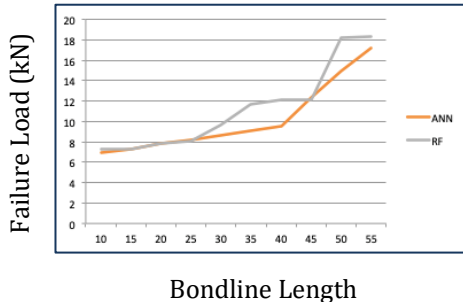


Figure 3: (left) Bondline Length vs. Failure Load

Aluminum + Composite Adherends		Composite Adherends		Aluminum + Aluminum Adherends		Green Composite Adherends	
Bondline length	Failure Mode	Bondline length	Failure Mode	Bondline length	Failure Mode	Bondline length	Failure Mode
10	D	10	C	10	C	10	A
15	D	15	C	15	C	15	A
20	D	20	C	20	C	20	A
25	D	25	C	25	C	25	A
30	D	30	C	30	C	30	A
35	D	35	C	35	C	35	A
40	D	40	C	40	C	40	A
45	C	45	C	45	C	45	A
50	C	50	C	50	C	50	A
55	C	55	C	55	C	55	A

Figure 4: (right) Bondline Length vs. Failure Mode for RF model

References

- [1] Ujjwalkarn. "A Quick Introduction to Neural Networks." *The Data Science Blog*, 10 Aug. 2016, <https://ujjwalkarn.me/2016/08/09/quick-intro-neural-networks/>.
- [2] Roy, Abhijit. "A Dive into Decision Trees." *Medium*, Towards Data Science, 6 Nov. 2020, <https://towardsdatascience.com/a-dive-into-decision-trees-a128923c9298#:~:text=A%20decision%20tree%20is%20a,dataset%20to%20the%20fullest%20purity.>
- [3] E R, Sruthi. "Random Forest: Introduction to Random Forest Algorithm." *Analytics Vidhya*, 24 June 2021, <https://www.analyticsvidhya.com/blog/2021/06/understanding-random-forest/>.

Wearable Biosensor Fabricated by Laser Direct Writing for Detection of Cortisol

Student Researcher: Anthony Romeo

Advisor: Dr. Byung-Wook Park

Youngstown State University
Chemical Engineering

Abstract

Wearable sensors have attracted much attention thanks to their promising applications in personalized medicine through remote monitoring of physiological parameters. Cortisol is a biomarker for numerous diseases and is important for blood pressure regulation, glucose levels and metabolism. The current project is to create a flexible, wearable biosensor to detect cortisol in body fluid by skin contact with the sensor. A laser-assisted processing technique is used to produce laser-induced graphene (LIG) by direct laser writing with a carbon dioxide laser on carbon materials. For non-invasive extraction of biomarkers, a hydrogel layer is incorporated onto the electrode surface. An antigen-antibody interaction is fabricated to take place on the working electrode to detect cortisol via surface chemistry. Both cyclic voltammetry (CV) and electrochemical impedance spectroscopy (EIS) are used to characterize the modified electrode and detection of cortisol. Specifically, the characterization will consist of detection limit, selectivity, sensitivity, response time, and linear range. Using 3D printed wristbands and wireless communication devices, it will be possible to monitor personnel in real-time during any sort of situations including long-term exposure to space environments, flight preparations, sleeping and take-off.

Objectives

- Using a gold nanoparticle modified LIG electrode, develop a self-assembled monolayer (SAM) that can accurately detect cortisol
- Processing to engrave polyimide film with a CO₂ laser engraver with different speed and power settings (Power Dose Assay) to determine optimum conditions producing lowest resistivity for the laser induced graphene (LIG)
- Using optimized LIG conditions, perform electrodeposition to form gold nanoparticles on the surface of the LIG electrode (AuNP-LIG) to further increase the conductivity and SAM
- Characterizing the fabricated electrode using CV, EIS, SEM and EDS

Methodology

First, the development of the proper SAM on the surface of the gold electrode is essential for immobilizing macromolecules, such as antibodies. The LIG could be modified with gold nanoparticles (AuNPs), which are formed via electrodeposition, and serve as a mass-productive conducting carbon material that could be alternative to a gold electrode. The Dithiobis(succinimidyl propionate) (DTSP) was chosen as the thiol chemistry. The SAM formation was the primary method of antibody immobilization. Clarifying, the sulfur bonds break from one another due to a high affinity for gold, which is called chemisorption. Then, the cortisol antibodies were bonded by the DTSP forming a covalent bond with the amino group on the carboxyl group of the DTSP. Thus, the antibodies could be attached to the DTSP layer formed on the AuNP-LIG electrode. Finally, the reactive groups of the SAM were blocked by Bovine Serum Albumin (BSA) solution containing Tween 20, which was used to prevent the cortisol from nonspecific binding. The BSA was the standard blocking protein for use of the sensor in biological media, where it would block nonspecific protein-surface interactions. This surface chemistry allows the sensor to specifically bind to cortisol in the cortisol detection experiment. This experiment worked by setting up

a three-probe electrochemical cell and cortisol detection was increased by an order of magnitude in the range of 1 pM to 100 nM.

Results

Figure 1 displays an EDS spectrum and SEM image that AuNPs on the LIG electrode were detected. Additionally, an SEM image of the sample is included which shows where the AuNPs were formed to the sample.

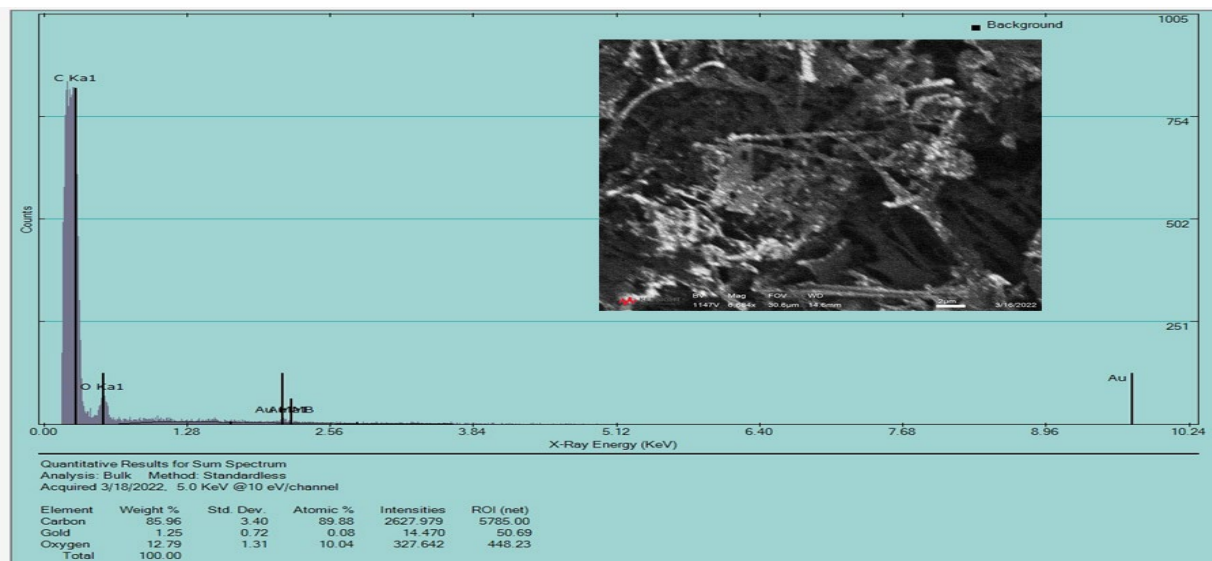


Figure 1: EDS and SEM of AuNP-LIG electrode surface

Figure 2 shows the EIS detection data for cortisol via the antibody-antigen binding in the form of a Nyquist plot. This is a measurement of the electrical double layer formed by the ions in the solution bounded to the outside of the antibody-antigen interaction.

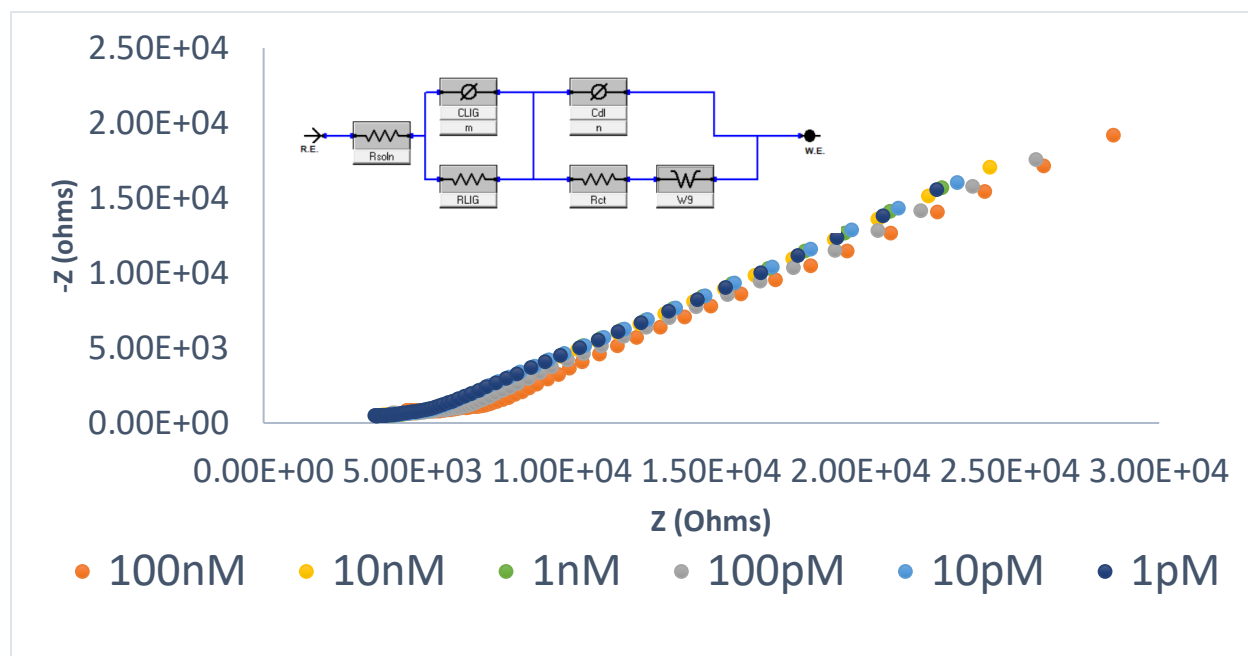


Figure 2: Nyquist Plot showing EIS Detection Data for Cortisol

Figure 3 shows the bode plot for detection of cortisol from the antibody-antigen binding interaction. This is used to acquire ratio of change between base LIG and respective concentrations of cortisol on LIG or a Zmod score which is displayed in figure 4.

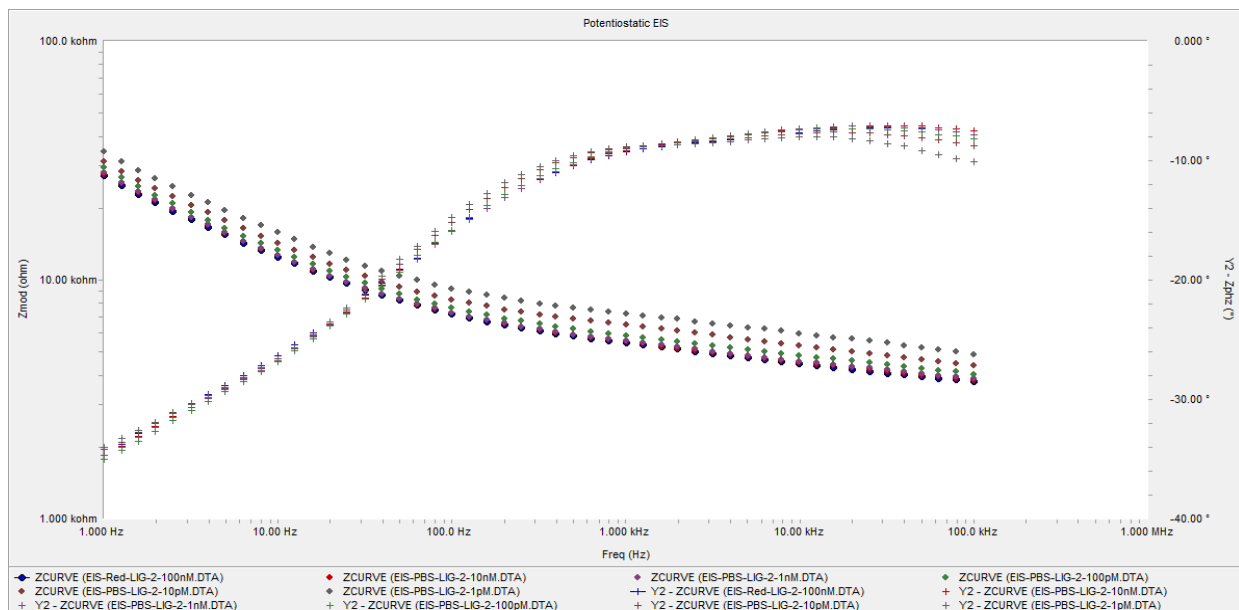


Figure 3: Bode Plot showing EIS Detection Data for Cortisol

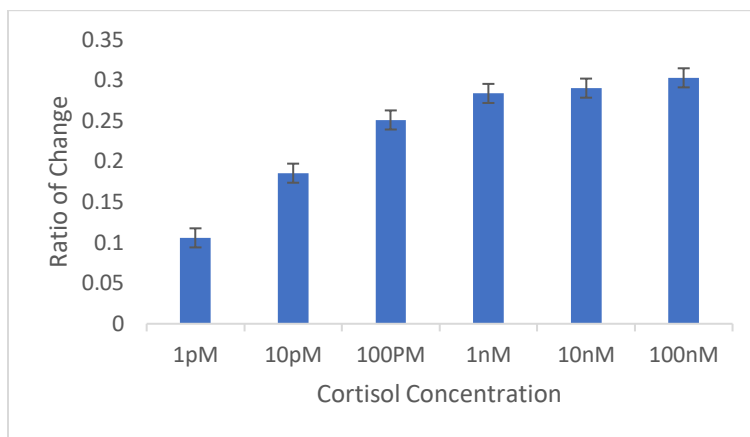


Figure 4: Zmod score

Discussion

Firstly, the electrode was characterized with EDS and SEM. It's confirmed that the electrodeposition of AuNPs on the surface of the LIG electrode was successful. Then, the electrode went through the cortisol detection experiment and relevant Nyquist and bode plots were acquired via EIS. The Nyquist plot shows higher capacitance reactance, as the resistivity is decreasing, which means a larger surface area of the electrode. Thus, it's concluded that cortisol binds to the antibodies immobilized on the electrode as its area is increasing in relation to the larger and larger concentration of cortisol in solution. The bode plot shows that with increasing cortisol concentration the capacitance reactance increase. By acquiring the Zmod scores from the bode plot, the percent differences from initial concentration were estimated. Each injection of higher concentration (10 times) produces a larger ratio of change meaning more reactance on the surface of the electrode.

Acknowledgements

The authors acknowledge Dr. Pedro Cortes, Dr. Bhargavi Mummareddy, Jose Gonzalez-Garcia, Kyle Duke and Ray Hoff for their assistance, continued guidance and inputs in the project. The authors would also like to thank the Ohio Space Grant Consortium (OSGC), University Research Council Grants at YSU and Assured Digital Microelectronics Education & Training Ecosystem (ADMETE) for their financial supports.

References

- [1] B.W. Park et al., A novel glucose biosensor using bi-enzyme incorporated with peptide nanotubes, *Biosens. Bioelectron.*, 2012, 38, 295.
- [2] A. Dallinger et al., Stretchable and skin-conformable conductors based on polyurethane/laser-induced graphene, *ACS Appl. Mater. Interfaces*, 2020, 12, 17, 19855.
- [3] Z. Ma et al., Advanced electronic skin devices for healthcare applications, *J. Mater. Chem. B*, 2019, 7, 173.

Exploration of Laser Induced Graphene Capacitors As a Possible Energy Storage Means

Student Researcher: Ryan Sauder

Advisor: Dr. Jed E. Marquart

Ohio Northern University

Department of Mechanical Engineering

Abstract

Electricity has becoming an increasingly important aspect of modern space craft and satellites. There are two primary means that electricity is generated for these missions. First, a *radioisotope* thermoelectric generator (RTG) generates power for long periods of time using a radioactive heat source. Another common means is to use solar cells. These cells generate energy from the sun and store this power in batteries. For missions that are staying close to Earth, more traditional battery technology, such as Lithium Ion batteries are adequate. However, for long range mission such as traveling to Mars, or long time frame missions such a base on the moon, a more robust means of energy storage should be explored. This is because on these longer missions the batteries experience many charge/discharge cycles and degrade over time. To overcome this, the use of laser induced graphene to create a bank of energy storage capacitors will be explored.

Laser induced graphene is a process of exposing a polyamide film to low power laser light under normal atmospheric conditions. This causes the film to decompose into a layer of graphene. Using a computer controlled laser, the pattern that the graphene takes can be precisely controlled to create capacitors. These capacitors can then be chained together to increase the total energy stored and create a small electrical power storage system. To be functional, the time that this system holds a charge will be maximized. Since capacitors operate on the simple principle of stored electrical charges they are able to be cycled many times without any degradation in performance, and thus are optimal for the next generation of space travel.

Project Objectives

The objective of this research is to determine an optimal laser power to expose a piece of polyimide tape. If a capacitor is to be made from laser induced graphene, the device would have a minimal internal resistance. A lower internal resistance would result in less electrical energy being dissipated from the general operation of the device, and therefore a more efficient capacitor.

Methodology Used

The methodology used was based off of the process set forth by Li et al [1]. The process utilized in this research began with modeling a pattern for a compact yet long electrode. This pattern is designed to optimize the total length of an irradiated trace within a confined space. This will results in the most electrical resistance of the graphene structure. This pattern was imported into CorelDraw and the laser programed to raster over the entire pattern. To prepare the polyimide for exposure a piece of polyimide tape of thickness 0.002 inches and width one inch was adhered to a cardboard backing such that the tape was made ridged and taught. This was then installed in the ULS VLS4.75 60 Watt Laser and the engraving program run. The speed was 100% for all tests. The power was set to 8%, 25%, and 40-

60% in 5% increments. For each of these tests a fresh piece of unexposed film was used. Lastly, the structural integrity of the film was analyzed, and the electrical resistance measured.

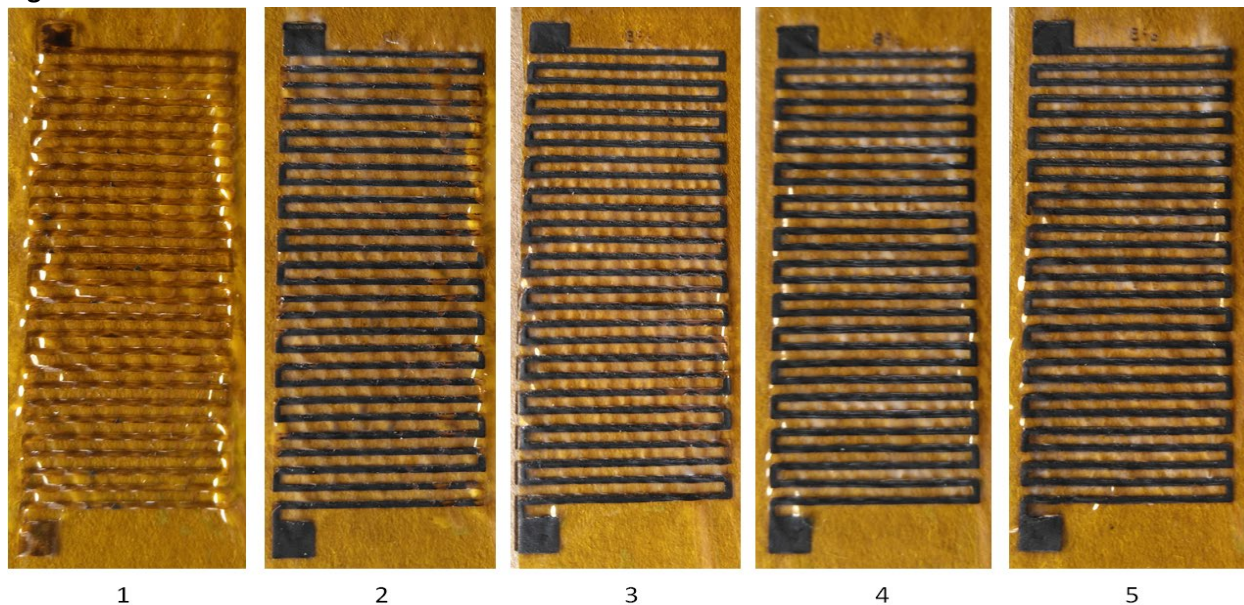
Results Obtained

The film that was exposed to 8% and 25% did not yield any change after being exposed. The laser began decomposing the film into a layer of graphene at 40%. Figures 1-5 show the graphene film created at the different power levels. When the resistance was measured only the samples exposed to 55% and 60% yielded low enough resistances to register. These values were 50.51 and 38.8 kOhm respectively. However, the sample exposed to 60% is weakened by the laser cutting through the film at the edges of the pattern in several locations.

Significant and Interpretation of Results

Using a consumer grade CO2 laser engraver, a layer of graphene was able to be created on the surface of the polyimide tape. This is a simple process that could be impended in a large scale roll to roll manufacturing process for large scale energy storage projects. If a laser similar to the ULS VLS4.75 used, a power level of 55% creates a conductive layer of graphene without significantly decreasing the structural integrity of the underlying film. For further testing and development, a thicker layer of polyimide film would allow higher laser power to be used to generate lower resistance structures while maintaining the strength of the polyimide film.

Figures



Figures 1-5: Polyimide tape samples exposed to 40%, 45%, 50%, 55%, and 60% laser power respectively.

Reference

[1] Li et al. "High-Performance Pseudocapacitive Microsupercapacitors from Laser-Induced Graphene" *Advanced Materials*. 2015

The Use of Indirect Clues to Solve Aircraft Accidents

Student Researcher: Abigail C. Schauer

Advisor: Dr. Jed Marquart

Ohio Northern University
Mechanical Engineering

Abstract

Air travel is heavily integrated into the modern world with continued trust in safety and reliability as a vital component of the system. When accidents happen, the cause must be quickly and accurately assessed and addressed. With many components contributing to an incident, authorities and industry must be able to decipher wreckage on the ground, evaluate human factors and the physical environment to determine the root cause, or causes. This paper will focus on the methods used in this process such as analyzing the origins of fires, reconstructing the flight path, and identifying structural failure points.

Project Objectives

The goal of this project was to identify some of the indirect methods that aircraft accident investigators use to identify root causes of an incident and the logical jumps that can be made from them. Due to the large number of relevant topics, only a handful of topics will be addressed in this paper.

Methodology Used

A study of technical papers and relevant textbooks was used to gather the information for this paper.

Results Obtained

“We need a consistent pattern of evidence; not just a single clue” [1, p 72]. This was the overarching theme throughout my research and is vital throughout each stage of an investigation.

Fire: It is common for vaporized fuel to ignite after a crash, it is significantly less common for a fire to start in flight, and these are incredibly dangerous. Smoke can quickly fill the small space and many items onboard produce toxic fumes when burnt. The origin of a fire is crucial to determining a cause of a crash. In flight fires frequently burn through the skin of the aircraft and reach the slipstream. If the fire was exposed to the slip stream, there will be small, droplets of aluminum fanned out the skin of the plane downstream from the origin. If it was a post impact fire, the aluminum drops will be larger and will move down the fuselage due to gravity. If a possible origin of fire is located, chemistry is used to see if a fire could exist in those conditions. Was it hot enough in the area to ignite or melt the materials near it? With the chemical structure of jet fuel, aluminum alloy sparks are not hot enough to ignite it, so very specific conditions are needed. Fires at flying altitudes burn at higher temperatures and are able melt or deform materials that a post impact fire could not. Scattered parts with clean scratches through soot could also indicate that the part was covered in soot before impact when it was likely scratched.

Power and Control Systems: Indirect evidence of a fire can be gathered by checking if the crew put on gas masks, lowered the cabin pressure to reduce available oxygen, or cut off power to electrical circuits. Another form of indirect evidence is to determine if a warning light was on that could have informed the pilot of an issue. Due to the brittleness of tungsten filament in light bulbs, observing a brittle fracture or a deformation of the filament is a reliable way to know if the bulb had been on (warm) or off (cold).

Field tests can be done to start narrowing down the list of possible causes. Oil, fuel, and hydraulic lines should be checked for blockages. Since they likely ruptured on impact, checking the pumps along the lines for fluid inside indicates that the lines were likely functional. More importantly, it can be assumed that systems that the fluid lines served were capable of being run. Fluid samples should be taken from targeted areas to check for excessive debris that could be from failing bearings. Fuel samples should be taken to check if it was the right type for the aircraft.

Impact Physics: The wreckage pattern can be useful to determine the trajectory at impact by analyzing how the wreckage fanned out. If the black box is unrecoverable, estimates of the speed and attitude of the aircraft at impact can be estimated using the depth of the ground scarring or triangulation from broken tree limbs, if present.

Materials: The structure needs to be analyzed to determine if parts failed before impact. Since machine parts frequently have varying levels of fatigue and a large volume of parts certainly failed under the force of impact, it is difficult to identify key parts for the cause of the crash. Metal that did not break in the direction of its intended load can be assumed have failed during the impact. If it broke in the expected direction and two or more distinct fracture zones can be identified, it could indicate the part failed in flight and that broke on impact. If a piece is suspected of fracturing in flight and its failure could have led to the crash, then lab testing is needed to determine the forces that had acted on the part.

Significance and Interpretation of Results

Every tragedy provides an opportunity for improvement and deepens the body of knowledge for the next incident. This body of knowledge supports the conclusions that can be made from the steps outlined, even if they are not inherently obvious. The logic behind seeing a deformed filament and knowing a warning light was on requires a reverse type of thinking that looks at an issue and identifies every possible root cause. While this logic is clearly useful in the field of investigation, it can be applied in a variety of environments. If more people become familiar with this type of thinking it could greatly expand the diversity of thought. More atypical approaches to issues in any field will aid new innovations and reap unknown benefits.

References

- [1] R. H. Wood, R. W. Sweginnis, and J. Lederer, *Aircraft accident investigation*. Casper, WY: Endeavor Books, 2006
- [2] D. F. Knutson and Society Of Automotive Engineers, *Basic science and art of aircraft wreckage reconstruction*. Warrendale, Pennsylvania: SAE International, 2020.
- [3] G.D. Bibel and R. Hedges, *Plane Crash: the Forensics of Aviation Disasters*. Baltimore: Johns Hopkins University Press, 2018.
- [4] J. Lowery, *A pilot's accident review: an in-depth look at high-profile accidents that shaped aviation rules and procedures*. Newcastle, Washington: Aviation Supplies and Academics, Inc, 2015.

Investigating the Complex Between Tertiary Amines and CO₂

Student Researcher: Lindsey A. Speare

Advisor: Michael Tubergen

Kent State University
Chemistry

Abstract

The complex formed by trimethylamine and carbon dioxide was probed for the first time using microwave spectroscopy. Currently the spectrum has obtained a fit of 26 kHz and exhibits a symmetric top pattern. Additionally, rotational transitions from ¹³C and ¹⁵N will be investigated to obtain a better understanding of this complex. Ultimately, this will assist in improving the absorption rate of tertiary amines.

Project Objective

Carbon dioxide (CO₂) is an abundant greenhouse gas that is necessary for life. However, at high concentrations it can be toxic. It is possible to reduce these emissions by absorbing them. Primary and secondary amines are known to absorb CO₂ by the formation of a stable carbamate. This reaction is possible due to the establishment of a zwitterion, a molecule with separate positively and negatively charged groups³. Tertiary amines form an unstable carbamate in the presence of water, but it can undergo an alternate reaction to create bicarbonate. The mechanism of this reaction is still undetermined. Despite the 1:1 mole ratio between CO₂ and a tertiary amine, the absorption rates are lower than that of primary or secondary amines. The regeneration of the amine requires less heat energy, making it desirable for gas removal, but the absorption rates would need to be increased². In this investigation the complex between trimethylamine (TMA), a tertiary amine, and carbon dioxide has been determined by cavity-based Fourier transform microwave spectroscopy. This allows a better understanding of CO₂ capture and how to improve it, along with the structure of the complex.

Methodology Used

The possible complexes were modeled using Avogadro. The Gaussian 16 package on the Owens cluster at the Ohio Supercomputer Center was utilized for all computational calculations. Then the models were optimized using the Becke three parameter Lee-Yang-Parr exchange-correlation (B3LYP) and the second-order Moller-Plesset perturbation theory (MP2), implemented with the aug-cc-pVTZ basis. Table 1 shows the predicted rotational constants and dipole moments, with the lowest energy conformer shown in Figure 1. A high resolution Flygare-Balle jet-cooled cavity-based Fourier-transform microwave spectrometer was used to measure the spectrum of the TMA-CO₂ complex from the frequency range of 8.9-17.88 GHz. It uses customized software to perform signal averages, display and save the transformed data, control the frequency and the delay generators, and scan the spectrometer by adjusting the cavity and frequency source. It has a range of 10-22 GHz and an experimental resolution of 2.5 kHz. More information about the specific aspects of the spectrometer can be found¹.

Results Obtained

With the aid of computational calculations, the modeled rotational constants $(B+C)/2$ were used to guide our experimental search. The first suspected rotational transitions were located at 11964.7-11970.1 MHz

as shown in Figure 2. The next region that was scanned was from 14934-14937 MHz, which showed rotational transitions similar to those initially found, indicating that the TMA-CO₂ complex is exhibiting symmetric top patterns. This indication provides evidence that there is a three-fold axis of symmetry. It was expected that CO₂ would have broken this symmetry, however, it is predicted that it rotates about the central axis, resembling a symmetric top on average (Figure 1). To treat the complex as a symmetric top, two of the rotational constants are equal, shown in Table 1. Once it was confirmed that these rotational transitions were dependent on carbon dioxide, the rotational quantum number (*J*) was estimated for the TMA-CO₂ complex. Its nearest transitions were calculated using $\nu = 2B(J + 1) - 4D_J(J + 1)^3 - 2D_{JK}(J + 1)K^2$, where *B* is the rotational constant, ν is the frequency, and *D_J* and *D_{JK}* are centrifugal distortion constants. In Table 2 it is apparent that the rotational constant is close to the B3LYP model 1 or MP2 model 1, which is expected since it is the lowest in energy. In Table 3, the hyperfine component (eQq) for model 1 resembles the experimentally determined value. This indicates that the complex formed is that of model 1. When searching for the next transition, a similar grouping of lines was found in the 8988 MHz region. These lines also exhibit hyperfine splitting that is consistent with nitrogen. The splitting is due to the nuclear spin of an atom, such as N, Cl, Br, I, etc., being greater or equal to one. This causes the magnetic field at the nucleus to interact, causing the rotational transition to split as shown in Figure. 2, where each line is split into three lines. The spectrum currently has a fit of 24kHz, however this can be improved by adding more rotational transitions. Isotopic studies are needed and are being performed currently to understand how this complex forms.

Significance

These results prove that there is a complex formed and it is that of a symmetric top rotor. This allows a mechanism to be considered. Then further investigation into the transitions from ¹³C and ¹⁵N will obtain a better understanding of the proposed mechanism. Ultimately, this will assist in maximizing tertiary amine's ability to absorb carbon dioxide.

Tables and Figures

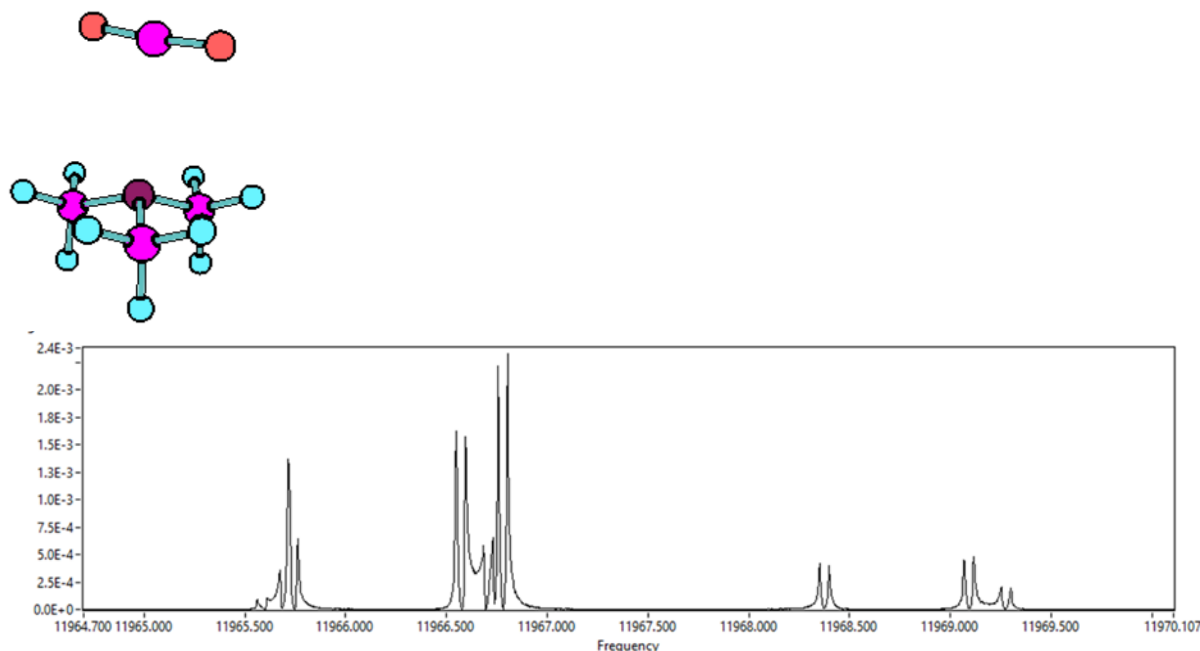


Table 1. Comparing the predicted conformers of TMA CO₂.

Model		Rotational Constants (MHz)			Dipole Moment (Debye)		
		A	B	C	m _a	m _b	m _c
B3LYP	1	3491.066	1637.942	1437.906	1.31	0.05	0.01
	2	3525.890	1668.069	1449.955	-1.43	-0.00	0.14
MP2	1	3506.520	1142.350	1038.781	-0.64	-0.00	-0.05
	2						

Table 2. Comparing predicted and experimentally determined B.

Model		(B+C)/2 (MHz)
B3LYP	1	1537.9
	2	1559.0
MP2	1	1090.6
	2	1500.8
Experimental		

Table 3. Comparing experimentally derived eQq to Mp2 models.

Model	eQq (MHz)
Experimental	3.77
1	2.07
2	-5.16

Acknowledgements

I would like to thank NASA, Kent State University, and Ohio Space Grant Consortium for this wonderful opportunity. I also like to thank Dr. Michael J. Tubergen, Dinesh Marasinghe, and Michael J. Carrillo for their help and guidance.

References

1. A. R. Conrad, N. H. Teumelsan, P. E. Wang, and M. J. Tubergen, *J. Phys. Chem. A* 114(1), 336–342 (2010).
2. Chowdhury, F. A.; Yamada, H.; Higashii, T.; Goto, K.; Onoda, M. CO₂ Capture by Tertiary Amine Absorbents: A Performance Comparison Study. *Ind. Eng. Chem. Res.* 2013, 52 (24), 8323–8331. <https://doi.org/10.1021/ie400825u>.
3. Dutcher, B.; Fan, M.; Russell, A. G. Amine-Based CO₂ Capture Technology Development from the Beginning of 2013—A Review. *ACS Appl. Mater. Interfaces* 2015, 7 (4), 2137–2148. <https://doi.org/10.1021/am507465f>.

Differential Expression of microRNA-145 and microRNA-449 in Glioblastoma Cells

Student Researcher: Aubrey Strong

Advisor: Dr. Kaleb Pauley

Cedarville University
Molecular Biology

Introduction

Glioblastoma Multiforme (GBM) is a type of cancer of neuroglial progenitor brain cells. The current treatment options are not often successful long term due to the aggressive behavior of GBM tumors. MicroRNAs are short, non-coding RNA segments made of 20-25 nucleotides and are involved in post-transcriptional gene regulation. Gaining a better understanding of the role of microRNAs in cancer could help the prognosis of patients with lethal, incurable cancer types - such as Glioblastoma. MiRNAs may serve as a biomarker that could lead to early diagnosis or could be used to develop more effective target therapies.

Abstract

The U87, U251, and NHA cell lines were used in the process of RNA isolation. Using the RNA collected from RNA isolation, reverse transcription was performed. Following the RT protocol, PCR was performed in order to quantify the concentrations of the miR-145 and miR-449 in each cell line. After PCR was completed, the cycle numbers for each sample and primer were recorded and analyzed.

Methodology Used

For trials 1 and 2 of this experiment, the average cycle numbers of the triplicate for miR-145 in the U251 cell line are 35.53 and 36.20. The third trial provided an undetermined value for the cycle number of miR-145 and U251 cells. These values are higher than the other cycle numbers for miR-145 in each trial. For trials one, two, and three the average cycle numbers of the triplicate for miR-449 in the U87 cell line are 27.53, 29.73, and 28.87 respectively. These values are lower than the other cycle numbers for miR-449 in each trial.

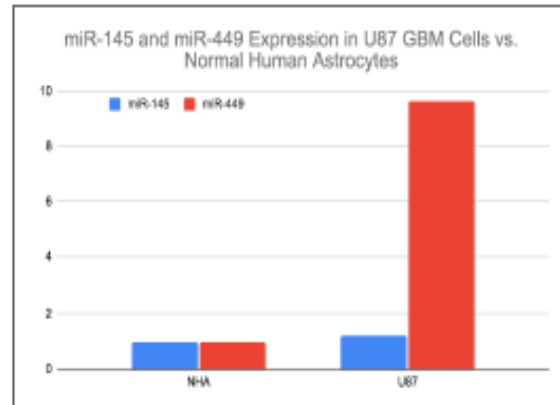
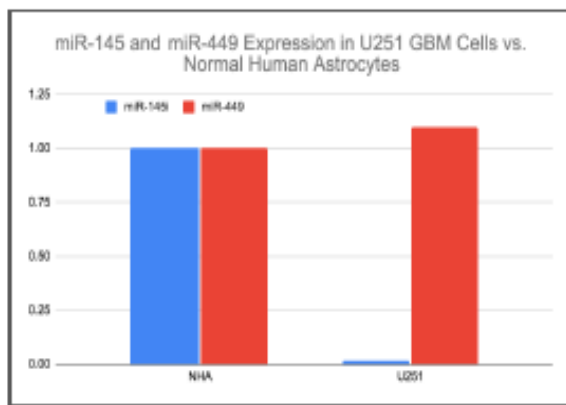


Figure 1: (left) miR-145 and miR-449 Expression in U251 GBM Cells vs. Normal Human Astrocytes

Figure 2: (right) miR-145 and miR-449 Expression in U87 GBM Cells vs. Normal Human Astrocytes

Each of the cycle numbers were compared to a standard of one that was established based on the concentration of the controls. Figure 1 demonstrates that miR-145 in the U251 cell line was relatively expressed at 0.015 compared to a relative expression of 1.23 in U87 cells and 1 in NHA cells. Figure 2 demonstrates that miR-449 is expressed at a relative expression of 9.65 compared to an expression of 1 for NHA and 1.1 for U251 cells.

Results Obtained

In this specific study, the process of quantitative PCR was used to gather quantitative data about the concentration of various miRNAs within the sample of Glioblastoma RNA. The qPCR used in this study essentially looks at the number of cycle numbers that it takes to amplify the sample enough to detect the PCR product. The thermocycler provides data for the number of PCR cycles each experimental sample required in order to be detected. Theoretically, a product that is of a low concentration in the sample should require more cycles of amplification in order to be detected.

Significance and Interpretation of Results

Because miR-145 is detected at a much higher cycle number in U251 cells compared to NHA and U87 cells, the data in this experiment suggests that miR-145 may play a tumor suppressor role in normal cells, because in cancer cells it is expressed at such a low level. The data also shows that miR-449 was detected at a much higher level in U87 cells compared to NHA and U251 cells based on the significantly lower cycle number. This data suggests that in normal cells, miR-449 may play a role in cell growth and proliferation, because in the cancerous cells, this microRNA was considered to be highly unregulated. As the field of cancer research begins to focus even more on microRNAs and the relationships between gene regulation and cancer, consistent data regarding the concentration of microRNAs in different cancer types is crucial. While there are still many limitations to microRNA targeting treatments, and these therapies are not used to clinically treat cancer right now, this field has shown promising results that could drastically improve Glioblastoma outcomes in the future.

Megafloods on Mars: Geomorphology and Terrestrial Comparison of Marte Vallis

Student Researcher: Andrew T. Swift

Advisor: John Whitmore

Cedarville University

Geology

Introduction

Mars geomorphology is a hot topic in the world of geology. Having an entire Geological Society of America conference session on it in 2021, it is one of the most exciting fields of science in the past decade. Earth geomorphology is interesting enough with evidences of catastrophes here and there carving out the landscape of the planet we call home. Yet now we are able to apply what we have learned on Earth to landscapes across the solar system as we explore our galactic neighborhood and its origins. This is truly a wonderful time in science and I am overjoyed to live in this era of new exploration. Now I have the privilege of contributing to it as I explore the geomorphology of Marte Vallis on the planet Mars.

Abstract

Marte Vallis is a largely understudied region in the Elysium Planitia on Mars. The few studies on it so far have identified it to be an outflow channel carved by a catastrophic release of water from underground aquifers. The valley is around 600 miles long and some channels at least 230 feet deep. The petrologic composition of this area is mostly volcanic rocks and displays the first columnar jointing ever discovered on the Mars. This study will investigate what available digital resources there are from NASA, USGS, and other organizations and persons studying the geology of Mars to collect a history of the region and how the landscape has changed over Mars' long history. The geomorphology of Marte Vallis and its geological structures can be compared to certain areas on Earth that have experienced similar megafloods such as the Channeled Scabland in Washington, USA and hold crucial information that can help geologists and planetary scientists understand both Martian and Earth history. Suggestions for geological field studies and the locating of potential water sources will be discussed for future sustained living and manned exploration on the Red Planet.

Methodology

For this study, I accessed various scholarly search engines such as GeoRef and Google Scholar to find and collect scientific papers and journal articles pertaining to Marte Vallis and the geomorphology of similar terrestrial landscapes. Using these, I compared the data, imagery, figures, and opinions of the authors to construct a very brief geomorphology of the Martian region as best as I am able with the limited resources available to the public. With all hope, some new insights may be given into landscape evolution on both planets and how we can put this information to practice in future manned missions to Mars.

Results

Marte Vallis is located in the Elysium Planitia in the Martian lowlands. It features aqueously carved channels that split and merge around streamlined, cratered islands. The flow of the water that carved this valley points to the northeast. It is difficult to pinpoint when the valley was carved so it is estimated around 10 to 500 million years during the Amazonian period according to the crater density time scale.

The theory of Marte Vallis' history is complex and not as concrete as one might hope. The bedrock itself is volcanic and an unconformity between lava flows indicates that there were at least two alternating volcanic periods with flooding in between (Voigt and Hamilton, 2018). In addition, Morgan et al. (2013) write that there were two separate phases of flooding erosion. The first was to erode the islands and the second to cut the main channel below the perched channels. Morgan et al. also add that the Cerberus Fossae troughs are the aquifer that provided the catastrophic waters. Moller et al (2001) bring the two together to say that volcanism and flooding both contributed to the megaflood and morphology of Marte Vallis. They reason that Marte Vallis resembles Kasei Valles which is thought to have theoretically formed from volcanic-induced flooding. There are terraces in the valley that indicate inflow to be from multiple sources. Volcanism is even more likely due to the presence of columnar jointing in Marte Vallis (Milazzo et al., 2009), the first ever discovered on Mars, which resemble that found in the Columbia River Basalt in the northwestern United States.

Key features of Marte Vallis are a gradient slope of 0.017 degrees (Moller et al, 2001), aforementioned columnar jointing, fluvial channels, and lava flows and cratered cones (Voigt and Hamilton, 2018).

For a terrestrial analogue, I chose to compare Marte Vallis to the Channeled Scabland in eastern Washington, USA. The Channeled Scabland were carved by a megaflood caused by the glacial dam failure of Glacial Lake Missoula in Pleistocene western Montana (Baker, 2009). A popular tourist destination is Dry Falls in the northern section of the Scabland. Glacial Lake Missoula was within the Cordilleran Ice Sheet which extended all the way down to Idaho. In the Pleistocene epoch, the melting of the sheet led to a failure in the glacial dam which released a catastrophic amount of water rushing westward, stripping the landscape and carving channels. This is the prevailing theory on the formation of the Channeled Scabland.

The key features of the Scabland are exposed Miocene lava basalt bedrock, anastomosed fluvial channels, and sub-fluvially placed gravel deposits and bars.

Comparing the two landscapes, they have many similarities. Both surfaces consist of exposed volcanic rock. They feature anastomosed outflow and inflow channels and streamlined hills. Structurally, we see current ripples and columnar jointing. However, the columnar jointing on Earth is not within the Scabland themselves but elsewhere in the same Columbia River Basalt formation. The key difference between the two is that the Scabland were carved by a glacial dam failure, whereas Marte Vallis was carved by an aquifer dam failure or similar mechanism.

Discussion

Comparing Marte Vallis and the Channeled Scabland brings some implications. One is that the features on Marte Vallis can have a starting point on formation history. If the two are similar in appearance, then perhaps they are similar in geomorphology. Another is that megaflooding occurred in the Amazonian which is not expected and brings more questions on Amazonian processes. I would predict that in the future, we would find gravel features on Marte Vallis like the Scabland as well as debris fans resembling the Ephrata fan west of the Scabland. Perhaps we would find that the megaflooding mechanism from Cerberus Fossae would resemble Lake Missoula. For future manned missions to Mars, it is imperative to study the geology of areas with aqueous features. This would help us explore possible sources of water not only for sustained human living but also for possibly finding evidence of past life on Mars. To find these possible water sources, erosional features displaying subaqueous characteristics would be the best bet which could be used to trace ancient aquifers.

Conclusion

To conclude, Marte Vallis can be better understood for now by studying the Channeled Scabland and other megaflooded landscapes. This would help us understand megafloods in general, interactions between volcanic and aqueous processes, and formation of columnar jointing. Martian hydrology is a gold mine of scientific research and future geological exploration of the Red Planet would help us understand that and the hydrology of our own planet and possibly how to keep our Earth from becoming like desolate Mars.

References

- Baker, V. R. (2009). Channeled Scablands: A Megaflood Landscape. *Geomorphological Landscapes of the World*, 21-28. doi:10.1007/978-90-481-3055-9_3
- Bretz, J. H., & Search for more articles by this author. (1969, September 01). The Lake Missoula Floods and the Channeled Scabland: *The Journal of Geology*: Vol 77, No 5. Retrieved from <https://www.journals.uchicago.edu/doi/abs/10.1086/627452>
- Lamb, M. P., Dietrich, W. E., Aciego, S. M., Depaolo, D. J., & Manga, M. (2008). Formation of Box Canyon, Idaho, by Megaflood: Implications for Seepage Erosion on Earth and Mars. *Science*, 320(5879), 1067-1070. doi:10.1126/science.1156630
- Milazzo, M., Keszthelyi, L., Jaeger, W., Rosiek, M., Mattson, S., Verba, C., . . . Mcewen, A. (2009). Discovery of columnar jointing on Mars. *Geology*, 37(2), 171-174. doi:10.1130/g25187a.1
- Moller, S. C., Poulter, K. E., Grosfils, E. B., Sakimoto, S. E., Mendelson, C. V., & Bleacher, J. E. (n.d.). Morphology of the Marte Valles Channel System, Mars. Retrieved from <https://ui.adsabs.harvard.edu/abs/2001LPI....32.1382M/abstract>
- Morgan, G. A., Campbell, B. A., Carter, L. M., Plaut, J. J., & Phillips, R. J. (2013). 3D Reconstruction of the Source and Scale of Buried Young Flood Channels on Mars. *Science*, 340(6132), 607-610. doi:10.1126/science.1234787
- Voigt, J. R., & Hamilton, C. W. (2018). Investigating the volcanic versus aqueous origin of the surficial deposits in Eastern Elysium Planitia, Mars. *Icarus*, 309, 389-410. doi:10.1016/j.icarus.2018.03.009

Analysis of Printing Parameters in 3D Printed Carbon Fiber Composites using Design of Experiments

Student Researcher: Jakub Sychla

Advisor: K.T. Tan

The University of Akron
College of Engineering and Polymer Science

Abstract

Additive manufacturing of carbon fiber reinforced polymers (CFRP) provides the ability for rapid prototyping of complex shapes and geometries that traditional manufacturing methods of CFRP could not achieve. In recent years, there has been significant development and advancement in commercially available composite 3D printers that use fused filament fabrication (FFF) technique to fabricate CFRP. This paper aims to investigate the effect of printing parameters on the flexural performance of 3D printed CFRP using the Design of Experiment (DoE) analysis. CFRP specimens were fabricated using a MarkForged Mark II 3D printer, with several configurations being set up, each of which printed three specimens. The configurations were set to push the extreme limits of the controlled aspects for the rectangular fill pattern that was used, including fill density, roof and floor layers, and wall layers. Each sample consisted of twenty-four layers, and inner layers with continuous carbon fiber remained consistently angled at $[0/90^\circ]$ orientation. Results from flexural bend test (load, deflection, and flexural strength, showed that the roof/floor layers had the largest impact on the flexural strength. The configurations with less roof/floor layers were able to take on a larger load, due to the presence of more carbon fibers in the internal layers. However, those that had more roof/floor layers were able to withstand less load and found to be observably ductile, due to the reduction in the number of internal layers with continuous carbon fibers. Using DoE analysis, contour plot can be generated to predict flexural strength of various printing parameters. Flexural damage were further characterized using X-ray micro-computed tomography to correlate with strength values.

Project Objectives

This study aims to examine the printing parameters of long fiber composites fabricated by additive manufacturing technology, and their respective flexural strength

Methodology Used

Using the Markforged Mark 2 3D printer, which utilizes a dual printer head, the onyx and carbon fiber composite specimens are able to be printed into eight different configurations with three samples each. Markforged's continuous fiber carbon fiber was fed using one of the nozzles on the dual head printer. The carbon fiber used has a flexural strength of 540 MPa and flexural stiffness of 60 GPa. These configurations, which are comprised of twenty-four layers of CFRP material, have constant overall dimensions of height 3 mm, width 15 mm, and length 58 mm. Along with the dimensional constants, the carbon fiber print angle remains alternating between 0° and 90° and a rectangular print pattern of the onyx is chosen. The variable components of the configurations are fill density of 10% or 92%, roof and floor layers of either 1 or 10, and wall layers of 1 or 4. The roof/floor layers acted as offset layers for the carbon fiber in the z-direction. The wall layers are surrounding the samples in the xy-plane. The three variable components are with reference to the onyx material

Results Obtained

Using the Design of Experiment (DoE), we compare how the different configurations perform under the load given to each sample. Configuration 1 has infill density of 92%, 4 wall layers, and 10 roof/floor layers.

The curves are roughly parabolic in shape, because of the ductile nature of this configuration, this sample does not take a heavy load. (Figure 1)

Significance and Interpretation of Results

We utilize DoE to confirm that the number floor/roof layers is the primary factor determining the strength of a given configurations (Figure 2). In testing, this is clear as configurations with 1 roof/floor layer are brittle snapped when they hit the peak of load as they are primarily carbon fiber. Contrarily, the 10 roof/floor layers are ductile during bending but do not have a clear break in the samples. The number of wall layers has comparatively small effects on the stress performance based on Figure 2

Figures/Charts

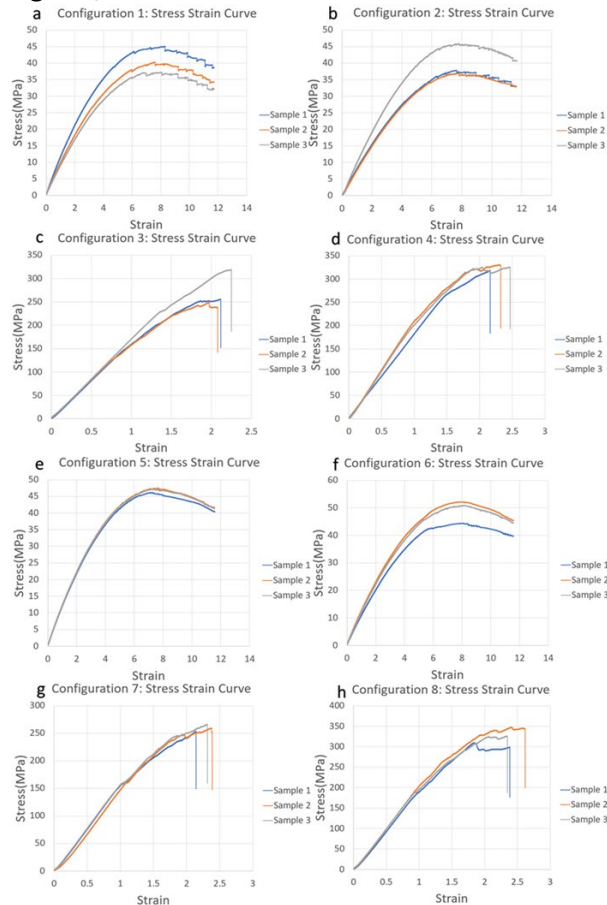


Figure 1. Stress-strain curves of each configuration.

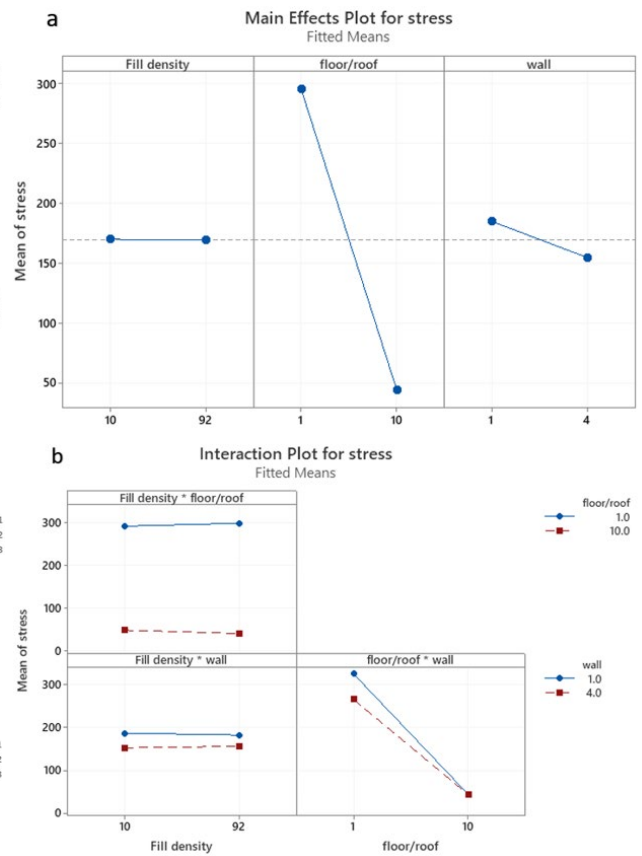


Figure 2. a) Main Effects plot, b) Interaction plot

Acknowledgments and References

I would like to express my gratitude to the Ohio Space Grant Consortium with the funding to help give me the possibility to work on this research. I would also like to express special gratitude to my advisor Dr. Tan, whose support and guidance has helped me reach this point

[1] Nawafleh, N. and E. Celik. 2020. "Additive Manufacturing of Short Fiber Reinforced Thermoset Composites with Unprecedented Mechanical Performance," *Addit Manuf.*, 33: 101109.
 [2] Yeong, W. Y., and G. D. Goh. 2020. "3D Printing of Carbon Fiber Composite: The Future of Composite Industry?" *Matt.*, 2(6): 1361-1363.

Systematic Classification of Meteorites

Student Researcher: Marcus J Terry

Advisor: Dr. Andrew Beck

Marietta College
Petroleum Engineering and Geology Department

Abstract

Diogenite meteorites are ultramafic cumulate rocks, mainly composed of the mineral orthopyroxene, from the asteroid 4Vesta (Beck and McSween 2010). A subgroup of diogenites contains higher abundances of the mineral olivine, and the petrogenesis of this subgroup is debated, partially due to the uncertainty of the exact abundance of olivine (Beck et al. 2013, Mandler and Elkins-Tanton 2013). In this study, we will attempt to ascertain a more accurate olivine abundance in diogenites by determining abundance in multiple thin sections per meteorite. This data will be collected via thin section point counting on a petrographic microscope, and meteorite thin sections will be supplied by the NASA Antarctic Meteorite Program.

Introduction

Meteorite classification is vital in allowing communication between the multitude of disciplines that utilize meteorite data for their respective fields. Classifying meteorites into individualized member groups also allows distinct trends to become more apparent. One of these particular group of meteorites focused on in this paper are diogenite meteorites. Diogenite meteorites are typically related to two other subgroups, Eucrite meteorites, and Howardite meteorites. All three of these groups are often referred to as the HED meteorites are a large group of meteorites believed to originate from Vesta. The classification utilized for this research can be seen in figure 1.

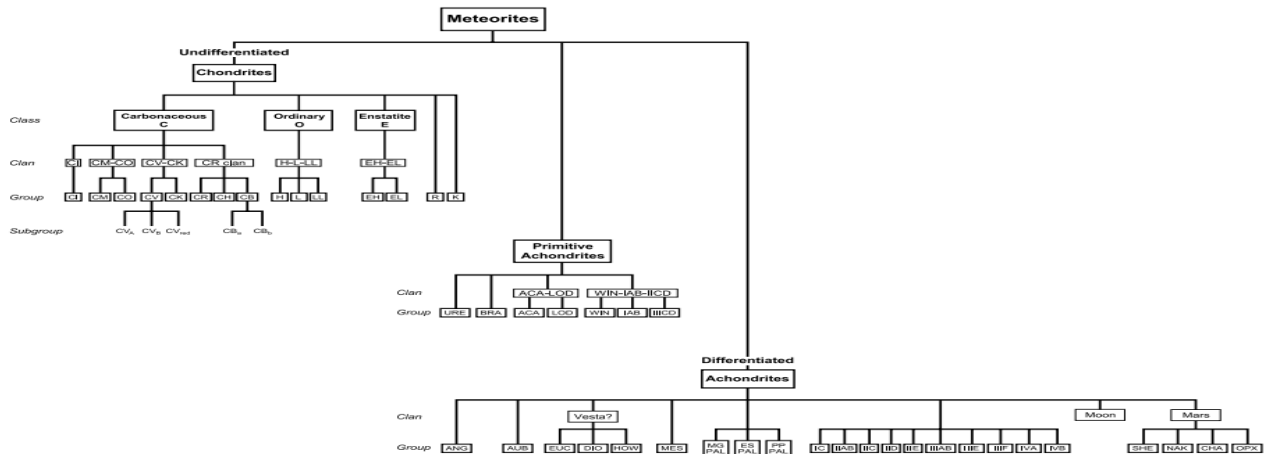


Figure 1. Diagram expressing the systematics of meteorite classification and showing the major meteorite divisions, classes, clans, and groups and relationships among meteorite groups. URE — ureilite, ACA — acapulcoite, LOD — lodranite, ANG — angrite, ALB — albrite, BRA — brachinite, WIN — winonaite, HED — howardite-eucrite-diogenite, MES — mesosiderite, MG PAL — main-group pallasite, ES PAL — Eagle Station pallasite, PP PAL — pyroxene pallasite, SHE — shergottite, NAK — nakhlite, CHA — chassignite, OPX — orthopyroxenite.

Figure 1

Methods

This study was completed utilizing meteorite samples supplied by the NASA Antarctic Meteorite Program via. Dr. Andrew Beck. These meteorites were divided and prepared into thick sections polished to 3µm. High-resolution mapping was performed for each sample using a petrographic camera to provide a method with which to navigate under the scanning electric microscope (SEM). Utilizing the SEM at Ohio State University (OSU), sections of the samples were subjected to atomic spectroscopy. This then provided precise elemental compositions based on the electronic spectra emitted by each atom. As our study focuses primarily on the presence of the mineral olivine, the spectra chosen for analysis were directed towards magnesium, iron, and silicon oxides. An example of this can be seen in figure 2.

Analysis

Twelve sections of meteorites were sampled for this study. The primary spectral analysis returned a variety of olivine samples similar to Figure 3. The section of most rarity and interest was a barred olivine chondrule. The complex mineralogy of this can be seen in figure 3. Despite this one complexity, the vast majority of olivine samples in this study were in line with the expected tolerances of HED meteorites.

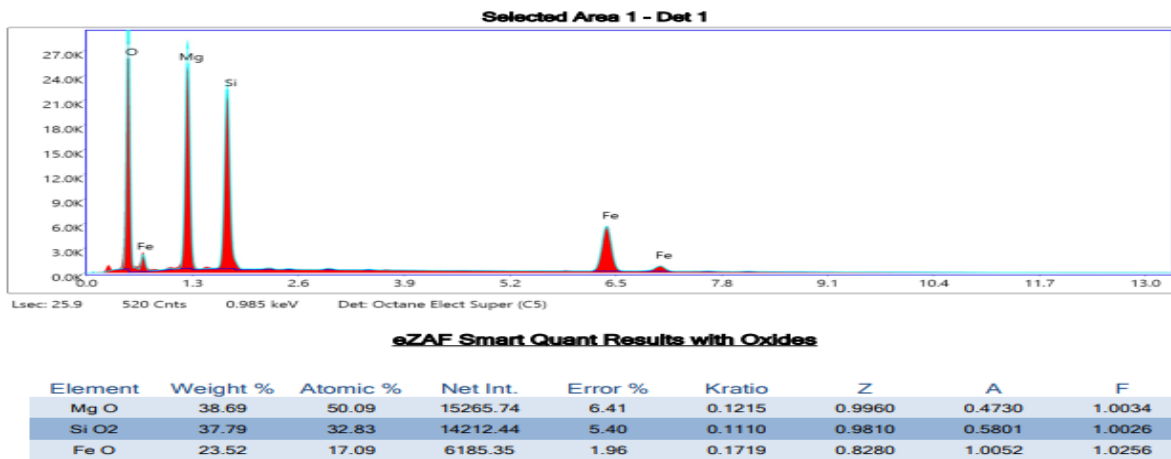


Figure 2

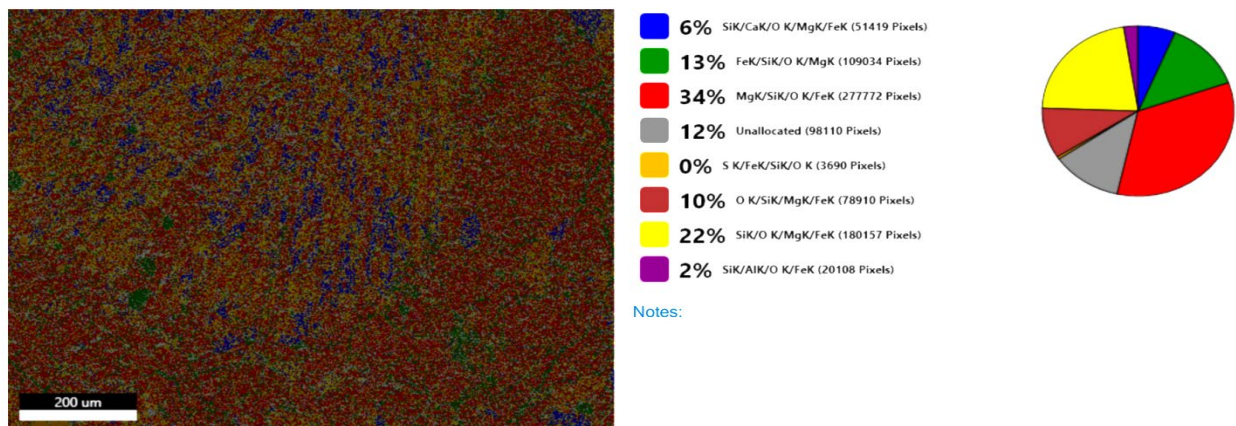


Figure 3

Investigation of AgNO₃ Sintering Aid for Nanosilver Particles

Student Researcher: Kevin J. Tomlin

Advisor: Dr. Daniel Young

Wright State University

Department of Mechanical and Materials Engineering

Abstract

Nanosilver particles are a potential bonding agent in electronics and die attach applications, where elevated temperatures are present. In this work, nanosilver particles were synthesized at Wright State University via reduction of silver acetate by ascorbic acid in a polyacrylic acid solution [1]. The purpose of this experiment is to determine the effects of an AgNO₃ sintering aid added to the nanosilver powder in different weight% (0.0, 2.5, 5.0, 7.5, 10, 20). Mixtures of silver nanoparticles and AgNO₃ were consolidated at 5 MPa of pressure for 20 minutes at 300°C. The density, microhardness, and microstructure were then evaluated. It is hypothesized that addition of the AgNO₃ will provide high-diffusivity pathways to enhance surface diffusion-based consolidation. The addition of AgNO₃ affects both the microstructure and its properties.

Objectives

The objectives of this experiment range from the AgNO₃ addition to the nanosilver, to learning and using multiple characterization techniques to understand key material properties. The nanosilver particles must be synthesized via reduction of silver acetate by ascorbic acid in a polyacrylic acid solution [1]. The mixture of AgNO₃ and nanosilver particles will be sintered under heat and pressure, which are then evaluated via microhardness, density (volume fraction solid), and SEM. It is hypothesized that addition of the AgNO₃ will provide high-diffusivity pathways to enhance surface diffusion-based consolidation.

Methodology

The nanosilver particles are synthesized via reduction of silver acetate by ascorbic acid in a polyacrylic acid solution [1]. To investigate this addition of AgNO₃ in nanosilver, the AgNO₃ will be tested at different weight% (wt%) in nanosilver. The different wt% of AgNO₃ per one gram of nanosilver powder are found in Table 1. A mortar and pestle are used to break up, as well as blend the AgNO₃ salt with the nanosilver powder. Upon completion of blending the AgNO₃ with the nanosilver powder, the specimens were formed using a die tool. This die creates a 9.525 mm diameter puck of sintered powder after heat and pressure of 5 MPa at 300°C for 20 minutes. Upon completion of sintering, specimens will be fractured into two pieces; one piece is used to observe fracture surface, while the other half is polished and used for observation of the overall microstructure. Both specimen halves are observed using an SEM (JEOL JSM-7900F). Microhardness (Wilson® VH1202) and density measurements are also taken for each specimen to determine the effectiveness of sintering.

Table 1: AgNO₃ wt% Nanosilver

Wt%	Nanosilver [g]	AgNO ₃ [g]
0.00	1.00	0.0000
2.50	1.00	0.0112
5.00	1.00	0.0224
20.0	1.00	0.0896

Results

Due to processing errors, specimens for 7.5 and 10.0 wt% were not suitable for testing and eliminated from the data. The results of density and volume fraction solid measurements can be found in Table 2. The results of microhardness for acceptable specimens can be found in Figure 1.

Table 2: Specimen Densities and Volume Fraction

Wt% AgNO ₃	Density [g/cc]	Volume Fraction Solid
0.00	7.61	0.73
2.50	6.92	0.66
5.00	6.86	0.65
20.0	6.04	0.58

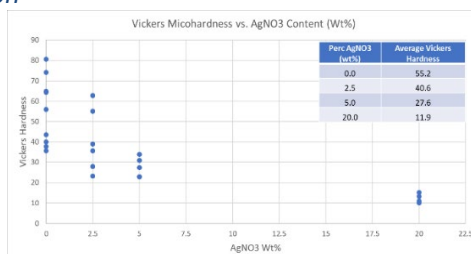


Figure 1: Microhardness

SEM micrographs were taken (Figure 2) for the specified specimens to observe consolidation effects of AgNO₃ on the microstructure.

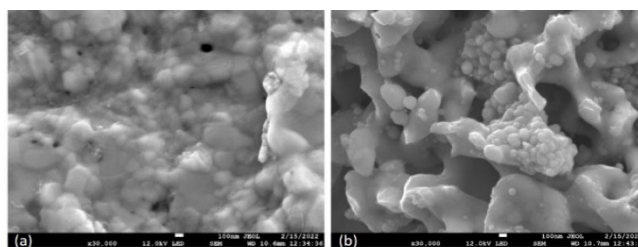


Figure 2: SEM of Fracture Surface (a) 0.0 wt% and (b) 2.5 wt%

Significance and Interpretation of Results

The results in Table 2 show that there was a decrease in volume fraction of solid, which indicates that porosity increased as the wt% of AgNO₃ increased. The microhardness in Figure 1 suggests that the addition of increased wt% of AgNO₃ significantly decreased the Vickers hardness for AgNO₃ containing specimens. The microhardness distribution for each individual specimen had varying distributions. As the wt% AgNO₃ increased, the spread between microhardness data significantly decreased. The fracture surfaces indicate that porosity is present within the specimens. There is strong evidence of plastic deformation from fracturing the specimens. The nanoparticle clusters could be partially sintered particles that did not fully consolidate, and elongated particles may represent fully consolidated particles. Overall, the addition of AgNO₃ did not provide high-diffusivity pathways to enhance surface diffusion-based consolidation in nanosilver particles. More research on additional sintering aids (that liquefy at 300°C) should be investigated to enhance particle consolidation.

Acknowledgments & References

The author is very grateful to OSGC for this scholarship opportunity. A special thanks to Dr. Daniel Young for mentoring this research and Wright State University for allowing use of their facilities.

[1] Magdassi, S.; Grouchko, M.; Berezin, O.; Kamyshny, A. Triggering the Sintering of Silver Nanoparticles at Room Temperature. *ACS Nano* 2010, 4 (4), 1943–1948.

XRTI: eXtended Reality based Telepresence Interface for Multiple Robot Supervision

Student Researcher: Naomi Wang

Advisor(s): Dr. Jong-hoon Kim

Kent State University
Computer Science

Abstract

As a part of the robot interface design aligning with the NASA Mission Directorate, this research aims to develop an eXtended Reality based Telepresence Interface (XRTI) for NASA's exploration extravehicular mobility unit (xEMU) in the AARON (Assistive Augmented Reality Operational and Navigation) System proposed by the ATR Flux team in NASA SUITS challenge 2020 and 2021. The XRTI system features an immersive hologram view of xEMU in the AARON System for augmented reality based supervision of the xEMU, which allows for the monitoring of multiple robots simultaneously. The extended immersive view will enhance the situational awareness and ease of operation for astronauts, as well as facilitate human-robot interaction. The use of augmented reality allows for a semi-transparent design preserves the ability to view and traverse safely through an environment while still maintaining robot data in the same field of view. The interface features an intuitive design to surround the human supervisor within a virtual space and will be configurable to user preference for data monitoring, including both one-on-one and group interaction possibilities among members of a robot team. The XRTI system development focused on the implementation of a single column-shaped design in which the user experiences a wrap-around data display. The interface layout can be modified by the user with drag-and-drop functionality, which may further be expanded to include hand tracking interaction. The aim of this research is to design a tool to facilitate decreased cognitive workload for a robot supervisor, ease of data access and retrieval, and improved management of data in robot teams.

The research continues to study metrics such as interaction effort and robot neglect tolerance in its efforts to increase the capacity for fan out, which is the ability of a single operator to control multiple robots. Currently, the accepted method of fan out is to decrease interaction effort is to allow a human operator to manage each robot with a lesser amount of active responsibility. This research challenges the accepted understanding by emphasizing the importance of human judgment in prioritizing the needs and data of each individual robot in a team. Our interface instead engages the user with an interface that allows an interactive experience with robot data such that human fatigue caused by a constant view of monotonous data display may be avoided.

Personal Objectives

The interface allows both a one-on-one experience with each robot's data as well as a multiple robot view for a large-perspective overview of the robot team. By offering both of these options as well as allowing for widget customizability of each widget within the interface, it is our goal to create a user-focused experience. Prioritizing the needs of the user and catering to their individual preferences should increase the participation and willingness of the operator to continuously interact with the robot for an extended period of time. Additionally, by allowing each user to customize the interface to their personal needs, data retrieval efficiency and a more comprehensive understanding of presented data should be achievable. The dynamically capable presentation of data should allow each user to have their own experience with the interface, which benefits both the user and the supervised robot team.

Significance of Results

Overall, this research designed and implemented an interface that facilitates an improved interaction between a single human supervisor and a multiple robot team. The design was based on metrics in human-robot interaction systems such as fan out. The research challenges the accepted understanding of the dynamic between single human, multiple robot teams.

Optimization of Supersonic Scramjet Engine Component Geometry to Maximize Thrust

Student Researcher: Joshua Ward

Advisor: Mitch Wolff

Wright State University
Mechanical Engineering

Abstract

A scramjet engine is a highly advanced jet engine in which the velocity of air and the subsequent temperature causes ignition of fuel, and allows for higher velocity air flow than standard turbine engines. This results in faster vehicles, and allows for supersonic flight easier than standard jet engines. A large issue in the field of supersonic travel is the highly sensitive nature of a scramjet engine to component geometry. There are 4 different components of a scramjet engine, the Inlet, Isolator, Combustor, and Nozzle. The scramjet engine itself has 8 geometric variables. A nonlinear constrained optimization problem needed to be designed to find the optimal geometry for maximum thrust.

Introduction

A standard scramjet engine is comprised of 4 different components, the inlet, isolator, combustor, and nozzle. These 4 components have a total of 8 different geometric design variables. The 8 design variables are the lengths of each component, the inlet capture diameter, the inlet throat diameter, the combustor outlet diameter, and the nozzle outlet diameter. The diameter of the isolator, and combustor inlet is equal to the inlet throat diameter, and the nozzle inlet diameter is equal to the combustor outlet diameter. Code has previously been developed for the use of calculations of different parameters, and output conditions of scramjet engines, given different geometric inputs. This code allowed for the development of an optimization problem.

Experiment

The code can be used to output temperature along the length of the entire engine, different efficiencies, thrust, and other different engine parameters. Thrust was the main output looking to be maximized. The begin some parametric studies were conducted to verify the need for an optimization problem. These parametric studies were done by holding 6 of the 8 design variables constant, and iterating through the other 2 design variables to get a 3 variable plot of thrust in relation to the 2 design variables. These were conducted because if thrust increases with each variable change then an optimization is not needed, rather but a Monte Carlo approach could be used. As a result of these parametric studies, thrust was found to have specific locations inside of the specific 2D design space with maximum thrust values. This verifies the need for an optimization approach.

The code was developed to maintain supersonic flight. When specific assumptions were violated because of component geometry an error would be output and no values could be calculated. This meant for any geometries in the 8D design space that would violate certain conditions thrust could not be calculated. This resulted in errors inside of the optimization problem. The minimize function inside of Python's SciPy package was used. This is a gradient based optimization solver. In looking to minimize the

objective function, the gradient, or slope of certain points in the design space point to negative or to the positive direction. This is used to find local minima. When thrust is not able to be calculated a value needs to be given to the optimizer, and any value given will artificially skew the gradient and result in the optimizer not being able to be solved.

A latin hyperspace (LHS) cube was used to create a surrogate. An LHS divides to n-D design space into N different blocks, and then one design point inside of each of those cubes is calculated. This allows an n variable function to be fitted to be used as a surrogate function for thrust optimization. For this case the 8D design space was sectioned into 10000 different blocks. An iterative loop was then used to run through the 10000 different design points.

Results and Discussion

In the use of the optimization problem, although the gradient based solver had issues calculating an optimal solution one was reached. The optimal thrust calculated was $F = 3612$ N. This value was calculated in 68 iterations through the objective function, with over 300 function evaluations.

Using the LHS method an optimal solution was found from 1 of the 10000 design points. Through the iterations a thrust values was found to be $F = 5642$ N. The concern with the design variables used in this calculation was the diameter of the inlet throat was about 8 mm. This geometry, although possible given the physics of supersonic conditions, is not feasible from a real world applications perspective because of boundary layer thickness of the airflow.

Conclusions

Although optimal solutions were found from both methods more work is to be conducted in the following field. The code will be worked on to develop portions that can still calculate thrust for subsonic flight conditions, and that will allow for a more accurate gradient based solver usage. Also the physics of the code will be looked into to add in any physical constraints necessary to accommodate for boundary layer thickness.

Mechanical Characterization of Metalized 3D Printed Polymers

Student Researcher: Kaitlin Willi

Advisor: Dr. Ahsan Mian

Wright State University
Mechanical Engineering

Abstract

Additive manufacturing (AM), or 3D printing, is the computer-controlled process by which a three-dimensional object is created layer by layer. The process used in this research is fused deposition modeling (FDM). FDM printing works by melting a polymer with a heated nozzle and depositing a line of melted material on the build plate. This process is repeated for each subsequent layer until the part is completed. AM is useful for many processes such as rapid prototyping, manufacturing parts with complex geometries, and researching the effects of various materials. Many different filaments are available on the market and have been tested for their mechanical properties. However, less research has been done on post-processing techniques to improve these properties. This research has been done to find the effects of the metalization of 3D printed objects. Testing has been done to find the reactions to heat and the thickness of the coating on copper-plated samples. This testing was done for applications on spacecraft and on military and personal UAVs. Copper-plated objects have been found to have low resistivity, high durability, a capability to protect the part against damage from UV light and moisture, and many other benefits. These benefits can be used on parts that will be exposed to the weather and the sun for long periods of time to reduce deterioration. In order to use this method for space travel and UAVs, testing was done on the effects of heating and coating thickness. The effects of metalization were tested to find the resulting changes in mechanical properties.

Objectives

There are many research papers describing the effects of metalization in regards to UV resistance, weatherization [1], impact resistance, and Young's modulus [2]. The objective of this project is to prove the potential of electroplating 3D printed objects with copper to improve mechanical properties and increase their resistance to heat-related damage and warpage. Additive manufacturing is capable of making prototypes that would be impossible with machinery. If these prototypes can be reinforced, they can be made into end-use components that can withstand more than the printed prototypes alone.

Methodology Used

Printing and Preparing for Electroplating

An Auxiliary Genius FDM 3D printer was used to print tensile test specimens according to the ASTM D638 14 Type IV specifications [3]. The specimens were printed with CR-PLA filament from Creality with a 180 °C nozzle and an 80 °C bed. PLA filament, and most other plastics, are characteristically nonconductive. In order to electroplate, a conductive surface is required. The parts were made conductive by painting on a thin layer of carbon [2]. The substance that was painted was made by combining Loudwolf Graphite Dry Lubricant and Higgins American Indian Ink. The parts were coated in the paint and were then left to dry for at least 12 hours.

Electroplating

The electroplating setup was made up of a glass container, a bubbler to agitate the solution while plating, a fixture to keep the specimen submerged, a pure copper anode, and a DC power supply. After the conductive paint dried, the specimen was placed in a fixture and submerged in Midas Bright Acid

Copper Plating Solution and connected to the negative lead. A pure copper anode was submerged in the electrolyte and connected to the positive lead of a Tektronix PS283 DC Power Supply. A direct current of 2 volts was supplied for the allotted time of coating. The specimen was then removed from the solution and rinsed with distilled water. It was then placed in a plastic bag with a silicon gel packet to reduce the risk of the remaining moisture affecting the sample. Figure 1 shows each step of this process.

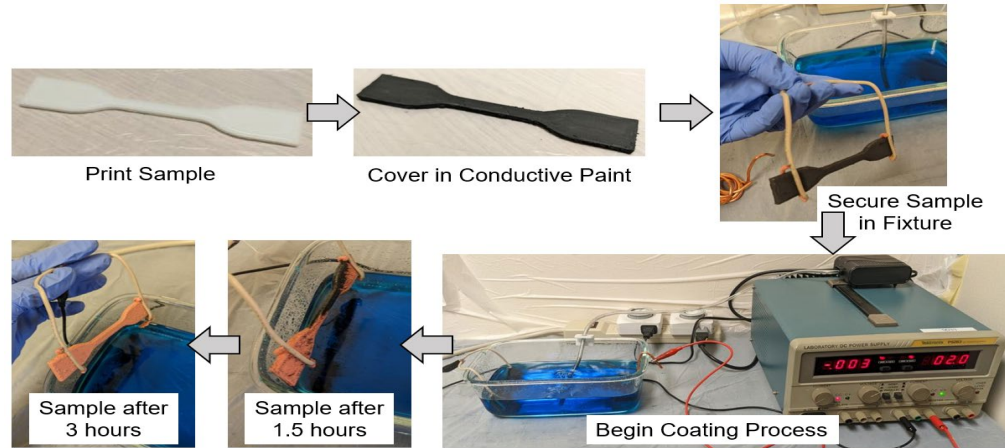


Figure 1: Electroplating Process

Heat Effects

In UAV and space applications, components may be heated to extreme temperatures and then cooled rapidly. Drones being used in desert climates may encounter temperatures of 50 degrees Celsius and satellites in orbit may reach temperatures of 127 degrees Celsius [4-5]. After reaching these temperatures the drones may be put into an airconditioned car or the satellite might move out of the sunlight and be shocked by a cooler environment. Sending 3D printed parts into either of these environments may result in changes in properties that could lead to premature failure.

For the testing of the resistance to heat, both uncoated and coated samples were placed in a Thermolyne Premium Large Muffle Furnace (F6020C-33) at specific temperatures to observe the effects on deformation [6]. The specimens were first tested at the upper limit of temperatures that a satellite may encounter. This resulted in a PLA sample that was too warped to be mounted in the tensile testing machine. The lower temperature limit a satellite may encounter was then tested. Despite having some slight warpage, the samples could be mounted in the tensile test machine. After the parts cooled at room temperature (21°C), tensile testing was conducted with an Instron 5500R [7].

Thickness

Testing was also completed on the effect of different thicknesses of copper coatings on the specimens' mechanical properties. This was tested for many reasons. The thicker the coat that is sought after, the longer it will take to produce the final product and the more raw materials will be needed. Thicker coats also add weight to the final product and have the potential for slight variations to grow into large defects. The impact of these considerations must be examined when designing UAVs and spacecraft and as such, the effects of the thicknesses were studied. If the same results are achieved with various coating thicknesses, thin coatings can be used which will reduce these effects. To test this, samples were electroplated for 3 hours and for 6 hours and the resulting tensile strengths were recorded.

Tensile tests were performed on both plain PLA parts and copper coated parts that were coated for either 3 or 6 hours. From this point forward, plain PLA parts will be referred to as PLA, parts that were coated for 3 hours will be referred to as Cu 3hr, and parts that were coated for 6 hours will be referred to as Cu 6hr.

Results

Heat Effects

A PLA sample and a Cu 3hr sample were placed in a 125 °C Thermolyne Furnace for 3 hours. The PLA sample deformed and warped from its original shape while the Cu 3hr sample remained in its original shape. Images of the warping are shown in Figure 2.



Figure 2: Results of Heating for 3 hours at 125 °C

The warping present in the PLA samples at this temperature and length of time made tensile testing the parts impractical. Various other temperatures and lengths of time were tested to find conditions that would result in minimal warping of the PLA samples so that tensile testing could be performed. The final conditions used were 80 °C for 30 min. These conditions caused slight warpage but the samples were able to be tested. Figure 3 shows the test strips before and after heating.



Figure 3: Samples Before and After Heating for 30 min at 80 °C

Three heated PLA samples and three heated Cu 3hr samples were tensile tested and compared to unheated samples in a stress versus strain plot. Figure 4 shows this plot.

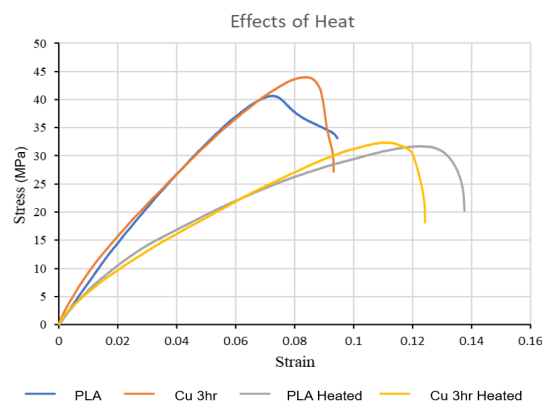


Figure 4: Effects of Heating on PLA and Cu 3hr

For both the plated and unplated samples, the ultimate strength was reduced when heated. Heating the samples also resulted in lower stiffness and lower strength. The strength of the PLA parts was reduced by 22.5% and the strain increased by 91.0%. The strength of the copper-plated parts was reduced by

26.3% and its strain increased by 37.6%. It is speculated that this is the result of delamination of the layers of the filament within the specimen. Because the inside composition changed from a solid block to many individual strands of plastic, each strand may be contributing to a spring-like reaction. This results in a more ductile material with higher energy absorption. Testing is being done to confirm this hypothesis.

Plating Thickness

Three specimens were printed and then left in the electroplating bath for 3 hours. Another three specimens were left in the electroplating bath for 6 hours. The average thickness of coating after 3 hours was 0.171 mm and had a standard deviation of 0.057 indicating a consistent coating. The average thickness after 6 hours was 0.350 mm with a standard deviation of 0.074. The thickness after 6 hours was less consistent than the plating after 3 hours due to small imperfections that got bigger over time. Each as well as three PLA samples were then tensile tested and a stress versus strain plot was made as shown in Figure 5.

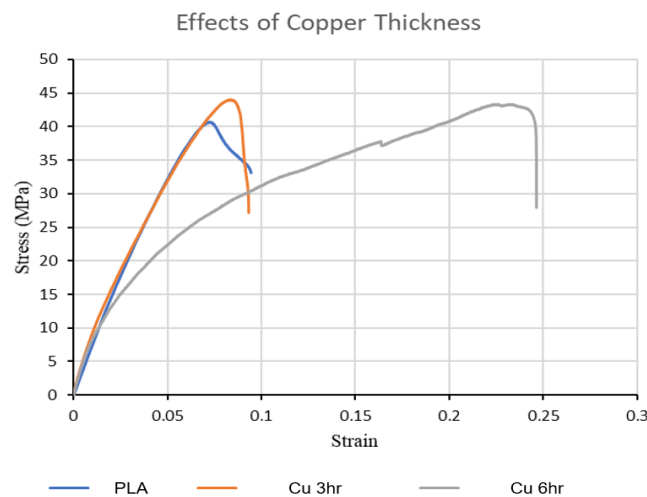


Figure 5: Effects of Copper Thickness

The ultimate strength of the Cu 3hr samples was 8.7% higher than the PLA samples and the strain for the Cu 3hr samples increased by 14.2%. The Cu 6hr samples had an increased ultimate strength of 6.3% and increased strain by 236% over the PLA samples. The Cu 6hr samples have a similar ultimate strength to the Cu 3hr results but have a lower stiffness. By plating the samples for 6 hours they became more ductile and had an increased energy absorption. It is speculated that the ductility of the copper plating absorbed the energy rather than the PLA and delayed the stresses on the PLA.

The results for the Cu 3hr sample in Figure 5 may be unreliable as they do not match the results from similar experimentation done in the past. This inaccuracy may be the result of many variables. A new pure copper anode was not used after each plating, the plating solution was not filtered after each plating, and the temperature in the room where the plating occurred varied from 21 °C to 24 °C. The most impactful uncertainty comes from the number of tests done. Due to time constraints, only three samples were tested for each coating and any individual issues had a large effect on the final outcome.

Discussion

Heat Effects

When copper-plated samples are heated, their stiffness is reduced similarly to PLA samples. These decreased strengths and stiffnesses can cause many negative impacts in real-world applications. Often

times UAVs and spacecraft need to be extremely accurate and have consistent predictable properties. Because coating does not strongly affect the stress and strain when heating, it may be considered to be unnecessary. However, the significant effect of plating the PLA when heated was the effects of warping. At each of the temperatures tested, the plain PLA sample deformed and warped while the copper-plated sample remained in its original shape. Because UAVs and space appliances are highly engineered, any warpage may affect the function of the original design. Highly accurate parts and components can be protected from warpage and deformation that would hinder their function by coating them in copper. While the plastic may soften and move as a result of internal stresses, the copper will stay solid as it has a much higher melting point. This design consideration can be used in any application where the component in question will be heated and cooled.

Plating Thickness

Plating the specimens for longer periods of time resulted in a thicker coating of copper, a higher ultimate strength, and larger energy absorption. Achieving these properties without a copper coating may involve adding ribs or gussets to the design or increasing the overall thickness of the PLA. All of these features could add more weight to the final design than a thin copper plating that would result in the same properties. It is also inferred that the thicker the copper coating, the more durable the part will be over time and the longer its lifespan. This, along with the improvements to weatherization and UV resistance makes copper electroplating a useful tool when designing.

Conclusions

Electroplating 3D printed PLA structures causes an increase in mechanical properties, eliminates the effects of warpage caused by heat, and has the potential to make a prototype into an end-use product. The metallization of PLA can circumvent many of the negatives that are associated with 3D-printed parts. Reducing the impact of weatherization, warpage, and the polymer's inherent lower mechanical properties can be achieved through copper plating. Being able to reduce these negative aspects while maintaining the positive functions, such as making complex designs and delicate structures, provides another useful tool to be utilized while designing. That being said, this research was subject to various inaccuracies. It is known that "properties such as hardness, ductility, strength and internal stress can be varied significantly by changing electrolyte composition and operating condition" [8]. Because the same electrolyte plating solution was used throughout the process, the electrolyte composition may have been changing. Another inaccuracy came from the copper anode. The anode used to provide the copper reduced in size and surface area with each sample coated. As a result, each sample was not provided with the same amount of copper in the same period of time. This resulted in variations in the coating thickness when the samples were plated for the same time period. The samples may have also been affected by the temperature in the room which ranged from 21 °C to 24 °C throughout the printing and coating process.

Copper-plating 3D printed parts results in structural stability when heat is applied. The low increases in ultimate strength may not have enough of an impact to offset the added weight, but the reduced risk of causing a total design failure due to deformation may make the added weight acceptable.

Acknowledgments

K. Willi would like to thank the Ohio Space Grant Consortium for supporting this research and providing this opportunity. K. Willi would also like to thank Dr. Ahsan Mian, Dr. Hasanain Sami Abdulhadi, and Dr. Tahseen Al Wattar for their continued support and guidance.

References

- [1] Afshar, Arash (School of Engineering, Mercer University, Macon; GA; 31207, United States); Mihut, Dorina Source: *Journal of Materials Science and Technology*, v 53, p 185-191, 15 September 2020
- [2] Saleh, N. (Wolfson Sch. of Mech. and Mfg. Eng., Loughborough University, Leicestershire, Loughborough, United Kingdom); Hopkinson, N.; Hague, R.J.M.; Wise, S. Source: *Rapid Prototyping Journal*, v 10, n 5, p 305-315, 2004
- [3] "Standard Test Method for Tensile Properties of Plastics." ASTM International - Standards Worldwide, American Society for Testing and Materials, <https://www.astm.org/standards/d638>.
- [4] "Desert Biome." *World Biomes | The Wild Classroom*, <https://thewildclassroom.com/biomes/desert/>.
- [5] Blumenthal, Amy. "How They Aim to Protect Your Netflix Access: Keeping Satellites Warm." *USC News*, 9 Jan. 2018, <https://news.usc.edu/133090/why-do-usc-engineers-try-to-keep-a-satellite-warm/#:~:text=In%20space%2C%20a%20satellite%20can,deplete%20on%2Dboard%20power%20reserves>.
- [6] "Thermolyne™ Premium Large Muffle Furnaces." *Thermo Fisher Scientific - US*, <https://www.thermofisher.com/order/catalog/product/F6010>.
- [7] "*Universal Testing Systems - INSTRON*. <https://www.instron.com/en-us/products/testing-systems/universal-testing-systems>.
- [8] Phull, Gurpreet Singh, et al. "Electroforming Defects During Metal Deposition on Plastic Substrate Produced by Additive Manufacturing." *International Journal of Scientific Research in Science and Technology*, vol. 4, no. 2, 2018, pp. 1179–1188.

OSGC Stem Scholarship: PIV Tests Of Rooftop Vortices And Correlation With Peak Pressures Over A Low-Rise Building

Student Researcher: Marcus W. Wittlinger

Advisor: Wei Zhang

Cleveland State University

Overview and Objectives

Windstorms, such as hurricanes and tornadoes, and associated flooding account for the most economic loss and fatalities in the United States among all weather hazards. Among the structures that are exposed to these disasters, low-rise buildings (residential homes, industrial and commercial buildings) are the most vulnerable. Post-disaster surveys have evidenced that failure of roofs and roof coverings account for the majority of the initial damages of such low buildings. The dislodging of roofing components such as shingles and tiles results in added windborne debris to windstorms, severe water intrusion, and in some cases, considerable damage to the building structure (Fig. 1). Roof failure is often initiated at windward roof edges and corners due to peak suctions induced by flow separation and vortex formation.

Despite extensive research via full-scale field tests, wind tunnel experiments, and computational models, the flow physics of such vortices' formation and development near roof edges is not well understood. The objective of this project is to correlate the rooftop vortex flow field and peak pressures utilizing synchronized flow field and pressure measurements. The work conducted thus far falls under the pressure measurement portion of the project. Experiments were conducted on a 1:100 scaled Texas Tech University (TTU) WERFL building model in a wind tunnel. In future experiments, unsteady vortices and roof surface pressures will be measured simultaneously using the Particle Image Velocimetry (PIV) technique and pressure scanning modules, respectively. This approach will allow new insight into rooftop vortex formation and the flow mechanism that governs peak pressure values. The desired outcomes of this study are: (1) correlation between complex rooftop vortical flow structures and surface pressures and (2) a better understanding of simultaneous flow field and pressure measurement prior to conducting large-scale tests under hurricane-type wind conditions.

Methodology Used – Wind Tunnel Measurements

To simulate hurricane-type winds, turbulent inflow conditions were created with an open-type wind tunnel at Cleveland State University. The 1:100 scaled building model was mounted on the bottom wall and subjected to an approach flow speed of 12 m/s, yielding a Reynolds number of 3.13×10^4 based on eave height. The model was mounted at a 90° wind angle of attack.



Figure 1: Severe damage to the roof framing during Hurricane Katrina.



Figure 2: Open-type wind tunnel to be used for project.

Fig. 2 shows the wind tunnel where experiments took place.

The building model was instrumented with arrays of pressure taps on the roof surface based on the NIST aerodynamic database layout. Time-series of differential pressures were sampled using a 16-channel Scanivalve DSA3217 pressure scanner. The first 10 channels of the scanner were connected to the pressure taps along the midspan of the roof, and the remaining channels were connected to neighboring taps for data validation purposes. Surface pressures were sampled at a rate of 500 Hz for 75 seconds. The time-series pressure data were converted to pressure coefficients by:

$$C_p(t) = \frac{p(t) - p_0}{\bar{q}H}$$

where $p(t)$ is the sampled pressure, p_0 is the freestream static pressure, and $\bar{q}H$ is the average dynamic pressure at eave height. The mean, RMS, and peak pressure coefficients were calculated using each pressure tap's time-series data.

Time-resolved (TR) PIV tests will be performed in addition to the surface pressure measurements. Equipment including a Quantel Evergreen double-pulsed Nd:Yag laser, an aerosol generator to produce tracer particles of approximately 1 μm , and a Photron Mini AX100 high speed camera of 1k pixels by 1k pixels, will be employed to measure the vortical flow structures over the roof. TR-PIV and pressure measurements will be synchronized to enable the correlation of flow and roof pressure data.

Fig. 3 compares the mid-span pressure coefficients over the TTU building roof (90° wind case) at the CSU wind tunnel with the results of a similar building model in the boundarylayer wind tunnel tests. It is evident that the regions of low mean and peak pressures are strongly associated with the flow separation near the roof edge. A longer region of low mean and peak pressure coefficients suggest the flow separation region could be longer, likely due to the approaching freestream with lower turbulence intensities. In this study, inflow turbulence intensity was not measured but will be characterized in future tests.

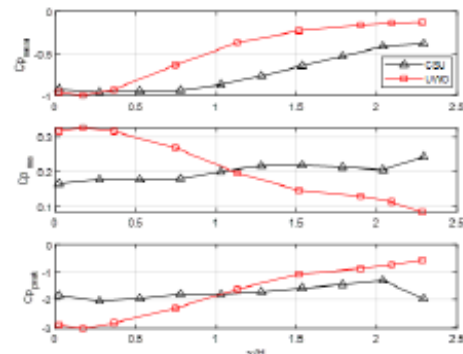


Figure 3: Mean, RMS and peak pressure coefficients in the midspan of the roof of the TTU building model. Wind approaches the building from the left (90° wind case).

This work presents mean, RMS, and peak pressure coefficients on the roof surface of a 1:100 scaled TTU building model. Strong correlations are confirmed between the rooftop vortices and the surface pressure distribution. The next step is to conduct time-resolved PIV to quantify the unsteady vortex dynamics and synchronize with pressure measurements. The Reynolds number of the current test cases is very low, and the inflow is a thin boundary layer rather than a thick boundary-layer flow. The planned experiments at large-scale flow facility will realize the boundary-layer type inflow conditions and high Reynolds numbers.

Lead (Pb) in Urban Soil

Student Researcher: Madison M. Wood

Advisor: Dr. David Singer

Kent State University
Department of Geology

Abstract

Lead (Pb) is commonly present in urban soils because of its wide range of industrial uses and its resistance to degradation. One way to identify if Pb is present in soils is using Scanning Electron Microscopy (SEM) coupled with Electron Dispersive Spectroscopy (EDS) which can be used to identify Pb and other elements present, assisting in understanding the phases Pb is bound in. Another way to identify Pb in soil is using X-Ray Fluorescence (XRF), which identifies the total concentration of elements within a sample. The identification of Pb-bearing phases present in soils, and the total concentration of Pb in soils will aid in identifying potentially bioaccessible Pb, which can assist in future targeted remediation.

Project Objectives

The U.S. Environmental Protection Agency has set a standard of 400 mg/kg of Pb in bare soils in residential areas to limit human exposure, however exposure to lower Pb concentrations (100-200 mg/kg) can still result in serious health consequences particularly for children. Exposure to Pb and potential bioavailability is dependent not just on total concentration, but also speciation; the chemical and physical form(s) of Pb present in soils and sediments. This project aims to identify physical and chemical speciation and total concentration to determine potential bio accessibility.

Methodology

Soil samples were taken along a transect from: home to road, home to back of yard, and a core near the home. Pb speciation is determined using Scanning Electron Microscopy coupled with Electron Dispersive Spectroscopy (SEM-EDS). This approach can determine grain-scale particle size, shape, morphology, texture, and elemental composition. Samples were dried and sieved prior to analysis in SEM-EDS. The total concentration of Pb is determined using X-Ray Fluorescence (XRF). Samples were dried, milled, and made into pressed powder pellets for analysis in XRF. This approach gives total concentration of all elements in a sample in ppm or weight percent (depending on the amount present). This is useful for determining the amount of Pb present, which is related to potential bioavailability because the likelihood of interacting with Pb is higher if there is more of it. Soil and sediment samples were analyzed from a home in an urban area within Northeast Ohio.

Results Obtained

Preliminary results indicate that physical speciation ranged from Pb coatings on larger grains to fine grained aggregates of Pb. Chemical Speciation showed that the Pb was often associated with iron oxides and clay minerals. Common elements found alongside Pb include (in no order): Fe, O, Al, K, Ca, Mg, Na, P, Cl, and S. Total concentration was measured along a transect from home to road and across depth. Findings show that there was a decrease in concentration from home to road with a small increase in concentration at the road. In addition, there was a general decrease in concentration from back of home to end of back yard. And finally, there was a decrease in concentration as a function of depth- with the concentration being highest at the surface.

Significance and Interpretation of Results

Physical speciation like the grain size can affect potential bioavailability with larger grains being more immobile and therefore having a lower potential for bioavailability, and coated grains potentially being more bioaccessible than discrete grains. Chemical speciation can also affect potential bioavailability with oxidized states being generally more reactive than reduced forms. Concentration is correlated to potential bioavailability in that higher concentration means higher potential bioavailability. So preliminary findings determine that there is higher risk of potential bioavailability near the home where concentrations are highest, and that Pb is present as coatings on larger grains (less mobile) and as small aggregates on larger grains (more mobile) and Pb is often associated with iron oxides and clay minerals.

Acknowledgments

Thank you to the Environmental Science and Design Research Initiative (ESDRI) and the Summer Undergraduate Research Experience (SURE). Thank you to the Ohio Space Grant Consortium for supporting this project.

Towards Development of an Empirical Model for Prediction of Screech and Coupling in a Supersonic Rectangular Twin Jet Screech Model

Student Researcher: Samuel T. Yoder

Advisor: Dr. Mo Samimy

The Ohio State University

Department of Mechanical and Aerospace Engineering

Abstract

Rectangular twin jet engines used on tactical aircraft have several advantages compared to circular twin jet engines, namely, reducing an aircraft's weight and drag, improving its maneuverability, and integration of propulsion and aerodynamics. However, relatively little research has been done on the flow and acoustic characteristics of rectangular twin jet engines. Coupling between the two jets due to their close proximity introduces unsteady pressure fluctuations in the near field and noise in the far field which, if not controlled, can cause high levels of sonic fatigue as well as intense radiated noise. This can damage critical components close to the nozzles and is a health concern for those nearby.

This project will investigate the use of Localized Arc Filament Plasma Actuators (LAFPAs) to control twin jets coupling, near-field pressure fluctuations, and far-field noise. LAFPAs, controlled electronically, create plasma arcs at the nozzle lip, producing thermal perturbations with desired frequencies in the flow which interrupt the predominant mechanism of jet noise, screech. Additionally, LAFPAs can alter the coupling behavior of the jets. However, due to the complex nature of the flow, it is difficult to predict the behavior of the jets to excitation by LAFPAs. As such, a physics-based empirical model has been developed to predict the response of the flow to certain actuation parameters. To accurately model this response, two important parameters must be determined: the locations of shock cells within the flow and the velocity of the large-scale flow structures convecting downstream within the jet, interacting with the shock waves, and generating screech tones. In this research, a method for empirically predicting streamwise shock locations based solely on flow Mach number is explored. Additionally, a novel method of estimating convective velocity is presented using Empirical Mode Decomposition (EMD) to isolate the hydrodynamic pressure from the measured overall (acoustic and hydrodynamic) pressure just outside the jets.

Project Objectives

The accurate prediction of screech and coupling behavior of twin jets requires the following quantities: the distance of shock cells from the nozzle lip, the average convective velocity (U_c) of large-scale turbulent structures (LSSs) in the flow, and the ambient speed of sound. It is trivial to determine sound speed using a thermocouple. However, predicting shock locations and convective velocity require further analysis. The purpose of this work is twofold. The first part of this research focused on an empirical method of predicting shock cell locations based on the flow Mach number (M_j). The latter focused on the estimation of convective velocity using Empirical Mode Decomposition (EMD) to isolate hydrodynamic pressure components from a linear array of near field microphones.

Methodology Used

All testing was done at the Gas Dynamics and Turbulence Laboratory of Ohio State's Aerospace Research Center using an anechoic chamber shown in Figure 1. The rectangular twin jet's nozzles have a design Mach number (M_d) of 1.50, an aspect ratio of 2, and an equivalent diameter (D_e) of 0.758 in.

They are shown in Figure 4. Each nozzle is fitted with boron nitride housings along the outboard lip perimeter which house the LAFPAs. For part of the research presented in this report, the LAFPAs were not used. A system of high-pressure air tanks store up to 16 MPa of air which is then conditioned before being exhausted from the nozzles. For both components of this work a range of underexpanded and overexpanded Mach numbers were tested.

The experimental setup, however, varied slightly between the two parts. Experimental shock location data was collected using time-averaged schlieren imagery on the plane of the twin jets minor and streamwise axes. Shock locations were determined manually after the fact. All shock locations, measured and predicted, were normalized by equivalent nozzle diameter. The basis for the empirical shock location prediction method was established by Pack (1950) who's work focused on underexpanded converging jets [1]. Pack's method predicted an initial shock location using Equation 1 governed by a coefficient κ and M_j but assumed that subsequent shocks were equally spaced. Harper-Bourne (1974) expanded on this method in a later paper by introducing a shock spacing coefficient α (see Equation 2) [2]. A code was written to compare predicted shock locations to experimental schlieren data using a range of values for each coefficient. Coefficient combinations which minimized the Euclidean norm of the error between predicted and experimental shock locations were determined to be the "best" coefficients for a given M_j . Over and underexpanded regimes were analyzed separately due to their different flow physics. Through a deterministic iterative process, a model of coefficient values which balanced accuracy and ease-of-application was developed for each regime with respect to M_j .

$$L_1 = \kappa \sqrt{M_j^2 - 1} \quad (1)$$

$$L_i = L_1((1 - \alpha)i + \alpha) \quad (2)$$

For the second part of this work, near field pressure data was collected by a linear array of 10 microphones in a different configuration for each flow regime (shown in Figure 3). The microphones were aligned on the center of the jet column over a single jet. The configuration geometry was chosen to maximize spatial resolution of the shock cells. Both configurations are mounted at an angle of 10° to the horizontal to avoid oversaturation and impinging into the jet mixing layer. Configurations 1 and 2 were optimized for the over and underexpanded flow regimes, respectively. The pressure data from each microphone was decomposed into seven physically-meaningful Intrinsic Mode Functions (IMFs) using Empirical Mode Decomposition (EMD). EMD is a time-frequency data analysis method similar in principle to a Fourier transform but can be used with nonlinear and nonstationary signals [3]. IMFs whose spectral peaks were at a frequency greater than some critical frequency were designated acoustic [4]. All other IMFs were hydrodynamic. The hydrodynamic signals were then combined for each microphone. The convective velocity was calculated using a cross correlation between microphones at each M_j .

Results Obtained

The final predicted shock locations are shown compared to experimental data in Figure 4. This empirical method showed remarkable accuracy with R^2 values above 0.99 in each M_j analyzed. The recommended values of κ and α vary between the flow regimes which is to be expected. These values are summarized in Table 1. Both regimes use a value of κ based on a linear fit with respect to M_j and a constant shock spacing coefficient α . The overexpanded regime uses a slightly altered method which

captures the change in flow physics between the two regimes. This method involves using the initial shock as the origin from which subsequent shocks are calculated. The actual initial shock location is then estimated as the halfway point between the nozzle lip and second shock. The results of the convective velocity estimations are shown in Figure 5 for both separated and unseparated pressure components along with expected data from literature. The separated pressure components do follow anticipated trends, notably that U_c decreases downstream as the jet core loses energy due to turbulence and also that U_c decreases at higher underexpanded Mach numbers. However, many data points were not included because they were nonphysical (typical values: $0.4 \leq U_c/U_j \leq 0.8$) or exceeded acceptable error limitations. This issue was more pronounced at stronger underexpanded Mach numbers and is likely due to the filtering method used to remove the jet screech tone. Future work should improve this filtering technique and iterate the critical frequency used to separate pressure components based on previous estimations until a solution converges.

Figures



Figure 1: Anechoic jet chamber at Ohio State's Aerospace Research Center

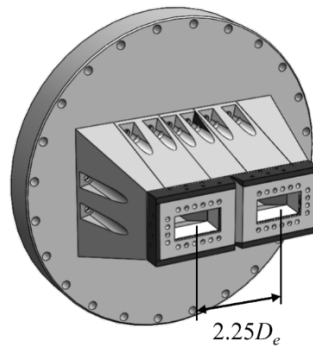


Figure 2: Rectangular twin jets nozzles with LAFPA housings on lip of design Mach number (M_d) 1.50

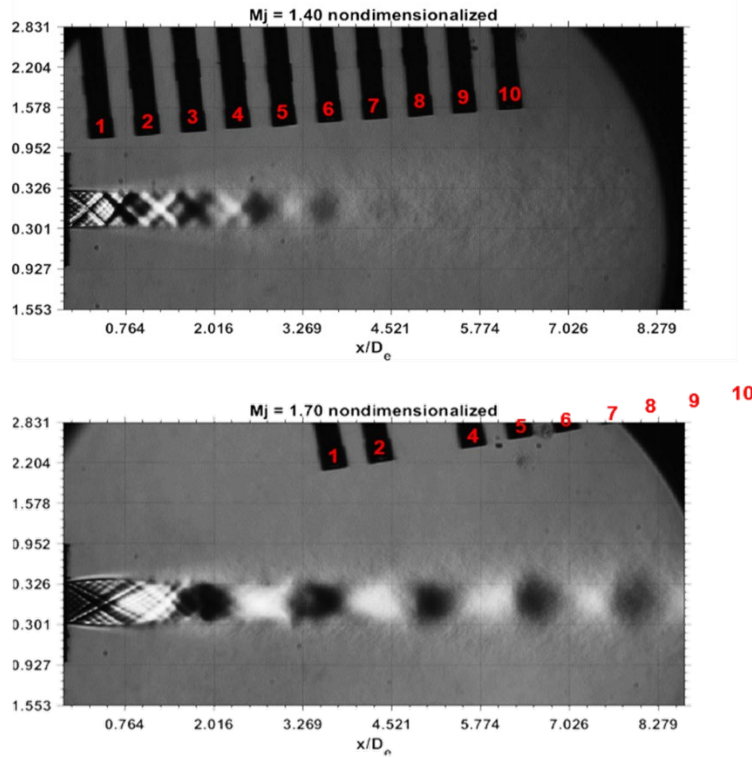


Figure 3: Time-averaged Schlieren images showing two microphone configurations used

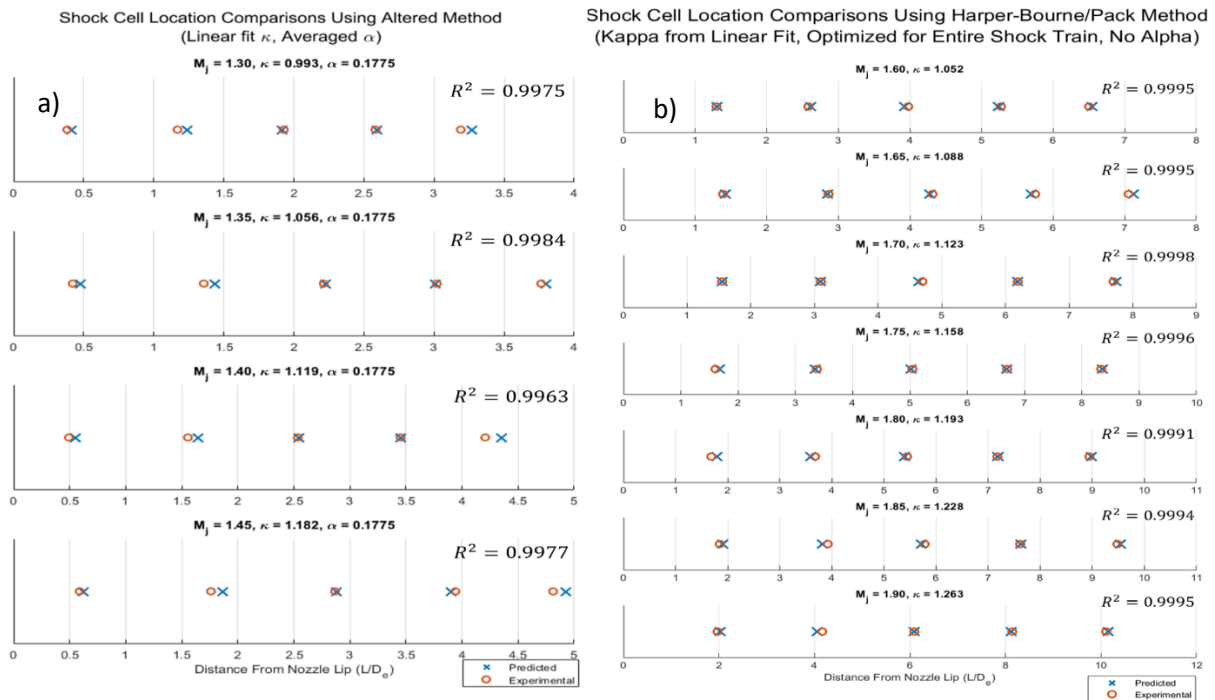


Figure 4: Final results of empirical shock location prediction over range of underexpanded and overexpanded M_j : a) overexpanded estimations using κ from linear fit with M_j and averaged α , b) underexpanded estimations using κ from linear fit with M_j and $\alpha = 0$

Table 1: Recommended coefficient values for both under and over expanded flow regimes

Flow Regime	Method	κ	α
Underexpanded ($M_j > 1.50$)	Original	$0.700M_j - 0.072$	0
Overexpanded ($M_j < 1.50$)	Altered	$1.260M_j - 0.6450$	0.1775

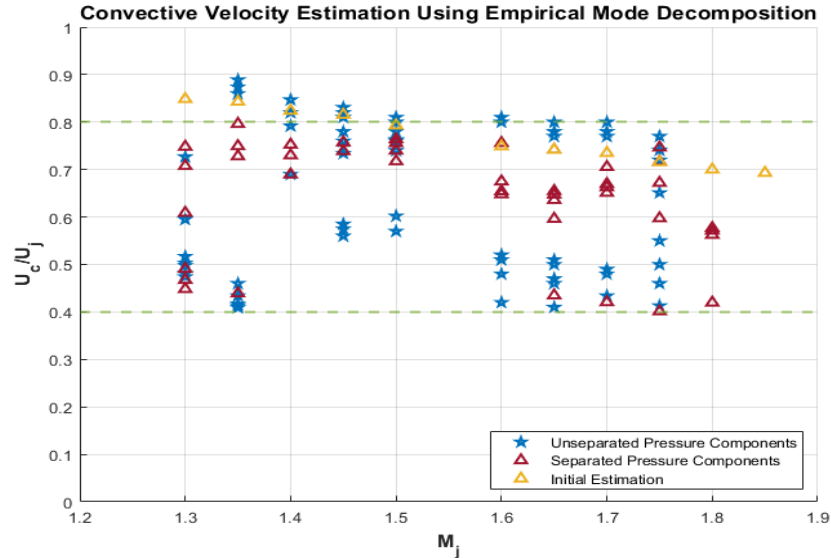


Figure 5: Convective velocity estimations for range of M_j using various methods

References

- [1] D. C. Pack, "A note on Prandtl's formula for the wave-length of a supersonic gas jet," *The Quarterly Journal of Mechanics and Applied Mathematics*, vol. 3, no. 2, pp. 173–181, Jan. 1950, doi: 10.1093/qjmath/3.2.173.
- [2] M. Harper-Bourne, "The noise from shock waves in supersonic jets-Noise Mechanism-," *AGARD CP-131*, 1974, Accessed: Apr. 01, 2022. [Online]. Available: <https://ci.nii.ac.jp/naid/10021111327/>
- [3] "The empirical mode decomposition and the Hilbert spectrum for nonlinear and non-stationary time series analysis | Proceedings of the Royal Society of London. Series A: Mathematical, Physical and Engineering Sciences." <https://royalsocietypublishing.org/doi/10.1098/rspa.1998.0193> (accessed Apr. 01, 2022).
- [4] A. Sinha, H. Alkandry, M. Kearney-Fischer, M. Samimy, and T. Colonius, "The impulse response of a high-speed jet forced with localized arc filament plasma actuators," *Physics of Fluids*, vol. 24, no. 12, p. 125104, Dec. 2012, doi: 10.1063/1.4772191.

Acknowledgements

First and foremost, I would like to thank the OSGC for its generosity. I would like to thank my advisor, Dr. Mo Samimy, for his careful guidance throughout this process and for being a great teacher. I would also like to thank Dr. Ata Esfahani for his thoughtful help through the duration of the project and for his endless patience. Thank you also to Dr. Nathan Webb who made a difficult subject matter extremely approachable. Thanks also to Ryan Leahy for his contributions to experimental setup and recommendations.

Community College

The Artificial Intelligence in Rover Perseverance

Student Researcher: Mickela Harris

Advisor: Abigail Yee MS

Cincinnati State Technical and Community College
Pre-Engineering

Abstract

Artificial Intelligence is the ability of a computer software or machine to learn or think and have become a critical part of this space mission from the very beginning to now. On February 18th 2021, the Rover Perseverance landed on Mars, specifically the Jezero Crater. Engineers nicknamed it “seven minutes of terror”, as it takes exactly 7 minutes to find out how the landing went due to delays in retrieving data from Mars to Earth. Thankfully due to AI from Terrain Relative Navigation System, the landing went smoothly. This technology included a camera that took images as the rover landed and used the images with the map provided to help Perseverance land safely. After the landing, the rover used AEGIS (Autonomous Exploration of Gathering Increased Science System), which is a software that uses AI to aim and control the chemistry camera. This project will analyze the AI systems that Rover Perseverance is currently using and how it impacts the mission at hand.

Project Objectives

The purpose of this project is to research the different instruments used on Rover Perseverance that involve Artificial Intelligence and how it impacted the Mars mission.

Methodology Used

With the Mars mission being a current event, the information used for the research came from the NASA Mars website, and research articles.

Results Obtained

Perseverance is a 2,260-pound rover with some of the newest technology on planet Earth. The goal of this mission is to look for signs of past microbial life within the samples collected on the planet. To accomplish this goal AI is used to lead the rover on the right path by not only using the information given by the researchers on Earth but by also making its own choices to keep itself safe from any dangers. Artificial Intelligence is simply defined as the concept of computers having human-like intelligence to problem solve, learn, and reason. Within the rover, AI is used within five components of this machine.

Terrain- Relative Navigation (TRN): Between the descent and the landing, there was no signal due to the events happening faster than the radio signals could reach to earth, this gap in time was nicknamed 'the 7 minutes of terror'. Researchers needed a plan to correct this issue to ensure the safety of the rover. Thus, TRN was created to help with this issue. This worked by Perseverance cutting the chute loose, dispensing its back shell, and using rocket thrusters to ease itself down. After this, the vehicle must tilt right away to avoid the falling parachute and backshell, thus deciding on its own where it is safe enough to land. Therefore, on February 18th, 2021, the rover landed safely in Jezero Crater.

Vision Compute Element (VCE): The partner of the TRN for the landing is the VCE and the LVS Camera (LCAM). The AI component is the VCE which processed the images the camera took, to help with the machine's final choices in where to land safely. This is a 3 slot 6U processor with a Computer Vision Accelerator Card, a general processor, and a power conditioning card.

Planetary Instrument for X-ray Lithchemistry (PIXL): This lunch box-sized instrument weighs about 10 pounds and is located at the end of the rover's robotic arm. The purpose of PIXL is to detect chemicals within the rocks on Mars to find signs of life that were once there. This works by using the instrument's powerful x-ray to detect over 20 chemical elements by pointing the beam at the rocks. With each element, there is a glow associated with it, which will be present within 10 seconds of the scan. Therefore, giving scientists the information needed for the mission.

Scanning Habitable Environments with Raman and Luminescence for Organics and Chemicals (SHERLOC): Partnered with PIXL, this instrument is mounted on the same robotic arm as well. SHERLOC uses an ultraviolet laser to find organic chemicals within the environment helping scientists with choosing the best samples to collect. This works by the rover placing the instrument about two inches about the location needed to scan, thus preventing any contamination that could happen. With the laser, there is also a use of cameras, and a spectrometer to use in search for the past of the planet. While also detecting chemicals in rocks, SHERLOC carries space suit material test how it handles the environment it is surrounded in.

Spaceborne Computer – 2 (SBC-2): Acting as a sort of hardware on Perseverance, this marks the first-time broad AI and edge computing capabilities have been available to NASA. To get to this point in 2017, the original SBC-1 was used at the International Space Station, and due to its success and positive reviews, the SBC-2 was created and sent on the Mars mission. With this, memory-driven AI is used for its success, which allows the hardware to use less energy and can complete tasks much faster than traditional systems.

Significance and Interpretation of Results

With all five of these systems being used on the rover, Artificial Intelligence has made a great impact on this mission. From using the navigation system to make sure that the landing was safe. To decide if the area the rover is located would be a good place to take samples. AI has not only created breakthrough discoveries but opened the doors for future space missions both robotic and even human.

Acknowledgments

I would like to acknowledge Dr. Carole Womeldorf for telling me about this scholarship and introducing me to the community of LSAMP. Abigail Yee, for helping me through this new experience as my advisor for this, and CState Accelerate for showing me it is never too late to follow your dreams.

References

“Artificial Intelligence, IOT Sensors Tech, Aboard NASA's Perseverance Rover.” *Artificial Intelligence, Big Data Analytics and Insight*, 25 Feb. 2021, <https://www.analyticsinsight.net/artificial-intelligence-iot-sensors-tech-aboard-nasas-perseverance-rover/>.

Greicius, Tony. “NASA's New Mars Rover Will Use X-Rays to Hunt Fossils.” NASA, NASA, 22 Sept. 2020, <https://www.nasa.gov/feature/jpl/nasas-new-mars-rover-will-use-x-rays-to-hunt-fossils>.

“Mars 2020 Perseverance Rover.” NASA, NASA, <https://mars.nasa.gov/mars2020/>.

Mars 2020/Perseverance - NASA's Mars Exploration Program.
https://mars.nasa.gov/files/mars2020/Mars2020_Fact_Sheet.pdf.

Finite Element Analysis of Surgical Implants for the Treatment of Scoliosis

Student researcher: Michael Kump

Adviser: Dr. Regan Silvestri

Lorain County Community College
Universal Science

Abstract

Scoliosis is a severe deviation of the spinal column that negatively affects the lives of those afflicted with the disorder. While there is no definitive cause for many instances of scoliosis, there are however treatments that can restore proper function to the spine. Among these are the use of surgically implanted constructs to correct the curvature of the spine. Using Abaqus, a computer program for modeling how designs will perform under stress, these constructs can be modeled and improved before implementing real world stress tests.

Introduction

Scoliosis affects approximately 2-3% of the population with many cases of it presenting without a known cause. Scoliosis can be treated in a number of different ways. One such way is the implantation of a surgical construct that can straighten the backs of those affected. The failure rate of these implants however is quite high, and failure of an implant necessitates additional surgeries. These constructs can be modeled in Abaqus using finite element analysis to identify and correct areas of stress concentrations within the constructs before physical models are constructed and tested in the real world.

Objective

The current objective is to make use of Abaqus's finite element analysis to test proposed design improvements. Design modifications can be tested using finite element analysis locating areas of stress concentrations to further refine the proposed designs.

Experiment

Using Abaqus to simulate different designs and modifications of said designs including modification to materials, to assess their performance under conditions that would mirror real world stresses.

Results

Results are currently in process.

Conclusion

The Abaqus finite element analysis software package can be used to model the stresses and strains in construct designs of surgical implants used to correct scoliosis. Modifications to construct designs can be made and these new construct designs can be tested, again using the Abaqus finite element analysis software package, to determine if the construct design modifications are viable without the need to physically make each proposed design modification.

References

Goldberg, C. J., Moore, D. P., Fogarty, E. E., & Dowling, F. E. (2007). Scoliosis: A Review. *Pediatric Surgery International*, 24(2), 129–144. <https://doi.org/10.1007/s00383-007-2016-5>

Janicki, J. A., & Alman, B. (2007). Scoliosis: Review of diagnosis and treatment. *Paediatrics & Child Health*, 12(9), 771–776. <https://doi.org/10.1093/pch/12.9.771>

Maruyama, T., & Takeshita, K. (2008). Surgical treatment of scoliosis: A review of techniques currently applied. *Scoliosis*, 3(1). <https://doi.org/10.1186/1748-7161-3-6>

Evaluation of Growing Rod Implants used in Pediatric Scoliosis Surgeries by Finite Element Analysis

Student Researcher: Sara Martin

Advisor: Dr. Regan Silvestri, PhD

Lorain County Community College
Division of Science and Math

Abstract

Pediatric scoliosis is characterized by an abnormal lateral curve in the spine of young children. Lorain County Community College has partnered with the University of Toledo to evaluate orthopedic devices used in corrective surgeries for pediatric scoliosis. One class of orthopedic devices commonly used in corrective surgeries for pediatric scoliosis are growing rods, named as such because following implant they allow for growth through adolescence. Current designs of growing rods are being evaluated for performance by computer modeling. Computer modeling of the stresses and strains in growing rods are being performed by Finite Element Analysis using the software suite Abaqus CAE. Modeling of the stresses in current growing rod designs locates areas of stress concentrations in the current designs, with hopes of working toward design modifications for increased performance.

Project Objective

The final goal of this project is to develop a construct for a new growing rod structure, create a computer model of this new structure, and test it by performing Finite Element Analysis using Abaqus CAE. In order to reach this final goal, initial milestones were set for the course of this study:

- Read and research treatment, surgery, and etiology of pediatric scoliosis.
- Utilize practice models from the University of Toledo in ABAQUS CAE to gain familiarity with Finite Element Analysis.
- Create an original sketch of a growing rod model with a unique design modification.
- Create a model of the new growing rod design using ABAQUS CAE, model the design by finite element analysis, and observe stress concentrations thereby determining the viability of the new design.

Methodology Used

To begin designing a new model for a growing rod, it was necessary to conduct a literature review to gain background information about the effects of pediatric scoliosis, current treatment options, and the fundamentals of Finite Element Analysis using ABAQUS CAE. Next, several practice models were created in ABAQUS CAE including several 2D and 3D models, as well as assemblies with multiple parts. Once experience with the workflow of ABAQUS was gained, we proceeded to design a new model for a growing rod based on original modifications of designs presented in "Mechanical Performance of Traditional Distraction-Based Dual Growing Rod Constructs" by Hill et al, shown below.

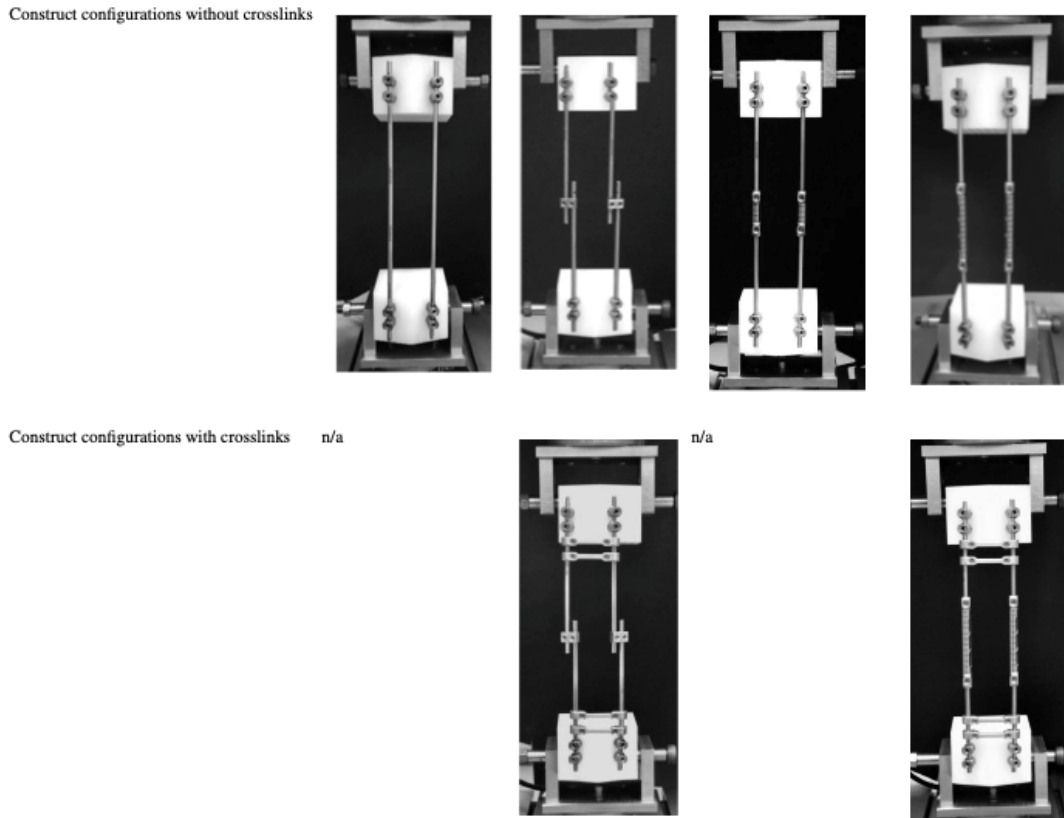


Figure 1

To make these improvements, an understanding of the surgical process must be obtained. The new design must be strong and decrease the likelihood of breaks in the rod, and the surgery to place and adjust the growing rods must be as minimally invasive as possible.

Results Obtained

The project is currently in the process of evaluating and testing original design modifications.

Acknowledgements

The author would like to extend her gratitude and thanks to the Ohio Space Grant Consortium for supporting this project, to her advisor Dr. Regan Silvestri for introducing her to a new field of research, and to the faculty and staff at University of Toledo for sponsoring and leading this project.

References

- Foltz, Mary H., et al. "Mechanical Performance of Posterior Spinal Instrumentation and Growing Rod Implants." *Spine*, vol. 44, no. 18, 14 Mar. 2019, pp. 1270–1278., <https://doi.org/10.1097/brs.0000000000003061>
- Goldberg, Caroline J., et al. "Scoliosis: A Review." *Pediatric Surgery International*, vol. 24, no. 2, 2007, pp. 129–144., <https://doi.org/10.1007/s00383-007-2016-5>
- Hill, Genevieve, et al. "Mechanical Performance of Traditional Distraction-Based Dual Growing Rod Constructs." *The Spine Journal*, vol. 19, no. 4, 5 Sept. 2018, pp. 744–754., <https://doi.org/10.1016/j.spinee.2018.09.006>
- Hill, Genevieve, et al. "Retrieval and Clinical Analysis of Distraction-Based Dual Growing Rod Constructs for Early-Onset Scoliosis." *The Spine Journal*, vol. 17, no. 10, 21 Apr. 2017, pp. 1506–1518., <https://doi.org/10.1016/j.spinee.2017.04.020>
- Janicki, Joseph A, and Benjamin Alman. "Scoliosis: Review of Diagnosis and Treatment." *Paediatrics & Child Health*, vol. 12, no. 9, 2007, pp. 771–776., <https://doi.org/10.1093/pch/12.9.771>
- Maruyama, Toru, and Katsushi Takeshita. "Surgical Treatment of Scoliosis: A Review of Techniques Currently Applied." *Scoliosis*, vol. 3, no. 1, 2008, <https://doi.org/10.1186/1748-7161-3-6>
- Millner, P. A., and R. A. Dickson. "Idiopathic Scoliosis: Biomechanics and Biology." *European Spine Journal*, vol. 5, no. 6, 12 Aug. 1996, pp. 362–373., <https://doi.org/10.1007/bf00301963>
- Shekouhi, Niloufar, et al. "Clinically Relevant Finite Element Technique Based Protocol to Evaluate Growing Rods for Early Onset Scoliosis Correction." *JOR SPINE*, vol. 3, no. 3, 22 July 2020, <https://doi.org/10.1002/jsp2.1119>

How the Collimation of Lighting Affects Productivity and Mood

Student Researcher: Ryan M. Palmer

Advisor: Johnny Vanderford

Lorain County Community College
Micro Electro-Mechanical Systems (MEMS)

Abstract

While the effects of varying optic spectral density of light on humans have been studied, the effect of the radiation pattern has been left mostly unstudied. If man made light is collimated in a way that resembles natural sun light it might affect the perceived quality of that light. To study this, volunteers were exposed to either collimated or diffused light. The volunteers' mood, anxiety levels, and performance on a simple test were gathered before and after exposure. The results showed that there was no significant difference between the two light sources.

Introduction

In 2016, new LED lights were delivered to the International Space Station to replace the fluorescent lights previously in use. These new lights output different optic spectral density depending on the time of day to help astronauts with their sleep schedule and increase their alertness. While these lights can change the composition of the light they output, they deliver the light the same way most lights do. By placing the light behind a diffuser, it disperses the light at many different angles. This is different from how most natural light is perceived, since the light from the sun is almost perfectly collimated by the time it reaches the Earth creating "beams" of light rather than the soft defused light that most man-made light sources produce. The project will test if the collimation of light affects how the light is perceived and what effect it has on productivity and mood.

Objective

To determine if the collimation of light has any effect on the mood or relative performance of people in simple tasks.

Experiment

The experiment was conducted in a 10ft-by-10ft study room with a light source that would be changed from collimated to diffused for the test and control groups of volunteers. Volunteers were randomly selected and incentivized to participate with a small gift. None of the volunteers were told what was being tested until after the experiment was conducted. The target time for volunteers to stay in the study room was 15 minutes. Ideally this would be closer to an hour but due to the limited time of the volunteers the time was kept to an average of 15 minutes. To get data on mood and productivity, all the volunteers were given a pre and post survey along with a simple test. Time was not accounted for in this test, only correct answers. To measure the change in mood of participants, a scale was provided in the pre and post survey so volunteers could self-report a mood between 1 and 5. This allowed the post mood to be subtracted from the pre mood to give total mood improvement or reduction (positive mood change represented as a positive number and mood reduction as a negative number). All the mood changes for the test and control group were added respectively to give total mood change for each of the groups.

Results

A total of 30 volunteers participated in the research project; they were split equally between test and control groups. The group that received the collimated light had an average mood increase greater than the control group. But the Z-score for the test group was only 0.12, to be considered statistically significant this value would have to be greater than 2 or less than -2.

Conclusion

No significant difference was found. The difference between the test and control groups was so little that there could easily have been other factors at play. If the control group had a mean mood change over 1.14 or under 1.14 then there would have been a strong correlation between exposure to collimated light and mood change. If this experiment was to be done again, the survey would have some questions replaced with questions that were easier, and more volunteers would have been studied, ideally for longer periods of time. This would have resulted in a more accurate data set. The quality of the collimated light would have been improved since the one used in the initial testing had a low-quality parabolic reflector.

References and Additional Content

Harbaugh, Jennifer. "Let There Be (Better) Light." NASA, NASA, 19 Oct. 2016,

https://www.nasa.gov/mission_pages/station/research/let-there-be-better-light

Pre, post, survey and simple test document.

<https://docs.google.com/document/d/1voPcETbxlwVmfDoj4fPKqv90KhqzhU3T9lBMIC0wUcM/edit?usp=sharing>

Results document.

https://docs.google.com/spreadsheets/d/1lv_LoB7HgM4ux29O8QF79GET9Fy3sMZc3TAC6YVDaXQ/edit?usp=sharing

An Assessment of Potential Wildlife Crossings in Ohio

Student Researcher: Nahaniel A. Surgeon

Advisor: Dean M. Bortz

Columbus State Community College
Construction Management

Abstract

By using data on already existing wildlife crossings, automobile accidents involving animals, and different maps of an area we can estimate the best locations for potential wildlife crossings within said area. I did an analysis on a county and on select highways within the state of Ohio. With the goal to show the viability and benefits of wildlife crossings within the state.

Methodology Used

When conceptualizing a process to determine locations, the primary method that I came up with was using GIS software to make a custom map. The map would be created by overlaying 4 primary maps. Those being: topography, roadways, animal-based automobile accident density, and the species that inhabit the area. Each one plays a major role in the construction of the new map. The roadway map serves as the backbone to be built upon.

Results

The accident density map points us to which highways put people and animals most at risk. The species map serves 2 purposes. The first is that it shows us which animals are at risk of harm and their status, such as endangered, species of concern, or special interest. The second purpose of knowing which animals are located around our highway of interest is knowing the habitats, migratory patterns, and potential sources of food. That these animals need to thrive. Finally, the topography map shows us if said habitats were cut by the highway or if the highway goes around it. Because if the habitat has minimal to no disruption there are better locations to pursue. It also shows us the feasibility of physically putting in a bypass or crossing. By showing the elevations and makeup of the surrounding area.

With the map made we then must assess the cost of going forward with the project. When estimating the financial cost of the project it is beneficial to consider already existing projects, and also take into consideration exceptions and outliers and their impact on the cost. It is valuable to use this information to formulate a potential maximum cost that shows us the worst possible circumstances. When calculating the cost of implementing the crossing we cannot just include the money required for construction. We also must take into account the value of the traffic disruptions that will be caused by said construction.

I started my process by using the Ohio State Highway Patrol's public data on deer-related accidents across the state from 2018-present day. Taking note of the counties and highways that have the most reported accidents. With the top 3 counties being Stark, Richland, and Hancock, and the top 3 highways being IR-71, SR-2, and US-30. Richland county contains the intersection of IR-71 and US-30. Both of these highways hold the highest density of crashes of all roads within the county and have an incredibly high average density themselves.

After determining that Richland county would be a good starting point, I then moved to look at the species located within the county and its topography. Using the Ohio Department of Natural Resources database

I found that there are 6 endangered and 5 threatened species within the county. However, the majority of species that have a status of special interest or higher are avians. The only non-flying endangered species in the area is the Black Bear, so a crossing would primarily be used by the more common animals. The topography of the county shows several small to medium forests majorly severed by roads. With IR-71 being responsible for a majority of the fragmentation. Despite the area not being of high environmental importance due to species, the amount of deer-related accidents across the area is still staggering.

Significance and Interpretation of Results

Applying my location finding process to the county of Richland allowed me to come up with several locations across IR-71 and OH-13 within the county. Some examples are located at $40^{\circ} 44' 53''$ N $82^{\circ} 26' 43''$ W and $40^{\circ} 41' 58''$ N $82^{\circ} 30' 12''$ W. Both of these demonstrate moderate to high levels of wildlife habitat fragmentation along with having flat topography for easy construction.

I think that the process could use some refinement, and I could make some improvements myself to get a more thorough result. A major point is the usage of GIS software. Spending more time learning and understanding the software would make the entire process simpler. Within the process itself, a major change that is needed is restructuring what we are looking for. Currently, we are looking for singular points across highway sections. These individual crossings are severely less effective than small series of crossings spanning a 2-5 mile stretch of highway. The second major change is finding a series of equations or algorithms that assess the financial cost and impact on traffic of construction in that location. With those revisions, I think that the capacity of what can be done in a short time frame can be drastically increased and the overall effectiveness of the process will increase.

Evaluation of Growing Rod Surgical Implants Used in the Treatment of Pediatric Scoliosis by Finite Element Analysis

Student Researcher: Nicholas W. Valescu

Advisor: Dr. Regan Silvestri, PhD

Lorain County Community College

Division of Engineering, Business, and Information Technologies

Abstract

Proposed design modifications for dual growing rod constructs used as orthopedic surgical implants to treat pediatric scoliosis are being evaluated using finite element analysis computer modeling.

Introduction

Scoliosis is a three-dimensional curvature of the spine, which is often idiopathic and resulting of an undetermined cause. Curvatures of greater than 45° are treated by surgeries that implant orthopedic hardware devices to correct the curvature and fuse the vertebrae. Early onset pediatric scoliosis however must be treated with implant devices that allow for continued growth of the patient through puberty. Various constructs of so called “dual growing rod” implants are used in surgeries to correct pediatric scoliosis, as the growing rods allow for extension of the hardware and continued growth of the patient. The failure rate of current state-of-the-art technology growing rods however is not acceptable. Our work herein is to evaluate new proposed designs of dual growing rod constructs using computer modeling.

Experimental

Abaqus/CAE finite element analysis software is used to model the stresses and strains in dual growing rod constructs. As such, the failure load and displacement of a construct design can be accurately predicted, as well as areas of stress concentration located. Therefore, computer modeling using the Abaqus software package can be used to test new proposed design modification to dual growing rod constructs without the time consuming need to fabricate and evaluate the constructs by mechanical testing.

Results

Current work is in progress with evaluating growing rod constructs that are designed to have connectors with more elastic properties. This is accomplished by modifying the material’s properties in the construct built in the Abaqus/CAE finite element analysis software. These design modifications are being evaluated using computer modeling, and comparisons made relative to control models. As such, proposed design modification can be evaluated.

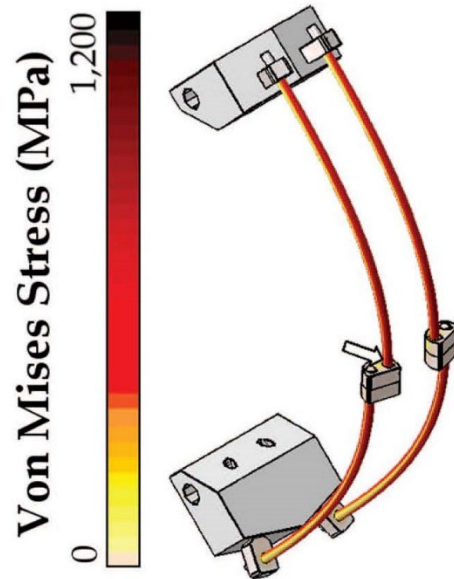


Figure 1: An example of how stress concentration can be located within a particular growing rod construct design using finite element analysis modeling. From reference 1.

Conclusions

Finite element analysis modeling can effectively be used to rapidly evaluate proposed modifications to construct designs for dual growing rod implants used in the treatment of pediatric scoliosis.

References

1. Foltz MH, Freeman AL, Loughran G, et al. Mechanical Performance of Posterior Spinal Instrumentation and Growing Rod Implants: Experimental and Computational Study. *Spine (Phila Pa 1976)*. 2019;44(18):1270-1278. doi:10.1097/BRS.0000000000003061
2. Hill G, Nagaraja S, Bridges A, Vosoughi AS, Goel VK, Dreher ML, Mechanical performance of traditional distraction-based dual growing rod constructs. *The Spine Journal (Elsevier)*. 2019; 19(4): 744-754. doi.org/10.1016/j.spinee.2018.09.006

Manufacturability of Micro-Scale Components with Modern SMT Equipment

Student Researcher: Emily T. Williams

Advisor: Johnny Vanderford

Lorain County Community College

Engineering Information Business Technology - Micro Electromechanical Systems (MEMS)

Abstract

Micro-scale components are commonly manufactured with modern electronic products. To achieve the lowest possible cost and highest possible yield in production, manufacturers have variable limitations such as the efficiency and capabilities of their equipment in addition to the relative size of the electronic part to be manufactured. A study was setup to test the manufacturability of SMT components on a PCB using high-volume PCB manufacturing equipment. Results showed that a relationship of yield versus process control on solder paste, pick & place nozzles, and the HASL finish of the PCB.

Objective

A potential solution for manufacturing microelectronic products containing components of sub-millimeter scale sizes, such as 0201 and 01005 chip resistors is using trial and error with different commercially available nozzle tips and a modern pick-and-place machine. Different sized nozzles with varying shape & size of vacuum pickup orifices can create variations in manufacturability in addition to how these components are programmed to be picked up including, but not limited to, pickup speed and mounting speed. Additionally, process variation in consumables and components including solder paste quality, circuit board quality, and variations in component sizes all add to manufacturing variation in microelectronics. The objective of this report is to study the process manufacturability of picking and placing 0201 and 01005 SMT components using the Panasonic NPM-W2 pick-and-place machine.

Methodology Used

A rigid FR4 Printed Circuit Board (PCB) was designed to include two 3x2 arrays with each PCB containing twenty-four 0201 resistors and twenty-four 01005 resistors lands. (Figure 2) Two PCB batches were ordered, one batch in green, and one batch in blue. Both batches of PCBs were printed on with AIM M8 SAC305 T4 solder paste using the Panasonic SPG stencil printer under an electropolished 736mm x 736mm stencil. The boards were then pick & placed with SMT components from tape & reel using Panasonic NPM-W2 pick & place system with electromechanical feeders and ceramic nozzles. After parts were placed, components were visually inspected using a stereo microscope at 30x magnification.

Interpretation and Significance of Results

Prior to stencil printing, the bare PCBs were inspected. A visible concavity difference was observed between the Hot Air Solder Leveling (HASL) finish on the pads on the two boards (Figure 3). The green PCB had more HASL finish with raised surfaces on the lands. After stencil printing solder paste onto both boards, it was observed that more solder paste printed on the flush surface of the blue PCB (Figure 4). Next, components were pick & placed with 40% pickup & mounting speed equating to 1-2 components per second (5,400 components per hour). Two pickup nozzles were selected for the 0201 components; each had a different sized pickup orifice. The first had 100% component coverage in the vacuum orifice, the other with only 80% (Figure 1). It was noted that the second nozzle had a pickup miss rate of 33%, whereas the first had almost 0%. The boards were inspected after pick & place in which some pads were missing components. Results in the chart [Table 1] show how many more parts were successfully pick &

placed onto the blue board when compared to the green board with raised HASL finish on pads. Cells with positive numbers represent a higher number of parts pick & placed onto the blue board; negatively numbered cells mean more parts were pick & placed onto the green board.

Conclusion

The blue boards with flatter finishes had more parts able to be pick & placed onto the board. This is likely due to the HASL free finish of the circuit board in addition to using fresh solder paste and an appropriately sized nozzle to match the size of the part. The red areas of Table 1 indicate a part was likely dropped in travel to the board or moved off the board after other parts were placed. The combination of correct nozzle, fresh solder paste, and flat HASL finish created better manufacturing results with a higher quantity of parts able to be pick and placed.

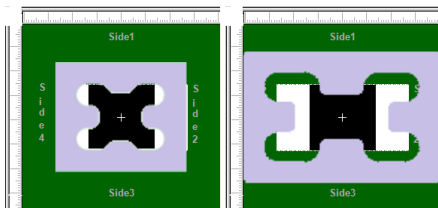


Figure 1: Nozzle size difference for 0201 Resistor

Images

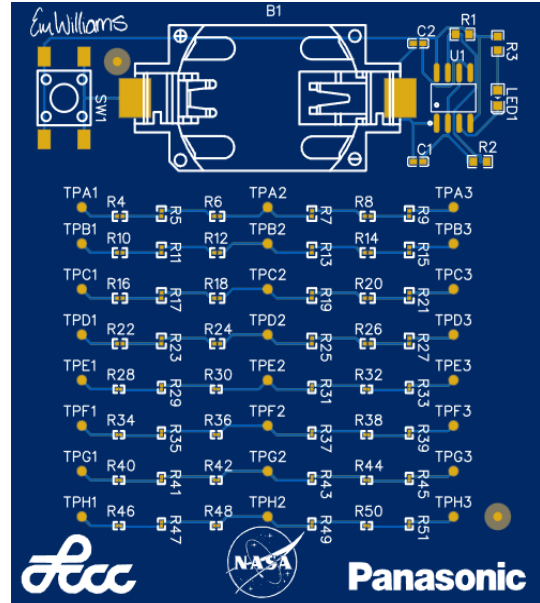


Figure 2: Test PCB designed on easyEDA.com

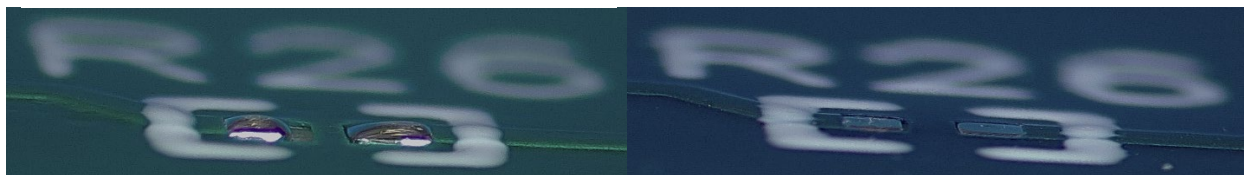


Figure 3: Left, green board has uneven tinned pads. Right, blue boards have uniformly tinned pads.

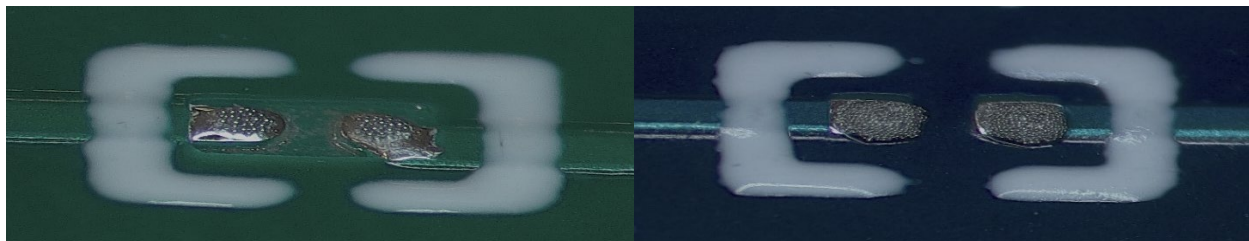


Figure 4: Left, green board has insufficient paste printed. Right, blue board has ideal amount of printed paste.

Table 1: The missing number of components on the blue PCB versus missing components on the green PCB

	Missing # Components on Blue PCB after Pick & Place 40%					
	Green - Blue					
	B1-1	B1-2	B1-3	B2-1	B2-2	B2-3
Row A - 0201	0	-1	0	0	0	0
Row B - 0201	1	3	0	0	1	1
Row C - 0201	2	1	0	0	1	0
Row D - 0201	2	0	0	0	2	0
Row E - 01005	0	0	0	0	4	0
Row F - 01005	1	3	-1	1	3	0
Row G - 01005	0	-1	-2	2	-2	-2
Row H - 01005	2	-1	-3	1	0	0
Positive GREEN numbers = more missing on green = Good						
Negative RED or Orange numbers = more missing on blue = Bad						

Education Scholars

Mars Ecosystem Proposal Project

Student Researcher: Alayna P. Ackley

Advisor: Dr. William Jones

Cedarville University

Department of Education/Science and Mathematics

Abstract

During the Ecology unit I will cover the standard 7.LS.2: In any particular biome, the number, growth and survival of organisms and populations depend on biotic and abiotic factors. This standard will be covered with a project where student's goal is to work in teams to come up with a researched proposal for creating an ecosystem on Mars. Students will be given resources such as NASA articles on plans to create an ecosystem on Mars. They will determine for themselves if Mars is suitable for life by exploring it themselves 3-dimensionally with NASA's free online resource. Students will write a proposal for the organisms that they believe should be used to start an ecosystem on Mars based on what they learn about the planet.

Project Objectives

The primary objective of this unit is of course for students to have a full understanding of biomes to the level of depth expected of the seventh grade level. In order to reach this objective, students will be completing this mars ecosystem proposal project at the end of the biome unit in order to demonstrate their knowledge of biomes as a full understanding which is a level of knowledge required in order to be able to apply what is known to a new context such as mars. As some secondary objectives, through this project the students will practice their collaboration skills and hopefully gain an appreciation for space research and the work NASA does.

Methodology

The biome unit will be covered over a span of ten days. As a quick overview, the bulk of material from the unit is covered through power point instruction, student-led illustrations, and short activities in the first three days. Three of the six major land biomes will be simulated in lab, with students using note cards to practice what they learned over the next three days. The next two days the Mars ecosystem proposal will be introduced and worked on. Wrap-up with group presentations is on day nine, and day ten is test day.

Now I will give more in-depth information on the methodology of the mars ecosystem proposal worked on during days 7-9. On day seven the topic is introduced by watching the Artemis I Mission video from NASA. The students will also receive a rubric so they know what is expected of them. Groups are assigned roles and allowed to begin work, which continues into day eight. Students hopefully finish research and compile their findings into a proposal on day eight, although an extension may be needed. The proposal includes explanation of the requirements for life, how these requirements would be met on Mars, and what organism would be used first. On day nine students will present their proposals to each other or in front of the whole class and receive constructive criticism. This project will capitalize on natural curiosity and enhance cooperation skills through the synthesis of previously known and researched information.

Results Obtained

Since this is a proposed lesson plan, it has not yet been practiced in the classroom. However, the biome unit was covered during field experience in the classroom in much the same way as outlined above. The main difference was that instead of three of the major land biomes being simulated in lab, the original lesson plan had all of the major land biomes simulated. This was in place of the mars ecosystem proposal project, which could be implemented instead. The pre and post-test results for the biomes test is shown in the figure below. It represents the amount of knowledge students gained about biomes from the unit, however as can be seen from the results they did not fully understand the content.

Significance and Interpretation of Results

Based on test results the first few days of instruction needed to be slowed down or information added intermittently between simulations. This is because rushing through the material caused the students to not fully grasp all the content. Since the next six simulation days simply put into practice what they already knew, it did not remedy this missing knowledge by test time although what the students did grasp they had mastered. Also, based on more specific results students struggled on critical thinking questions and expressing their knowledge in writing. This conclusion was made based off of the lack of well-developed responses to short answer questions despite the fact that students aced the multiple choice sections covering the same material. Despite these weaknesses, the biome unit also had a lot of strengths. Students were very engaged in predictions and simulations due to multiple modes of learning when in lab. Also, having multiple days of applying knowledge in new contexts (the different biomes) created confidence and mastery. In the future proposed plan for this unit, the biome background will segway well into the mars proposal and help maintain interest. Also, instead of doing all the instruction at the beginning of the unit the instruction will be staggered in steps between the biome simulation days so that it is not rushed and students don't miss information.

Figures

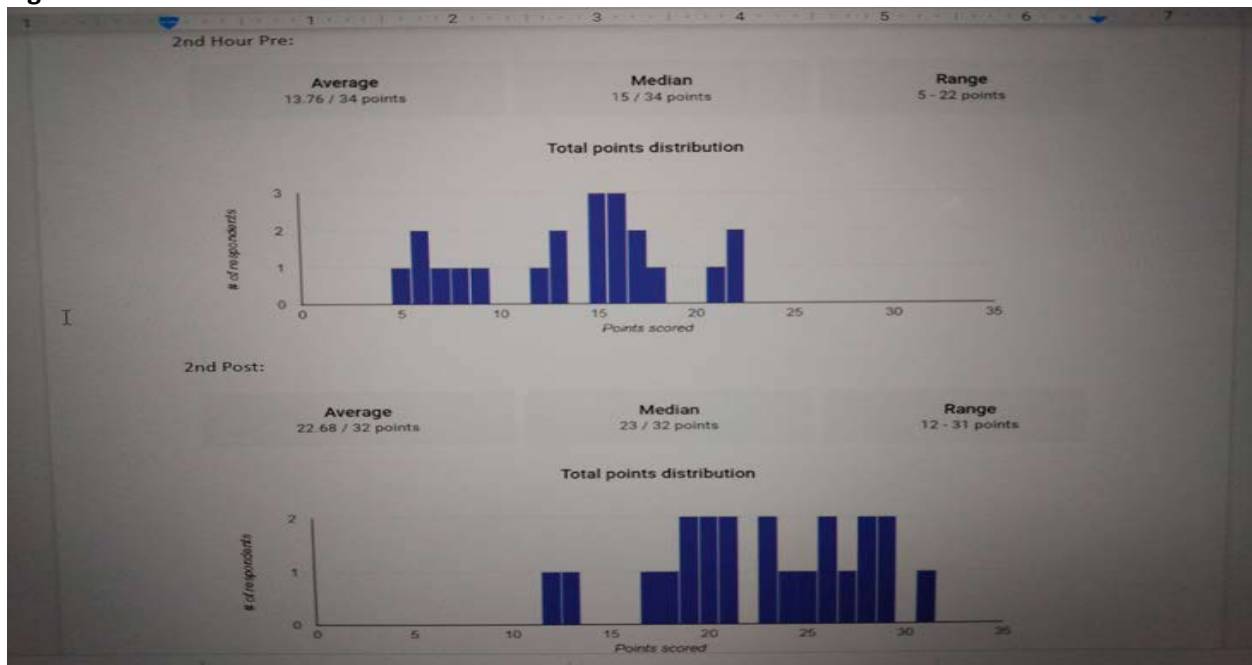


Figure 1: 2nd hour class biomes test pre and post unit instruction.

How Fast is a Launch Vehicle?

Student Researcher: Joelena F. Brown

Advisor: Dr. Tena Roepke

Ohio Northern University
School of Science, Technology, and Mathematics

Abstract

Using activities from the Science Mission Directorate resource page, I was able to create a mini unit plan for junior high students on analyzing and graphing functions. Students will learn about the rockets used to launch satellites into space and the speed at which they do so. Students will use data from the Atlas V 421 launch vehicle to calculate instantaneous speeds. They will use this information to make graphs and to make predictions. Students will then create and launch their own “rocket”. They will perform multiple trials, collecting data on the time and distance travelled. Students will calculate the average speed of each trial and organize the data from their trials. The purpose of this lesson is to raise students’ interest in NASA and space while covering Ohio’s Learning Standards for mathematics.

Project Objectives

The learning objectives of this project for junior high students are to graph and interpret relationships between time and distance, to create a graph and table using experimental data, and to research and learn about space launch vehicles. The objectives for mathematical practice are to reason abstractly and quantitatively, to model with mathematics, and to use appropriate tools strategically.

Methodology Used

This mini unit will be split up into two parts: a research worksheet and a project. This mini unit would likely take 2-3 days to complete. Students will dive into NASA’s informational web pages to explore the Atlas V rocket and launch vehicles. In the worksheet, students will use real data to create graphs and interpret relationships. Students will then use these methods on their own experimental data when they create and launch their own rockets.

Results Obtained

I have yet to test out my mini unit plan, since I am currently placed at a high school for field experience. But I would like to use this plan in my upcoming years as a teacher or student teacher. The mini unit was created for a junior high level but could be adapted for upper-level mathematics.

Significance and Interpretation of Results

Since I have not tested out this unit in the classroom quite yet, I am unable to discuss any results. However, when the project from the OSGC Education Workshop was executed, it was successful. My project is similar and would be conducted in a similar manner. Therefore, I would expect good results. Creating mathematical content that is relevant and models the real world is important in the classroom. Many students often ask, “When will I ever use this?” Using NASA’s many resources and data is a great way to show students the relevancy of mathematics education today. I have learned that creating hands-on projects and utilizing real data are two helpful ways to get students using the various mathematical practices and multiple levels of Bloom’s Taxonomy.

Figures/Charts

Table 1. Table Used in the “Compute the Speed of the Launch Rocket” Activity

Time (sec)	Height (m)	Speed (m/sec)
0	0	0
1	26	
2	58	
3	96	
4	140	

Acknowledgments and References

Activity Adapted From: NASA. “MMS EPO Math Guide.” *Nasa.gov*, mms.gsfc.nasa.gov/epo_math_guide.html. Accessed 14 Jan. 2022.

Project activity inspired by the “Designing a Crew Exploration Vehicle” activity from the NASA/OSGC Education Workshop

Building a Miniature Solar Car using the Engineering Design Process

Student Researcher: Makenna R. Chappell

Advisor: Dr. Todd France

Ohio Northern University

Department of Engineering and Department of Teacher Education

Abstract

Students will create and design a miniature solar car using provided materials and the engineering design process. The students will be given a wide variety of materials with the main goal to create a car that fits the given criteria and constraints. Using the engineering design process, students are expected to brainstorm, sketch, and design the car and once they build a final product, it will be tested, revised, and tested again. Students will determine how mass, the type of light (natural or artificial), and the amount of light (shade or full exposure) affect the speed and position of the car. The students will work separately, but at the end they will race their cars to see which goes the furthest. The main goal of this activity is for students to gain understanding of solar power while utilizing all six steps of the engineering design process

Objectives

By the end of this activity, students should be able to:

1. Create a table for the given experiment
2. Follow the engineering design process for any given problem
3. Sketch and create a design
4. Determine how natural vs. artificial light affect the position traveled by their car
5. Create a presentation or report for their understanding of their results and the engineering design process

Methodology Used

This activity will start with an explanation of the engineering design process.

Similar to the scientific method, the engineering design process requires that the engineer uses specific criteria and constraints provided by the client in order to develop a solution.

After receiving the assignment (the objective), students will read through the assignment to establish the criteria and constraints that their solar car must meet— this includes materials they are limited to, dimensions, what they have to test, etc.

Students will then sketch multiple design ideas and choose whichever one they find best fits the given criteria and constraints.

Students will then construct their design using the provided materials and then test their model with natural and artificial light, determining which one allows for the car to go the farthest over multiple trials. If their first iteration fails, student can evaluate and go forth with a 2nd iteration until the car functions. Students will then put together a presentation or report of their findings to explain their designs.

Assessments / Results

As I am currently not in a field placement, I will not be able to use this lesson this semester. However, I am excited to utilize this in my future classroom.

If I am able to use this activity in the future, I will assess my students in the following ways:

1. Throughout the activity I will observe and ask questions to gauge their understanding of the engineering design process.
2. Collecting and grading their final presentation/report

Conclusion

This activity is aimed towards early high school students but can be easily altered to be used in early grade levels as well. This activity can not only be used to study the effects of different types of light on how far the car may go but can also be used to study the affect the angle of the solar panel has on the speed and/or distance traveled by the car. Teachers can alter what they want their students to measure for this activity to fit different units of study. After I use this activity in a future classroom, my students will be more prepared to solve problems in various classes through the use of the engineering design process.

Mathematics All Over the Space

Student Researcher: Rachael D. Harbaugh

Advisor: Dr. Tena Roepke

Ohio Northern University

Department of Mathematics and Department of Teacher Education

Abstract

This lesson was made to take place in a high school mathematics classroom and is based on the Ohio's Learning Standards. The main idea is for students to be able to create a proportion in order to convert different measurements and weights from Earth to different planets in our solar system. Students will work on a packet that will guide them through the process of learning and applying this information. Here are some conversions they will be working with: miles to lightyears, the temperature of the sun in Celsius and Kelvins, their weight on Earth versus on the moon. This lesson is made to spark interest in the different kinds of mathematics that take place in our solar system.

I plan to take some time to dig into some history of NASA and some key mathematicians. One of my favorite movies is Hidden Figures. I will show a video/ clip from the movie for students to hopefully find motivation and excitement about mathematics.

Objectives

By the end of this lesson, students should be able to:

1. Convert different measurements and weights from Earth to different planets in our solar systems
2. Work with proportions and conversions involving: Miles to lightyears, The temperature of the sun in Celsius and Kelvin, and Their weight on Earth versus the moon
3. Know basic knowledge about the history of NASA and space.

Methodology

This lesson going to be split in to 3 days:

- Day 1 is titled History of NASA and key mathematicians. This day will consist of an introductory reading and then a quick trivia game. We will finish class by watching a short clip from the movie Hidden Figures.
- Day 2 is titled Setting up the Proportions. Students will spend the day researching in groups. They will be finding different conversions that need to be done between Earth and various planets and the moon. I want the students to feel as if they are a team working for NASA and these calculations are important to send an astronaut into space.
- Day 3 is titled Working with the numbers. Now students will be given a packet with specific numbers and problems. These problems will be a mix of both basic computations and conversions.
- These lessons use a mix of learning strategies. All students work in different ways and at different paces. If needed, I will add a fourth day to finish up the assignment.

Results obtained/Significance and Interpretations

I will be unable to do this lesson in my field placement where I am placed this semester because it does not match with the grade level I am teaching. If I am able to teach this lesson in the future, here is how I would plan to assess the students:

- The trivia game would be for fun and just for participation points.
- The research would have no points involved.
- The packet would be collected and graded.
- Throughout the 3 days, I will be sure to ask engaging and intriguing questions and get their responses

Next Generation Scientists Explore Green Energy

Student Researcher: Emily Hippich

Advisor: Bridget Mulvey

Kent State University

Early Childhood Education

Abstract

This lesson is designed as a problem-based learning project and was taught in a third-grade classroom. Students became NASA research scientists and were tasked with designing and implementing a renewable energy resource into their community. This project combined both science and social studies together, as students had to conduct research on the community that they live in. Students became specialists in one type of renewable energy, and then presented their findings to the class. Students were given new groups that had representatives from each type of renewable resource. In these groups, students discussed which renewable energy resource they wanted to design for their community. Students drew a model of their energy resource that included the location it would be placed in their community. This information was pulled together to create a poster board about the renewable energy source each group chose.

Project Objectives

Through this lesson, students will be able to

- distinguish the differences between renewable and nonrenewable resources.
- research a renewable energy resource in their specialist groups using resources given to them.
- apply the information they learned about renewable energy by designing an energy source that is based off a need in their community.

This lesson falls under the 3rd Grade Ohio Science Standard: 3.ESS.2: Earth's resources can be used for energy.

Methodology Used

Problem based learning is an approach used in the classroom in which students work collaboratively to learn about a subject through the experience of solving an open-ended problem. During this lesson, students were able to work collaboratively to research a renewable energy resource. They worked together to read and highlight the important information in a combination of NASA and internet resources. Students were then put into new groups with one representative from each specialist group. Students had to tell their peers what they learned about their renewable energy resource and then work as a group to decide which one they wanted to focus on.

Results Obtained

I was very impressed with the poster boards that the groups created. While the groups were working, I was walking around listening to them as they collaborated and shared ideas. I wanted to be able to hear what they were thinking as well as the ideas they had. This helped me check their understanding of the content and allowed me to see if I needed to clarify any information. I also wanted to check in and make sure the groups were working collaboratively, with everyone in the group having a voice.

Group one designed a blueprint of a rocket ship with solar panels that would supply energy to their community (see figure 1). Group two decided they wanted to create two solar panel designs; one of a

solar panel rocket and another of solar panels on their school roof (see figure 2). Group three designed solar panels that were to be placed on the roof of the school (see figure 3). Group four designed a wind turbine that was going to be placed in a field in their community (see figure 4). I was excited to see that many of the groups decided to include the information they had collected from their research on their poster board.

Significance and Interpretation of Results

The students were all very excited when I introduced this project to them. This excitement contributed to the exceptional amount of work and effort that the students put into their work. The students worked tirelessly for 45 minutes over a two-day span on their research and the final poster board design. The students were able to demonstrate that they can read through articles of information about a given topic and pick out the important details. Students were also able to demonstrate how they could use this information and apply it to a project that was based in their community.

Figures/Charts



Figure 1: Group One's Poster Board on Solar Power



Figure 2: Group Two's Poster Board on Solar Power



Figure 3: Group Three's Poster Board on Solar Energy

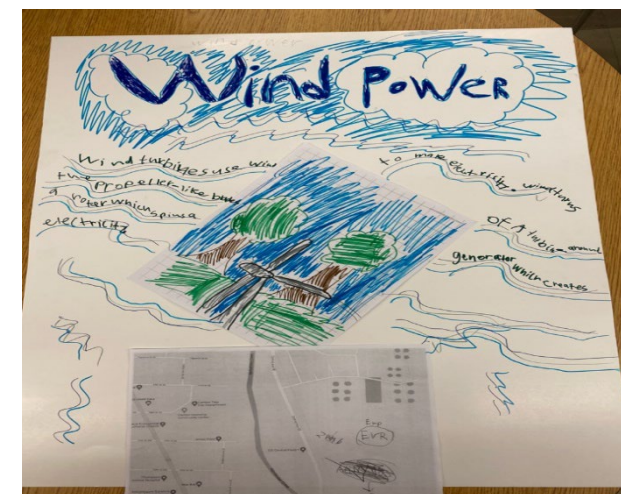


Figure 4: Group Four's Poster Board on Wind Energy

Acknowledgment

I would like to thank my advisor Dr. Bridget Mulvey for the support, guidance, and her time throughout the duration of this project. I would also like to thank my cooperating teacher Kirstie Saunders for giving me the time to work with her students over the course of two days. I would like to thank the Ohio Space Grant Consortium for this amazing opportunity and experience. Last, but certainly not least, I would like to thank my students for the amazing work they did on this project and for giving me the opportunity to work with them every day.

References

- Advantages and challenges of wind energy*. Energy.gov. (n.d.). Retrieved March 21, 2022, from <https://www.energy.gov/eere/wind/advantages-and-challenges-wind-energy>
- How do wind turbines work?* Energy.gov. (n.d.). Retrieved March 21, 2022, from <https://www.energy.gov/eere/wind/how-do-wind-turbines-work>
- Hydropower basics*. Energy.gov. (n.d.). Retrieved March 21, 2022, from <https://www.energy.gov/eere/water/hydropower-basics>
- NASA. (2019, October 9). *Catching rays in the Desert*. NASA. Retrieved March 21, 2022, from <https://earthobservatory.nasa.gov/images/145738/catching-rays-in-the-desert>
- NASA. (2020, July 6). *Capturing wind on Maui*. NASA. Retrieved March 21, 2022, from <https://earthobservatory.nasa.gov/images/147527/capturing-wind-on-maui>
- National Aeronautics and Space Administration. (2009, March). *NASA Green Initiatives*. nasa.gov. Retrieved March 22, 2022, from https://www.nasa.gov/pdf/481133main_NASA_Green_Initiatives.pdf
- Nunez, C. (2021, May 3). *Hydropower Facts and Information*. Environment. Retrieved March 21, 2022, from <https://www.nationalgeographic.com/environment/article/hydropower>
- Patel, K. (2020, February 2). *The largest solar power plant in Europe (for now)*. NASA. Retrieved March 21, 2022, from <https://earthobservatory.nasa.gov/images/146374/the-largest-solar-power-plant-in-europe-for-now>
- Robertson, B. (n.d.). *A Student's Guide to Solar Energy*. A students guide to Solar Energy. Retrieved March 21, 2022, from <https://solarpower.guide/students-guide-to-solar-energy>
- Wind and Hydropower Technologies Program: Advantages and ...* U.S. Department of Energy Energy Efficiency and Renewable Energy. (2006, August 14). Retrieved March 22, 2022, from <https://www.envirothonpa.org/documents/19bHydropowerAdvantagesandDisadvantages.pdf>

NASA Lesson: Ecology on Mars

Student Researcher: McKenna Marcus

Advisor: Brandi Seither, Ed.D.

Baldwin Wallace University
Early Childhood Education

Abstract

This lesson is based on Ohio's Learning Standards for elementary science. For this lesson, students will be studying the environment on the planet Mars. Students will research Mars and its environment. Students will create their own Mars ecosystems with the information gained from their research. Students will develop ecosystems to see how they will interact with the environment on Mars; students will choose to create an ecosystem to see how plants or humans will survive on Mars. Students will receive materials that will allow them to create their own Mars ecosystems. Students will learn about the difference between Mars and Earth's environments during their research. For example, the average temperature is -81 degrees Fahrenheit while the atmosphere is 96% carbon dioxide on Mars. Students will take this information and create ecosystems to see how they will interact with the environment on Mars. For example, one student may make an ecosystem for plants and discover how to survive Mars's environment, while another may choose to create an ecosystem for humans to see what they would need to live on Mars.

Introduction

Ecology on Mars lesson was implemented in a fourth and fifth-grade classroom over the course, where students learned about ecology on Mars. On the first day, students learned about Mars and its environment. Students compared and contrasted Mars's environment to Earth's environment during this time. Students had a class discussion on Mars, which created many questions the students had about Mars and its environment. Students then watched a short video that explained Mars. Students used what they had learned from the video to answer their questions. Students shared their thoughts about Mars. We discussed what would happen if we lived on Mars.

After the discussion, students found out they would be making ecosystems to see if we would be able to live on Mars. Students first had to do more research on Mars. Students use materials and information to create their ecosystems. Students share their findings.

The lesson promoted interdisciplinary learning by providing the students with materials to help them be creative and innovative. Students must develop a design on how they will create their ecosystem and what they will use. Students could redesign and go back to get more materials to redesign their ecosystem throughout this experiment; this allows for ample time for the students to problem solve and modifies their designs.

On the day of the ecosystem, students made their hypothesis on whether or not living things could survive on Mars. Students recorded their observations. Students recorded what modifications would have to be implemented for living things to survive on Mars.

Conclusion

Students successfully understood the ideas through exploration and research during this lesson, which allowed them autonomy over their learning. Students designed an ecosystem for living things to survive on Mars. Throughout the study, students learned new information about Mars's environment. At the end of the lesson, students were able to take their hypothesis and come up with a conclusion to the study.

Students Advocating for Change at the Top

Student Researcher: Kayleigh Penton

Advisor: Dr. Gary Holliday

The University of Akron
Language Arts and Social Studies

Abstract

The purpose of this project is to encourage students to contact policymakers and inquire about issues and challenges they feel closely connected to, especially ones related to sustainability, climate change, STEM education, pollution, and technology. The process is aimed to enhance student knowledge of congressional operations through an innovative approach and inspire them to learn more about our nation and contribute to building a better future. The approach exposes students to interdisciplinary elements and facilitates a valuable opportunity for them to learn how to become active in their community and advocate for change.

Methodology

While learning about the legislative branch in social studies, student took part in a twelve week “Fantasy Congress” competition to further explore the duties, actions, and activity of our nation’s representatives. Students selected a group of 3-4 classmates and together they researched legislators and the potential they have to earn their group points. Based on this research they have the opportunity to “draft” a team of four Senators and six Representative from the pool of U.S congress people. An online platform, organizes and facilitates this process for the students and gives them access to a scoreboard and point breakdown (Loodis Inc., 2018). Members of the group had assigned weeks they had to complete the Fantasy Congress Template (Stuthard, 2020). The template required them to analyze congressional activity such as, sponsorship of bills, speaking on the floor, and even appearances in the news. Each week the drafted legislators acquire points based on their activity and the groups competed for the most points.

Towards the end of the twelve-week period, students had the opportunity to select an issue or challenge they felt connected to and compose an email to an Ohio Senator or Representative either urging them to take action or commending them for actions they have already taken. Students were encouraged to address an issue related to STEM but had the freedom to address other challenges as well. Following a provided template, students stated their position, three supporting points, their personal connection to the issue and its importance, then their proposed plan of action. The students requested a response from their chosen legislator and currently await replies. To conclude, students completed a survey to measure the intended outcomes and gather any additional feedback on their experience.

Results

The focus students highlighted in this study wrote about space exploration and increasing NASA funding, combatting climate change, and preserving and protecting parks all of which expressed incredible points. These students wanted to travel to space, preserve their beloved parks, and prevent the melting of glaciers in Alaska. The final survey results suggested a majority of students felt confidence composing a letter to their representative, inspired to learn more about our nation, and viewed the project as an innovative learning approach.

Conclusion

Students voiced their enjoyment of the Fantasy Congress competition and expressed a better understanding of congressional powers. Majority of the letters indicated a personal connection to the issue and thoroughly researched information. By encouraging them to write these, they became connected to their learning and invested into issues and challenges presented in the community. Upon reflection, I would have provided more guidance as they wrote the letters and engaged in more discussion about their experience, but unfortunately time did not allow this. I hope students feel inspired to advocate for issues they are passionate about, especially ones relating to NASA's core missions, and we look forward to hearing from our legislators.

References

Loodis Inc. . (2018). *Welcome to fantasy congress: Fantasy sports for U.S. politics*. Fantasy Congress. Retrieved March 25, 2022, from <https://fantasycongress.com/>

Stuthard, M. (2020). Fantasy Congress Weekly Report [Class Handout]. Google Classroom.

Liftoff on Mars

Student Researcher: Isaiah A. Reinhard

Advisor: Dr. Lori Ferguson

Cedarville University

Middle Childhood Science Education

Abstract

“Liftoff on Mars” is an educational project that creates an opportunity for students to learn about the concepts of gravitational force, lift, air vehicles, and how they can be applied to earth along with other planets. This project utilizes the mathematics concepts of learning and applying ratios and proportional relationships. Students will first be introduced to concepts of gravity, lift, air vehicles, and the recent milestones made on Mars with NASA’s Mars Helicopter. They will then be tasked with discovering how much lift is required for a helicopter to fly off of the ground on Mars. Students will be given needed information throughout their inquiry of how a helicopter gets off the ground on earth to help guide them. Students will utilize the mathematics concepts and the information about gravitational pull found on the NASA website pertaining to the two different planets. Students will use this to discover how much lift is required to get the helicopter in the air on Mars. This lesson utilizes real-world information and situations to spark interest for students to learn scientific and mathematical concepts.

Project Objectives

The goal for these lesson activities is that students will use concepts of gravity, lift, air vehicles, and proportional relationships to discover how much lift is required to get the Mars helicopter in the air on Earth and compare and contrast this with the paper model helicopter they create.

1. Students will explore air vehicles, lift, and flight and give explanations for what is needed for flight.
2. Students will use their knowledge about gravity, weight, proportional relationships, and ratios to determine how much lift would be required for the Mars Helicopter to fly on Earth and Mars.
3. Students will build a paper model of the Mars Helicopter and compare and contrast it with the real one.

Methodology Used

This mini unit is divided into 3 major segments/lessons. Segment 1: Students will explore air vehicles, lift, and flight and give explanations for what is needed for flight. Segment 2: Students will use their knowledge about gravity, weight, proportional relationships, and ratios to determine how much lift would be required for the Mars Helicopter to fly on Earth and Mars. Segment 3: Students will build a paper model of the Mars Helicopter and compare and contrast it with the real one.

These 3 segments utilize the 5E Model of Instruction: Engage, Explore, Explain, Elaborate, and Evaluate

Lesson

Segment 1: (Engage and Explore) Utilize videos and resources to engage students with content and concepts about lift, gravity, weight, and the NASA Mars Helicopter. Begin with the “Helicopter taking off” and/or “I Fly” videos linked in resources. Now think about asking questions like: Why does this happen? How does this helicopter leave the ground? What keeps the helicopter on the ground when it is not running? How can this person fly? What normally keeps humans on the from flying? How did this human overcome this gravity and weight? Now show the “Mars Helicopter Flight 13” video. Ask

questions like: Where do you think this video was taken? How is it possible for a helicopter to take off? (The goal with these questions is to begin exploring lift and gravity. If students are not reaching these concepts, further prompt them with questions to redirect them. Students can collect and organize information and data however you would like. (i.e. Guided notes, Google Docs, Idea whiteboard, Question worksheet) This day is about gathering the big picture ideas of what is needed for flight.

Segment 2: (Explain and Elaborate) Today you will be explaining and elaborating on the big picture ideas from segment 1. Use the following resources and questions how you see fit to best guide your class in this inquiry. This is a fine details day of the why and the how! Use the Gravity webpage to learn about the relationship between weight on each planet. Use the picture of the different weights in the middle of the NASA gravity webpage to introduce and begin teaching students how to create ratios and proportional relationships. Ask students questions like: “What is the job of a propeller?”, “What normally keeps the helicopter on the ground?”, “How much weight and gravity must be overcome for the helicopter to fly?”, “Let’s pretend that our helicopter weighs 100 lbs. on earth...looking at this chart, how much would it weigh on the moon? What about on mars?”. Say: Did you know that there actually is a helicopter on mars and you’ve already seen pictures it has taken? Have students Draw what they think an air vehicle looks like. Go to NASA webpage for Mars Helicopter to show students. Show students pictures on NASA website of mars helicopter pictures and also of its recent achievements. Now that we know how much the actual helicopter weighs from the website, have students use their new knowledge of lift, gravity, weight, and ratios to figure out how much lift is required on earth and mars to get the helicopter off the ground. The mars helicopter weighs 4 pounds, how much lift would be needed on earth? How much lift would be needed on earth? How much would it weigh on mars? How much lift would be needed on mars? What about the other planets?

Segment 3: (Evaluate) This segment is focused on creating an opportunity for Evaluation. Today you will utilize the “Make a Paper Mars Helicopter” resource from NASA to have students build their own “Mars Helicopter”. Students will compare and contrast the actual Mars helicopter with the one they build today. Have students answer the following questions as their assessment: Compare and Contrast the real Mars Helicopter you learned about with the one that you build. What are the primary differences between the way the one you built works and the actual Mars Helicopter? What are some similarities? (Hint: Think about weight, gravity, and lift.)

Results

I have not yet been able to teach this lesson to students. However, I was able to create lesson plans to highlight purpose, state objectives, give resources, and a general structure. This lesson is extremely flexible and moldable to fit your classroom, teaching style, and student needs. This is not to be a step-by-step procedural unit, but rather a student led inquiry. If done correctly, every time you teach this set of lessons it will look different. I was unable to pilot this mini unit in my classroom because of the curriculum pacing at the school I am student teaching at.

Conclusion

Utilizing NASA resources and recent milestones proves to be a great way to drive student learning. Not only is it interesting, but it is real-life! Utilizing the 5E Model of Instruction is the perfect way to have student centered learning. This model provides the opportunity for students to explore and construct understanding of scientific concepts. Making every student a scientist in your classroom is the goal of a science classroom and utilizing NASA and the 5E Model of Instruction can prove to be an affective coupling. Not only do students take part in the learning process, they can become familiar with the work of NASA and the resources available through NASA.

Acknowledgements and References

5E Model of Instruction:

5E model of instruction. (n.d.). Retrieved April 18, 2022, from <https://ngss.sdcoe.net/Evidence-Based-Practices/5E-Model-of-Instruction>

Segment 1 References:

Video of helicopter taking off:

<https://www.youtube.com/watch?v=klhN6uNFrj0>

Video of “I Fly”

<https://www.youtube.com/watch?v=GB6MHFfEX1k>

Video of Mars Helicopter Flight 13 on the NASA website:

<https://mars.nasa.gov/resources/26363/ingenuity-mars-helicopters-flight-13-zoomed-in-view-from-perseverance/>

Segment 2 References:

NASA Webpage about Lift:

<https://www.nasa.gov/audience/forstudents/k-4/dictionary/Lift.html>

NASA Webpage about Gravity:

<https://spaceplace.nasa.gov/what-is-gravity/en/>

NASA Webpage about Mars Helicopter:

<https://mars.nasa.gov/technology/helicopter/#Quick-Facts>

Segment 3 References:

<https://www.jpl.nasa.gov/edu/learn/project/make-a-paper-mars-helicopter/>

NASA integrated Lesson: Force and Motion in Second Grade

Student Researcher: Erica Schwartz

Advisor: Dr. Brandi Seither

Baldwin Wallace University
Early Childhood Education

Abstract

This lesson is based on Ohio's Learning Standards for elementary science. Students have been introduced to forces and motion. Students will be introduced to gravity and how it affects us here on Earth. At the time the Perseverance Rover had just had its first drive on Mars. Students used Chromebooks to explore all the information NASA had to offer on the rover before a secret mission came in; The Perseverance Mission. NASA called on our class specifically to help. The rover has found a rare alien egg on Mars! The rover was to drop this egg into the Earth's atmosphere to succumb to the dangers that gravity may bring. We tested what might happen dropping a regular chicken egg in the classroom to see some daunting results. Then came the mission, to protect this egg found by the rover we must create our own devices for it to be dropped in using only a variety of found materials.

Students were to construct a sketch of the materials they would use keeping in mind the effect of gravity on Earth. Students must then purchase materials needed from the class store and stay on budget when creating and testing a prototype with a fake egg. Our student scientists rose to the occasion and the teams did not disappoint. After numerous prototypes and testing, the students were ready. After weeks of preparation, students went outside, dropped their egg device from the highest point to demonstrate which final egg protecting devices would be selected. After, the students will reflect on what they accomplished and how Gravity plays its role on Earth.

Introduction

At such a young age, students are only beginning to learn science concepts. This segment was done in a second grade classroom over the course of a week where students are learning about force and motion. On the first day, they are simply learning what a force is (a push or pull). They will then learn speed, and gravity. During our gravity lesson, student begin by answering a think, pair, share about gravity starting their discussion on the subject. Students will then watch a short video then explains gravity to young children. We will use what they learned to answer what would happen if I dropped an egg. Students shared their thoughts in relation to gravity and why the egg would fall to the floor and break. I then dropped an egg from the highest point in our classroom. We discussed what would happen if we didn't have gravity and how our classroom would look.

After all this discussion, students are told that NASA sent a secret mission just for them. As true scientists, students are first have to research the Perseverance Rover. Students use NASA materials and information to find out how it takes samples, sends information, and what its main purpose is. Students share with each other their findings. Students were told the Perseverance Rover found a rare alien egg on Mars and needs to drop it into the Earth's atmosphere without breaking once it lands.

In order to promote interdisciplinary learning, students must purchase materials from the class store using fake money. Once they formulate a plan with their group and purchase their materials, they will test their design with plastic eggs. When testing, students can redesign and purchase more materials if their budget allows. This allows for ample time for the students to problem solve and modify their designs to ensure the egg drop is successful.

On the day of the egg drop students are asked to make a prediction as to what will happen with their egg. We spend time outside dropping each group's egg drop device with an egg inside. We also record each drop in slow motion so students can watch back to see what parts of their device were beneficial or detrimental in the drop. Students submit one last proposal drawing for us to submit to NASA as a potential design. After all this work, students add their thoughts on force and motion to a jamboard.

Conclusion

Creating a hypothetical 'mission' allowed for students to be fully engaged in this project. Students were successful in understanding the ideas through exploration and research that allowed them autonomy over their own learning. Students built on their social emotional skills while working in a variety of grouping to promote a collaborative learning environment. Students were able to learn valuable skills and utilize NASA's online resources.